

**EXPERIMENTAL INVESTIGATIONS OF
PLASMA PARAMETERS AND
SPECIES-DEPENDENT ION ENERGY DISTRIBUTION
IN THE PLASMA EXHAUST PLUME OF A HALL THRUSTER**

by

Sang-Wook Kim

A dissertation submitted in partial fulfillment
of the requirements for the degree of
Doctor of Philosophy
(Aerospace Engineering)
in The University of Michigan
1999

Doctoral Committee:

Associate Professor Alec D. Gallimore, Chairperson
Associate Professor Luis P. Bernal

Associate Professor Mary L. Brake
Professor Ronald M. Gilgenbach

© Sang-Wook Kim 1999
All Rights Reserved

To my parents Myung-Hyun Kim and Hee-Ja Park

ACKNOWLEDGMENTS

This work would not have been possible without the support of great many people. First of all, I would like to express my sincere gratitude to my advisor, Professor Alec Gallimore for his fruitful suggestions, insightful reviews, and his patience. His broad AND deep knowledge of electric propulsion and plasmadynamics is a tribute to his passion for and commitment to his work. Perhaps this is the most important thing I will take from my experience at Michigan.

I would like to thank the members of my dissertation committee, Prof. Bernal, Prof. Brake, and Prof. Gilgenbach for their time in evaluating this thesis.

I am also grateful to Tom Griffin, Gary Gould, and Dave McLean for technical advice and maintenance of the facility. I would like to specially thank Terry Larrow for fabrication of the **ExB** probe components. His helpful suggestions and prompt work made the experiments possible.

I would like to acknowledge the financial support from the Department of Aerospace Engineering at the University of Michigan. I would also like to give thanks to Mr. Mike Day of Space Systems/Loral for the generous loan of the SPT-100 thruster and the PPU.

I am also indebted to my fellow students at PEPL: Frank, Matt, James, George, and Tim, and the past students Brad, Colleen, John, Shawn, and Mark. PEPL is a unique place where each student pursues his/her own study, yet everybody helps everybody else out; a situation rarely seen. I am richer for all the problems we faced and for all the discussions we had. Now you guys can take out the tapes that you have been hiding from me.

I would like to thank my parents for their unconditional and undying support. They have provided me with an environment in which I could get the best opportunities to grow and gain necessary knowledge and skills to be successful in life. This work is the result of their foresight and efforts.

I would like to express my sincere thanks to the Mulherns. I could not have survived my life in America if it had not been for them. I would like to especially thank Dan, who has been my brother, counselor, and best friend, who has been there and supported me always. I would like to thank Etsu who has also been there for me no matter what. The way he lives his life is a source of inspiration for me.

Finally, I would like to express my deepest thanks to my wife, Miki, who gave me the strength to finish this work when I thought I was never going to. She has believed in me and supported me in every way humanly possible. I thank her for that. And to my newborn daughter, Naomi; thanks for making me smile.

PREFACE

This research focuses on characterizing plasma properties and species-dependent ion energy distribution in the plasma exhaust plume of a Hall thruster. These characteristics can provide much insight into the behavior of multiply charged propellant ions in the thruster. Understanding and characterizing the behavior of multiply charged propellant ions is an important aspect of engine development because the production of these ions affects the efficiency and lifetime of the thruster. Also, the presence of multiply charged propellant ions in the thruster plume has significant effects on the operation and lifetime of the spacecraft.

To characterize the plasma properties in the Hall thruster plume, plasma parameters were measured using electrostatic probes over an extensive volume of the thruster plume from the very-near-field region (10 mm to 200 mm downstream of the thruster exit) to the near- and far-field region (25 cm to 1 m downstream of the thruster exit). Although there have been many studies of Hall thruster plume characteristics, the combined data of the very-near-field and the near- and far-field plume studies provided the most comprehensive collection of plasma parameters in the Hall thruster plume.

To characterize the species-dependent ion parameters in the Hall thruster plume, an **ExB** probe was utilized to measure ion energy distributions of each ion species over a large volume of the thruster plume in the near- and far-field region. The measured probe traces were curve-fitted with a distribution function model based on the kinetic theory of gases to obtain ion energy distribution functions of each ion species at various locations in the thruster plume. The **ExB** probe technique was the first high-resolution, species-dependent, direct measurements of ion energy distribution in the Hall thruster plume.

The ion energy distributions measured by the **ExB** probe revealed the existence of Xe^{4+} ions. This was the first experiment that had directly measured the Xe^{4+} ions in the Hall thruster plume. The angular profiles of beam energy and ion species fractions obtained from the ion energy distribution functions gave rise to a simple ionization and acceleration mechanism in the Hall thruster discharge chamber. The proposed mechanism matched very well with the behavior of the ion parameters within -20° 20° off thruster axis. The sharp change in the ion species fractions near -20° -10° and 10° 20° implied a significant fact that the region of the primary production for Xe^{1+} ions and the region of the primary production for multiply charged ions were clearly separated by a narrow boundary in the discharge chamber. The angle at which this sharp change occurred, along with a simple geometric calculation, suggested that the discharge chamber geometry was not the only factor limiting the angle of ion velocities exiting the thruster. Another factor limiting the exiting angle of ions was believed to be the accelerating force of the electric field in the discharge chamber, which makes the ion trajectories in the discharge chamber parabola-like rather than straight lines. The data of ion energy spread showed that the results of two previous studies on the subject, which seemed to disagree by an order of magnitude, were actually describing the same parameter from different points of view. The primary factor that cleared the confusion was the three-dimensional nature of the ion distribution function.

It is author's hope that the results of this work will provide meaningful assistance to the development of Hall thruster technology and, ultimately, contribute to the exploration of our solar system and beyond.

TABLE OF CONTENTS

DEDICATION	ii
ACKNOWLEDGMENTS	iii
PREFACE	v
LIST OF FIGURES	xi
LIST OF TABLES	xvii
LIST OF SYMBOLS	xviii
 CHAPTERS	
1 INTRODUCTION	1
<i>1.1 Electric Propulsion</i>	<i>1</i>
<i>1.2 Motivation</i>	<i>9</i>
<i>1.3 Review of Past Research</i>	<i>14</i>
1.3.1 Performance Evaluation of SPT-100	14
1.3.2 Exhaust Plume Study of SPT-100	15
<i>1.4 Overview of This Research</i>	<i>19</i>
<i>1.5 Experimental Facility</i>	<i>21</i>
<i>Reference to Chapter 1</i>	<i>23</i>
2 LANGMUIR PROBE AND FARADAY PROBE ANALYSIS	27
2.1 Langmuir Probe Theory	27
2.2 Langmuir Probe Measurement Error.....	31

2.3	<i>Faraday Probe Theory</i>	33
2.4	<i>Faraday Probe Measurement Error</i>	34
	<i>Reference to Chapter 2</i>	37
3	VERY-NEAR-FIELD PLUME STUDY OF THE SPT-100	38
3.1	<i>Introduction</i>	38
3.2	<i>Experimental Set-Up For Very-Near-Field Study</i>	38
3.3	<i>Description of Langmuir Probe Used in Very-Near-Field Study</i>	41
3.4	<i>Description of Faraday Probe Used in Very-Near-Field Study</i>	42
3.5	<i>Results and Discussion</i>	43
3.5.1	<i>Ion Current Density in Very-Near-Field</i>	44
3.5.2	<i>Electron Temperature in Very-Near-Field</i>	48
3.5.3	<i>Electron Number Density in Very-Near-Field</i>	51
3.6	<i>Conclusions</i>	55
	<i>Reference to Chapter 3</i>	56
4	NEAR- AND FAR-FIELD PLUME STUDY OF THE SPT-100.....	58
4.1	<i>Introduction</i>	58
4.2	<i>Experimental Set-Up For Near- and Far-Field Study</i>	58
4.3	<i>Description of Langmuir Probe Used in Near- and Far-Field Study</i>	63
4.4	<i>Description of Faraday Probe Used in Near- and Far-Field Study</i>	63
4.5	<i>Results and Discussion</i>	63
4.5.1	<i>Ion Current Density in Near- and Far-Field</i>	64
4.5.2	<i>Electron Temperature in Near- and Far-Field</i>	71
4.5.3	<i>Electron Number Density in Near- and Far-Field</i>	73
4.5.4	<i>Plasma Potential in Near- and Far-Field</i>	75
4.5.5	<i>Comparison With Very-Near-Field Study</i>	76
4.6	<i>Conclusions</i>	78
	<i>Reference to Chapter 4</i>	77
5	EXB PROBE ANALYSIS	80
5.1	<i>Introduction</i>	80

5.2	<i>Theory of ExB Probe</i>	82
5.3	<i>Description of ExB Probe</i>	87
5.4	<i>ExB Probe Output Current Considerations</i>	96
5.5	<i>ExB Probe Measurement Error</i>	100
5.5.1	Uncertainty in Probe Current and Voltage Measurements and Probe Calibration	100
5.5.2	Uncertainty in Energy Measurements due to Probe Resolution	101
5.5.3	Uncertainty in Energy Measurements due to Particle Interactions inside the ExB Probe	105
5.5.4	Summary of ExB Probe Measurements Error	113
5.6	<i>Experimental Set-Up for ExB Probe Measurements</i>	113
	<i>Reference to Chapter 5</i>	117
6	EXB PROBE MEASUREMENTS OF THE SPT-100 PLUME	121
6.1	<i>Introduction</i>	121
6.2	<i>Identification of Peaks in ExB Probe Trace</i>	122
6.2.1	Charge Exchange Collisions	122
6.2.2	Elastic Collisions	123
6.2.3	Entrainment of Background Gases	124
6.3	<i>Ion Energy Measurements at 25 cm from the Exit Plane</i>	129
6.4	<i>Ion Energy Measurements at 50 cm from the Exit Plane</i>	137
6.5	<i>Ion Energy Measurements at 75 cm from the Exit Plane</i>	144
6.6	<i>Ion Energy Measurements at 1 m from the Exit Plane</i>	149
6.7	<i>Conclusions</i>	155
	<i>Reference to Chapter 6</i>	155
7	KINETIC ANALYSIS OF EXB PROBE RESULTS	158
7.1	<i>Introduction</i>	158
7.2	<i>Modeling of Ion Energy Distribution Function</i>	159
7.3	<i>Curve-Fit Results and Discussions</i>	166
7.3.1	Exponential Factor n of the Ion Energy Distribution Functions.....	167
7.3.2	Beam Energy E_b	171
7.3.3	Ion Energy Spread	187
7.3.4	Ion Species Fractions	197

7.4 Conclusions	202
Reference to Chapter 7.....	198
8 CONCLUSIONS AND SUGGESTED FUTURE WORK	206
8.1 Conclusions	206
8.2 Future Work.....	209
Reference to Chapter 8.....	206
BIBLIOGRAPHY	213

LIST OF FIGURES

Figure

Figure 1-1	Comparison of initial spacecraft mass and propellant mass between an electric propulsion system with 3000 sec I_{sp} and a chemical propulsion system with 450 sec I_{sp}	3
Figure 1-2	Schematic of an Arcjet (Electrothermal acceleration).....	4
Figure 1-3	Schematic of a MPD thruster (Electromagnetic acceleration).....	5
Figure 1-4	Schematic of a Hall thruster (Electrostatic acceleration).....	6
Figure 1-5	Photograph of the SPT-100.....	7
Figure 1-6	Schematic of a basic SPT-100 operation. It shows the dominant axial electric field, dominant radial magnetic field, the electrons from the cathode trapped in the ExB drift, and the electrons from the cathode for neutralizing the ion beam.	8
Figure 1-7	Schematic of the 9 by 6 meter vacuum chamber. Positions of the thruster and probes for each study are indicated.....	22
Figure 2-1	A typical Langmuir probe characteristic.....	28
Figure 2-2	A typical plot of $\ln(I_p+I_+) vs$ Probe Voltage.	30
Figure 3-1	Schematic of the experimental set-up for the very-near-field study (not to scale).....	40
Figure 3-2	Probe circuit used in the very-near-field study.	41
Figure 3-3	Schematic of the miniature Langmuir probe used in the very-near-field study.....	42
Figure 3-4	Schematic of the miniature Faraday probe used in the very-near-field study.	43
Figure 3-5	Radial profiles of ion current density at different axial locations from the SPT-100 exit plane in the very-near-field.	45
Figure 3-6	Radial profiles of electron temperature at different axial locations from the SPT-100 exit plane in the very-near-field.	49
Figure 3-7	Radial profiles of electron number density at different axial locations from the SPT-100 exit plane in the very-near-field.	52
Figure 4-1	Schematic of the thruster-probe arrangement for the near- and far-field study (not to scale)....	60

Figure 4-2	Schematic of the experimental set-up for the near- and far-field study (not to scale).....	61
Figure 4-3	Faraday probe circuit used in the near- and far-field study.	62
Figure 4-4	Angular profiles of ion current density at 25 cm, 50 cm, 75 cm, and 1 m from the SPT-100 exit plane in logarithmic scale.....	65
Figure 4-5	Angular profiles of ion current density at 25 cm, 50 cm, 75 cm, and 1 m from the SPT-100 exit plane in linear scale.....	66
Figure 4-6	Ion current densities at 25 cm, 50 cm, 75 cm, and 1 m from the thruster exit plane, normalized to a distance of 1 m from the thruster using $1/r^2$ dependence.	69
Figure 4-7	Angular profiles of electron temperature at 25 cm, 50 cm, 75 cm, and 1 m from the SPT-100 exit plane.	72
Figure 4-8	Angular profiles of electron number density at 25 cm, 50 cm, 75 cm, and 1 m from the SPT-100 exit plane.	74
Figure 4-9	Angular profiles of plasma potential at 25 cm, 50 cm, 75 cm, and 1 m from the SPT-100 exit plane.	76
Figure 4-10	Comparison of the near- and far-field data with the very-near-field data at 20 cm from the SPT-100 exit plane.....	77
Figure 5-1	Schematic of ExB probe. A uniform electric field is formed by applying a voltage between the two parallel E-field plates. A uniform magnetic field is formed by four permanent magnets (not shown in the figure).	83
Figure 5-2	Schematic of the ExB probe viewed through the top plate. Collimated ion beam enters the ExB section from the left. The shaded parts are made of carbon steel in order to focus the magnetic field energy in the ExB section. The collimator and collector tubes were made of stainless steel. The other parts are made of aluminum. Coax cables are attached to the E-field bias plate at one end and a BNC connector at the other end. The CEM collector has two coax cables; one of which is a high voltage coax cable for supplying the power to the CEM and the other is for measuring the collector current. The schematic also shows the path of the ions collected by the CEM and the path of the deflected ions.	88
Figure 5-3	Schematic of the ExB probe viewed through an end plate. The shaded parts are made of carbon steel in order to focus the magnetic field energy in the ExB section. The other parts are made of aluminum. The electric field formed between the two E-field bias plates is in the horizontal direction. The magnetic field formed by the permanent magnets is in the vertical direction. The collimated ion beam enters the ExB section in the direction perpendicular to the page.	89
Figure 5-4	Photograph of the ExB probe on the supporting platform. The cylindrical tube in front attached to the probe body is the collimator. The probe body was isolated electrically from the platform using Teflon sheets, so that it was at the plasma floating potential.	90
Figure 5-5	Photograph of the collimator. The collimator is covered by fiberglass tape to prevent material damage.	90

Figure 5-6	Photograph of the CEM detector housing. The coax cables supplying the E-field bias voltage are shown. Also shown are the collector current signal cable and the power cable of the CEM. The CEM housing was covered by non-conducting, highly-heat-resistant material to prevent plasma particles from leaking into the detector.	91
Figure 5-7	Comparison between ExB traces obtained with different CEM inlet voltages. The bottom graph shows the comparison of the traces in the top graph normalized with each trace's maximum value. It shows no influence of the CEM inlet voltage on the shape of the ExB probe traces, though there is a tendency for noisier traces with increased CEM inlet voltage...	94
Figure 5-8	An example of an ExB probe trace for a multi-species ion plasma flow where each ion species has a single energy. The width of the peak, $2w$, is the probe resolution.....	101
Figure 5-9	Schematic of the ExB probe resolution calculation. The curved line represents the path of an ion whose energy appears at $V_p = V_c + w$ (or $V_p - w$) on the ExB probe trace, but would have at $V_p = V_c$ if the ion came into the ExB section in the direction parallel to the probe axis (the normal entrance in the z-direction).	102
Figure 5-10	Comparisons of ExB traces obtained over a period of time at various positions in the thruster plume.....	107
Figure 5-11	Comparisons of ExB traces obtained over a period of time at various positions in the thruster plume.....	108
Figure 5-12	Comparisons of normalized ExB traces obtained over a period of time at various positions in the thruster plume.....	111
Figure 5-13	Comparisons of normalized ExB traces obtained over a period of time at various positions in the thruster plume.....	112
Figure 5-14	Schematic of the experimental set-up for the ExB probe measurements (not in real scale)...	115
Figure 5-15	Photograph of the experimental set-up showing the relative position of the SPT-100 and the ExB probe. Also shown are the rotary platform and the positioning system.....	115
Figure 5-16	Photograph of the experimental set-up. The thruster-probe position shown here represents a measurement point at -90 degrees off thruster axis. During the measurements, the entire platform supporting the ExB probe was covered with low-sputter-yield flexible graphite sheets to prevent material damage and to minimize sputtering due to high energy ion impacts.....	116
Figure 5-17	Schematic of the ExB probe circuit.	117
Figure 6-1	Ion current as a function of ion energy at 0° , 5° , 10° , 11° , and 20° off the thruster axis at 50 cm from the center of the SPT-100 exit plane.	127
Figure 6-2	Ion current as a function of ion energy at 0° , 5° , 9° , 10° , and 15° off the thruster axis at 25 cm from the center of the SPT-100 exit plane.	132
Figure 6-3	Ion current as a function of ion energy at 20° , 30° , 40° , 50° , and 60° off the thruster axis at 25 cm from the center of the SPT-100 exit plane.	133
Figure 6-4	Ion current as a function of ion energy at -3° , -5° , -10° , -15° , and -20° off the thruster axis at 25 cm from the center of the SPT-100 exit plane.	134

Figure 6-5	Ion current as a function of ion energy at -30° , -40° , -50° , -57° , and -60° off the thruster axis at 25 cm from the center of the SPT-100 exit plane.	135
Figure 6-6	Ion current as a function of ion energy at -80° , -100° , and -105° off the thruster axis at 25 cm from the center of the SPT-100 exit plane.	136
Figure 6-7	Ion current as a function of ion energy at 0° , 5° , 10° , 11° , and 12° off the thruster axis at 50 cm from the center of the SPT-100 exit plane.	139
Figure 6-8	Ion current as a function of ion energy at 14° , 15° , 20° , 30° , and 40° off the thruster axis at 50 cm from the center of the SPT-100 exit plane.	140
Figure 6-9	Ion current as a function of ion energy at 50° , 60° , and 66° off the thruster axis at 50 cm from the center of the SPT-100 exit plane.	141
Figure 6-10	Ion current as a function of ion energy at -5° , -10° , -11° , -12° , and -15° off the thruster axis at 50 cm from the center of the SPT-100 exit plane.	142
Figure 6-11	Ion current as a function of ion energy at -20° , -30° , -40° , and -50° off the thruster axis at 50 cm from the center of the SPT-100 exit plane.	143
Figure 6-12	Ion current as a function of ion energy at 0° , 5° , 10° , 14° , and 20° off the thruster axis at 75 cm from the center of the SPT-100 exit plane.	145
Figure 6-13	Ion current as a function of ion energy at 30° , 40° , 50° , 60° , and 70° off the thruster axis at 75 cm from the center of the SPT-100 exit plane.	146
Figure 6-14	Ion current as a function of ion energy at -5° , -10° , -11° , -13° , and -15° off the thruster axis at 75 cm from the center of the SPT-100 exit plane.	147
Figure 6-15	Ion current as a function of ion energy at -20° , -30° , -40° , and -50° off the thruster axis at 75 cm from the center of the SPT-100 exit plane.	148
Figure 6-16	Ion current as a function of ion energy at 0° , 5° , 10° , 15° , and 18° off the thruster axis at 1 m from the center of the SPT-100 exit plane.	150
Figure 6-17	Ion current as a function of ion energy at 19° , 20° , 25° , 30° , and 40° off the thruster axis at 1 m from the center of the SPT-100 exit plane.	151
Figure 6-18	Ion current as a function of ion energy at 50° , 60° , and 70° off the thruster axis at 1 m from the center of the SPT-100 exit plane.	152
Figure 6-19	Ion current as a function of ion energy at -5° , -10° , -15° , -16° , and -18° off the thruster axis at 1 m from the center of the SPT-100 exit plane.	153
Figure 6-20	Ion current as a function of ion energy at -19° , -20° , -30° , and -40° off the thruster axis at 1 m from the center of the SPT-100 exit plane.	154
Figure 7-1	Comparisons between the Maxwellian fit, Druyvesteyn fit, and curve-fit of Eqn. 7-9 to the Xe^{2+} ion peak of the measured ExB probe trace on the thruster axis at 50 cm from the thruster exit.	164
Figure 7-2	Sum of the curve fits of Eqn. 7-9 for Xe^{1+} , Xe^{2+} , Xe^{3+} , and Xe^{4+} ion peaks overlaid on the measured ExB probe trace on the thruster axis at 50 cm from the thruster exit.	165

Figure 7-3	Exponential factor n for Xe^{1+} , Xe^{2+} , and Xe^{3+} ions energy distribution functions obtained from the curve-fits of the ExB probe data at 25 cm from the thruster exit.....	169
Figure 7-4	Exponential factor n for Xe^{1+} , Xe^{2+} , and Xe^{3+} ions energy distribution functions obtained from the curve-fits of the ExB probe data at 50 cm from the thruster exit.....	169
Figure 7-5	Exponential factor n for Xe^{1+} , Xe^{2+} , and Xe^{3+} ions energy distribution functions obtained from the curve-fits of the ExB probe data at 75 cm from the thruster exit.....	170
Figure 7-6	Exponential factor n for Xe^{1+} , Xe^{2+} , and Xe^{3+} ions energy distribution functions obtained from the curve-fits of the ExB probe data at 1 m from the thruster exit.....	170
Figure 7-7	Angular profiles of beam energy per charge of Xe^{1+} , Xe^{2+} , and Xe^{3+} ions in the SPT-100 plume at 25 cm from the thruster exit.....	172
Figure 7-8	Schematic showing the relationship between the location of ionization and the possible angle of ion velocity vector with respect to the thruster axis. It shows that the possible exit angle of ion velocity vector increases as the location of ionization moves downstream in the thruster discharge chamber. Also shown is a schematic of the electric field line in the discharge chamber formed between the cathode and the anode.....	173
Figure 7-9	Angular profiles of the differences in beam energy per charge between Xe^{2+} and Xe^{1+} ions and between Xe^{3+} and Xe^{1+} ions in the SPT-100 plume at 25 cm from the thruster exit.....	175
Figure 7-10	Angular profiles of beam energy per charge of Xe^{1+} , Xe^{2+} , and Xe^{3+} ions in the SPT-100 plume at 50 cm from the thruster exit.....	179
Figure 7-11	Angular profiles of the differences in beam energy per charge between Xe^{2+} and Xe^{1+} ions and between Xe^{3+} and Xe^{1+} ions in the SPT-100 plume at 50 cm from the thruster exit.....	180
Figure 7-12	Angular profiles of beam energy per charge of Xe^{1+} , Xe^{2+} , and Xe^{3+} ions in the SPT-100 plume at 75 cm from the thruster exit.....	182
Figure 7-13	Angular profiles of the differences in beam energy per charge between Xe^{2+} and Xe^{1+} ions and between Xe^{3+} and Xe^{1+} ions in the SPT-100 plume at 75 cm from the thruster exit.....	183
Figure 7-14	Angular profiles of beam energy per charge of Xe^{1+} , Xe^{2+} , and Xe^{3+} ions in the SPT-100 plume at 1 m from the thruster exit.....	184
Figure 7-15	Angular profiles of the differences in beam energy per charge between Xe^{2+} and Xe^{1+} ions and between Xe^{3+} and Xe^{1+} ions in the SPT-100 plume at 1 m from the thruster exit.....	185
Figure 7-16	Comparison of beam energy per charge of Xe^{1+} ions in the SPT-100 plume between the data at 25 cm, 50 cm, 75 cm, and 1 m from the thruster exit.....	186
Figure 7-17	Comparison of beam energy per charge of Xe^{2+} ions in the SPT-100 plume between the data at 25 cm, 50 cm, 75 cm, and 1 m from the thruster exit.....	186
Figure 7-18	Comparison of beam energy per charge of Xe^{3+} ions in the SPT-100 plume between the data at 25 cm, 50 cm, 75 cm, and 1 m from the thruster exit.....	186
Figure 7-19	Comparison between the ion energy spread obtained from the distribution function and T_{eff} for Xe^{2+} ions at 50 cm from the thruster exit.....	190

Figure 7-20 Comparison between the ion energy spread to the left of the peak and that to the right of the peak for Xe^{2+} ions at 50 cm from the thruster exit	191
Figure 7-21 Ion energy spread for Xe^{1+} , Xe^{2+} , and Xe^{3+} ions in the SPT-100 plume at 25 cm from the thruster exit.....	193
Figure 7-22 Ion energy spread for Xe^{1+} , Xe^{2+} , and Xe^{3+} ions in the SPT-100 plume at 50 cm from the thruster exit.....	194
Figure 7-23 Ion energy spread for Xe^{1+} , Xe^{2+} , and Xe^{3+} ions in the SPT-100 plume at 75 cm from the thruster exit.....	195
Figure 7-24 Ion energy spread for Xe^{1+} , Xe^{2+} , and Xe^{3+} ions in the SPT-100 plume at 1 m from the thruster exit.....	196
Figure 7-25 Ion species fractions of Xe^{1+} , Xe^{2+} , and Xe^{3+} ions in the SPT-100 plume at 25 cm from the thruster exit.....	199
Figure 7-26 Ion species fractions of Xe^{1+} , Xe^{2+} , and Xe^{3+} ions in the SPT-100 plume at 50 cm from the thruster exit.....	199
Figure 7-27 Ion species fractions of Xe^{1+} , Xe^{2+} , and Xe^{3+} ions in the SPT-100 plume at 75 cm from the thruster exit.....	200
Figure 7-28 Ion species fractions of Xe^{1+} , Xe^{2+} , and Xe^{3+} ions in the SPT-100 plume at 1 m from the thruster exit.....	200

LIST OF TABLES

Table

Table 3-1	Total ion current at different distances from the SPT-100 exit plane in the very-near-field.	46
Table 4-1	Total ion current at different distances from the SPT-100 exit plane in the near- and far-field. .	70
Table 6-1	Probe voltages V_p and energies E_i of the entrained species in the SPT-100 plume when the entrained species are accelerated by the potential of 229 V. The energies are calculated as though these species were xenon ions. The bold numbers in the energy column indicates the energies less than 1200 eV, the maximum possible E_i for quadruply ionized xenon.	125
Table 7-1	Comparison between ExB probe-measured ion species fractions with values obtained by King [2] and Manzella [17]......	197

LIST OF SYMBOLS

Symbol

A_c	current collector area
A_p	probe area
\mathbf{B}	magnetic field
B	magnetic field strength
c	speed of light
d	distance between the two E-field bias plates of the \mathbf{ExB} probe
dE_i	ion energy element
\mathbf{E}	electric field
E	electric field strength
e	elementary charge; base of natural logarithms
E_b	ion beam energy
E_i	ion energy [eV]
\mathbf{F}	force vector
$f(E_i)$	ion energy distribution function
$f(u_i)$	ion speed distribution function
$f(\mathbf{u}_i)$	ion velocity distribution function
G_{CEM}	gain of CEM
i_+	ion saturation current
I_i	CEM collector current
i_p	probe current
j_i	ion current density

k	Boltzmann's constant
M_i	ion mass
n_e	electron number density
n_i	ion number density
N_i	total ion number density
q_i	charge state of ion
R	probe distance from the center of the thruster exit plane
T_e	electron temperature
T_i	ion temperature
u_b	ion beam speed
\mathbf{u}_b	ion beam velocity
u_i	ion speed
\mathbf{u}_i	ion velocity
V_d	thruster discharge voltage
V_f	floating potential
V_i	acceleration voltage
V_p	probe voltage with respect to ground
Z	axial probe distance from the thruster exit plane
	mean free path
	probe angle off thruster axis

CHAPTER 1

INTRODUCTION

1.1 Electric Propulsion

Electric propulsion has attracted much attention in the past few decades as the exploration of the solar system and beyond grew and the missions became more energetic. The field of electric propulsion as we know it today began in the 1960's with the goal of developing new and improved propulsion devices for future space missions. The primary attraction of electric propulsion systems lies in their highly efficient utilization of propellant [1, 2].

The challenge for a rocket system is to deliver as much payload as possible with maximum efficiency. The necessary energy for any mission is related to its v , the necessary change in velocity during the mission. And the propulsion requirement for the mission is characterized by the rocket equation:

$$\frac{M_{\text{initial}}}{M_{\text{final}}} = \exp \frac{v}{u_e} , \quad \text{Eqn. 1-1}$$

where M_{initial} is the initial mass of the rocket including fuel, M_{final} is the final mass of the rocket at the end of the thrust period, and u_e is the equivalent exhaust velocity. Since the quantity of energy (per unit mass of propellant) that can be released during combustion is limited by the fundamental chemical energy of the propellant(s), u_e is essentially fixed for chemical rockets. Then, the mass of propellant required increases exponentially with

increasing v for chemical rockets. Therefore, the mission will suffer a decrease in payload mass or an increase in cost with increasing v .

Electric propulsion systems, on the other hand, generate thrust by converting electrical energy to propellant kinetic energy. Thus, it is possible to minimize the mass ratio $M_{\text{initial}}/M_{\text{final}}$ by increasing the exhaust velocity for a given v . Consequently, these systems are suited for those missions with high v . These systems are typically low thrust (thus for use in space only) and require a longer thrust period to achieve the required v than chemical rocket systems. Another advantage of electric propulsion systems over conventional chemical rockets is high specific impulse I_{sp} , which is defined as:

$$I_{\text{sp}} = \frac{T}{\dot{m}g_0} = \frac{u_e}{g_0} \quad \text{for constant thrust and flow rate in space,} \quad \text{Eqn. 1-2}$$

where T is the thrust, \dot{m} is the propellant mass flow rate, and g_0 is the acceleration due to gravity at the earth's surface. In MKS units, u_e and I_{sp} are thus conveniently related by a factor of approximately 10. A specific impulse is often interpreted as a measure of how efficiently the propellant is used. Then, it would seem desirable to have as large a specific impulse as possible. This conclusion holds directly for chemical rockets. However, for electric propulsion systems, high specific impulse implies massive power-generating equipment; hence maximum specific impulse does not generally mean the best system performance. Despite this, electric propulsion systems can attain much higher specific impulse than their chemical rocket counterparts because of their high exhaust velocity. For example, the maximum exhaust velocity a chemical rocket can achieve is roughly 5000 m/s which corresponds to a specific impulse of 510 sec. Meanwhile, a 1.5 kW Hall thruster can achieve an exhaust velocity of 15000 m/s which corresponds to a

specific impulse of approximately 1500 sec. Even a low power arcjet, which generally has among the lowest specific impulses of all electric propulsion systems, can attain a 600 sec specific impulse. Therefore, electric propulsion systems, through their high exhaust velocity and high specific impulse, can deliver more payload mass or save more launching mass for large v missions. This is demonstrated graphically in Figure 1-1 which compares the initial spacecraft mass and propellant mass between an electric

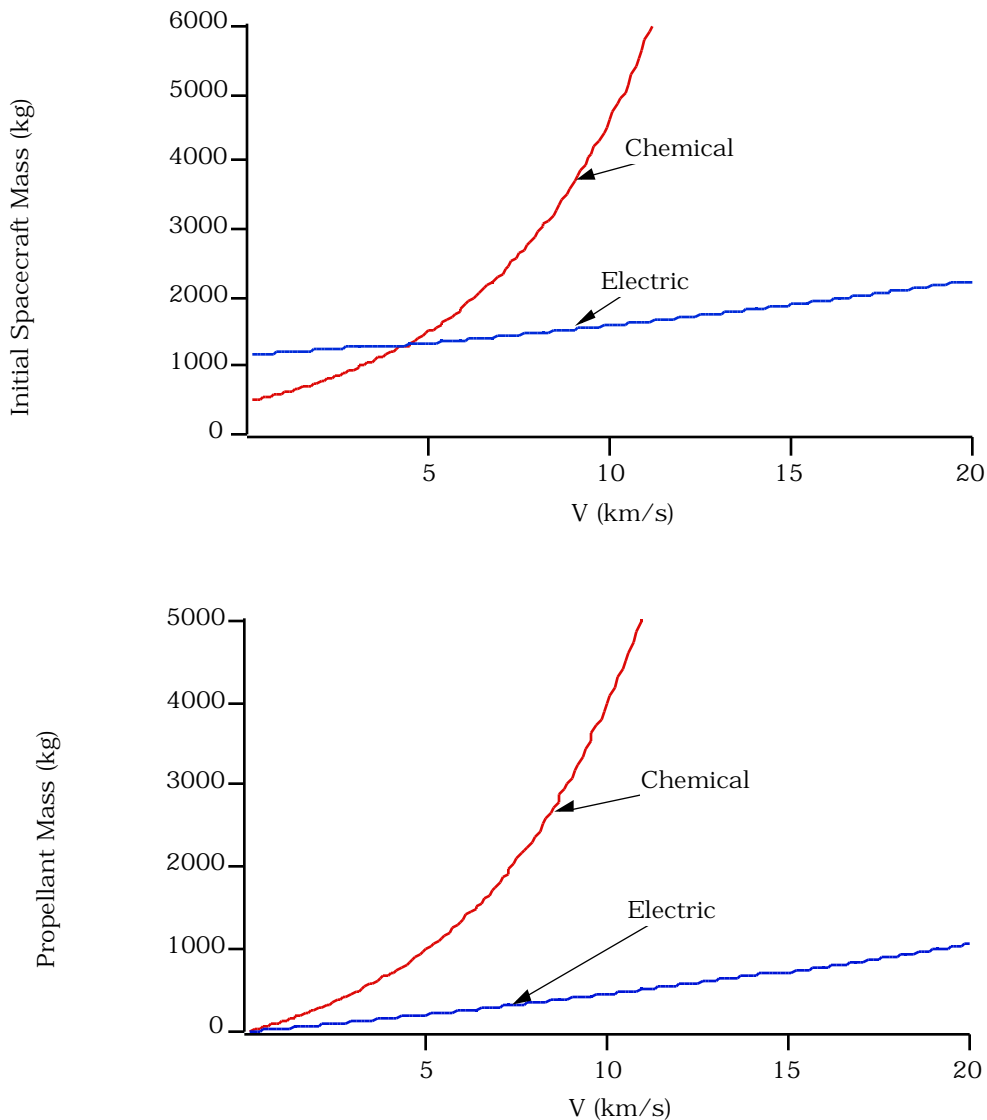


Figure 1-1 Comparison of initial spacecraft mass and propellant mass between an electric propulsion system with 3000 sec I_{sp} and a chemical propulsion system with 450 sec I_{sp} .

propulsion system with 3000 sec specific impulse and a chemical propulsion system with 450 sec specific impulse. The electric propulsion system is assumed to carry a 900 kg, 3 kW solar array for power generation, and the payload mass is assumed to be 100 kg. It is clear from Figure 1-1 that electric propulsion systems are more suited for large v (> 5 km/s) missions than chemical propulsion systems. Electric propulsion systems provide great benefit to missions such as orbit-transfer, station-keeping of satellites, and deep space probes, which require large v and high specific impulses.

Electric propulsion is a type of rocket propulsion that utilizes electric and/or magnetic processes to accelerate propellant. In general, the various electric propulsion devices can be categorized into three groups. The first category is electrothermal acceleration. The engines in this category, which are in general the simplest, generate thrust by electrically heating the propellant. Figure 1-2 shows an illustration of an electrothermal system called an arcjet, in which the propellant is heated and partially ionized by an electric arc struck between the anode and cathode. The heated gas is expanded thermodynamically and is accelerated to supersonic speeds through a nozzle as in a chemical rocket.

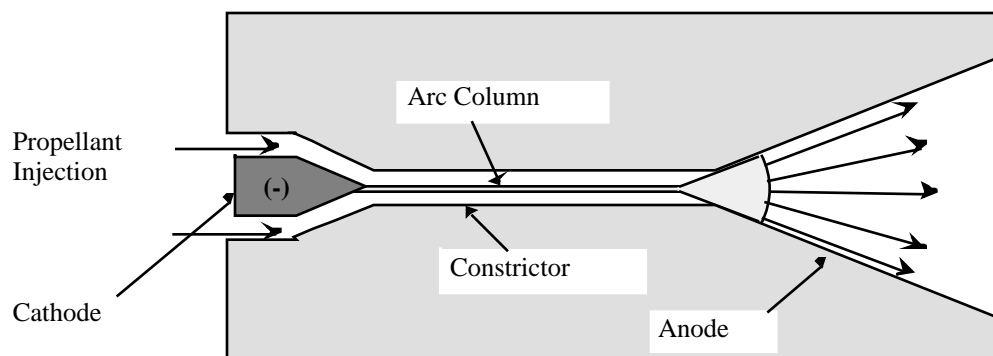


Figure 1-2 Schematic of an Arcjet (Electrothermal acceleration).

The second category of electric propulsion is electromagnetic acceleration. Ionized propellant is accelerated by the Lorentz force created from the interaction

between the current carried by the plasma and the magnetic field which could be either self-induced or externally-applied. Figure 1-3 shows an illustration of a electromagnetic system called magnetoplasmadynamic (MPD) thruster. In this device, a large discharge arc generates a strong self-induced magnetic field. This field interacts with the plasma current, and the resulting Lorentz force accelerates the plasma out of the device, thereby generating thrust.

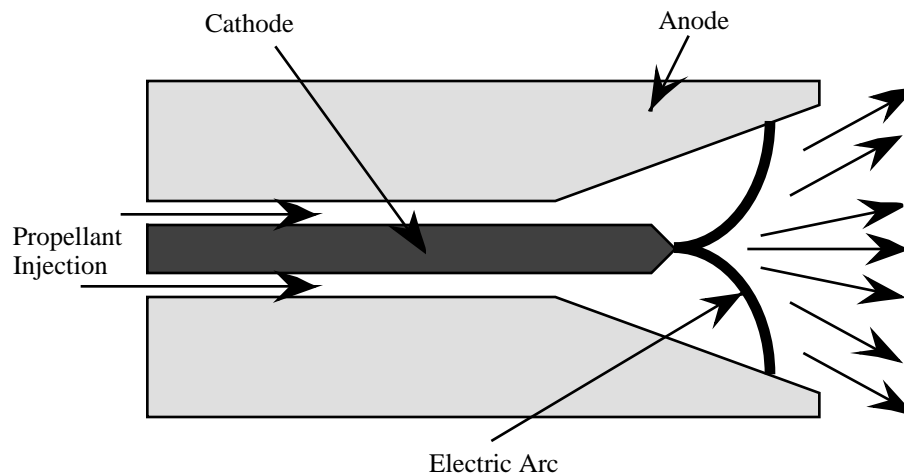


Figure 1-3 Schematic of a MPD thruster (Electromagnetic acceleration).

The final category of electric propulsion is that of electrostatic acceleration. Here, large electric fields are used to accelerate charged particles of a plasma to generate thrust. Figure 1-4 shows an illustration of a Hall thruster, an electrostatic electric propulsion engine. The Hall thruster utilizes the electric field formed in the discharge chamber between the anode and cathode to accelerate the ions. The cathode serves both as a source of electrons that ionize propellant atoms while traveling towards the anode and as a neutralizer that is used to inject electrons into the ion beam to neutralize it and to prevent the engine and spacecraft from charging negatively. It is the Hall thruster that was investigated for the work reported here.

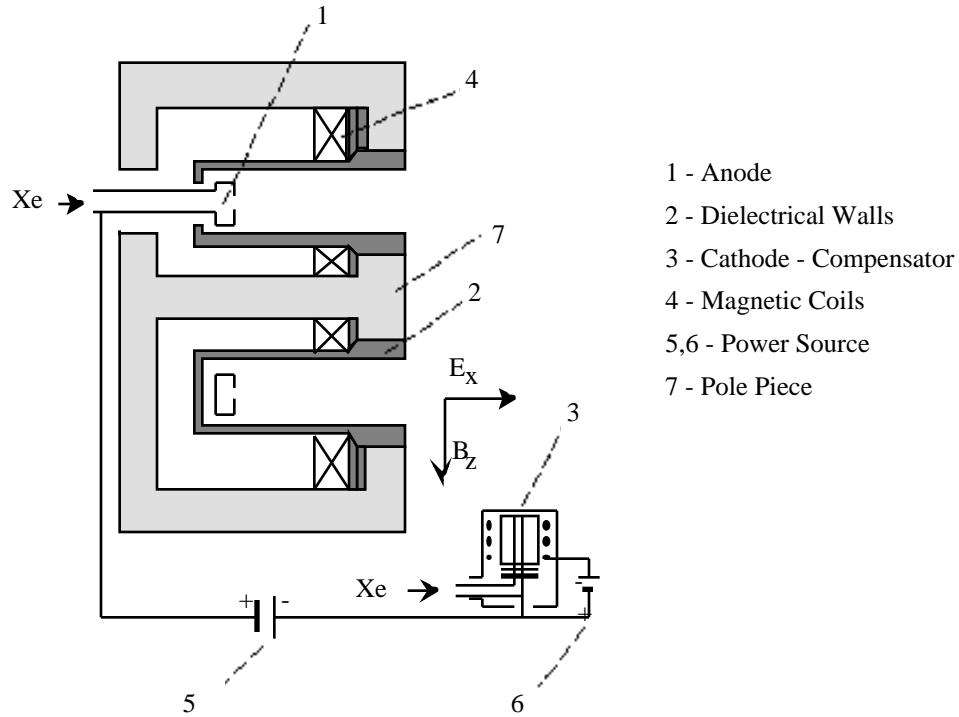


Figure 1-4 Schematic of a Hall thruster (Electrostatic acceleration).

The concept of Hall thrusters was developed in the 1960's. Although the interests in the Hall thrusters did not disappear entirely in U.S. [3, 4], the focus had been on gridded ion engines, another form of electrostatic acceleration thrusters. That left the former Soviet Union as the only country to continue to develop and use Hall thrusters in space flights throughout 1960's, 70's, and 80's [5, 6, 7, 8, 9, 10, 11]. Over 80 Hall thrusters have flown on-board Soviet and Russian satellites to date. The Russian Hall thruster technology became available to spacecraft manufacturers in U.S. in the early 90's. The first Russian Hall thruster made available to the Western world was the stationary plasma thruster (SPT-100) built by the Russian firm Fakel [12], shown in Figure 1-5.

The SPT-type thrusters were successfully developed during the 1960's and 70's by Morozov [7] and others to obtain a unique combination of specific impulse and



Figure 1-5 Photograph of the SPT-100.

efficiency. The SPT-100 drew much attention for its high specific impulse and high efficiency, especially from the commercial space industry because the SPT-100 has been shown to be advantageous over conventional chemical propulsion systems for use in orbit-transfer and north-south station-keeping of communication satellites [13, 14, 15]. In addition, the features of the SPT-100 are particularly appealing for the New Millennium spacecraft series whose main emphasis is on smaller, lighter, and less expensive systems [16]. These, along with more on-board electric power made available by recent technological advances such as the improved solar arrays, have prompted many to conduct research on the SPT-100.

In general, Hall thrusters can be classified into two types; extended-acceleration type and anode layer type. The SPT-100 falls into the first category, a closed-drift extended-acceleration, or CDEA, thruster. Operation of CDEA thrusters (and anode layer thrusters) can be found in an extensive literature [3, 4, 5, 11, 12, 13, 17]. Here, a brief description of the SPT-100 operation will be given.

A closed-drift thruster, or a Hall thruster is defined as a thruster in which ions are accelerated in the thrust direction with the accelerating electric field established by an electron current interacting with a transverse magnetic field. One component of the electron motion is in the opposite direction of the ion flow, and the other component is normal to that direction. The electron current associated with this normal component is called the Hall current. In a Hall thruster, there is a complete, or closed, path for the Hall current, thus the name closed-drift Hall thrusters. Figure 1-6 shows a schematic of a basic SPT-100 operation. The inner and outer electromagnet solenoids are carefully arranged, so that the resulting magnetic field is essentially in the radial direction only. In addition, a discharge voltage V_d is applied between the anode and cathode. As the

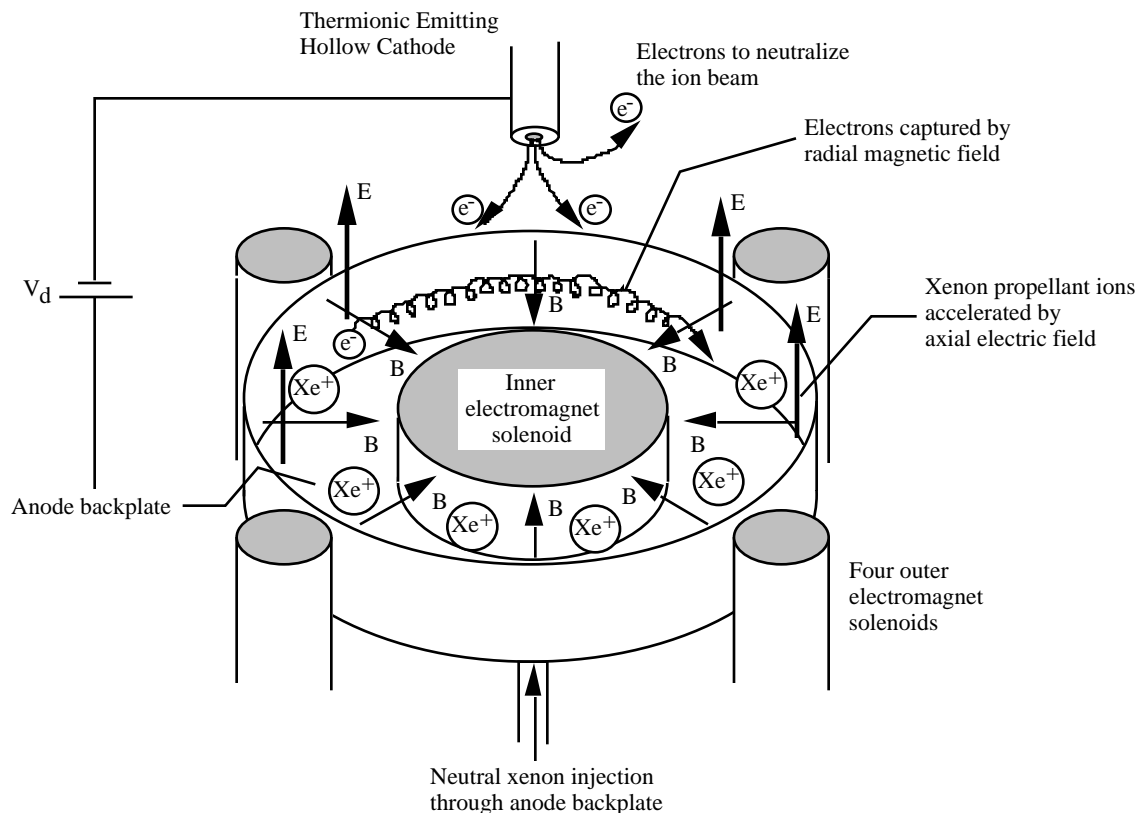


Figure 1-6 Schematic of a basic SPT-100 operation. It shows the dominant axial electric field, dominant radial magnetic field, the electrons from the cathode trapped in the $E \times B$ drift, and the electrons from the cathode for neutralizing the ion beam.

electrons ejected from the cathode proceed towards the anode under the influence of V_d , the magnetic field in the radial direction and the applied electric field in the axial direction trap the electrons in an ExB drift in the azimuthal direction, impeding their progress towards the anode. This azimuthal ExB drift (Hall current) completes a closed path in the annular discharge chamber. Now, the trapped electrons can move in the axial direction only when they collide with the wall and other particles in the discharge chamber. Thus, the plasma can sustain a large axial voltage gradient in the discharge chamber due to the highly suppressed axial mobility of the electrons. Also, the slow diffusion of electrons towards the anode benefits the ionization efficiency because the propellant atoms are ionized by collisions with these electrons. The propellant atoms (xenon in this case) are injected into the discharge chamber through small holes in the annular anode. These atoms are ionized by collisions with the drifting electrons, and are accelerated by the large axial electric field, thereby generating thrust. The strength of the magnetic field is such that the ion Larmor radius is large compared to the thruster dimensions. Thus, the ions' trajectories are little influenced by the magnetic field. The cathode also serves as a neutralizer that injects electrons into the ion beam to neutralize it and to prevent the engine and spacecraft from charging negatively.

1.2 Motivation

As mentioned in the previous section, electric propulsion systems have unique advantages over conventional chemical rockets because of their high exhaust velocities and, thus, high specific impulses. However, one cannot strive blindly for extreme exhaust velocities since all electric propulsion systems require separate electric power supplies. In general, the mass of the power supply scales monotonically with the power level involved, and hence directly with the specific impulse. A simple analysis of the power supply mass and specific impulse by Jahn [1] shows that there is an optimum I_{sp} to

maximize deliverable payload fraction on each mission. This optimum value depends on the specific power supply mass, the conversion efficiency (from input energy to propellant kinetic energy), and the mission time, but is independent of the thrust. One of the most important points emerging from this analysis is that a premium should be placed upon the efficiency with which the thruster converts electric power input to thrust power of the jet.

One of the principal effects leading to a loss of effective thrust and, thus, a reduction in efficiency is the presence of multiply charged propellant ions in the beam of a Hall thruster. For example, consider an ion beam with the total beam current of I_B . When the ion beam consists of singly charged and doubly charged ions, the total beam current is given by:

$$I_B = I_{1+} + I_{2+}. \quad \text{Eqn. 1-3}$$

The thrust can be divided into two components; one generated by the singly charged ions and the other generated by the doubly charged ions:

$$= \dot{m}_{1+} u_{e,1+} + \dot{m}_{2+} u_{e,2+}, \quad \text{Eqn. 1-4}$$

where \dot{m}_{1+} and \dot{m}_{2+} are the mass flow rates of singly charged and doubly charged ions, respectively, exiting the thruster, and $u_{e,1+}$ and $u_{e,2+}$ are the exhaust velocities of singly charged and doubly charged ions, respectively. Assuming that both ion species are accelerated through the same acceleration voltage V_i , which is a good approximation for the SPT-100, the exhaust velocity of each ion species can be written as:

$$u_{e,1+} = \sqrt{\frac{2eV_i}{M_i}}, \quad u_{e,2+} = \sqrt{\frac{4eV_i}{M_i}}. \quad \text{Eqn. 1-5}$$

The mass flow rate of each ion species can be written in terms of the beam current as:

$$\dot{m}_{1+} = M_i \frac{I_{1+}}{e}, \quad \dot{m}_{2+} = M_i \frac{I_{2+}}{2e}. \quad \text{Eqn. 1-6}$$

Combining Eqn. 1-4, Eqn. 1-5, and Eqn. 1-6, the actual thrust is:

$$= \sqrt{\frac{2M_i V_i}{e}} I_{1+} + \frac{I_{2+}}{\sqrt{2}} = \sqrt{\frac{2M_i V_i}{e}} I_B - 1 - \frac{1}{\sqrt{2}} I_{2+}. \quad \text{Eqn. 1-7}$$

However, if the same ion beam consists of only singly charged ions, the thrust would be:

$$= \sqrt{\frac{2M_i V_i}{e}} I_B. \quad \text{Eqn. 1-8}$$

Thus, the presence of doubly charged ions decreases the thrust.

The production of multiply charged propellant ions in a Hall thruster also causes a reduction of mass utilization, which is defined as:

$$m = \frac{\dot{m}_{\text{ion}}}{\dot{m}_{\text{total}}}, \quad \text{Eqn. 1-9}$$

where \dot{m}_{total} is the total propellant mass flow rate, and \dot{m}_{ion} is the mass flow rate of the ions exiting the thruster. When the ion beam consists of singly charged and doubly

charged ions, \dot{m}_{ion} can be divided into two parts; one for the singly charged ions and the other for doubly charged ions. Then, using Eqn. 1-6, the mass utilization becomes:

$$\eta_m = \frac{M_i}{e} \frac{I_{1+} + \frac{I_{2+}}{2}}{\dot{m}_{\text{total}}} = \frac{M_i}{e} \frac{I_B - \frac{I_{2+}}{2}}{\dot{m}_{\text{total}}} . \quad \text{Eqn. 1-10}$$

But, if only the singly charged ions are present in the same ion beam, the mass utilization would be:

$$\eta_m = \frac{M_i}{e} \frac{I_B}{\dot{m}_{\text{total}}} . \quad \text{Eqn. 1-11}$$

Therefore, the presence of doubly charged ions caused the reduction of mass utilization. The reduction in the effective thrust and mass utilization will increase if there are higher charge state ions.

Another adverse effect of multiply charged propellant ions is the increased sputtering due to these ions. The plume impingement of a Hall thruster poses serious problems to a spacecraft because the plume ions have such high energies (~250 eV for Xe^{1+} ions). This is true especially for earth-orbiting satellites where the plume ions cannot always be directed away from all the important components of the spacecraft. Sputtering causes the erosion of exposed surfaces as the high energy plume ions remove surface material upon impact. Also, the spacecraft surfaces can be contaminated by the deposition of the discharge chamber insulator material that has been sputtered away by the impacting high energy ions. The most critical surface subject to these effects is the surface of the solar array whose sputtering threshold is approximately 30 eV. These problems caused by the already high energy singly charged ions are worsened by the presence of multiply charged ions. Since the ions experience similar acceleration voltages in the discharge chamber, the multiply charged ions have larger energy, thus causing more sputtering. Furthermore, near the threshold of sputtering, not only the

kinetic energy, but also the neutralization energy of the bombarding ion affects the sputtering yield, and this energy is especially great for multiply charged ions [18]. The ion impacts ionize the target atoms just beneath the bombarded surface (Auger ionization), and cause an accumulation of positive charge. This is followed by ejection of target ions by Coulomb repulsion.

As discussed above, production of multiply charged propellant ions in a Hall thruster is a loss mechanism for the thrust, thruster efficiency, and mass utilization. It also causes more erosion and contamination of exposed spacecraft surfaces. Furthermore, the erosion of the discharge chamber, which causes the contamination of spacecraft surfaces, is directly related to the thruster lifetime. In other words, the presence of multiply charged propellant ions affects the efficiency and lifetime of the thruster and, ultimately, the operation and lifetime of the spacecraft. Therefore, understanding and characterizing the behavior of multiply charged propellant ions is an important aspect of engine development. A great deal of insight in terms of understanding the behavior of these ions can be obtained from the plasma properties in the thruster plume. The primary goal of this research is, then, to characterize plasma properties in the thruster plume and to understand the ionization and acceleration processes of each ion species. These objectives are undertaken by thoroughly investigating plasma parameters and species-dependent ion energy distributions in the exhaust plume of a SPT-100. The results of this research can be used in improving the existing thrusters and in developing new thrusters. They can also help the development of computer codes for simulating the Hall thruster operations, which is becoming a major research area due to the recent advances in computing power [19, 20, 21].

1.3 Review of Past Research

The obvious commercial interests in near-earth space missions have led the overwhelming bulk of SPT development activities to focus on performance, lifetime, and integration issues in an effort to fully flight-qualify the thrusters. As a result, the baseline operating conditions of SPTs are now well established. Previous studies of the SPT-100 may be classified into two major categories: performance evaluation and study of exhaust plumes which is used ultimately to characterize integration issues, i.e. interaction between the plasma and spacecraft surfaces. Naturally, the two categories of studies are closely related.

1.3.1 Performance Evaluation of SPT-100

One of the earliest studies of SPT-100 performance parameters by U.S. institutions was an evaluation of SPT-100 performance by Brophy, et al. [22]. The experiments were conducted in Russia, and showed that the nominal performance with xenon propellant was a specific impulse of 1600 sec, an over all thruster efficiency of 50%, at an input power of 1.35 kW. These results substantiated the performance claims that the Russians had made. The encouraging results of this trip prompted the U.S. to acquire a SPT-100 from Russia for independent evaluation at U.S. facilities.

A series of tests conducted at NASA's Lewis Research Center (now the John Glenn Research Center at Lewis Field (GRC)) [23] demonstrated the robustness of the thruster system by reliably starting throughout the entire test program which extended over 148 hours. The performance data obtained at the lowest facility pressure of 0.0004 Pa showed a specific impulse of 1600 sec at an efficiency of 50%. However, the stability envelope of the thruster drastically decreased over the course of operation possibly due to erosion of the insulator (the discharge chamber wall). Also, decrease in performance was observed during periods of current instability. The magnetic field characteristics,

accelerating channel geometry, and its walls contamination were found to affect thruster performance and intensity of plasma oscillations significantly, and their effects depended on thruster operation time [24].

A cyclic endurance test of the SPT-100 was conducted at Jet Propulsion Laboratory to characterize the long term operating behavior of the thruster and to determine its lifetime [25, 26]. The test was performed for 6,925 on/off cycles and 5,730.3 hours of operation at the nominal thruster input power of 1.35 kW. Thruster efficiency decreased from 50% to 42% over the first 1,000 hours. The efficiency increased slowly over the next 1,000 hours and then slowly decreased to 45% by the end to the test. The SPT-100 has an additional redundant cathode for fail-safe purpose, and the ignitor and radiation shields of the unused cathode were found to erode at an extremely high rate. Thus, the primary failure mechanism for this thruster was thought to be the short-circuiting of the ignitor to the emitter of the cathode by the material eroded in the unused cathode. This had actually happened during the test, but the short was cleared without opening the vacuum tank. Thruster operating characteristics such as propellant consumption rate, thrust, and floating voltage were stable over the duration of the test despite significant wear in the thruster insulators and thruster body. This endurance test proved that the SPT-100 was fully adequate to perform station-keeping functions for large commercial communication satellites.

1.3.2 Exhaust Plume Study of SPT-100

Before the thruster can be used in an actual spacecraft, the interaction between the thruster and the spacecraft must be characterized. As discussed earlier, one of the most crucial integration issues is the sputtering and contamination of spacecraft surfaces caused by high energy plume ions. These high energy plume ions sputter away surface material upon impact and cause the erosion of the exposed surfaces where a typical

sputtering threshold is approximately 20 eV. Also, the efflux of the discharge chamber insulator material which has been sputtered away by the impacting high energy ions can be deposited on and contaminate the spacecraft surfaces. The most critical component subject to these effects is the surface of the solar array. In order to characterize sputtering and contamination effects, many measurements of plasma parameters in the SPT-100 plume have been performed.

A comprehensive study of plume properties and their effects on spacecraft components was first conducted by Absalamov, et al. [27]. This test utilized a Faraday probe to measure ion current density and a gridded Retarding Potential Analyzer (RPA) to measure ion energy distribution. It also obtained the erosion and contamination model of the SPT-100 plume by placing various samples in the plume that were made of materials characteristic of the solar panels. The findings of this study confirmed the need to protect the solar array from the thruster plume.

Myers and Manzella investigated the SPT-100 plume characteristics using Langmuir probes, Faraday probes, and a RPA in the region of the plume extending $\pm 60^\circ$ off thruster axis between 0.3 m and 4 m from the thruster exit [28]. The ion current density measurements showed that the plume was sharply peaked on the thruster axis, dropping by a factor of 2.6 within 22 degrees off thruster axis. The ion energy at 4 m from the thruster exit was found to be approximately 270 eV, which showed that the ions did not lose energy as they move away from the thruster. Another study by Manzella and Sankovic measured the distribution of ion current density in a wide range of angular locations within $\pm 100^\circ$ off thruster axis at 60 cm from the thruster exit [29]. The results were similar to the study by Myers and Manzella, and the claimed $1/r^2$ dependence of current density (Current density changes as $1/r^2$ where r is the distance from the center of the thruster exit plane.) was verified. Also, the calculation of total ion beam current implied that approximately 25% of plume ions were multiply charged ions. Other studies also measured various plasma parameters within wide angles off thruster axis ($\pm 60^\circ$) in

the SPT-100 plume [30, 31]. Note that although these studies provided a great amount of plume data, the data were limited to a few number of spatial locations in the thruster plume.

The studies mentioned above utilized various electrostatic probes to measure plume parameters of charged particles. To overcome the limitations of electrostatic probes, Manzella used laser diagnostics to study plume characteristics. Optical diagnostics can provide detailed, species-specific, non-intrusive measurements on neutral particles and ions. In his laser induced fluorescence (LIF) study of the ion velocity in the SPT-100 plume, Manzella obtained circumferential, radial, and axial ion velocities at several radial locations in front of the discharge chamber 11 mm downstream of the exit plane [32]. The average axial ion velocity was found to be approximately 16000 m/s. From Doppler broadening of the measured fluorescence excitation spectrum, Manzella also determined that the spread in axial ion velocity corresponded to an approximately 3.4 eV variation in ion energy. This value was approximately an order of magnitude smaller than the data obtained by RPA-based experiments. This became a source of confusion, but one of the results in the work reported here has shown that the discrepancy was only apparent. Manzella also investigated plume properties of the SPT-100 using emission spectroscopy [33]. The emission spectrum was measured at the thruster exit plane. The results showed that the plasma was over 95% ionized at the thruster exit plane. Between 10 and 20% of the ions were found to be doubly charged. On the subject of facility effects on experiments, ingestion and ionization of background gas at elevated background pressure was detected. This “entrained” gas would have measurable effect on thrust and, thus, thruster performance measurements.

Randolph, Pencil, and Manzella constructed a sputter erosion model to predict erosion rates of typical construction materials for earth-orbiting satellites in the SPT-100 plume [34, 35]. The model used Faraday-probe-based data to describe ion current density and RPA-based data to describe ion energy. However, as the emission

spectroscopy study by Manzella showed, approximately 15% of plume ions were doubly charged, and those electrostatic probes were insensitive to the charge state of the ions. Therefore, although the model's prediction was in good agreement with the measured erosion rate, the model could be improved by including the contribution of multiply charged propellant ions to the erosion rate, which depends not only the energy but also the charge state of the ions.

A recent study by King utilized a molecular beam mass spectrometer (MBMS), which consisted of a 45-degree electrostatic energy analyzer and a time-of-flight system, to measure mass and energy of ions in the SPT-100 plume [36]. The MBMS operated in a quasi-steady mode (i.e. with the time-of-flight system turned off) provided ion energy distributions similar to RPA-based data. These data provided a great deal of insight into the collisional processes occurring in the SPT-100 plume. This study produced the first ever measurements of the ion energy at large angles off thruster axis (360 degrees at 50 cm from the thruster exit). This study was also the first to document the evidence of triply and quadruply charged propellant ions in the SPT-100 plume. But, these energy measurements were not able to provide any species-dependent information. Through the simultaneous use of the 45-degree energy analyzer and the time-of-flight system, the MBMS was able to measure propellant ionization states and construct species-dependent ion energy distribution functions. However, this indirect approach resulted in the energy distribution with discrete energy values (20 eV intervals).

Other major areas of Hall thruster research are the study of plasma oscillation and the development of computer code for modeling the thruster plasma. For more detail regarding these studies, the reader is referred to the literature [37, 38, 39, 40, 41, 42] for plasma oscillation and [19, 20, 21, 43] for computer modeling.

1.4 Overview of This Research

The primary goal of this research is to characterize plasma properties in the thruster plume and to understand the ionization and acceleration processes of each ion species. This research was motivated by the need to understand and characterize the behavior of multiply charged propellant ions in the thruster plume due to the fact that the presence of these ions affects the efficiency and lifetime of the thruster and, ultimately, the operation and lifetime of the spacecraft on which the thruster will be used. A great deal of insight into the behavior of multiply charged propellant ions can be obtained from the plasma properties in the thruster plume. Therefore, the objectives of this research were undertaken by thoroughly investigating plasma parameters and species-dependent ion energy distribution in the exhaust plume of the SPT-100.

To this end, radial profiles of ion current density, electron temperature, and electron number density were measured in the very-near-field region (10 mm to 200 mm downstream of the thruster exit plane) of the SPT-100 plume using electrostatic probes specifically designed for the very-near-field plume study. This was the first study to characterize the very-near-field plume of a Hall thruster, and still is the only such study of the SPT-100. Also, angular profiles of ion current density, plasma potential, electron number density, and electron temperature were measured in the near- and far-field region (25 cm to 1 m downstream of the thruster exit plane) of the SPT-100 plume using electrostatic probes. The combined data of the very-near-field and the near- and far-field plume studies provided the most comprehensive collection of plasma parameters over an extensive volume of the SPT-100 plume.

In order to obtain direct measurements of species-dependent ion energy distributions in the SPT-100 plume, an \mathbf{ExB} probe was constructed. The velocity-filtering characteristic of the \mathbf{ExB} probe, along with the acceleration mechanism in the SPT-100 allowed the measurements of species-dependent ion energy distribution. Ion

energy distributions were measured in the near- and far-field region of the SPT-100 plume at wide range of angles off thruster axis using the **ExB** probe. The ion energy distribution functions of each ion species at various locations in the thruster plume were obtained by curve-fitting the measured probe traces with a distribution function model based on the kinetic theory of gases. Several ion parameters were obtained from these energy distribution functions. This study is the first attempt to obtain direct measurements of species-dependent ion energy distribution functions in a Hall thruster plume.

Chapter 2 provides the theory of electrostatic probes used in this work and discusses measurements error associated with these probes.

Chapter 3 provides the descriptions of the Langmuir and Faraday probes specifically designed and constructed for the very-near-field plume study. It also provides the description of the experimental set-up and presents the results and implications of the obtained data.

Chapter 4 provides the experimental set-up and the descriptions of the Langmuir and Faraday probes used in the near- and far-field plume study. The results of the measurements and their implications are discussed.

Chapter 5 describes the **ExB** probe and provides the theory of operation and its application to the measurement of ion energy distributions in the SPT-100 plume. The probe measurements error and the experimental set-up are also discussed.

Chapter 6 shows the measured **ExB** probe traces and provides qualitative discussions of the ion energy distributions in the SPT-100 plume.

Chapter 7 describes the scheme of the distribution function model and its limitations. Ion parameters obtained from the energy distribution functions are presented, and their implications are discussed.

Finally, Chapter 8 provides the summary conclusions of this work and suggests future work.

1.5 Experimental Facility

A detailed description of the facility used for the work reported here can be found in Gallimore, et al. [44]. A brief version of this description is reproduced in this section for convenience. All experiments were performed in a 9-m-long by 6-m-diameter stainless-steel vacuum chamber (cf. Figure 1-7). At the time of these tests, the facility was supported by six 81-cm-diameter diffusion pumps each rated at 32,000 l/s on nitrogen (with water-cooled coldtraps) backed by two 2,000 cfm blowers, and four 400 cfm mechanical pumps. These pumps gave the facility an overall pumping speed of ~30,000 l/s on xenon at 10^{-5} Torr. It typically took four hours to evacuate the chamber to 5×10^{-5} Torr (calibrated for xenon) from atmospheric pressure.

Chamber pressure was measured with MKS model 919 hot-cathode ionization gauges, which were corrected for xenon, located on vacuum ports on either side of the chamber. Base chamber pressure was approximately 5×10^{-5} Torr. Background chamber pressure was maintained to less than 1.2×10^{-4} Torr while the thruster operated on 5.5 mg/s of xenon.

Xenon propellant was supplied to the thruster from compressed gas bottles (99.999% purity) through stainless-steel feed lines. Propellant flow was controlled and monitored with an MKS 1159B mass flow controller specifically calibrated for xenon. The system was capable of handling up to 120 SCCM of xenon with an accuracy of 1%.

A Macintosh based data acquisition system, developed by National Instruments (LabVIEW), was used to record all experimental data. Analog voltage signals were recorded on a 1 GHz digitizing oscilloscope (Tektronix model TDS-540) and transferred to computer via IEEE-488.2 (GPIB) interface.

The probes for the very-near-field study and the thruster for the other studies were mounted to a custom-made positioning system developed by NEAT (New England Affiliated Technologies). The table contains two rotary platforms on a 1.8-m-long linear

stage in the radial direction that is mounted on a 0.9 m travel axial stage, allowing data to be obtained over a large volume of the thruster plume. The system allows for sweeps in the radial direction in excess of 60 cm/s with an absolute position accuracy of 0.15 mm. The table is controlled by a Macintosh-based control system coordinated by a National Instrument's LabVIEW platform.

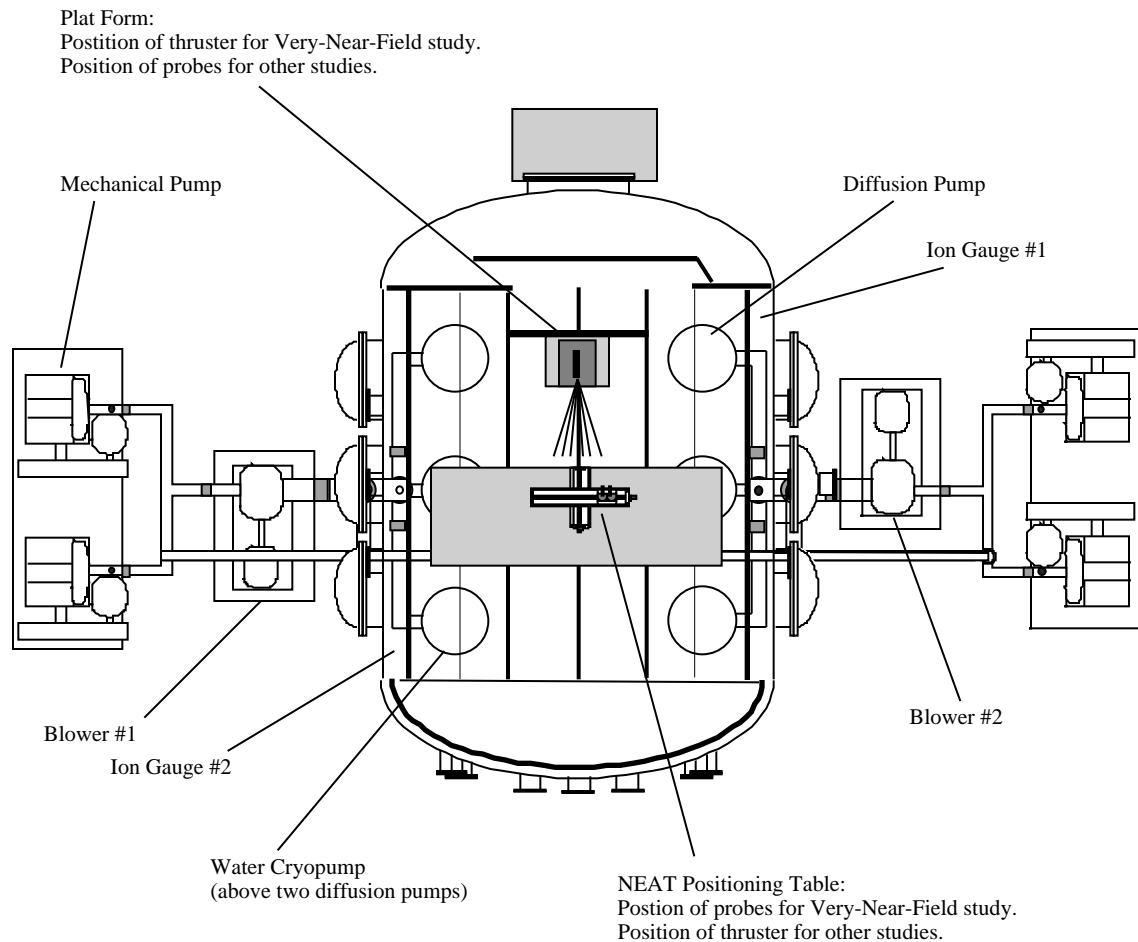


Figure 1-7 Schematic of the 9 by 6 meter vacuum chamber. Positions of the thruster and probes for each study are indicated.

Reference to Chapter 1

- 1 Jahn, R.G., The Physics of Electric Propulsion, McGraw-Hill Book Company, New York, 1968.
- 2 Hill, P. and Peterson, C., Mechanics and Thermodynamics of Propulsion, Second Edition, Addison-Wesley Publishing Company, Reading, MA, 1992.
- 3 Kaufman, H.R., "Technology of Closed-Drift Thrusters," AIAA-83-1398, June 1983.
- 4 Kaufman, H.R., "Theory of Ion Acceleration with Closed Electron Drift," *Journal of Spacecraft*, Vol. 21, No. 6, pp. 558-562, Nov.-Dec. 1984.
- 5 Zharinov, A.V. and Popov, Y.S., "Acceleration of Plasma by a Closed Hall Current," *Soviet Physics, Technical Physics*, Vol. 12, No. 2, pp. 208-211, Aug. 1967.
- 6 Zubkov, I.P., Kislov, A.Y., and Morozov, A.I., "Experimental Study of a Two-Lens Accelerator," *Soviet Physics, Technical Physics*, Vol. 15, No. 11, pp. 1796-1800, May 1971.
- 7 Morozov, A.I., Esipchuk, Y.V., Tilinin, G.N., Trofimov, A.V., Sharov, Y.A., and Shchepkin, G.Y., "Plasma Accelerator with Closed Electron Drift and Extended Acceleration Zone," *Soviet Physics, Technical Physics*, Vol. 17, No. 1, pp. 38-45, July 1972.
- 8 Morozov, A.I., Esipchuk, Y.V., Kapulkin, A.M., Nevrovskii, V.A., and Smirnov, V.A., "Effect of The Magnetic Field on a Closed-Electron-Drift Accelerator," *Soviet Physics, Technical Physics*, Vol. 17, No. 3, pp. 482-487, Sept. 1972.
- 9 Bishaev, A.M. and Kim, V., "Local Plasma Properties in a Hall-Current Accelerator with an Extended Acceleration Zone," *Soviet Physics, Technical Physics*, Vol. 23, No. 9, pp. 1055-1057, 1978.
- 10 Gavryushin, V.M. and Kim, V., "Effect of the Characteristics of a Magnetic Field on the Parameters of an Ion Current at the Output of an Accelerator with Closed Electron Drift," *Soviet Physics, Technical Physics*, Vol. 26, No. 4, pp. 505-507, 1981.
- 11 Morozov, A.I., "Stationary Plasma Thruster (SPT) Development Steps and Future Perspectives," IEPC-93-101, Sept. 1993.
- 12 Bugrova, A., Kim, V., Maslennikov, N., and Morozov, A.I., "Physical Processes and Characteristics of Stationary Plasma Thrusters with Closed Electrons Drift," IEPC-91-079, Oct. 1991.

-
- 13 Kaufman, H.R., Robinson, R.S., Day, M.L., and Haag, T.W., "End-Hall Thrusters," AIAA-90-2595, July 1990.
- 14 Oleson, S, Myers, R., Kluever, C., Riehl, J., and Curran, F., "Advanced Propulsion for Geostationary Orbit Insertion and North-South Station Keeping," AIAA-95-2513, July 1995.
- 15 Gulczinski, F.S. and Spores, R.A., "Analysis of Hall-Effect Thrusters and Ion Engines for Orbit Transfer Missions," AIAA-96-2973, July 1996.
- 16 Dudzinski, L. and Myers, R., "Advanced Propulsion Benefits to New Millennium Class Missions," Presented at 9th AIAA/Utah State University Conference on Small Satellites, Sept. 1995.
- 17 Komurasaki, K., Hirakawa, M., and Arakawa, Y., "Plasma Acceleration Process in a Hall-Current Thruster," IEPC-91-078, Oct. 1991.
- 18 Palmer, D.W., Thompson, M.W., and Townsend, P.D., Editors, Atomic Collision Phenomena in Solids, (North-Holland Publishing Company, Amsterdam, 1970.), Parilis, E.S., "A Mechanism for Sputtering of Non-Metals by slow Multiply-Charged Ions," pp. 324-327.
- 19 Oh, D. and Hastings, D., "Axisymmetric PIC-DSMC Simulations of SPT plumes," IEPC-95-160, Sept. 1995.
- 20 Oh, D. and Hastings, D., "Experimental Verification of a PIC-DSMC Model for Hall Thruster Plumes," AIAA-96-3196, June 1996.
- 21 Rhee, M.S. and Lewis, M.J., "Numerical Simulation of Stationary Plasma Thruster Exhaust Plume," AIAA-95-2928, July 1995.
- 22 Brophy, J.R., Barnett, J.W., Sankovic, J.M., and Barnhart, D.A., "Performance of the Stationary Plasma Thruster: SPT-100," AIAA-92-3155, July 1992.
- 23 Sankovic, J.M., Hamley, J.A., and Haag, T.W., "Performance Evaluation of the Russian SPT-100 Thruster at NASA LeRC," IEPC-93-094, Sept. 1993.
- 24 Gavryushin, V.M., Kim, V., Kozlov, V.I., Kozubsky, K.N., Popov, G.A., Sorokin, A.V., Day, M.L., and Randolph, T., "Study of the Effect of Magnetic Field Variation, Channel Geometry Change and Its Walls Contamination upon The SPT Performance," AIAA-94-2858, June 1994.
- 25 Garner, C.E., Polk, J.E., Pless, L.C., Goodfellow, K.D., and Brophy, J.R., "Performance Evaluation and Life Testing of The SPT-100," IEPC-93-091, Sept. 1993.

-
- 26 Garner, C.E., Brophy, J.R., Polk, J.E., and Pless, L.C., "A 5,730-Hr Cyclic Endurance Test of The SPT-100," AIAA-95-2667, July 1995.
- 27 Absalamov, S.K., Andreev, V.B., Colbert, T., Day, M., Egorov, V.V., Gnizdor, R.U., Kaufman, H., Kim, V., Korakin, A.I., Kozubsky, K.N., Kudravzev, S.S., Lebedev, U.V., Popov, G.A., and Zhurin, V.V., "Measurement of Plasma Parameters in The Stationary Plasma Thruster (SPT-100) Plume and Its Effect on Spacecraft Components," AIAA-92-3156, July 1992.
- 28 Myers, R.M. and Manzella, D.H., "Stationary Plasma Thruster Plume Characteristics," IEPC-93-096, Sept. 1993.
- 29 Manzella, D.H. and Sankovic, J.M., "Hall Thruster Ion Beam Characterization," AIAA-95-2927, July 1995.
- 30 King, L.B. and Gallimore, A.D., "Ionic and Neutral Particle Transport Property Measurements in the Plume of an SPT-100," AIAA-96-2712, July 1996.
- 31 Gallimore, A.D., Gilchrist, B.E., King, L.B., Ohler, S.G., and Ruffin, A.B., "Plume Characterization of the SPT-100," AIAA-96-3298, July 1996.
- 32 Manzella, D.H., "Stationary Plasma Thruster Ion Velocity Distribution," AIAA-94-3141, June 1994.
- 33 Manzella, D.H., "Stationary Plasma Thruster Plume Emissions," IEPC-93-097, Sept. 1993.
- 34 Randolph, T., Pencil, E., and Manzella, D., "Far-Field Plume Contamination and Sputtering of the Stationary Plasma Thruster," AIAA-94-2855, June 1994.
- 35 Pencil, E., Randolph, T., and Manzella, D., "End-of-Life Stationary Plasma Thruster Far-Field Plume Characterization," AIAA-96-2709, July 1996.
- 36 King, L.B., Ph.D. Thesis, University of Michigan, Department of Aerospace Engineering, 1998.
- 37 Simon, A., "Instability of a Partially Ionized Plasma in Crossed Electric and Magnetic Fields," *The Physics of Fluids*, Vol. 6, No. 3, pp. 382-388, March 1963.
- 38 Esipchuk, Y.V., Morozov, A.I., Tilinin, G.N., and Trofimov, A.V., "Plasma Oscillations in Closed-Drift Accelerators with an Extended Acceleration Zone," *Soviet Physics, Technical Physics*, Vol. 18, No. 7, pp. 928-932, Jan. 1974.

-
- 39 Shishkin, G.G. and Gerasimov, V.F., "Plasma Instabilities in Accelerators with Closed Electron Drift," Soviet Physics, Technical Physics, Vol. 20, No. 9, pp. 1171-1174, Sept. 1975.
- 40 Esipchuk, Y.V. And Tilinin, G.N., "Drift Instability in a Hall-Current Plasma Accelerator," Soviet Physics, Technical Physics, Vol. 21, No. 4, pp. 417-423, April 1976.
- 41 Zhurin, V., Kahn, J., Kaufman, H., Kozubsky, K., and Day, M., "Dynamic Characteristics of Closed Drift Thrusters," IEPC-93-095, Sept. 1993.
- 42 Darnon, F., Lyszyk, M., and Bouchoule, A., "Optical Investigation on Plasma Oscillations of SPT Thrusters," AIAA-97-3051, July 1997.
- 43 Baranov, V.I., Nazarenko, Y.S., Petrosov, V.A., Vasin, A.I., and Yashnov, Y.M., "Energy Model and Mechanisms of Acceleration Layer Formation for Hall Thrusters," AIAA-97-3047, July 1997.
- 44 Gallimore, A.D., Kim, S-W, Foster, J.E., King, L.B., and Gulczinski III, F.S., "Near- and Far-field plume studies of a 1 kW arcjet," Journal of Propulsion and Power, Vol. 12, No. 1, Jan-Feb 1996.

CHAPTER 2

LANGMUIR PROBE AND FARADAY PROBE ANALYSIS

In order to begin the process of characterizing transport processes in Hall thruster plumes, profiles of electron temperature, electron number density, and ion current density were obtained over an extensive volume of the SPT-100 plume. The primary diagnostics used for this purpose included single Langmuir probes and Faraday probes. Different probes of each type were constructed for diagnosing different regions of the thruster plume. This chapter provides the theory of each probe and discusses the measurement error associated with each probe.

2.1 Langmuir Probe Theory

The Langmuir probe is one of the most widely used plasma diagnostic techniques. There are many documents describing its operation [1, 2, 3, 4].

A single Langmuir probe consists of a biased conductor inserted in the plasma. The current induced on the probe by the surrounding ions and electrons is recorded as a function of imposed probe voltage. The resulting curve is known as the probe characteristic. When the probe is biased very negative with respect to the plasma, it collects ions. As the bias voltage becomes more positive and approaches the plasma potential, electrons are collected. The probe characteristic, therefore, contains information about the thermodynamic state of the electrons and ions, and can be used to determine various plasma parameters.

A typical probe characteristic is shown in Figure 2-1. In the ion saturation region, essentially all the ions approaching the probe are collected, and thus the probe current changes slowly with voltage because the plasma can supply only a limited current of ions

to the probe. A slight increase in the ion saturation current for more negative probe voltage results from the fact that the space charge sheath that forms around the probe electrode grows as the probe bias voltage becomes large with respect to the plasma potential. Information about the plasma density can be obtained from the ion saturation current.

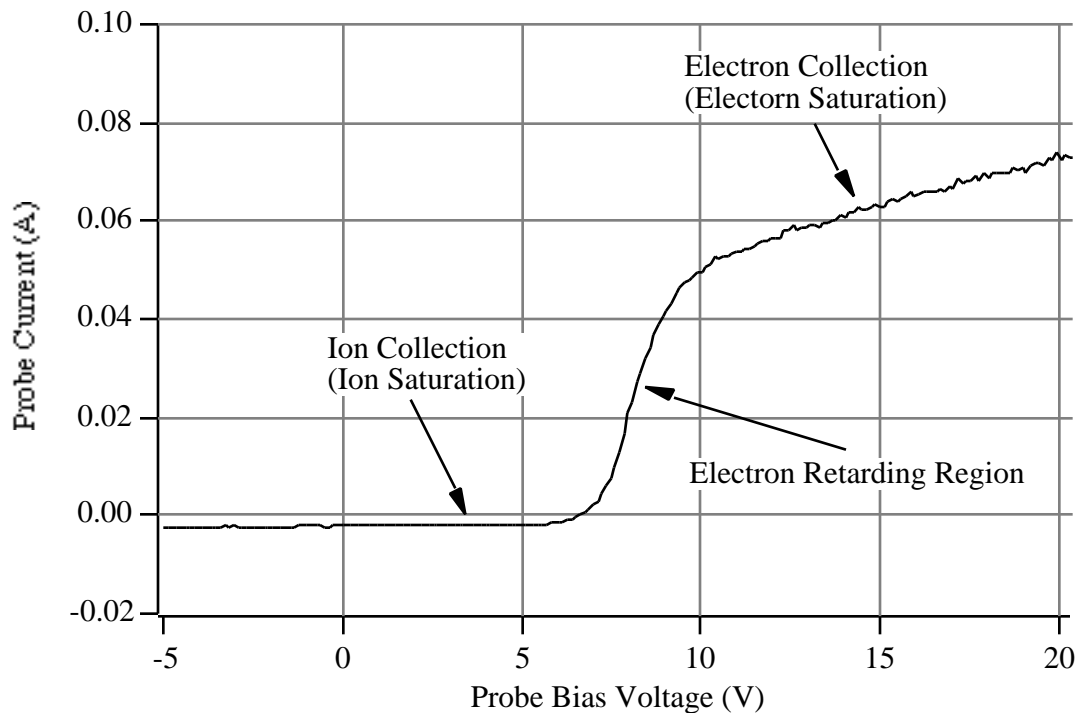


Figure 2-1 A typical Langmuir probe characteristic.

The shape of the electron retarding region is determined by the electron distribution function, and is used to determine the electron temperature. For the studies reported here, it is assumed that the electrons are in thermal equilibrium and hence have a Maxwellian energy distribution. As it will be discussed in Chapter 7, although the ions in the SPT-100 plume are not all Maxwellian, they are not far from Maxwellian. Considering the fact that the electrons in the plume are more mobile and therefore collide

with other electrons much more frequently than the ions, it is reasonable to assume that the electrons have a Maxwellian energy distribution.

There are several fundamental lengths in a plasma. Depending on the size of the probe compared to these lengths, different interpretations of the probe characteristic must be made. The probes were constructed separately for different regions of the plume, so that the probe radius was always much larger than the local Debye length. In the very-near-field region of the plume (10 mm to 200 mm from the thruster exit), the probe radius was approximately seven times larger than the Debye length and several times smaller than the electron gyro-radius, which was induced by the magnetic fields employed by the thruster for propellant acceleration. In the near- and far-field regions of the plume (25 cm to 1 m from the thruster exit), the probe radius was approximately 90 times larger than the Debye length. The magnetic field in the near- and far-field regions is insignificant, and the plasma can be considered unmagnetized.

Because the magnetic field reduces the transverse flux available to the probe, the electron saturation current becomes a function of the magnetic field in a magnetized plasma. Therefore, the electron saturation current cannot be used to obtain the electron number density [4]. Instead, the ion saturation current must be used to determine electron number density. For the plasma conditions in the very-near-field region of the SPT-100 plume, the ion motion is not appreciably influenced by the magnetic field. Furthermore, the ion Larmor radius is large compared with probe dimensions. For these reasons, magnetic field effects are not expected to significantly impact the density measurements when the ion saturation current is used.

In summary, the plasma conditions combined with the corresponding probe dimensions studied in this report implies that the standard thin sheath Bohm ion saturation current model of Langmuir probe analysis applies. For a single cylindrical Langmuir probe, the electron number density is obtained from the ion saturation current via the relation [3]:

$$i_+ = 0.61 e n_e A_p \sqrt{\frac{q_i kT_e}{M_i}}. \quad \text{Eqn. 2-1}$$

The ion saturation current is determined as the probe current in the ion saturation region that is closest to the electron retarding region. This is because, as the bias voltage becomes large (negatively in this case), the space charge sheath that surrounds the probe grows. The actual current collection area is not the probe surface area but the surface area of this space charge sheath. Therefore, since the probe surface area is used in Eqn. 2-1 to calculate the electron number density, it is critical to use the ion saturation current at the minimum sheath thickness to obtain the most accurate electron number density measurements.

The electron temperature is obtained by plotting $\ln(i_p+i_+)$ versus V_p . An example of this plot is shown in Figure 2-2.

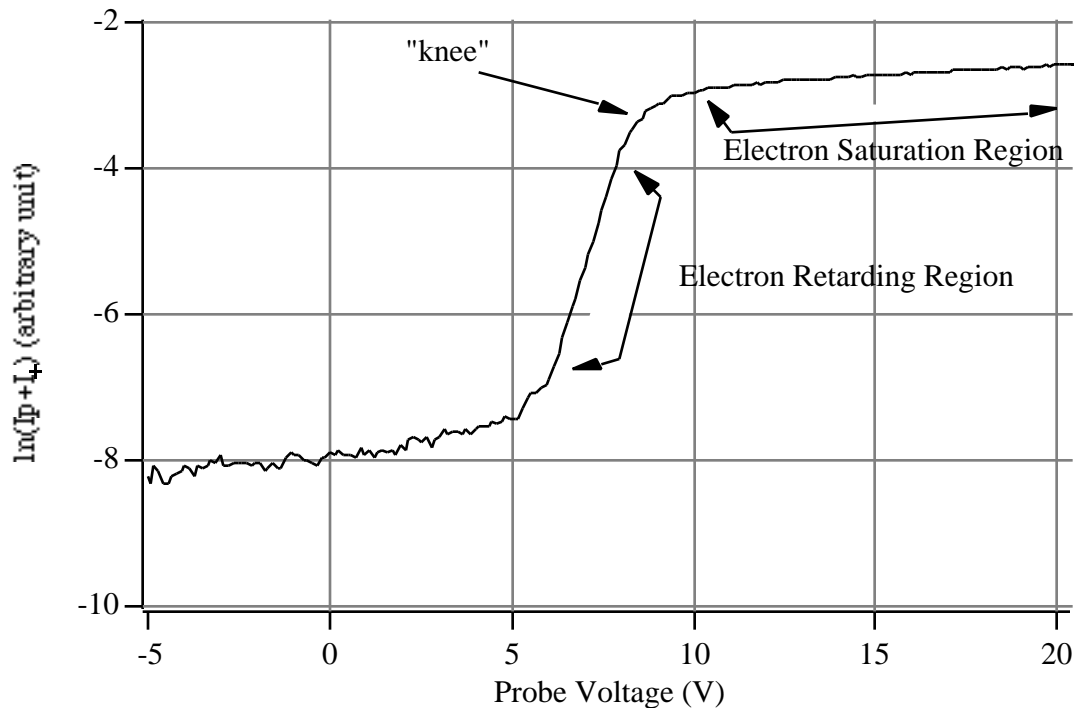


Figure 2-2 A typical plot of $\ln(I_p + I_+)$ vs Probe Voltage.

The slope of the electron retarding region of the resulting curve is $1/T_e$ if T_e is measured in eV, assuming that the electron energy distribution is Maxwellian. The plasma potential is obtained by locating the “knee” in the plot (cf. Figure 2-2). In general, the intersection of the electron retarding region and the electron saturation region is taken to be the “knee.”

2.2 Langmuir Probe Measurement Error

Plasma parameters such as the electron temperature, electron number density, and plasma potential measured by a Langmuir probe are subject to error associated with uncertainty in the measuring electrostatic probe. For the reasons discussed in the previous section, the errors associated with the deviation from the standard thin sheath Bohm ion saturation current model are minimized by using single Langmuir probes of appropriate sizes. Also discussed above, the error associated with the magnetic field effects are minimized by using the ion saturation current instead of the electron saturation current to calculate the electron number density. In this respect, error in the Langmuir probe measurements in this study for the most part is associated with the disturbance in the local plasma due to the presence of the probe in the plasma, the uncertainty in the probe current due to the secondary electrons produced by high energy ions impacting the probe surface, the uncertainty in the current collection area, and the uncertainty in the measurements of probe voltage and current.

Under ideal conditions, the Langmuir probe does not disturb the surrounding plasma appreciably, so that the measured plasma parameters provide an accurate representation of the plasma in the region where the probe is located. This is true as long as the probe potential relative to the plasma potential is kept from penetrating the plasma, and the probe body does not disturb the plasma flow, i.e. the probe is sufficiently small and aligned with the plasma flow vector.

The probe potential is usually shielded from the surrounding plasma by the space charge sheath that forms around the probe electrode. The probe measurements will reflect the plasma properties outside the sheath if collisions and ionization occur infrequently inside the sheath. The conditions in all the regions of the thruster plume studied are such that the Debye length is much smaller than the probe radius, and the electron mean free path is large compared to the probe radius. Therefore, the error associated with the plasma disturbance caused by the probe potential is considered to be minimal.

Misalignment of the probe to the plasma flow vector causes not only the disturbance in the plasma flow but also an increase in the collected ion current. It is well documented that supersonic ion flow, perpendicular to a cylindrical probe, increases the collected ion current significantly [5, 6]. The ions ejected from a Hall thruster follow diverging velocity vectors with respect to the thruster axis [7, 8]. In the near- and far-field study, the probe axis was always pointed at the center of the thruster at an angle relative to the thruster axis. Therefore, the probe was sufficiently aligned with the plasma flow vector. On the other hand, in the very-near-field study, the probe axis was always parallel with the thruster axis, and thus the probe was misaligned, especially at large radial positions away from the thruster centerline. It is difficult to quantify the error caused by the probe misalignment. However, it will be discussed along with the probe data when the experimental results are discussed in Chapter 3.

In order to minimize the secondary electron emissions, the probes were constructed with tungsten which has a very low secondary electron yield. The secondary electron emission yield for xenon ions bombarding tungsten is virtually constant at 0.02 over the range of possible ion energies (0 ~ 1 keV) [9]. This contributes an uncertainty of 2% to the ion saturation current measurements.

Error in the electron temperature measurements is mostly from the uncertainty in the least significant digits of the probe voltage and current. The average error in the electron temperature is estimated to be 15%.

Error in the electron number density depends on the uncertainties in the determination of the electron temperature, the ion saturation current, and the effective probe area (cf. Eqn. 2-1). The arbitrariness of the location where the ion saturation current is evaluated, coupled with the uncertainty in the electron temperature measurements, the effective probe area, and the error due to the secondary electron emissions yields a total uncertainty of approximately 50%. When the error due to the probe misalignment is added for the results of the very-near-field study, the total error is estimated to be roughly 60%.

Error in the plasma potential arises mostly from the uncertainty in the measurements of probe voltage and current and the arbitrariness of the location of the “knee,” since the “knee” is not usually very sharp (cf. Figure 2-2). These factors yield an uncertainty of approximately 2 Volts.

2.3 Faraday Probe Theory

The Faraday probe is another widely used and documented plasma diagnostic technique [1, 2]. Its theory, however, is much simpler compared to that of the Langmuir probe.

A Faraday probe is a planar conducting surface exposed to a plasma flow. The probe current due to the ion flux into the probe surface is recorded and divided by the surface area to measure the ion current density. The probe is biased to a suitably large negative potential with respect to the local plasma potential, so that all the electrons in the plasma are repelled, and that only the ion current is collected by the probe.

2.4 Faraday Probe Measurement Error

The ion current density measured by a Faraday probe is subject to error associated with uncertainty in the measuring electrostatic probe. Major sources of error in the Faraday probe measurements which include:

- the uncertainty in the collected ion current due to the magnetic field effects the ion motion
- the uncertainty in the collected ion current due to the disturbance in the plasma caused by the presence of the probe in the plasma
- the uncertainty in the collected ion current due to the secondary electron emissions by high energy ions impinging on the probe surface
- the uncertainty in the calculated ion current density due to the edge effect
- the uncertainty in the measurements of the probe current

will be discussed in this section.

For the plasma conditions in the very-near-field region of the SPT-100 plume, the ion motion is not appreciably influenced by the magnetic field. Furthermore, the ion Larmor radius is large compared with probe dimensions. In the near- and far-field region of the thruster plume, the magnetic field is negligible. For these reasons, magnetic effects are not expected to significantly impact the ion current measurements.

The probe dimensions are much larger than the Debye length, and the electron mean free path is large compared to the probe radius in all regions of the thruster plume studied. Therefore, the disturbance in the local plasma caused by the probe potential should be small as discussed in Section 2 of this chapter for the Langmuir probe measurement error.

The probe in the near- and far-field study was sufficiently aligned to the plasma flow vector (like the Langmuir probe), so that the error due to the misalignment was negligible. In the very-near-field study, the probe was always parallel with the thruster

axis, and thus the probe was misaligned with the plasma flow vector except near the thruster centerline. When the plasma flow is not perpendicular to the probe collection surface, the projected collection area becomes smaller, and hence the actual ion current density will be higher than the calculated value. This error becomes larger as the probe moves radially away from the thruster centerline.

A SPT-100 plume possesses high energy ions. These ions have enough energy to cause secondary electron emissions on the probe surface. These secondary electrons are minimized, as for the Langmuir probes, by constructing the probe surface with tungsten which has a very low secondary electron yield. The secondary electron emission yield for xenon ions bombarding tungsten is virtually constant at 0.02 over the range of possible ion energies (0 ~ 1 keV) [9]. Therefore, the error associated with the secondary electron emissions is estimated to be 2%.

In order to keep all the electrons in the plume from reaching the probe surface, the probe surface is biased to a large negative potential with respect to the local plasma potential. This causes the sheath on the probe surface to grow, and the actual ion current collection area becomes no longer a plane, but a three-dimensional surface like a part of a flattened sphere. Now, the actual ion current collection area is larger than the probe surface area. This phenomenon is known as the edge effect. A guard ring, a shield electrode surrounding the edges of the collector electrode, can be used to eliminate the edge effect. This guard ring is biased at the same potential as the collector, but is electrically isolated from the ion collection surface. The effect of the guard ring is to create a uniform planar electric field upstream of the collector surface, so that the ions are extracted only through an area equal to that of the collector surface.

The edge effect extends from the probe surface to a distance on the order of a Debye length. Thus, for the guard ring to be effective, the gap distance between the guard ring and the collector electrode must be on the order of a Debye length. For the near- and far-field ion current density measurements, a Faraday probe with a guard ring

was used to eliminate the edge effect. For the very-near-field measurements, the Faraday probe did not have a guard ring because the thickness of the protective alumina sleeve, which surrounded a tungsten rod and would otherwise separate the guard ring from the ion collecting tungsten rod, was much larger than the Debye length. Thus, a guard ring would be ineffective in eliminating the edge effect. However, since the Debye length in this region of the plume was much smaller compared to the probe, the error due to the edge effect should be small.

Error due to the uncertainty in the probe current measurements is the uncertainty in the least significant digits of the probe current, and this error is estimated to be on the order of 2%. Combined with the error associated with the secondary electron emission by high energy ions impacting the probe surface, the total error is estimated to be approximately 5%. When the error due to the probe misalignment is added for the results of the very-near-field study, the total error is estimated to be in the range of 5% to 50% with 5% for the data near the thruster centerline and 50% for the data at the farthest radial position.

Reference to Chapter 2

- 1 Lochte-Holtgreven, W., Editor, Plasma Diagnostics, AIP Press, Woodbury, New York, 1995.
- 2 Hutchinson, I., Principles of Plasma Diagnostics, Cambridge University Press, New York, 1987.
- 3 Lecture Notes for the Course, "Production and Diagnosis of Process Plasmas," Princeton Scientific Consultants, Inc., Princeton, New Jersey, Nov. 1984.
- 4 Huddlestone, R.H. and Leonard, S.L., Editors, Chen, F.F., Contributing author, Plasma Diagnostic Techniques, Chapter 4, Academic Press, New York, 1965
- 5 Sonin, A.A., "Free Molecular Langmuir Probe and its Use in Flowfield Studies," AIAA Journal, Vol. 4, No. 9, pp. 1588-1596, 1966.
- 6 Godard, R. and Laframboise, J.G., "Total Current to Cylindrical Collectors in Collisionless Plasma Flow," Planet. Space Sci., Vol. 31, No. 3, pp. 275-283, 1983.
- 7 Gavryushin, V.M. and Kim, V., "Effect of the Characteristics of a Magnetic Field on the Parameters of an Ion Current at the Output of an Accelerator with Closed Electron Drift," Soviet Physics, Technical Physics, Vol. 26, No. 4, pp. 505-507, April 1981.
- 8 Manzella, D.H., "Stationary Plasma Thruster Ion Velocity Distribution," AIAA-94-3141, June 1994.
- 9 Brown, S.C., Basic Data of Plasma Physics, AIP Press, New York, 1994.

CHAPTER 3

VERY-NEAR-FIELD PLUME STUDY OF THE SPT-100

3.1 Introduction

The ion current density, electron number density, and electron temperature of the very-near-field (10 mm to 200 mm downstream of the thruster exit plane) plume of the SPT-100 were measured using a miniature Langmuir probe and a miniature Faraday probe. The radial profiles of these plasma parameters were obtained at axial distances of 10 mm, 25 mm, 50 mm, 100 mm, and 200 mm. The data revealed distinct peak structures in the thruster plume, providing insight into the plume plasma conditions.

General probe theories and the sources of error in the measurements were described in Chapter 2. This chapter provides the experimental set-up and the descriptions of the single Langmuir probe and the Faraday probe specifically designed and constructed for the very-near-field study of the SPT-100, and presents the results of these diagnostics and discusses the implications of those results.

3.2 Experimental Set-Up For Very-Near-Field Study

The stationary plasma thruster studied in this work is the Fakel SPT-100. The description of this thruster is presented in Chapter 1. The operating point that was investigated with this thruster was 300 V and 4.5 A with a total xenon flow rate of 5.5 mg/s, with 0.28 mg/s of this going through the hollow cathode. The SPT-100 was stable over the measurement period. Prior to taking measurements, the thruster was allowed to run approximately 30 minutes to reach thermal equilibrium.

Experiments were conducted in a 9-m-long by 6-m-diameter stainless-steel vacuum chamber (cf. Chapter 1, Section 5). In addition, a Polycold water cryopump located above two of the oil diffusion pumps enhanced the overall water pumping speed. During thruster operation, the background pressure was 7×10^{-5} Torr (calibrated for xenon).

In order to acquire the radial profiles of the ion current density and the electron temperature and number density, the probes were mounted to a custom-made probe positioning system (cf. Chapter 1, Section 5). The thruster was placed on a stable, fixed platform in front of the positioning system. The radial table provided roughly 188 cm of travel while the axial table provided up to 91 cm of travel. The radial translation speeds, which are in excess of 60 cm/s, allowed for quick sweeps in and out of the plume thus avoiding excessive heating of the probes. The schematic of the experimental set-up is shown in Figure 3-1.

All radial profile measurements were taken in steps of 5.08 mm (0.2 in.) from the centerline of the thruster (0 mm position) to 200 mm outward opposite to the side where the cathode is located. The axial position was varied from 10 mm to 200 mm downstream of the thruster exit plane. Although the positioning system has the absolute position accuracy of 0.15 mm, initial alignment of the probes with a reference point (“zero” position of the measurements) was only accurate to within 2 mm in both radial and axial directions. Hence, the absolute positions for all data had an uncertainty of 2 mm.

To collect data this close to the exit plane, the probes were quickly moved to the collection site, kept there long enough to collect data (~ 0.5 sec.), and rapidly moved out of the plasma flow to allow for probe cooling. This approach also served as an effective means of cleaning the probes.

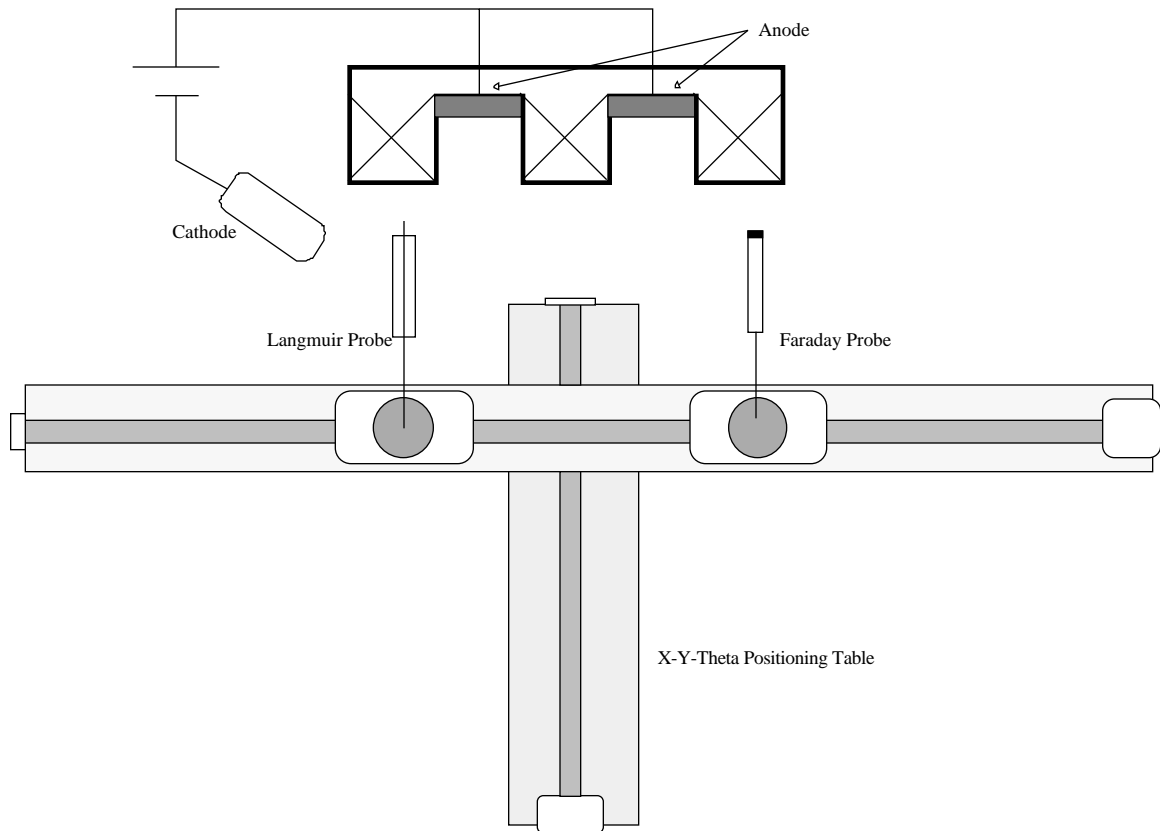


Figure 3-1 Schematic of the experimental set-up for the very-near-field study (not to scale).

Since the probes used for the very-near-field study have their outer shell made of alumina which is a non-conducting material, the disturbance in the local plasma caused by the probe body is only of a fluid dynamic nature. As it will be described in the following sections, the probes were made very small to minimize this disturbance.

Plasma data from both probes were obtained using the circuit illustrated in Figure 3-2. The collection electrode is biased relative to tank ground using a Kepco model BOP 100-2M programmable bi-polar power supply. The current signal is measured via a Tektronics AM501 operational amplifier which sends the voltage signal which develops across the 10.02 k resistor to a Tektronics TDS 540 digital oscilloscope. The probe voltage is sent directly to the oscilloscope. The current-voltage characteristic stored in the oscilloscope is then exported for analysis to a computer using a National Instruments

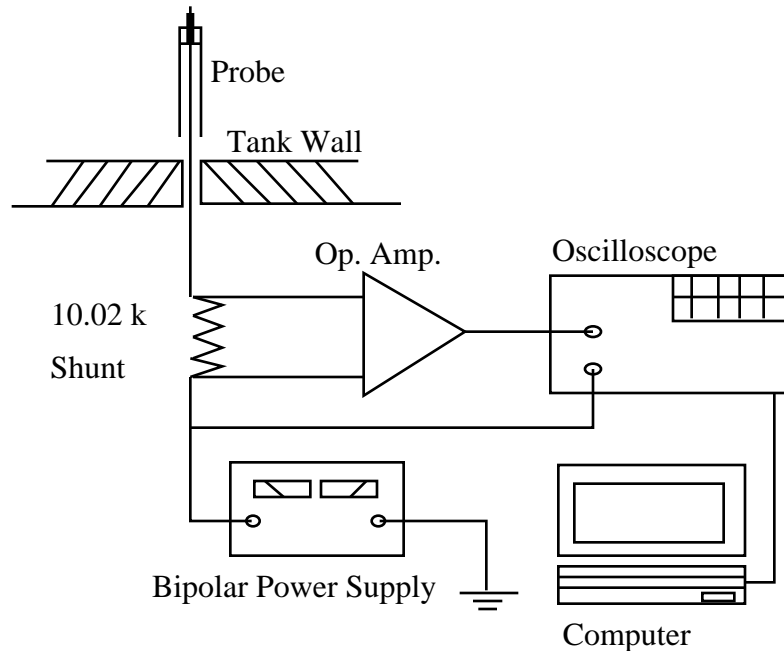


Figure 3-2 Probe circuit used in the very-near-field study.

GPIB interface. In the case of the Langmuir probe, the bipolar power supply's voltage was ramped in order to obtain the current voltage characteristic. In the case of the Faraday probe, the collector was maintained at a bias voltage of -47 V with respect to ground to repel electrons and thus collect primarily the ion flux.

3.3 Description of Langmuir Probe Used in Very-Near-Field Study

For the very-near-field study of the SPT-100 plume, a miniature Langmuir probe was designed and constructed. The size of the probe was chosen in such a way that it was small enough to minimize the probe disturbance of the plasma flow, but large compared to the Debye length so that the thin sheath Langmuir probe analysis could be used.

The schematic of the miniature Langmuir probe is shown in Figure 3-3. The cylindrical Langmuir probe consisted of a 0.127 mm diameter, 0.88 mm long tungsten

wire collection surface which was separated from the remaining wire via a Pyrex casing.

A half-and-half mixture of hydrofluoric and nitric acids was used to trim the tip of the 0.127 mm Diameter

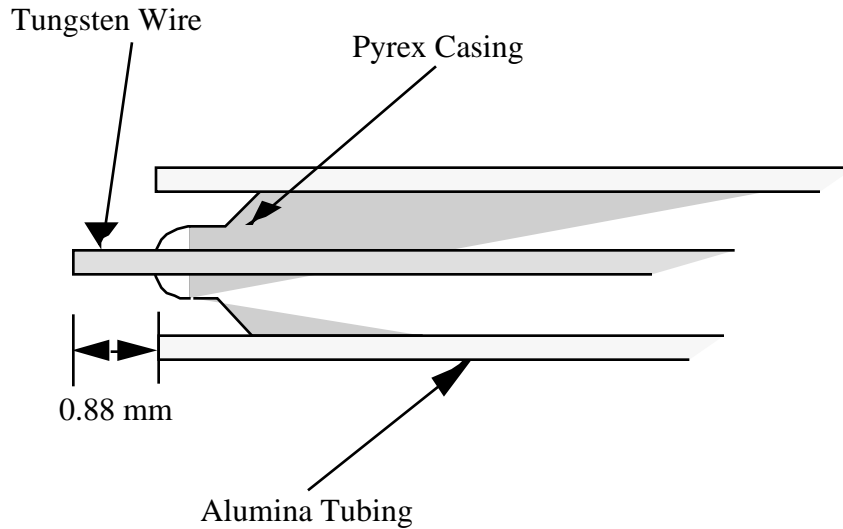


Figure 3-3 Schematic of the miniature Langmuir probe used in the very-near-field study.

tungsten wire. This casing was further protected by an alumina sleeve that fit over the casing's outer surface. The overall length of the probe was 30 cm.

3.4 Description of Faraday Probe Used in Very-Near-Field Study

A miniature Faraday probe was also designed and constructed for the very-near-field study. The Faraday probe consisted of a 2.4 mm diameter tungsten rod that was surrounded by an alumina sleeve so that only the end surface was exposed to the plasma. The schematic of the miniature Faraday probe is shown in Figure 3-4. A guard ring was not used because the thickness of the protective alumina sleeve which would otherwise separate the guard ring from the actual probe was much larger than a Debye length. Since the edge effect extends from the probe surface to the distance on the order of a Debye length, the gap distance between the guard ring and the collector electrode must be

on the order of 9 microns for the guard ring to be effective in the very-near-field region of the plume. It was beyond our capability to construct such a probe. Fortunately, the

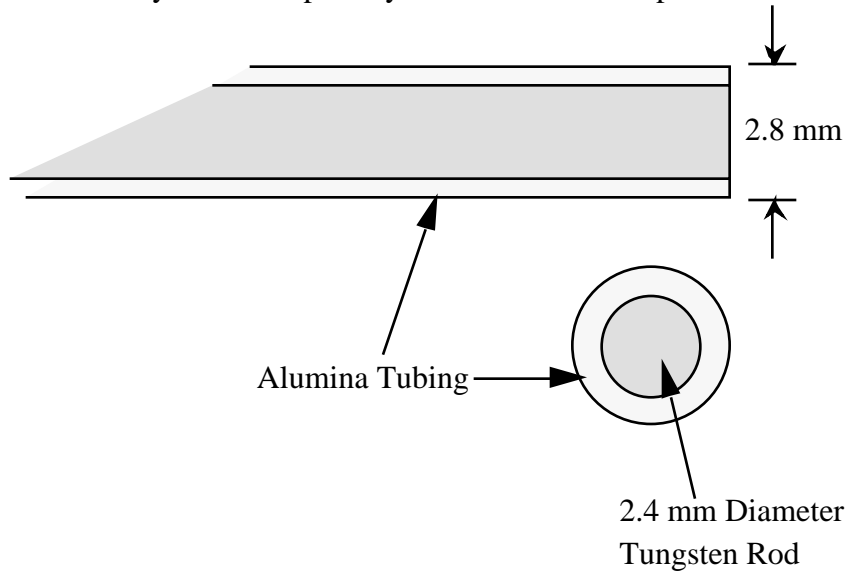


Figure 3-4 Schematic of the miniature Faraday probe used in the very-near-field study.

error due to the edge effect should be small due to the same reason that a guard ring could not be added to the probe; that is, because the Debye length in this region of the plume was much smaller than the diameter of the tungsten rod.

3.5 Results and Discussion

This section will discuss each parameter of the plasma measured in the very-near-field of the SPT-100 plume. In order to avoid crowding the plots, error bars are not shown. The error in the ion current density is between 5% to 50%, with 5% for the data at the thruster centerline and 50% for the data at the farthest radial position. The average error in the electron temperature is 15%. The error in the electron number density measurements is 60%. For detailed error analysis, please refer to Chapter 2, Sections 2 and 4. Also, note that “Z” will be used in this section to denote axial distance from the thruster exit plane (e.g. $Z = 50$ mm).

3.5.1 Ion Current Density in Very-Near-Field

Figure 3-5 shows the radial distributions of ion current density measured at different axial positions. Note that there is a pair of dashed lines on the plot indicating the location of the thruster discharge chamber channel.

The variation of the ion current density with axial distance from the thruster indicates that the ion beam begins as an annulus, and then merges into a single-body beam.

At $Z = 10$ mm, the ion current density has a very sharp and large peak in front of the thruster discharge chamber. This indicates that the ions are coming out of the thruster channel as a narrow beam, perhaps narrower than the width of the discharge chamber. Farther downstream, the peak in front of the discharge chamber decreases in magnitude and broadens. This implies that the ions are diverging from the exit of the thruster discharge channel both inward and outward radially.

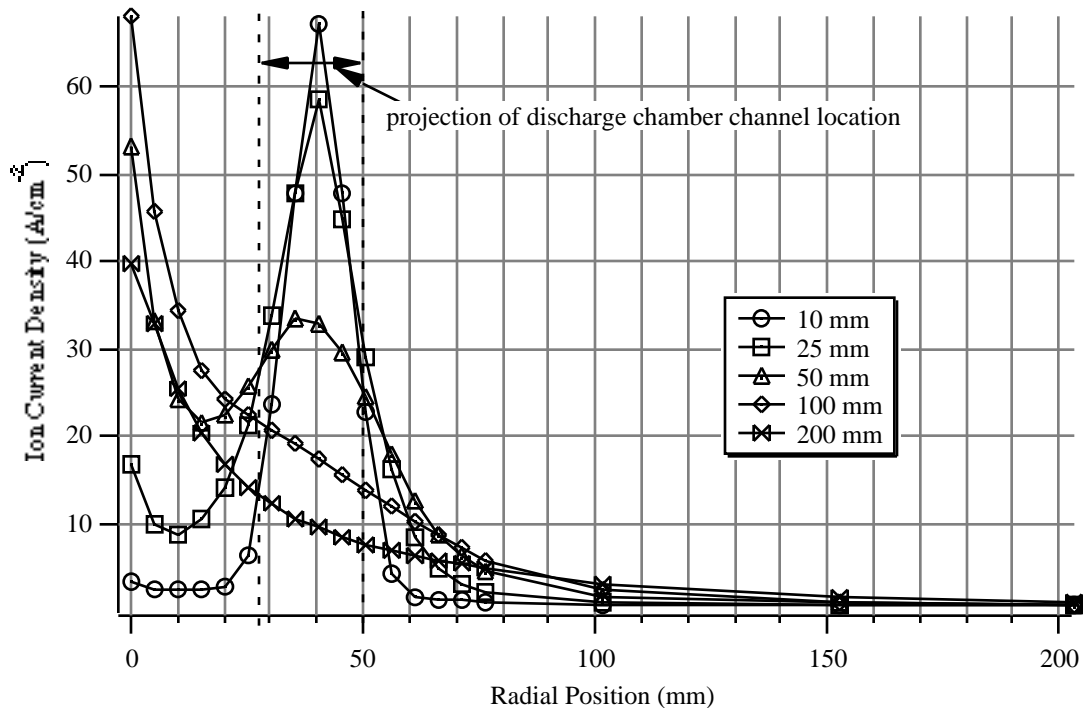


Figure 3-5 Radial profiles of ion current density at different axial locations from the SPT-100 exit plane in the very-near-field.

The ion current density at 0 mm radial position (on centerline) is almost zero at $Z = 10$ mm, and increases and forms a peak at larger axial positions. These peaks are attributed to the fact that the diverging annular ion beam overlaps at the centerline of the thruster. The ion current density at the center increases up to $Z = 100$ mm, and then begins to decrease at larger axial positions. This implies that the inner boundary of the annular ion beam converges on the centerline at or near $Z = 100$ and defocuses at larger axial positions. Therefore, the angle of the inner boundary of the annular ion beam with respect to the thruster axis is calculated to be approximately 16 degrees with respect to the thruster axis when it is assumed that the inner boundary originates from the exit of the inner discharge chamber wall. Downstream of this focal point, the overlapping annular beam forms one broad plume. The flat ion density profile in front of the discharge chamber at $Z = 100$ mm in Figure 3-5 is another indication that this distance is where the

transition is occurring. The ion current densities on centerline (0 mm radial position) were normalized to a distance of 1 m from the thruster using a $1/r^2$ dependence and were compared to previous studies [1], which showed that this normalization was valid in the far-field region of the SPT-100 plume. The ion current density at $Z = 200$ was in good agreement with previous investigations. The ion current densities at the closer axial locations were, however, much lower than the calculated normalized values. This further supports the above conclusion that the ion beam begins as an annulus, merges into a single-body beam at or near 100 mm downstream of the thruster exit, and defocuses at larger axial positions.

Total ion current at each axial location, calculated by integrating the ion current density with appropriate differential area assuming that the ion distribution in the SPT-100 plume is axisymmetric, is tabulated in Table 3-1.

axial position (mm)	total ion current (A)
10	3.97
25	4.92
50	4.95
100	4.51
200	3.86

Table 3-1 Total ion current at different distances from the SPT-100 exit plane in the very-near-field.

The lower total ion currents at $Z = 100$ mm and 200 mm are attributed to the fact that the measurements did not encompass the entire plume at those axial positions. For example, at $Z = 100$ mm, the farthest radial position measured corresponds to 64 degrees

off the thruster axis. The near- and far-field study, which will be discussed in Chapter 4, showed that there was measurable ion current beyond this angle.

The total ion current that would be measured if each xenon atom was singly charged can be calculated based on the measured xenon flow rate through the anode, assuming that 100% of xenon atoms were ionized in the discharge chamber. The total ion current calculated in this manner was 3.8 A. As the ionization fraction of the SPT-100 is less than 100% (between 95% and 100%) [2], the calculated ion current will be even lower. The measured total ion currents tabulated in Table 3-1 were higher than the calculated value. A similar result was found in a previous study [1], which attributed the high measured total ion current to the presence of multiply charged propellant ions.

Another possible explanation for the high measured total ion current is the measurement error due to the edge effect. As discussed in Chapter 2, Section 4, the Faraday probe used in this study did not have a guard ring. The error associated with the edge effect is more apparent for the data at larger axial positions because the Debye length, which provides a measure of the edge effect (cf. Chapter 2, Section 4), increases with axial positions in the thruster plume. From the electron temperature and number density data, the Debye length at larger axial positions is calculated to be about 10% larger than the Debye length at 10 mm axial position. Consequently, the total ion currents at $Z = 25$ mm and beyond are overestimated due to the edge effect. A simple calculation gives the percentage increase in the actual current collection area of approximately 15%. This error, coupled with the Faraday probe measurements error of 5%, would lower the measured total ion current to approximately 4.1 A at $Z = 25$ mm and 50 mm. This value is, however, still higher than the calculated total ion current of 3.8 A. It should also be noted that the probe angle was not varied, and that the probe was always parallel to the thruster axis. When the plasma flow is not perpendicular to the Faraday probe collection surface, the projected collection area is smaller than the probe surface area used to calculate the ion current density, and thus, the ion current density will be

higher than the measured values. This error becomes larger as the probe moves away radially. Therefore, the total ion current will be higher than the values in Table 3-1.

In summary, the total ion current density calculated from the measured xenon flow rate assuming that the thruster plume plasma consists of only singly charged xenon ions is at most 3.8 A, and the measured total ion current density corrected for the edge effect and the measurement error is at least 4.1 A. Hence, the edge effect and the measurement error cannot, by themselves, account for the discrepancy between the two values of the total ion current. This result leads to a conclusion that there must be multiply charged xenon ions in the thruster plume. Past spectroscopic studies of the SPT-100 have shown that the 80% of the ions were singly charged, and that the other 20% were doubly charged in the plume of the SPT-100 [3]. When these fractions are used, the calculated total ion current based on the xenon flow rate becomes 4.5 A. This is more in agreement with the measured total ion current.

The above discussion demonstrates that detailed study of each ion species present in the plume plasma is essential to a complete analysis of the SPT-100 plume. This will be the subject of Chapters 6 and 7.

3.5.2 Electron Temperature in Very-Near-Field

Figure 3-6 shows the radial profiles of electron temperature measured at different axial locations. Note that there is a pair of dashed lines on the plot indicating the location of the thruster discharge chamber channel.

At very close axial positions ($Z = 10$ mm and 25 mm), the electron current approached saturation very slowly, and thus, there was no clear saturation “knee” in the $\ln(i_p+i_+)$ versus V_p plots (cf. Chapter 2, Section 1). Therefore, the slopes of those curves were taken at the probe voltages near the floating potentials. The data are consistent with an earlier study which measured electron temperature at the discharge chamber exit of a

Hall thruster to be 12 eV with large spatial gradient [4]. However, this result did not agree with the emission spectra data presented later in this section. This discrepancy will be discussed later.

The radial profile of the electron temperature is similar in shape to that of the ion current density at the same location. The peak structure in front of the discharge chamber channel is still apparent at $Z = 50$ mm. However, the peak decreases in magnitude and broadens as the electrons move away axially from the thruster. As the electrons move axially, they continue to cool, and the magnitude of the radial variation disappears. This is seen by the virtually flat profiles of the electron temperature at $Z = 100$ mm and 200 mm. This trend agrees with the ion current density data discussed in the previous subsection since the electrons follow the ions to maintain quasineutrality in the thruster plume.

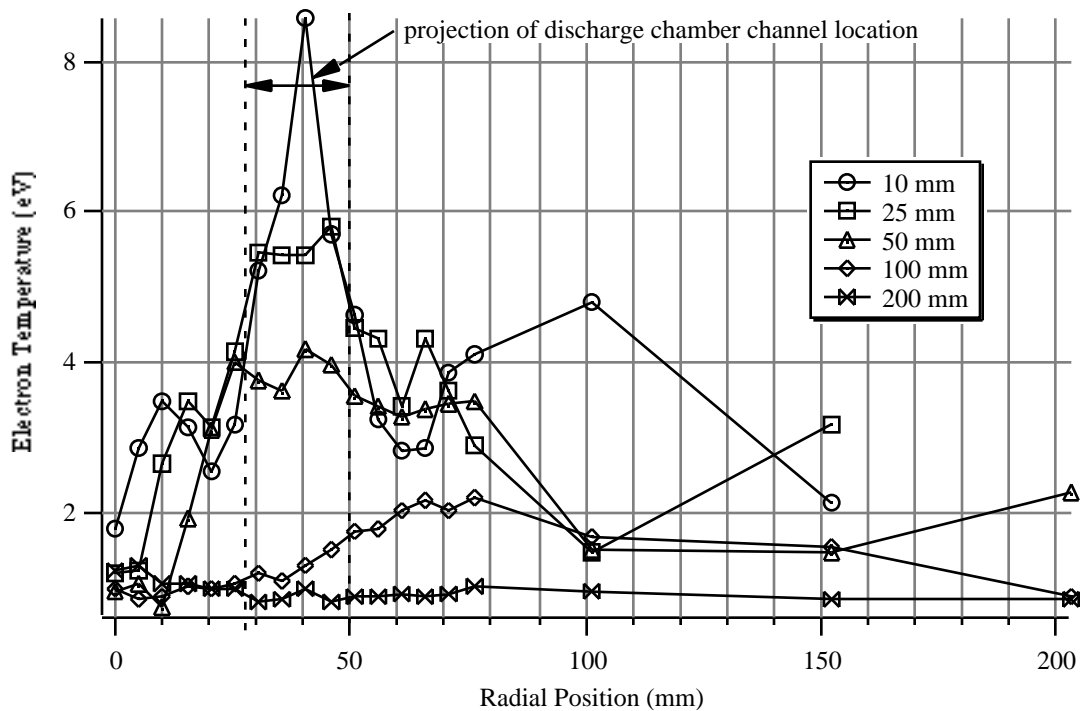


Figure 3-6 Radial profiles of electron temperature at different axial locations from the SPT-100 exit plane in the very-near-field.

Xe II emission spectra were acquired along a chord extending across the cross section of the exit plane to determine the equilibrium state of the plasma near the source. By plotting $\ln[I_{ki} \lambda_{ki} / g_k A_{ki}]$ versus E_k/k , a Boltzmann excitation temperature was obtained, where E_k is the energy of the excited state, I_{ki} is intensity of the transition, λ_{ki} is the wavelength of the transition, A_{ki} is the transition probability, g_k is the degeneracy of the upper state, and k is Boltzmann's constant [5]. At equilibrium, $\ln[I_{ki} \lambda_{ki} / g_k A_{ki}]$ versus E_k/k should be a straight line. Scatter in the Boltzmann plot obtained from the measured spectra suggests that the atomic energy level populations are not completely in Local Thermal Equilibrium (LTE) with the electrons. This is due in part to the low electron number density which is insufficient to collisionally dominate excitation and de-excitation processes. One can approximate the electron temperature by using the excitation temperature if Partial LTE exists. For Partial LTE to be valid, the electron number density must satisfy the following condition [5]:

$$n_e \geq 7 \times 10^{18} \frac{z^7}{n^{17/2}} \frac{kT}{z^2 E_H} \quad \text{in cm}^{-3}, \quad \text{Eqn. 3-1}$$

where $z - 1$ is the charge state (i.e. $z = 1$ for neutral atoms, $z = 2$ for singly charged ions, etc.), n is the principal quantum number, T is the excitation temperature, and E_H is the ionization energy of hydrogen (13.6 eV). From the Boltzmann plot's slope, the excitation temperature was determined to be 2.7 eV. This result is consistent with an earlier spectroscopic measurements of the SPT-100 [3]. For all the transitions that the outer electrons make, the principal quantum number n is 3. Then, n_e must be equal to or larger than $2.7 \times 10^{14} \text{ cm}^{-3}$ for Partial LTE to be valid in the plume plasma. However, as will be seen in the next subsection, the calculated n_e had the maximum value of $3.5 \times 10^{11} \text{ cm}^{-3}$, and thus, the plume plasma is not in Partial LTE. The Boltzmann excitation temperature is smaller than the electron temperature measured by the Langmuir probe by roughly a

factor of three, which is consistent with the fact that the excitation temperature gives a lower bound in the electron temperature.

3.5.3 Electron Number Density in Very-Near-Field

Figure 3-7 shows the radial profiles of electron number density measured at different axial positions. Note that there is a pair of dashed lines on the plot indicating the location of the thruster discharge chamber channel.

Again, the radial profile of the electron number density is similar in shape to that of the ion current density at the same location. The axial variation in the peak structure is also similar to that of the ion current density. This implies that the electrons follow the beam ions, and provides an evidence of quasineutrality of the SPT-100 plume plasma. A first order calculation of the beam ion number density based on the local ion current density and a 245 V acceleration voltage chosen from the **ExB** probe data, which will be discussed in Chapter 7, resulted in number densities that are within 25% of the measured

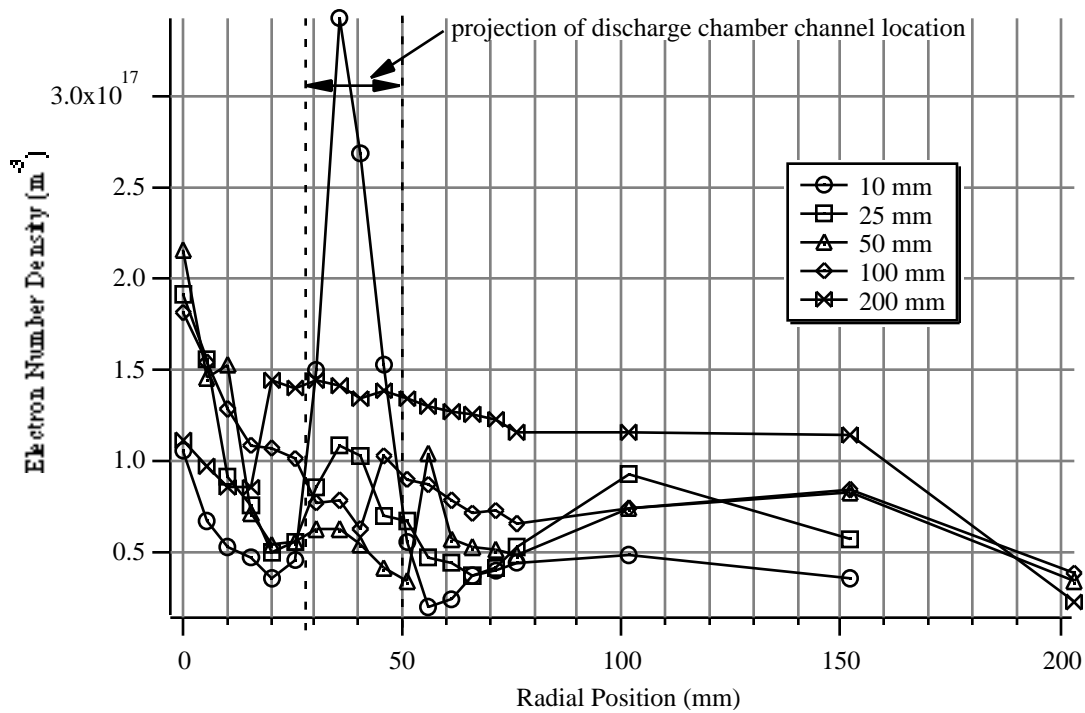


Figure 3-7 Radial profiles of electron number density at different axial locations from the SPT-100 exit plane in the very-near-field.

electron number densities, except at the locations in the plume very close to the thruster. (These exceptions will be discussed in the following.) Considering that the total error in the electron number density measurements is approximately 50% (cf. Chapter 2, Section 2), this further validates the quasineutrality condition in most part of the thruster plume.

An exception to the electrons following the beam ions is the peaks in the electron number density on centerline (0 mm radial position) at small axial positions, specifically at $Z = 10$ mm, 25 mm, and 50 mm. The ion current density at these locations either did not exhibit an appreciable peak or exhibited a small peak compared to the other peaks at farther axial locations (cf. Figure 3-5). Those peaks on centerline at the small axial positions are attributed to electrons confined by the magnetic field cusp formed by the thruster magnetic coils. Meanwhile, those peaks on centerline at larger axial positions are attributed to electrons attracted to the corresponding high ion density at those

locations so as to maintain quasineutrality in the plasma. The amplitudes of these centerline peaks at different axial positions are comparable to each other, which is not the case for the ion current density data (cf. Figure 3-5). The first order calculation of the beam ion number density mentioned above shows that the calculated beam ion number densities on centerline (0 mm radial position) at the small axial positions are an order of magnitude smaller than the measured electron number densities at the same locations.

Another exception to the electrons following the beam ions is a disproportionately large concentration of electrons just in front of the discharge chamber at $Z = 10$ mm. The peak electron number density at this location is approximately 3 times larger than that at $Z = 25$ mm, whereas the peak ion current density at this location is only a fraction higher than that at $Z = 25$ mm (cf. Figure 3-5). This high electron population can be attributed to three different sources of electrons; 1) electrons from the cathode drifting into the discharge chamber, 2) electrons produced by the ionization processes, and 3) the secondary electrons produced by the high energy ions hitting the thruster chamber wall. The electrons from the cathode are attracted to this location by the electric field between the cathode and the anode, and are trapped there by the magnetic field formed by the thruster magnetic coils. The other two kinds of electrons are produced at or near the exit plane and are trapped there by the same magnetic field. Thus, these electrons are directly related to the thruster mechanism of the SPT-100. Therefore, the electron population in the thruster plume is controlled by the competing effects of two phenomena; the electric and magnetic field influences and the quasineutrality in the plasma. The former is dominant in the plume region close to the thruster exit plane, and the latter is dominant in the plume farther downstream of the exit plane. The boundary of the two regions is somewhere between 50 mm and 100 mm downstream of the thruster exit plane.

The exceptions to the electrons following the beam ions at the locations very close to the thruster discussed above must, however, be viewed with some cautions. Recall that the electron number density was deduced from the ion saturation current, and

hence, the charge neutrality in the plasma was assumed in the Langmuir probe analysis. The apparent charge non-neutrality is between the electrons and the *beam* ions. The Faraday probe measured high energy beam ions accelerated and ejected from the thruster. However, there are low energy propellant ions resulting from charge exchange collisions and many other stray ions floating in the vacuum chamber due to facility pumping limitations. The electron number density was deduced primarily from these low energy ions, and therefore, it is important to distinguish beam ions measured by the Faraday probe from the electrons deduced from the low energy ions in the vacuum chamber. The effect of charge neutrality between the electrons and the beam ions on the plume characteristics in the absence of the low energy ions cannot be known from the data reported here. A study in a ultra-high vacuum environment or in space is needed to resolve this issue.

The axial variation in the peak structure in front of the discharge chamber channel demonstrates the diverging annular shape of the electron number density profile. The peak can be clearly seen at $Z = 10$ mm, 25 mm, and 50 mm. This peak is poorly defined at $Z = 100$ mm, and disappears at $Z = 200$ mm. This finding, coupled with quasineutrality in the thruster plume plasma 100 mm downstream of the thruster exit plane and beyond, further supports the conclusion drawn in the discussion of ion current density that the diverging annular ion beam overlaps on center line at or near 100 mm downstream of the thruster exit, forming one broad plume at farther axial locations.

It should be noted that the probe angle was not varied, and that the probe was always parallel to the thruster axis. The electron number density at large radial positions are higher than expected since the electron number density should decrease rapidly as a function of increasing radial position [6]. The error due to a misaligned probe can affect not only the absolute values of the measured electron number density but the relative profiles as well. As discussed in Chapter 2, Section 2, supersonic ion flow, perpendicular to a cylindrical probe, increases the ion current significantly. Since the ion saturation

current was used to calculate the electron number density, the actual electron number density at those large radial positions would be much smaller than the measured electron number density, therefore explaining the unusually high density measured at large radial positions in this study.

One puzzling feature of the electron number density profiles in Figure 3-7 is that the electron number density at $Z = 200$ mm is higher than those at intermediate axial positions, which is opposite to what is expected. If the number density at $Z = 200$ mm is assumed to be less than that at $Z = 100$ mm, the probe radius is of the order of the Debye length at $Z = 200$ mm, and thus, the sheath must be considered thick. This could account for the high electron number density measurement at $Z = 200$ mm. The numerical analysis of Laframboise [7, 8] can be used to compute a more accurate solution for the electron number density. This was not done in this study.

3.6 Conclusions

Radial profiles of ion current density, electron temperature, and electron number density were measured at various axial positions in the very-near-field plume of the SPT-100. The radial ion current density profile exhibited distinct peak structures. The variation of the ion current density with axial distance from the thruster indicated that the ion beam began as an annulus diverging from the exit of the thruster channel both inward and outward radially, and then, merged into a single body beam at or near 100 mm from the thruster exit plane and defocused at larger axial positions. The angle of the inner boundary of the annular ion beam with respect to the thruster axis was calculated to be approximately 16 degrees. The total ion current data revealed that the SPT-100 plume consisted of both singly charged and multiply charged xenon ions.

The radial electron temperature profile was similar in shape to the ion current density at the same location. As the electrons moved away axially, they continued to

cool, and the magnitude of the radial variation disappeared. The excitation temperature obtained from the Boltzmann plot could not be used to approximate the electron temperature since the electron number density did not satisfy the condition for Partial LTE.

The radial electron number density profile was also similar in shape to the ion current density at the same location. The axial variation of the electron number density was also similar to that of the ion current density. The electron number density profiles, compared with the ion current density profiles, revealed that the electron population in the SPT-100 thruster plume was controlled by the competing effects of two phenomena; the electric and magnetic field influences on the electrons which was dominant in the plume region close to the thruster exit, and the quasineutrality in the plasma which was dominant in the plume farther downstream of the thruster exit. The boundary of the two regions was somewhere between 50 mm and 100 mm downstream of the thruster exit. The charge non-neutrality was observed very close to the thruster between the electrons and the beam ions. However, the quasineutrality in the plasma was believed to be maintained by the low energy ions resulting from charge exchange collisions and other stray ions in the vacuum chamber which were not measured by the Faraday probe.

Reference to Chapter 3

- 1 Manzella, D.H. and Sankovic, J.M., "Hall Thruster Ion Beam Characterization," AIAA-95-2927, July 1995.
- 2 Bobei, A., Kim, V., Loroteev, A., et al, "State of Work on Electrical Thrusters in the USSR," IEPC-91-003, 1991.
- 3 Manzella, D.H., "Stationary Plasma Thruster Plume Emissions," IEPC-93-097, Sept. 1993.
- 4 Bishaev, A.M. and Kim, V., "Local Plasma Properties in a Hall-Current Accelerator with an Extended Acceleration Zone," Soviet Physics, Technical Physics, Vol. 23, No. 9, pp. 1055-1057, 1978.
- 5 Griem, H.R., Plasma Spectroscopy, McGraw-Hill, New York, 1964.
- 6 Ohler, S., Gilchrist, B., and Gallimore, A.D., "Microwave Plume Measurements of an SPT-100 using Xenon and a Laboratory Model SPT using Krypton," AIAA-95-2931, July 1995.
- 7 Laframboise, J.G., "Theory of Spherical and Cylindrical Langmuir Probes in a Collisionless, Maxwellian Plasma at Rest," UTIAS Report No. 100, Toronto, Ontario, June 1966.
- 8 Chung, P.M., Talbot, L., and Touryan, K.J., "Electric Probes in Stationary and Flowing Plasmas: Part 1. Collisionless and Transitional Probes," AIAA Journal, Vol. 12, No. 2, pp. 133-154, Feb. 1974.

CHAPTER 4

NEAR- AND FAR-FIELD PLUME STUDY OF THE SPT-100

4.1 Introduction

The ion current density, plasma potential, electron number density, and electron temperature of the near- and far-field (25 cm to 1 m downstream of the thruster exit plane) plume of the SPT-100 were measured using a Langmuir probe and a Faraday probe. The angular profiles of these plasma parameters were obtained at axial distances of 25 cm, 50 cm, 75 cm, and 1 m. The data revealed differences between the very-near-field plume and the near- and far-field plume, providing insight into the plume plasma conditions.

General probe theories and the sources of error in the measurements were described in Chapter 2. This chapter provides the experimental set-up and the descriptions of the single Langmuir probe and the Faraday probe used for the near- and far-field study of the SPT-100, and presents the results of these diagnostics and discusses the implications of those results.

4.2 Experimental Set-Up For Near- and Far-Field Study

The stationary plasma thruster studied in this work is the Fakel SPT-100. The description of this thruster is presented in Chapter 1. The operating point that was investigated with this thruster was 300 V and 4.5 A with a total xenon flow rate of 5.5 mg/s, with 0.28 mg/s of this going through the hollow cathode. The SPT-100 was stable over the measurement period. Prior to taking measurements, the thruster was allowed to run approximately 30 minutes to reach thermal equilibrium.

Experiments were conducted in a 9-m-long by 6-m-diameter stainless-steel vacuum chamber (cf. Chapter 1, Section 5). Unlike for the very-near-field study, the Polycold water cryopump was not used. During thruster operation, the background pressure was 1.2×10^{-4} Torr (calibrated for xenon).

The plasma potential, the electron temperature and number density, and the ion current density were measured at various angles off thruster axis at a constant axial distance from the thruster exit plane. The thruster was mounted to a rotary table of the positioning system described in Chapter 1, Section 5. The thruster was mounted in such a way that the rotational axis of the rotary table coincided with the center of the thruster exit plane. The probes were placed on a stable, fixed platform in front of the positioning system, and aligned with the center of the thruster exit plane. With this arrangement, the thruster plume was sampled as a function of angular position at a fixed axial distance from the exit plane by rotating the thruster relative to the fixed probes. The schematic of the experimental set-up is shown in Figure 4-1 and Figure 4-2. Throughout this thesis, the zero degree position indicates the probe position aligned with the thruster axis. The positive angles represent the probe data in the cathode side of the thruster plume, and the negative angles represent the probe data in the non-cathode side of the thruster plume. The angular measurements were taken at axial distances of 25 cm, 50 cm, 75 cm, and 1 m from the center of the thruster exit plane. At these distances, probe heating by the impinging high energy ions in the plume was not enough to warrant special considerations as it was the case for the very-near-field study. Angular profiles of the plume data at different distances from the exit plane were obtained by moving the thruster and rotary table axially with the axial translation stage of the positioning system. Although the positioning system has the absolute position accuracy of 0.15 mm in the axial direction and 0.1 degree in the rotational direction, initial alignment of the probes with a reference point (“zero” position of the measurements) was only accurate to within 5 mm in the axial direction and 3 degrees in the rotational direction. Hence, the absolute

positions for all data had an uncertainty of 5 mm and 3 degrees in the respective directions.

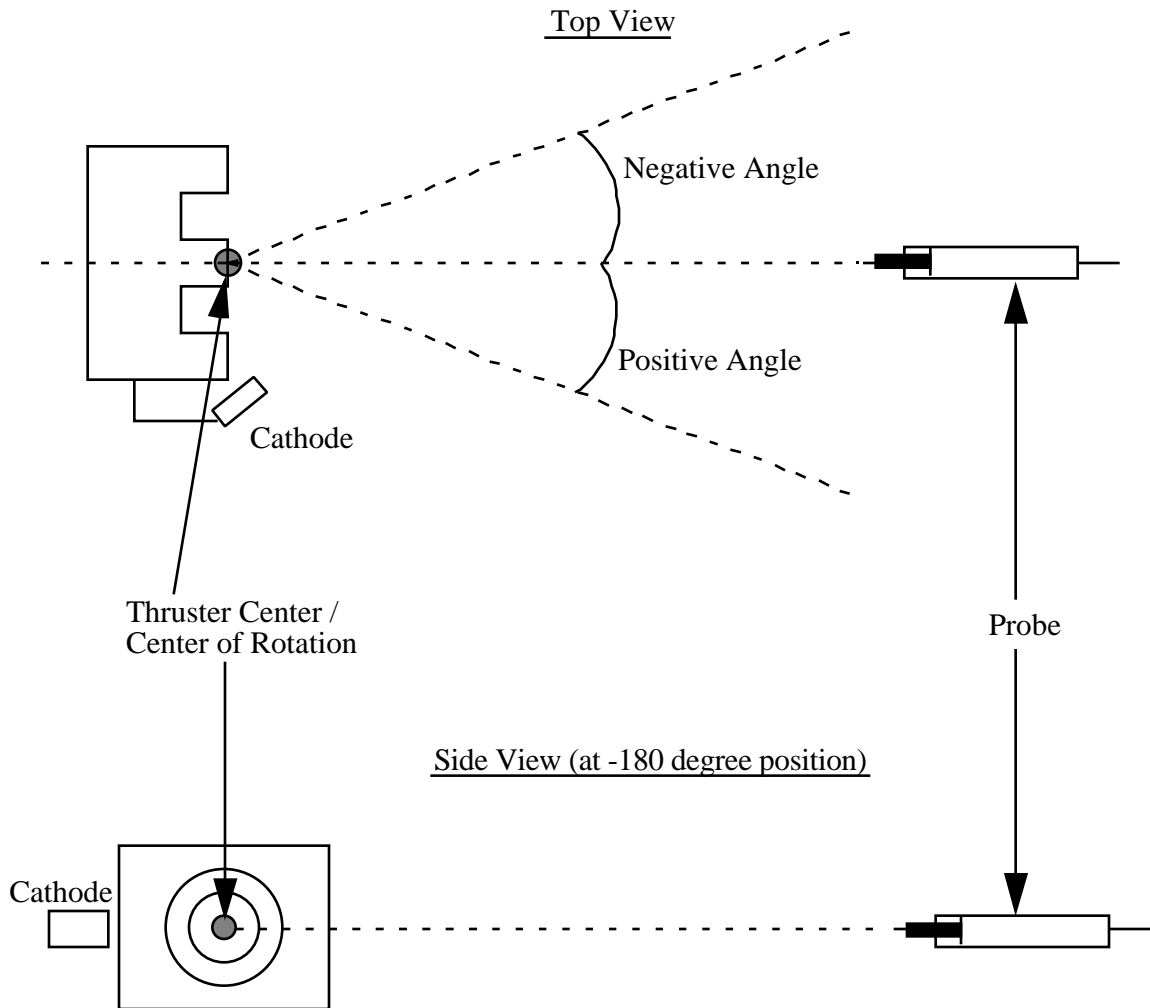


Figure 4-1 Schematic of the thruster-probe arrangement for the near- and far-field study (not to scale).

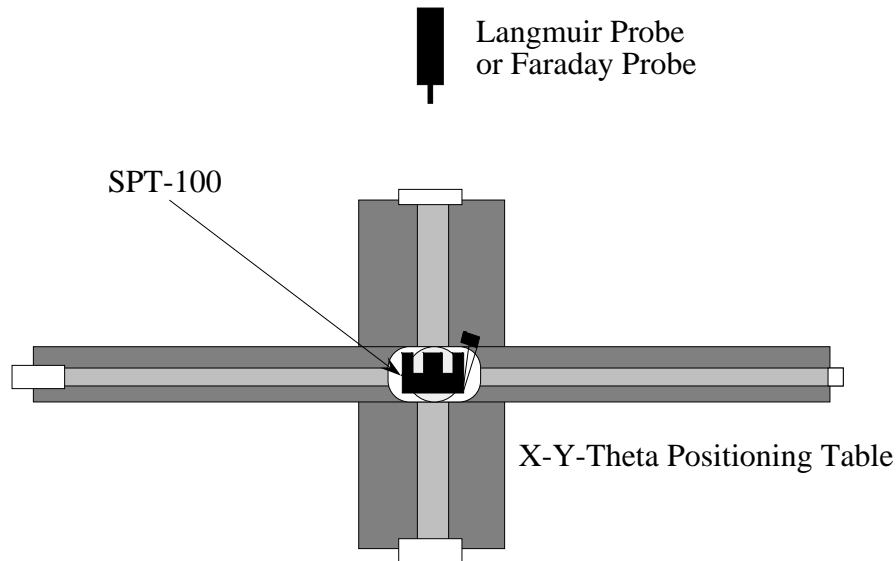


Figure 4-2 Schematic of the experimental set-up for the near- and far-field study (not to scale).

The Langmuir probe used for the near- and far-field study has a stainless steel probe boom, at the tip of which a tungsten electrode is attached. The boom is electrically isolated from the electrode. The error associated with the disturbance in the local plasma caused by the probe potential is minimal as discussed in Chapter 2, Section 2. A biasing voltage is not applied to the probe boom, and therefore, the disturbance in the plasma caused by the boom should be smaller than that caused by the probe electrode. However, the probe boom was kept not at the ground potential, but at the floating potential during the measurements to further minimize electrical disturbance in the local plasma caused by the probe boom.

Before each angular measurement, the probes were kept in the plasma for about 30 seconds with no voltage applied at zero degree position at the axial position of 25 cm to clean the probe surface by bombarding ions.

Plasma data from the Langmuir probe were obtained with the same circuit used in the very-near-field study (cf. Figure 3-2), except that a 1.4 high power resistor for the

data at the 25 cm axial position and a 10.02 Ω resistor for the data at other axial positions were used for the shunt instead of the 10.02 k Ω resistor.

Plasma data from the Faraday probe was obtained using the circuit illustrated in Figure 4-3. The collector electrode is biased relative to tank ground using a Kiethly 2410 high precision sourcemeeter. The current signal is measured using this sourcemeeter, and recorded directly to a spreadsheet by hand. The guard ring is biased relative to tank ground using a Kepco mode BOP 100-2M programmable bi-polar power supply. The collector was maintained at a bias voltage of -30 V with respect to ground to repel electrons and thus collect primarily the ion flux. The guard ring was maintained at the same bias voltage. The two voltages were measured using a high precision multimeter to make sure that they were the same, so that the guard ring was effective in eliminating the edge effect.

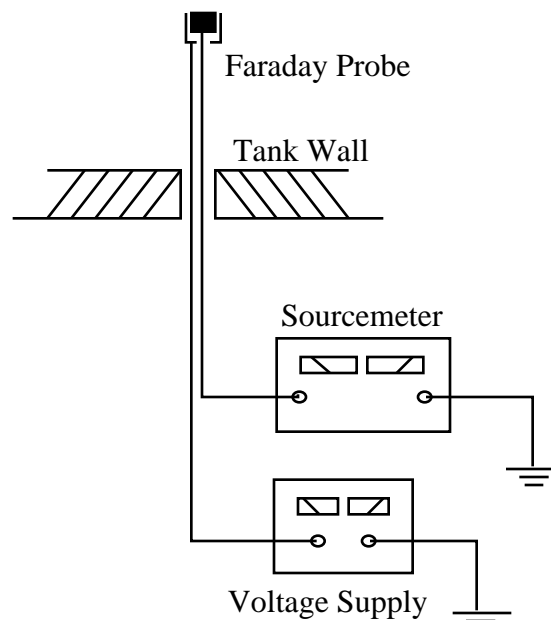


Figure 4-3 Faraday probe circuit used in the near- and far-field study.

4.3 Description of Langmuir Probe Used in Near- and Far-Field Study

The cylindrical Langmuir probe consisted of a 0.42 cm diameter, 5.1 cm long rhenium electrode and a 30 cm long stainless steel boom. The collector electrode was formed by vapor-depositing rhenium on a molybdenum mandrel, which had a threaded hole at the end and was screwed onto the boom. The collector electrode and the boom were electrically isolated. The probe radius is approximately 90 times larger than the Debye length, so that the thin sheath analysis of Langmuir probe could be used.

4.4 Description of Faraday Probe Used in Near- and Far-Field Study

The Faraday probe had a 2.4 cm diameter, stainless steel circular collector electrode which was spray-coated with tungsten. This disk was mounted flush with the end of a stainless steel cylindrical body, which served as a guard ring to eliminate the edge effect

4.5 Results and Discussion

This section will discuss each parameter of the plasma measured in the near- and far-field of the SPT-100 plume. In order to avoid crowding the plots, error bars are not shown. The error in the ion current density is 5%. The average error in the electron temperature is 15%. The error in the electron number density measurements is 50%. The measured plasma potential has an uncertainty of approximately 2 Volts. For the error analysis, please refer to Chapter 2, Sections 2 and 4.

It should be noted again that, in the results of this study, the zero degree position indicates the probe position aligned with the thruster axis, that the positive angles represent the probe data in the cathode side of the thruster plume, and that the negative

angles represent the probe data in the non-cathode side of the thruster plume (cf. Figure 4-1). Also, note that, in this section, “R” will be used to denote the probe distance from the thruster center, and θ will be used to denote the probe angle with respect to the thruster axis (e.g. $R = 50$ cm, $\theta = -30^\circ$).

4.5.1 Ion Current Density in Near- and Far-Field

Figure 4-4 and Figure 4-5 shows the angular distributions of ion current density at different distances from the SPT-100 exit plane in logarithmic scale and linear scale, respectively.

At $R = 25$ cm, there is a central region of the plume at θ between -10° and 10° where the ion current density is sharply peaked. From there, the ion current density stays constant or increases slightly towards θ of $\pm 20^\circ$, and then, it decreases with large θ . These regions of the plume (-20° to -10° and 10° to 20°) corresponds to the inner boundary of the annular ion beam coming out of the thruster exit (cf. Chapter 3, Section 5.1). The angle of the inner boundary was calculated to be approximately 16 degrees with respect to the thruster axis. If the inner boundary were to be extended to $R = 25$ cm, the probe angle that intersects the inner boundary would be ± 10 degrees. This may seem to suggest that the ion beam diverging from the thruster exit keeps the annular shape beyond 25 cm downstream of the thruster exit plane. However, the detailed analysis in Chapter 3, Section 5.1 concluded that the ion beam lost the annular shape and formed a single-body beam at or near 10 cm downstream of the thruster exit. Therefore, the observed low ion current density at -20° to -10° and 10° to 20° at $R = 25$ cm is not due to the annular shape of the ion beam at that distance, but is an indirect result of the annular ion beam in the very-near-field region of the SPT-100 plume.

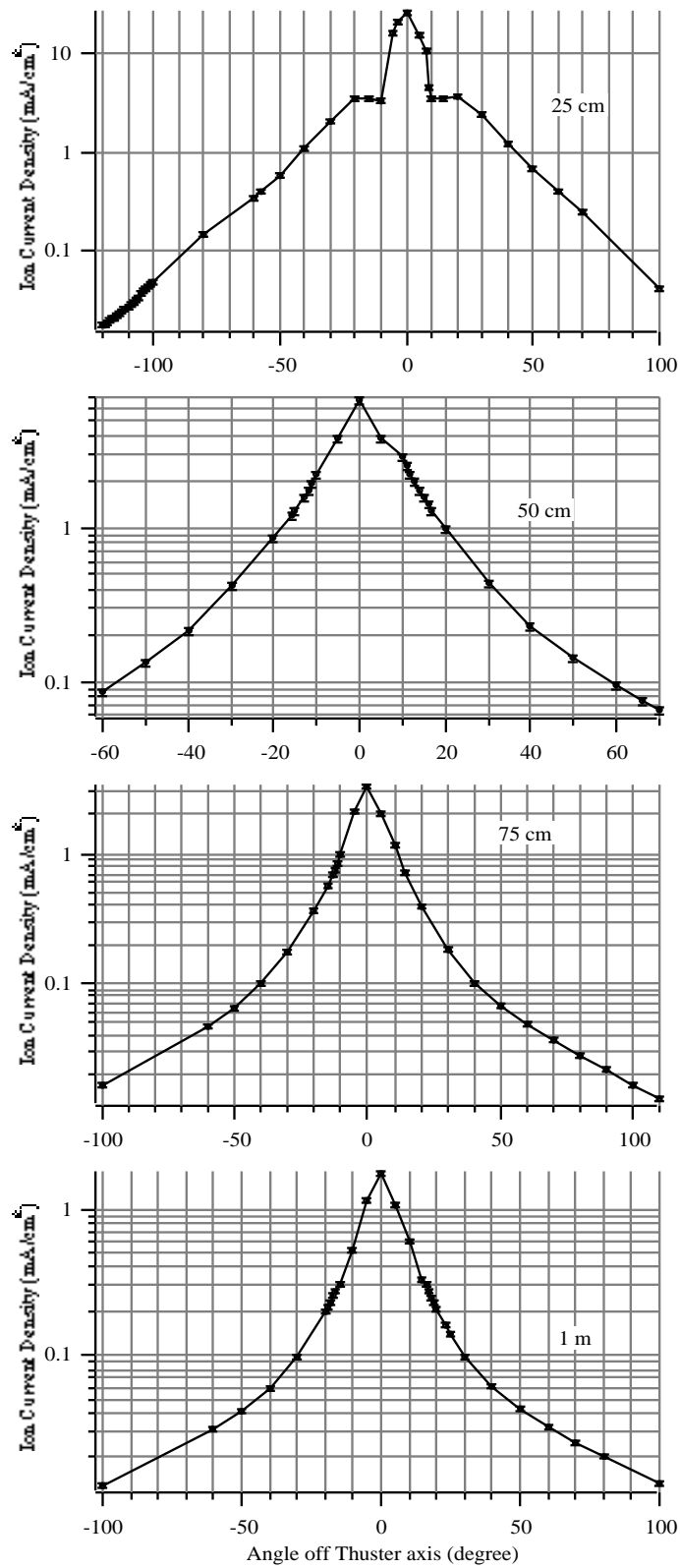


Figure 4-4 Angular profiles of ion current density at 25 cm, 50 cm, 75 cm, and 1 m from the SPT-100 exit plane in logarithmic scale.

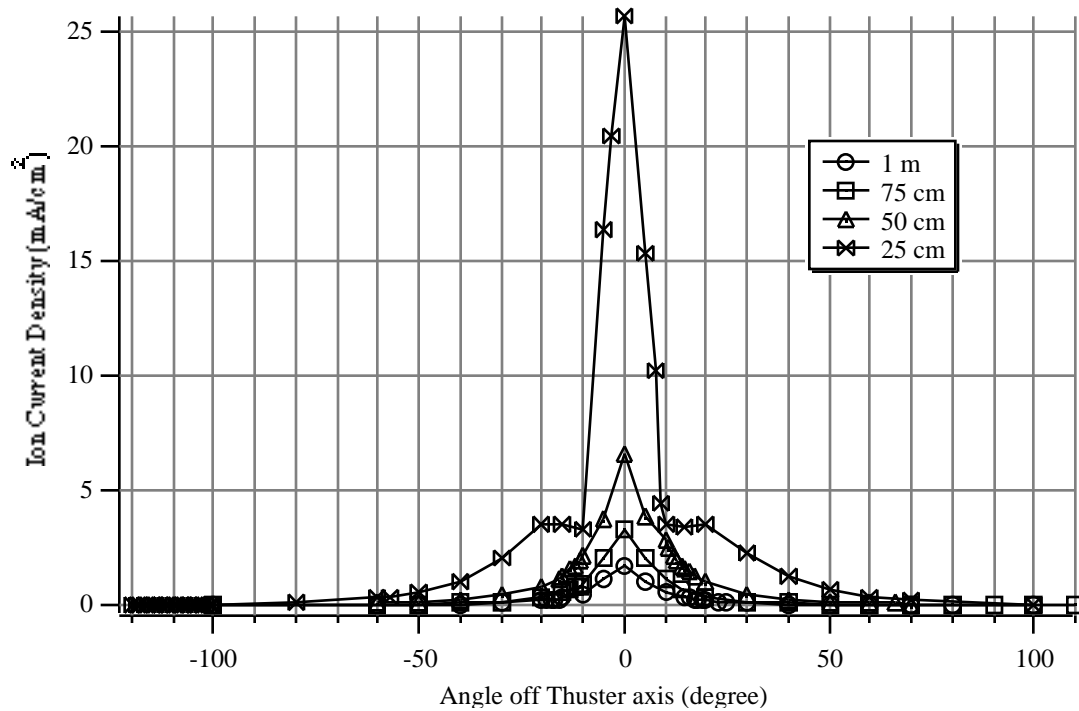


Figure 4-5 Angular profiles of ion current density at 25 cm, 50 cm, 75 cm, and 1 m from the SPT-100 exit plane in linear scale.

A previous study of the SPT-100, which showed that there was high neutral flux within 20 degrees of the thruster axis [1], suggests that the observed low ion current density at -20° -10° and 10° 20° is a result of charge exchange collisions. The conic region surrounded by the inner boundary of the annular ion beam in the very-near-field region of the plume contains neutral atoms, consisting of xenon atoms from the anode and cathode and some ambient background gas due to vacuum pumping limitations, although most of the xenon atoms come from the cathode [2]. These neutral atoms undergo charge exchange collisions with fast moving directed ions, which results in fast moving directed neutrals and slow ions moving in arbitrary directions. The probability of these charge exchange collisions is greatest near the inner boundary of the annular ion beam where the high number of ions and neutrals meet.

Since the ion current density is written as:

$$\mathbf{j}_i = n_i e q_i \mathbf{u}_i, \quad \text{Eqn. 4-1}$$

these charge exchange collisions manifest themselves as low ion current density at a larger distance from the thruster exit plane at -20° , -10° and 10° , 20° . At the same time, the slow ions moving in arbitrary directions will be subsequently measured at large angles, adding to the already existing plume ions. Consequently, the charge exchange decreases the ion current density at -20° , -10° and 10° , 20° , and increases the ion current density at large angles. This effect becomes less pronounced at the central part of the plume (where the ion current density is reduced due to charge exchange) and more pronounced at large angles (where the ion current density is added due to charge exchange) with increasing distance from the thruster exit plane as the SPT-100 plume defocuses at larger distances from the thruster exit plane. It is interesting that even though the plume has lost its annular shape and becomes a single-body beam, the imprint of the original annular structure of the ion beam extends throughout the entire plume. Although the fraction of the charge exchange ions is no more than 5 ~ 7% of the total xenon flow in the SPT-100 plume [2], the presence of neutral flow in the SPT-100 plume leads to an ion backflow in the direction opposite to the main flow, and qualitatively changes the structure of the SPT-100 plume [3]. It should be noted that since the charge exchange collisions between the plume ions and the background neutrals would be negligible in space, interpretation of ground test data must include consideration of this effect when assessing spacecraft integration.

The ion current density appears to be axisymmetric from Figure 4-4 and Figure 4-5. A detailed examination of the traces, however, reveals that the ion current density is on the order of 10% higher on the cathode side of the thruster plume (positive side)

than on the non-cathode side at the corresponding opposite angles at all distances from the thruster exit plane. This is believed to be a real physical phenomenon because the uncertainty in the ion current density measurements is conservatively estimated to be 5%. The ions gain their kinetic energies through the acceleration voltage V_i , and thus, from Eqn. 4-1, the ion current density is related to the ion number density, charge state, and acceleration voltage in the following manner:

$$j_i = n_i q_i^{3/2} V_i^{1/2}. \quad \text{Eqn. 4-2}$$

Therefore, higher ion density, higher charge state, or higher acceleration voltage will result in a higher ion current density. One could theorize that the observed asymmetry is due to the cathode itself where the cathode simply attracts and, hence, bends the ion beam slightly, resulting in a higher ion current density on the cathode side of the plume. However, the opposite was observed within $\pm 5^\circ$ off thruster axis at all distances from the thruster exit plane, i.e. the ion current density was always higher in the non-cathode side of the thruster plume within ± 5 degrees off thruster axis. Therefore, the reason for these observations is not known at this time.

Figure 4-6 shows the ion current densities at different distances from the thruster exit plane normalized to a distance of 1 m from the thruster using a $1/r^2$ dependence. This was done to verify the claimed $1/r^2$ current density dependence with the distance from the thruster. Aside from the data at $R = 25$ cm, the agreement between the normalized ion current densities at different distances from the thruster exit plane within ± 50 degrees off thruster axis is very good. The disagreement between the data at $R = 25$ cm and the data at other distances within ± 20 degrees off thruster axis stems from the influence of charge exchange collisions on the ion current density previously discussed.

The normalized ion current density outside of ± 50 degrees off thruster axis increases with increasing distance from the thruster exit plane. This is also attributed to the same charge exchange collisions between plume ions and background neutral atoms.

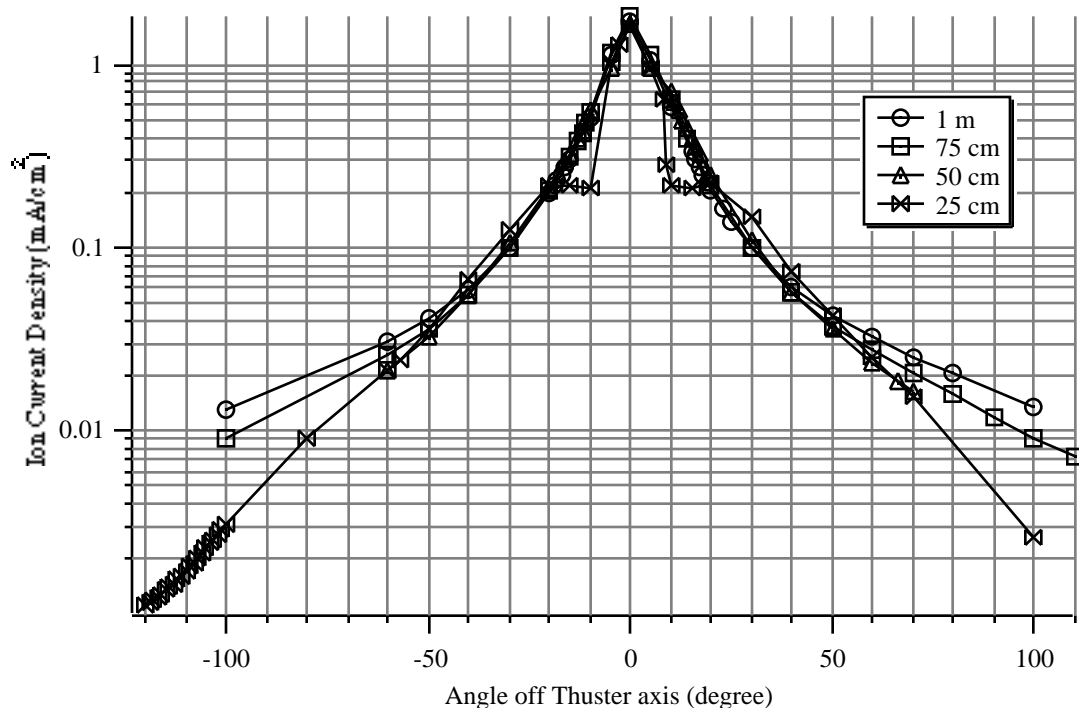


Figure 4-6 Ion current densities at 25 cm, 50 cm, 75 cm, and 1 m from the thruster exit plane, normalized to a distance of 1 m from the thruster using $1/r^2$ dependence.

As discussed earlier, this charge exchange results in the increased ion current density at large angles which becomes more pronounced at larger distances from the thruster exit plane.

The peak of the ion current density at $= 0^\circ$ becomes smaller with increasing distance from the thruster exit plane as the same ions occupy a larger area, but the base width of the peak (-50° 50°) remains fairly constant (cf. Figure 4-5, Figure 4-6).

This implies that the ions in the SPT-100 plume have linear trajectories, and that their trajectories vary little as they move away from the thruster exit plane.

Total ion current at each axial distance, calculated by integrating the ion current density with appropriate differential area assuming that the ion distribution in the SPT-100 plume is symmetric with respect to the measurement plane, is tabulated in Table 4-1.

distance from the thruster exit	total ion current (A)
25 cm	3.84
50 cm	4.26
75 cm	4.44
1 m	4.61

Table 4-1 Total ion current at different distances from the SPT-100 exit plane in the near- and far-field.

Increasing total ion current with increasing axial distance from the thruster exit plane is, again, attributed to the charge exchange between the plume ions and the neutral atoms discussed earlier. Charge exchange collisions conserve charge in the plasma, so there should not be an increase in total ion current. However, the statement above is correct for a very subtle reason. As discussed earlier with Eqn. 4-1, charge exchange collisions reduce the ion current density near the thruster axis and increases it at large angles. The subtle issue is how one integrates the data. The drop in the ion current density near the thruster axis is small (e.g. from 1 mA/cm² to 0.99 mA/cm²). But, at high angles, this absolute increase (0.01 mA/cm²) is significant. Also, since the charge exchange ions diffuse to the outside of the plume, one has to integrate over a much larger area at high angles in order to calculate the total ion current when charge exchange collisions occur in the plume. This increases the apparent ion current that is being produced. Furthermore, there are many stray ions floating in the vacuum chamber due to the facility pumping limitations which increase the ion current at large angles even more. These problems become worse with increasing distance from the thruster since the integration is over a

larger area. Hence, the total ion current increases with increasing axial distance from the thruster exit. As mentioned previously, interpretation of ground test data must include consideration of this effect. It should be noted that the uncertainty in the total integrated ion current can be strongly affected by the relatively low signal-to-noise ratio of the ion current density data in the outer region of the plume (> 60 degrees). However, since 80% of the total ion current is within 50 degrees of the thruster axis, the accuracy of the integrated ion current is expected to be high.

Following the same analysis discussed in Chapter 3, Section 5.1, the total ion current that would be measured if each xenon atom was singly charged is at most 3.8 A. The measured total ion current at $R = 25$ cm, which is affected the least by the charge exchange discussed above, is larger than the calculated value. Thus, the near- and far-field study reaches to the same conclusion with the very-near-field study that there exists multiply charged xenon ions in the SPT-100 plume plasma.

4.5.2 Electron Temperature in Near- and Far-Field

Figure 4-7 shows the angular profiles of electron temperature measured at different distances from the SPT-100 exit plane.

As discussed in Chapter 2, the magnetic field is negligible in the near- and far-field of the SPT-100 plume. This was confirmed by the fact that the electron current approached saturation quickly (seen in Figure 2-1 as an example) at all data points, except near centerline ($\theta = 0^\circ$) at $R = 25$ cm where the slopes of $\ln(i_p + i_+)$ versus V_p plots (cf. Figure 2-2) were taken at the probe voltages near the floating potentials. The slow electron saturation at the positions near $\theta = 0^\circ$ at $R = 25$ cm is believed to be caused by the probe collecting large current and thus changing the local plasma conditions. This could be corrected by using a smaller probe. Recall from Chapter 3, Section 5.3 that the dimension of the Langmuir probe used in the very-near-field study was too small for the

thin sheath analysis at 200 mm axial position. Perhaps, a third Langmuir probe, whose dimension is between that of the probe used in the very-near-field study and the probe used in the near- and far-field study, was needed to study the region of the SPT-100 plume between 10 cm and 50 cm from the thruster exit plane if the thin sheath analysis is to be used at all data points.

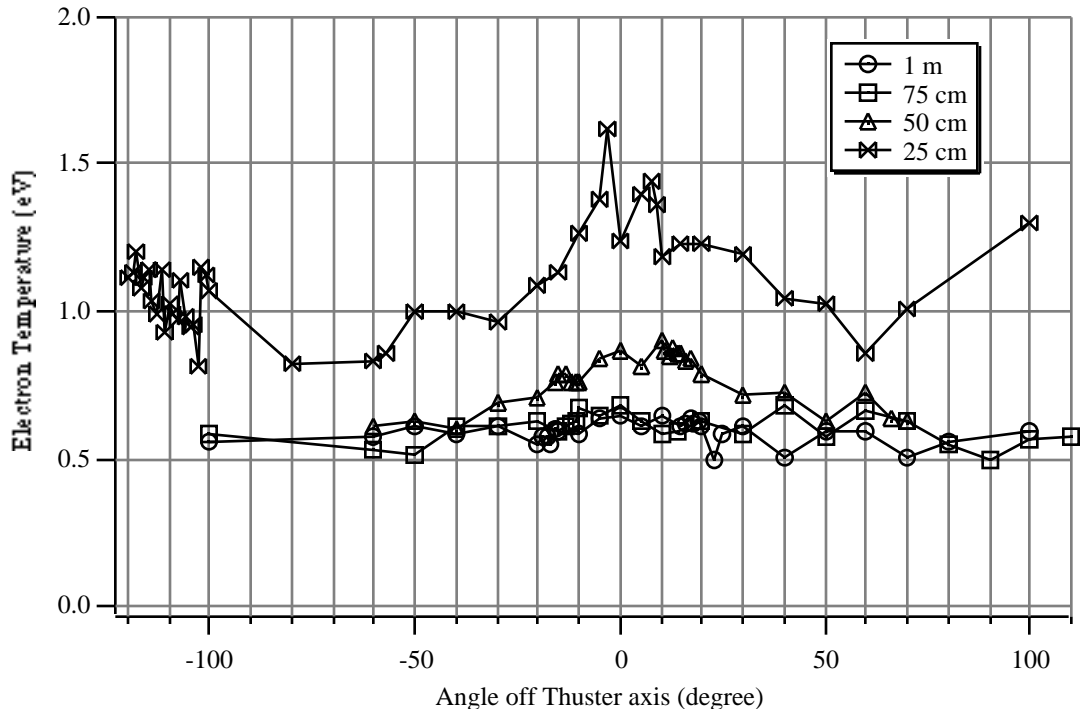


Figure 4-7 Angular profiles of electron temperature at 25 cm, 50 cm, 75 cm, and 1 m from the SPT-100 exit plane.

The electron temperature has a maximum of 1.5 eV near the centerline at $R = 25$ cm. This peak structure is still apparent at $R = 50$ cm, but the peak is much smaller compared to the data at $R = 25$ cm. The peak structure disappears at $R = 75$ cm, and the angular profile of the electron temperature becomes virtually flat. The electron temperatures at $R = 75$ cm and $R = 1$ m are indistinguishable. This trend in axial variation is similar to that of the ion current density in Figure 4-5. However, the electron temperature profile loses the peak structure much faster with increasing distance from the

thruster exit plane than the ion current density, due to the high mobility of the electrons. The measured electron temperatures are less than those in the earlier studies of the SPT-100 [4] which measured electron temperature of 4 eV at $R = 31$ cm.

4.5.3 Electron Number Density in Near- and Far-Field

Figure 4-8 shows the angular profiles of electron number density measured at different distances from the SPT-100 exit plane.

Each angular profile of the electron number density has a peak at $\theta = 0^\circ$. The peak becomes smaller with increasing distance from the thruster as expected, but the base width of the peak (-20° to 20°) remains constant at different distances from the thruster. At larger angles outside of the peak base, the electron number density is virtually constant on both sides of the thruster center, and has approximately the same value for all distances from the thruster. Similar results were observed in the angular profiles of the ion current density (cf. Figure 4-5). However, the peaks at $\theta = 0^\circ$ at $R = 75$ cm and 1 m are less defined compared to the corresponding peaks in the ion current density data. This is attributed to the high mobility of the electrons in the SPT-100 plume plasma compared to the ions.

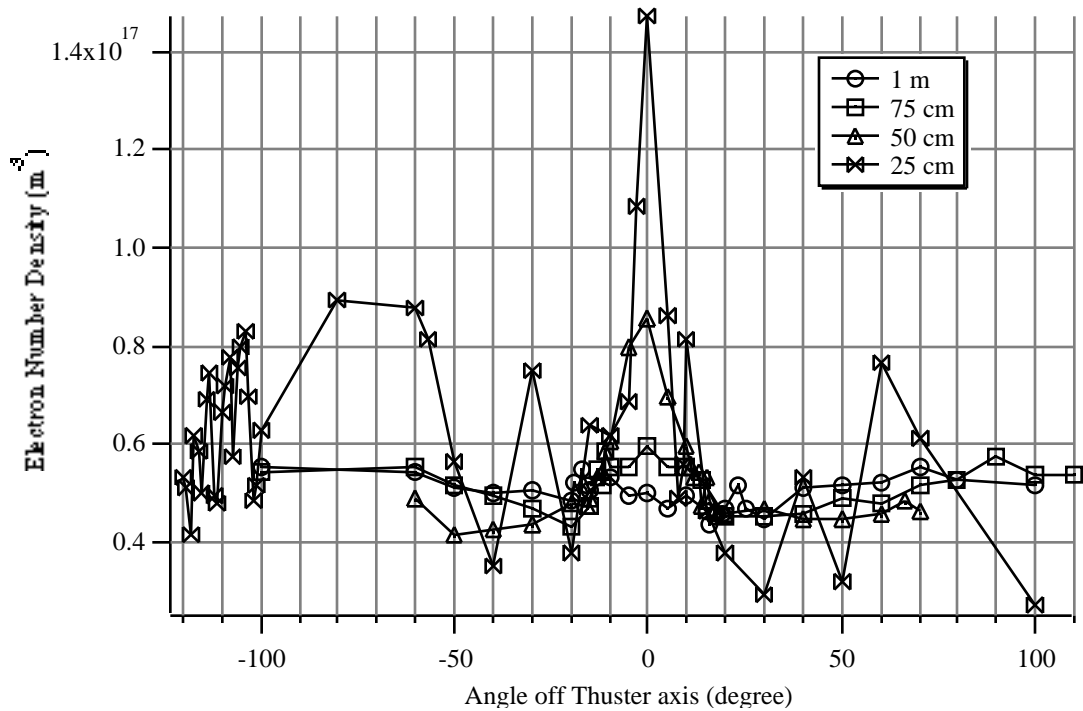


Figure 4-8 Angular profiles of electron number density at 25 cm, 50 cm, 75 cm, and 1 m from the SPT-100 exit plane.

A puzzling aspect of the electron number density data in Figure 4-8 is the unexpectedly high densities at 104° and $= -80^\circ, -60^\circ, -57^\circ, -30^\circ,$ and 60° at $R = 25$ cm. Although the ion saturation current was somewhat constant (within 15%) beyond $= \pm 50^\circ$, the angular zones of high density above are regions where low electron temperatures were measured (cf. Figure 4-7), thus resulting in calculated high number density (cf. Eqn. 2-1). More study is needed to determine the origin of these low electron temperatures.

The first order calculation of the beam ion number density performed in Chapter 3, Section 5.3 was repeated using the ion current density data in the near- and far-field study. The calculated beam ion number density was on average 80% less than the measured electron number density at the same measurement point. Therefore, there must be a significant number of charge exchange ions and other stray ions in the vacuum

chamber to maintain quasineutrality in the plasma. Nonetheless, the similar shape and behavior of the electron number density profiles with the beam ion current density profiles suggest that the electrons follow the path of the beam ions in the SPT-100 plume.

4.5.4 Plasma Potential in Near- and Far-Field

Figure 4-9 shows the angular profiles of plasma potential in the SPT-100 plume plasma. It should be noted that the cathode potential was approximately -15 V with respect to ground at $R = 25$ cm, and varied from -20 V to -12 V with respect to ground as the probe angle changed from the thruster axis to the high angles at $R = 50$ cm, 75 cm, and 1 m. The similarity in shape and magnitude of the plasma potentials at different distances from the thruster exit further supports the conclusion that the ions in the SPT-100 plume have linear trajectories, and that their trajectories vary little as they move away from the thruster exit plane. It is interesting to note that the angular profile of the plasma potential for the SPT-100 plume is opposite to that of an ion engine plume where the plasma potential has a peak on the thruster axis [5].

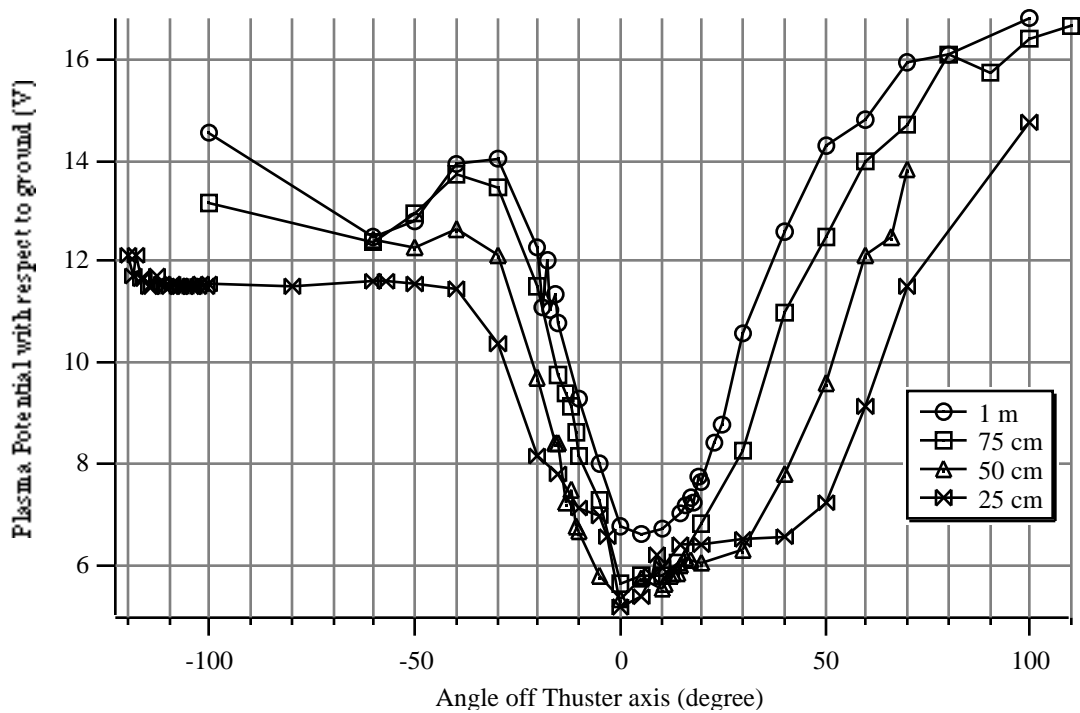


Figure 4-9 Angular profiles of plasma potential at 25 cm, 50 cm, 75 cm, and 1 m from the SPT-100 exit plane.

4.5.5 Comparison With Very-Near-Field Study

Figure 4-10 shows the near- and far-field data combined with the very-near-field data at 200 mm from the SPT-100 exit plane. Although the transition from the very-near-field data to the near- and far-field data is not smooth, the overall trend in each profile matches between the two data sets. As mentioned earlier, a third Langmuir probe, whose dimension is such that the thin sheath analysis can be used for investigating the region of the plume between 10 cm and 50 cm from the thruster exit plane, could possibly produce data that provide a smooth transition between the two data sets.

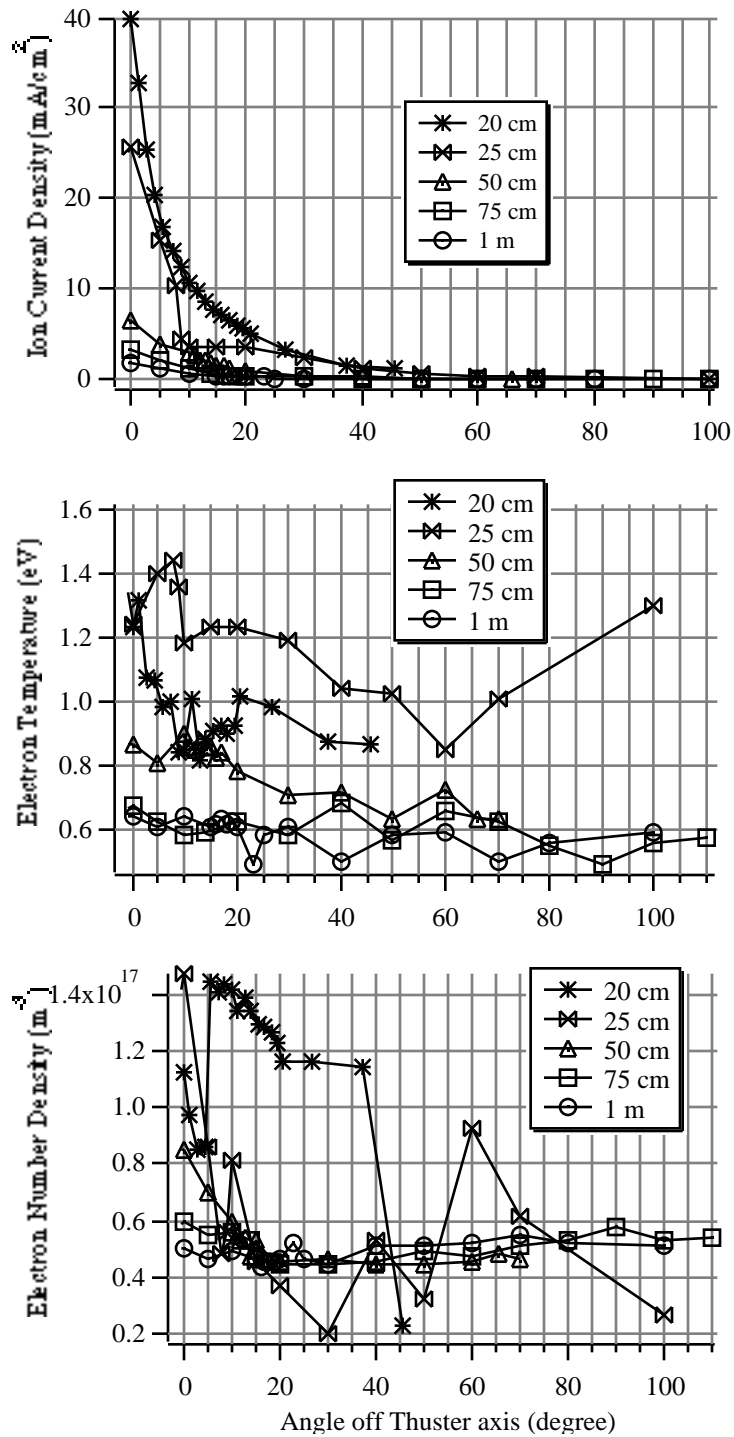


Figure 4-10 Comparison of the near- and far-field data with the very-near-field data at 20 cm from the SPT-100 exit plane.

4.6 Conclusions

Angular profiles of ion current density, electron temperature, electron number density, and plasma potential were measured at various distances from the thruster exit plane in the near- and far-field plume of the SPT-100. The angular profile of ion current density exhibited a peak on the thruster axis. The low ion current density observed at -20° , -10° and 10° to 20° at $R = 25$ cm was a result of charge exchange occurring near the inner boundary of the annular ion beam in the very-near-field of the SPT-100 plume. This charge exchange also caused the increase in measured ion current density at large angles. The ion current density was slightly higher on the cathode side of the plume than on the non-cathode side perhaps due to the cathode attracting and, hence, bending the ion beam slightly. The ion current densities normalized to a distance of 1 m from the thruster using $1/r^2$ dependence verified the validity of the $1/r^2$ current density dependence. The variation of the ion current density with increasing distance from the thruster suggested that the ions in the SPT-100 plume moved in linear trajectories, and that those trajectories varied little as the ions moved away from the thruster. The similarity in shape and size of the plasma potentials at different distances from the thruster also supported this conclusion. The measured total ion current was larger than the total ion current that would be measured if each xenon atom was singly charged. This implied that there were multiply charged xenon ions in the SPT-100 plume.

The angular profiles of the electron temperature and electron number density had similar shape with that of the ion current density. The variation of those profiles with increasing distance from the thruster was also similar. These results suggested that the ions and electrons in the SPT-100 plume followed the same path as they moved away from the thruster.

Reference to Chapter 4

- 1 King, L.B., Ph.D. Thesis, University of Michigan, Department of Aerospace Engineering, 1998.
- 2 Day, M., Gnizdor, R.U., Kaufman, H., Kim, V., et al, "Measurement of Plasma Parameters in the Stationary Plasma Thruster (STP-100) plume and its Effect on Spacecraft Components," AIAA-92-3156, July 1992.
- 3 Volkov, V., Morozov, A., Sveshnikov, A., Jakunin, S., "Numerical Modeling of Ion Dynamics in Systems with Closed Drift," Fizika Plazmi, Vol. 7, No. 2, pp. 245-253.
- 4 Myers, R.M. and Manzella, D.H., "Stationary Plasma Thruster Plume Characteristics," IEPC-93-096, Sept. 1993.
- 5 Pollard, J.E., "Plume Angular, Energy, and Mass Spectral Measurements with the T5 Ion Engine," AIAA-95-2920, July 1995.

CHAPTER 5

EXB PROBE ANALYSIS

5.1 Introduction

Past researches have shown that the Hall thruster plume consists of multiply charged propellant ions [1]. The Faraday probe measurements performed in this thesis have also implied that multiply charged propellant ions exist in the SPT-100 plume (cf. Chapter 3, Section 5.1 and Chapter 4, Section 5.1). Production of multiply charged propellant ions in the thruster discharge chamber is a loss mechanism for the thrust, thruster efficiency, and mass utilization [2]. It also causes more erosion of the discharge chamber wall due to the higher energy of those ions. Measuring the distribution of each ion species in a Hall thruster plume provides thrust correction factors (thrust loss, thruster efficiency loss, and mass utilization efficiency loss), and can help to make a more accurate assessment of the erosion of the thruster discharge chamber which is directly related to the thruster lifetime. Therefore, it is vitally important to investigate plasma parameters of individual ion species for a complete analysis of the Hall thruster plume. In order to begin this task, an attempt was made to measure the ion energy distribution of each ion species in the SPT-100 plume.

There have been many studies which have explored ion energy distributions in the Hall thruster plume using retarding potential analyzers (RPAs). However, RPAs cannot provide information on ion charge state [3].

Recently, an ion mass composition and energy investigation of the SPT-100 plume was performed by King at the University of Michigan [4]. This study utilized a sophisticated time-of-flight mass spectrometer combined with an electrostatic energy

analyzer to obtain ion species mass spectra for different ion energies. It also provided the ion distribution with respect to acceleration voltage using the electrostatic energy analyzer alone. The ion distribution with respect to acceleration voltage provided insight on collisional processes occurring within the SPT-100 plume. However, since different ion species that have experienced an identical (or similar) acceleration voltage would appear at the same (or similar) voltage in the distribution, the instrument could not distinguish the ion energy distributions of different ion species. The compilation of the ion mass spectra for different ion energies provided the energy distribution function of individual ion species. However, this indirect method of obtaining ion species energy distribution resulted in poor voltage resolution since the ion mass spectra was acquired for voltages in 20 V intervals.

An **ExB** probe is a simple diagnostics technique that can separate different ion species according to their velocities which are determined by the acceleration voltages. Its use in electric propulsion research has been limited to the investigations of ion thrusters, another form of electrostatic electric propulsion engines [2, 5, 6, 7, 8, 9]. In these studies, **ExB** probes were utilized to measure the ratio of doubly charged ions to singly charged ions in order to provide the thrust correction factors and the optimal operating condition for minimum production of multiply charged propellant ions. More recently, **ExB** probes were used to study dissociation or fragmentation of Buckminsterfullerene (C_{60}) propellant in ion thrusters [10, 11]. The ions in the ion thruster plume are essentially accelerated over the same potential, and thus, the resulting probe trace gives a mass spectra of the ion composition in the plume. The ion ratio is calculated directly from the peak heights of the collected ion currents of each species. The ions in the Hall thruster plume, on the other hand, are produced at different positions in the discharge chamber, and thus experience different acceleration voltages. Therefore, the resulting probe trace will have peaks with some widths. Since the ion velocities are related to their energies, the probe trace provides the ion energy distributions in the

thruster plume. The study reported here is the first attempt to use an **ExB** probe to obtain the ion energy distributions in the Hall thruster plume.

This chapter provides the theory, the description, and the experimental set-up of the **ExB** probe used in this study. This chapter also provides a discussion of the errors associated with the probe measurements.

5.2 Theory of ExB Probe

An **ExB** probe, also known as a Wien filter, is a simple example of a mass spectrometry device. As the name Wien filter suggests, the **ExB** probe is a velocity filter [12, 13], mostly used in front of a more elaborate mass spectrometer such as a magnetic sector mass spectrometer or in recent years a quadrupole mass analyzer.

When electric and magnetic fields act on a charged particle simultaneously, the force has both an electric and a magnetic component:

$$\mathbf{F} = e \cdot q_i \cdot \mathbf{E} + e \cdot q_i \cdot \mathbf{u}_i \times \mathbf{B}. \quad \text{Eqn. 5-1}$$

This is the well-known Lorentz force.

An **ExB** probe utilizes uniform crossed electric and magnetic fields which are perpendicular to each other and the particle velocity vector. Thus, the two fields and the particle velocity vector form orthogonal axes. Therefore, from Eqn. 5-1, the crossed fields exert opposing forces in the same plane on the charged particle traversing through such crossed fields. The fields can be adjusted, so that the opposing forces exerted by the two fields will cancel each other, and that there is no net force on the charged particle. Then, the charged particle will travel undeflected through the **ExB** section. This is shown schematically in Figure 5-1. The equation describing this is:

$$e q_i E = e q_i u_i B. \quad \text{Eqn. 5-2}$$

Eqn. 5-2 can be rearranged to give:

$$\frac{E}{B} = u_i \quad \text{Eqn. 5-3}$$

Thus, the probe acts as a velocity filter. Notice that neither mass or charge state of the analyzed particle appears in Eqn. 5-3, showing that the filtered velocity is independent of these parameters for the measurements of the **ExB** probe. This was the

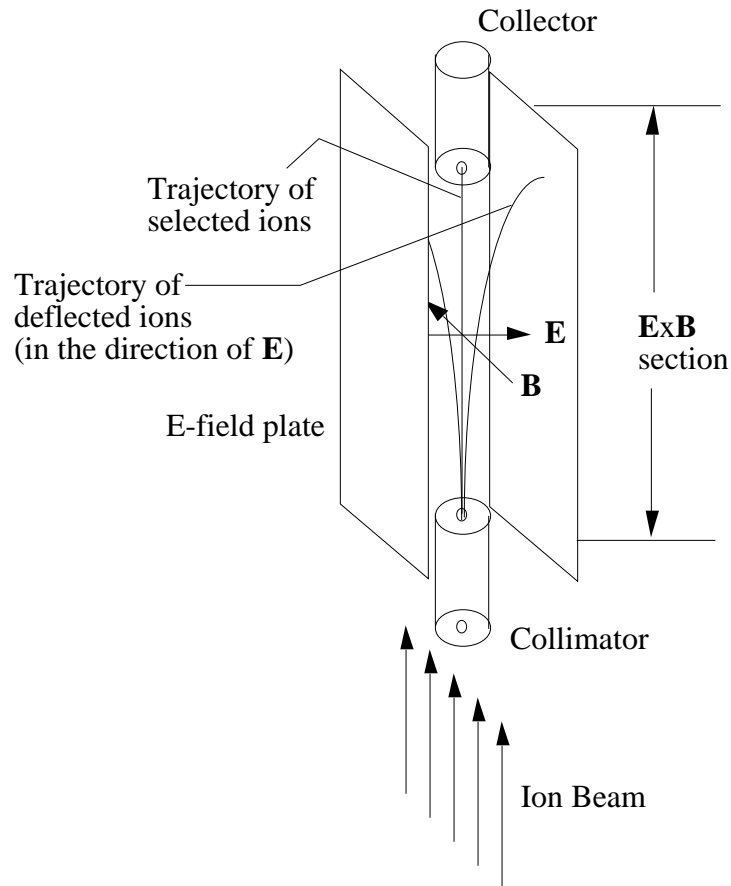


Figure 5-1 Schematic of ExB probe. A uniform electric field is formed by applying a voltage between the two parallel E-field plates. A uniform magnetic field is formed by four permanent magnets (not shown in the figure).

basis of Thomson's and Wien's classical experiments in which the velocities of electrons and simple ions were first determined around 1900. For the SPT-100, neutral xenon atoms enter the discharge chamber from the anode with virtually zero kinetic energy. The atoms are ionized by collisions with the closed-drifting electrons, and the ions are subsequently accelerated by the voltage gradient present in the discharge chamber in the direction parallel to the thruster axis. Since ions with different charge states experience similar acceleration voltages in the discharge chamber, the speed of the ions will be proportional to their charge state. Hence, the \mathbf{ExB} probe can distinguish ions with different charge states.

As discussed above, the ions in the SPT-100 plume gain their kinetic energies through the voltage gradient in the discharge chamber. Then, the kinetic energy of an ion in eV is written in terms of the acceleration voltage of the ion, V_i , as:

$$E_i = \frac{1}{2} \frac{q_i^2}{M_i} V_i^2 = q_i V_i. \quad \text{Eqn. 5-4}$$

Substituting for velocity using Eqn. 5-3, Eqn. 5-4 becomes:

$$E = B \frac{2 e q_i V_i^{1/2}}{M_i}$$

or

$$E = B \frac{2 e E_i^{1/2}}{M_i}. \quad \text{Eqn. 5-5}$$

Let d be the distance between the two parallel E-field plates and V_p (probe voltage) be the potential difference applied across the E-field plates (cf. Figure 5-1). The electric field is expressed in terms of d and V_p according to $E = V_p / d$. Then, for a given value of applied probe voltage, only ions with energy (in eV),

$$E_i = q_i V_i = \frac{M_i}{2e} \frac{V_p^2}{d B}, \quad \text{Eqn. 5-6}$$

will reach the collector and be recorded as ion current. It is obvious from Eqn. 5-6 that the **ExB** probe will be able to identify each ion species separately. Also, Eqn. 5-4 and Eqn. 5-6 show that E_i , u_i , V_i , and V_p are equivalent to each other.

An **ExB** probe trace was obtained by recording the collector current as a function of V_p while V_p was being ramped. The current collector employed by the probe was a ceramic channel electron multiplier (CEM). The important aspect of the CEM for the application in this study is that it serves as an ion counter rather than a charge counter. Therefore, the collector current of the probe is proportional to the ion number density at the measurement point. Thus, for a constant magnetic field, the collector current as a function of V_p can readily be converted into an ion energy distribution. This can be demonstrated by analyzing the output of the CEM. Since the CEM produces a current proportional to the number of ions incident on the CEM inlet surface, the current output can be written as:

$$I_i(V_p) = G_{\text{CEM}} A_c n_i(V_p) u_i(V_p). \quad \text{Eqn. 5-7}$$

The curve, $I_i(V_p)$ vs V_p , (i.e. the probe trace) can be converted to a curve, $I_i(E_i)$ vs E_i , by simply changing the scale of the abscissa according to Eqn. 5-6. The ion speed, u_i , can be written in terms of E_i via the relation in Eqn. 5-4. Also, from the kinetic theory of gases, the ion number density, n_i , in terms of the distribution function is given as:

$$n_i(E_i) = N_i f(E_i) dE_i. \quad \text{Eqn. 5-8}$$

Then, Eqn. 5-7 can be rewritten as:

$$I_i(E_i) = G_{\text{CEM}} A_c N_i \frac{2 e E_i^{1/2}}{M_i} f(E_i) dE_i. \quad \text{Eqn. 5-9}$$

Note that I_i is not stating the collector current for all values of E_i , but only for the specific value of E_i . (Thus, in the sense of the kinetics theory, I_i could be expressed as dI_i .)

Therefore, the energy distribution function is directly proportional to the **ExB** probe trace in the following manner:

$$f(E_i) = \frac{I_i(E_i)}{E_i^{1/2}}. \quad \text{Eqn. 5-10}$$

Hence, the ion energy distribution function can be obtained from the **ExB** probe trace by scaling the horizontal axis of the probe trace according to Eqn. 5-6 and by dividing the collector current by $E_i^{1/2}$. It should be noted that V_p was originally recorded with respect to ground. Thus, before being scaled according to Eqn. 5-6, the abscissa of the probe trace was corrected for the energy imparted to the ions as they fell from the ambient plasma potential through the probe to ground potential along the axis of the probe. The magnitude of the required correction is the plasma potential with respect to ground, which was measured by the Langmuir probe as discussed in Chapter 4, Section 5.4.

The above discussion showed that each peak on the **ExB** probe trace represents the energy distribution of an ion species. However, care must be taken for the interpretation of the probe trace, especially when comparing different peaks on the probe trace. This problem stems from the fact that the output current of the CEM depends on the energy and charge state of the ions impacting the CEM inlet surface. The resultant

effect is the increase in the output current for ions of higher energies and higher charge state. This effect will be discussed in detail later in this chapter.

5.3 Description of ExB Probe

The design of the **ExB** probe used in this study followed those of the **ExB** probes used in Ref. 2 and Ref. 5. The **ExB** probe consisted of three primary parts; the collimator, the main body which contained the **ExB** section, and the collector. The dimensions of each part were chosen to provide the following:

- 1) The collimator must focus on a sufficiently small area of the plume, yet provide a readily measurable signal.
- 2) The **ExB** section must provide clear separation of the ion species.
- 3) The length and aperture diameter of the collector must be adjusted with relation to the collimated ion beam to provide high resolution, yet insure that the entire beamlet is collected.

After the length of the collimator and the dimensions of the **ExB** section and collector were decided according to a desired resolution, several collimators of different aperture diameters were experimented with in order to find the optimal diameter for the highest resolution with a measurable collector current.

The overall length became longer than the probes used in previous studies. Although this caused the probe to weigh more than 75 lb., it was necessary to improve the resolution as much as possible because, unlike the previous studies performed on ion thrusters, the peaks of different ion species on a **ExB** probe trace were expected to overlap each other due to the energy spread of ions in the SPT-100 plume.

Figure 5-2 and Figure 5-3 show schematics of the **ExB** probe viewed from top and end, respectively. Figure 5-4, Figure 5-5, and Figure 5-6 show photographs of the **ExB** probe, the collimator, and the collector.

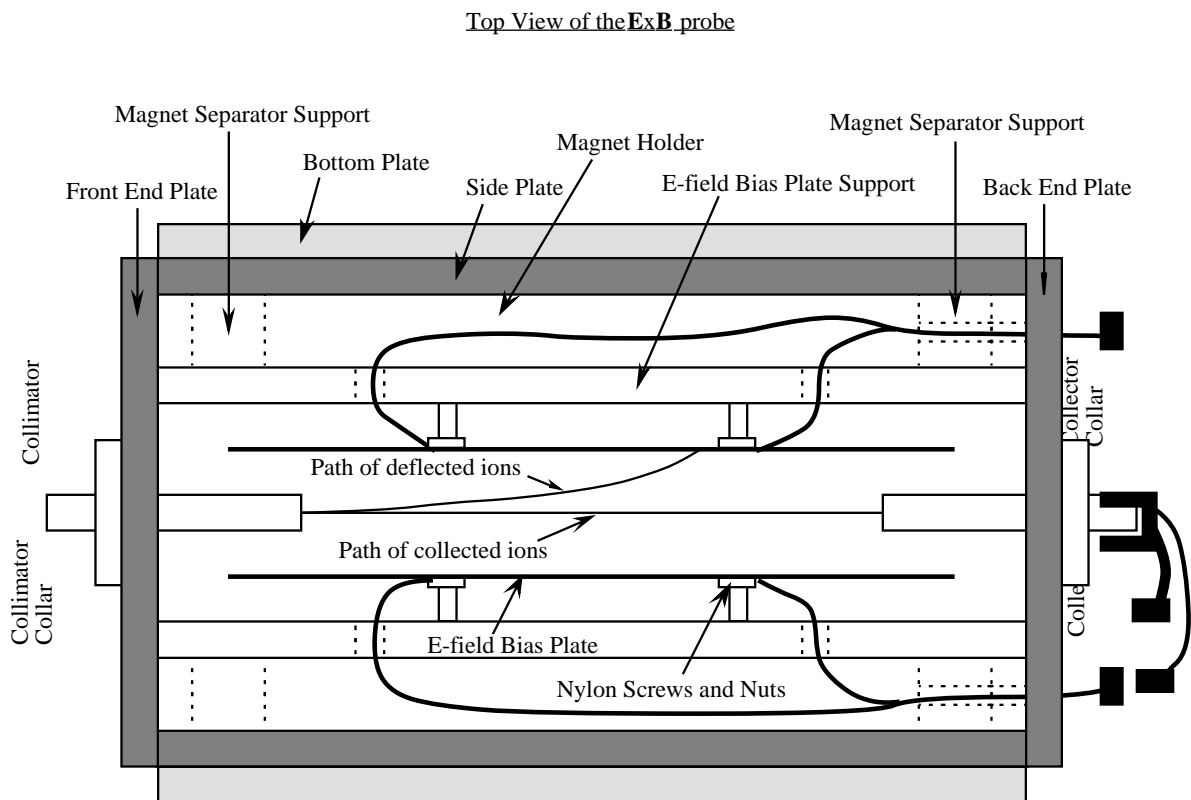


Figure 5-2 Schematic of the **ExB** probe viewed through the top plate. Collimated ion beam enters the **ExB** section from the left. The shaded parts are made of carbon steel in order to focus the magnetic field energy in the **ExB** section. The collimator and collector tubes were made of stainless steel. The other parts are made of aluminum. Coax cables are attached to the E-field bias plate at one end and a BNC connector at the other end. The CEM collector has two coax cables; one of which is a high voltage coax cable for supplying the power to the CEM and the other is for measuring the collector current. The schematic also shows the path of the ions collected by the CEM and the path of the deflected ions.

End View of the ExB probe

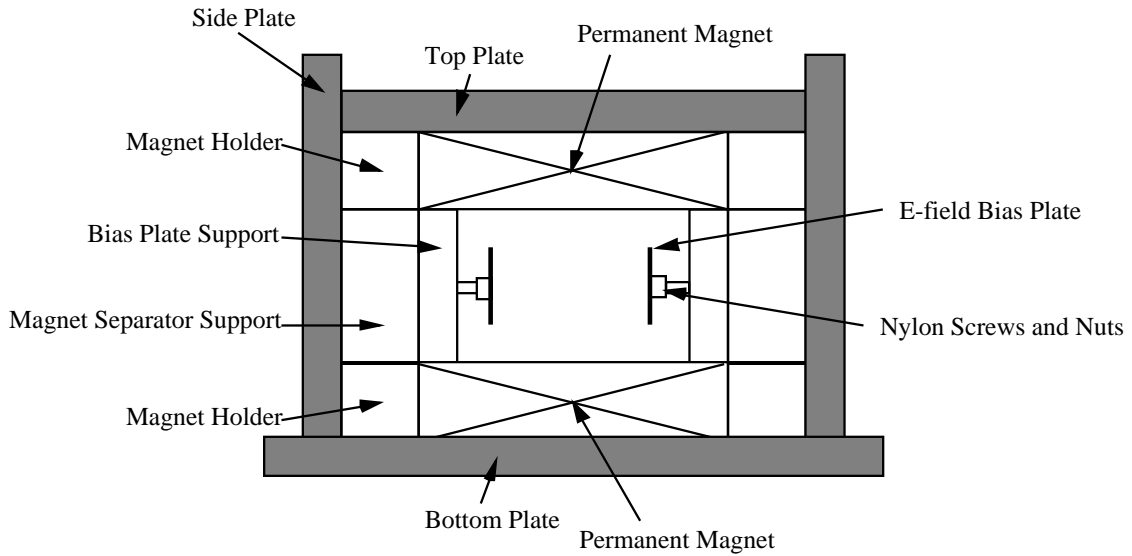


Figure 5-3 Schematic of the ExB probe viewed through an end plate. The shaded parts are made of carbon steel in order to focus the magnetic field energy in the ExB section. The other parts are made of aluminum. The electric field formed between the two E-field bias plates is in the horizontal direction. The magnetic field formed by the permanent magnets is in the vertical direction. The collimated ion beam enters the ExB section in the direction perpendicular to the page.

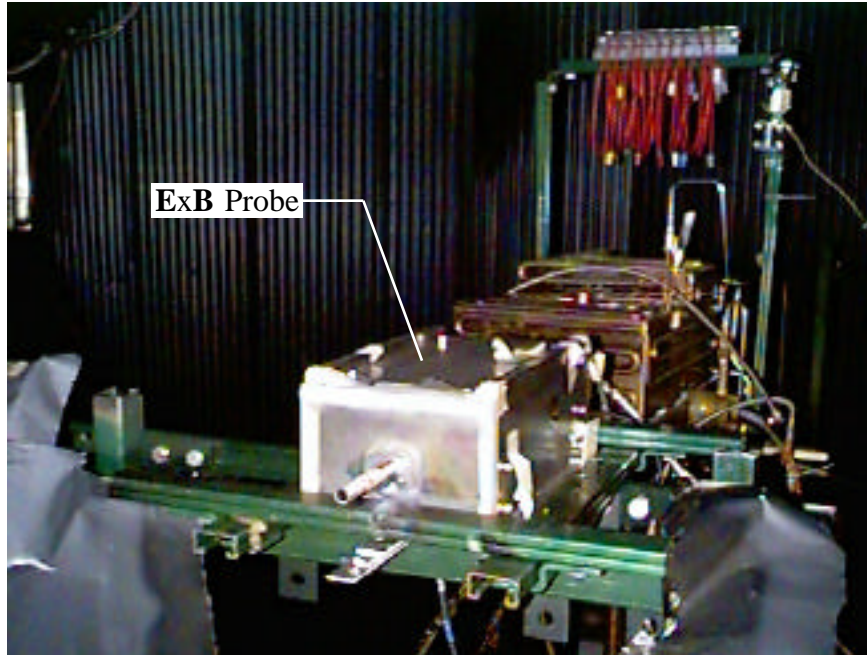


Figure 5-4 Photograph of the ExB probe on the supporting platform. The cylindrical tube in front attached to the probe body is the collimator. The probe body was isolated electrically from the platform using Teflon sheets, so that it was at the plasma floating potential.

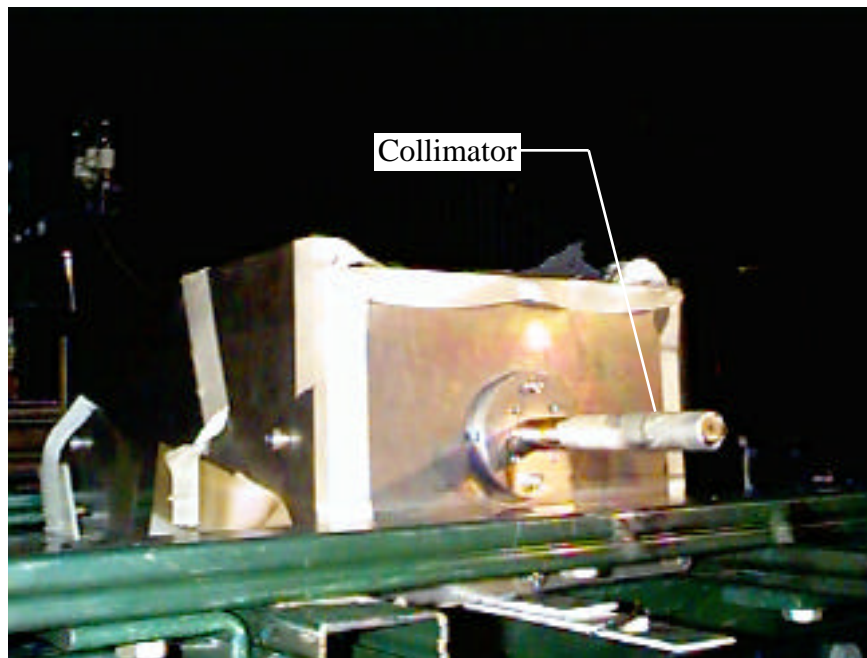


Figure 5-5 Photograph of the collimator. The collimator is covered by fiberglass tape to prevent material damage.

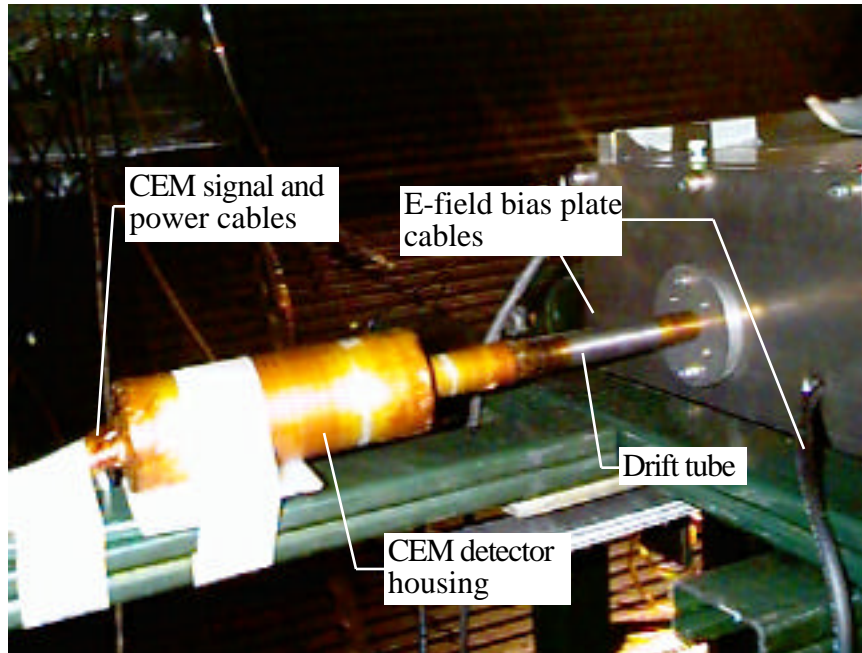


Figure 5-6 Photograph of the CEM detector housing. The coax cables supplying the E-field bias voltage are shown. Also shown are the collector current signal cable and the power cable of the CEM. The CEM housing was covered by non-conducting, highly-heat-resistant material to prevent plasma particles from leaking into the detector.

In order to detect ions in a sufficiently small area of the plume plasma and to allow measurements to be directionally-sensitive, a collimator was used to collimate the ion beam flux into the probe. The collimator was a 15.24 cm-long stainless steel cylindrical tube that had 1.27 mm apertures at the center of both ends aligned with each other (cf. Figure 5-5). An acceptance half angle of 0.48° was achieved, and thus, at an axial distance of 25 cm from the thruster exit plane, the probe viewing area was 0.136 cm^2 . The stainless steel tube and the small aperture sufficiently shielded the ions from the electric and magnetic fields while they were in the collimator before entering the **ExB** section.

In order to focus the magnetic field energy inward to the **ExB** section of the probe, the six plates forming the outer shell of the probe body were made of highly magnetic carbon steel (the shaded parts in Figure 5-2 and Figure 5-3). This not only strengthened the field, but also helped to create a uniform field.

The magnetic field was formed by four blocks of ceramic permanent magnets with the maximum magnetic flux density of 0.3900 tesla at the surface of the magnet (Magnet Sales & Manufacturing Inc. model Ceramic 8); two of them at the top and the other two at the bottom of the **ExB** section (cf. Figure 5-3). The magnetic flux density was measured at various points in the **ExB** section, and was found to be only in the vertical direction. The average magnetic flux density was 0.162 tesla, and the flux density varied by 10% along the center axis of the probe. Since the effect of the non-uniform field on the ions traversing through the **ExB** section would be same on all ions, the relationship between ion energy and the E-field bias voltage in Eqn. 5-6 would be still valid after the probe is calibrated with an ion of known energy.

The electric field in the **ExB** section was formed by the voltage gradient between two 27.9 cm-by-3.8 cm aluminum plates that were parallel to each other (cf. Figure 5-2 and Figure 5-3). The voltage between the two plates was varied from 0 V to 300 V. One plate was ramped positive and the other was ramped to the same voltage magnitude

negative with respect to ground, so that the potential on the probe center axis is at ground. The probe will still work if one plate is held at ground potential while the other plate is ramped. (This will cause a shift in the voltage at which the ions appear on a **ExB** probe trace.) However, since the correction in the ion energy measurements was required for the energy imparted to the ions as they fell from the plasma potential as discussed at the end of Section 2 in this chapter, and since the plasma potentials with respect to ground were measured in Chapter 4, the two E-field bias plates were ramped to the same voltage magnitude of opposite sign with respect to ground.

The collector consisted of a drift tube and a casing which housed the current detector (cf. Figure 5-6). The drift tube was a 15.24 cm-long stainless steel cylindrical tube, which had a 3.2 mm aperture at the center of one end to the **ExB** section side and a 8.7 mm opening at the other end that led to the inlet of the detector. The housing was carefully taped with non-conducting, high-heat-resistant material in order to prevent plasma particles leaking into the detector. The current detector employed by the **ExB** probe was a ceramic channel electron multiplier (CEM; K-M Electronics model 7550m) capable of amplifying the input ion current by a factor greater than 1×10^8 with a maximum output current of approximately 5 μ A. The theory of the electron multiplier operation is documented in many publications [12, 13, 14, 15]. The gain of the CEM was adjusted by varying the high voltage potential applied to the inlet of the CEM between -1.2 kV and -2 kV. The ions were sufficiently shielded from the electric and magnetic fields after they entered the stainless steel drift tube that led them to the CEM. The small aperture also prevented the high voltage applied to the inlet of the CEM from affecting the electric and magnetic fields. This was confirmed by the experiments which obtained the probe traces with various CEM inlet voltage and found no difference in shape between the probe traces after they were normalized with respect to each trace's maximum. This is shown in Figure 5-7.

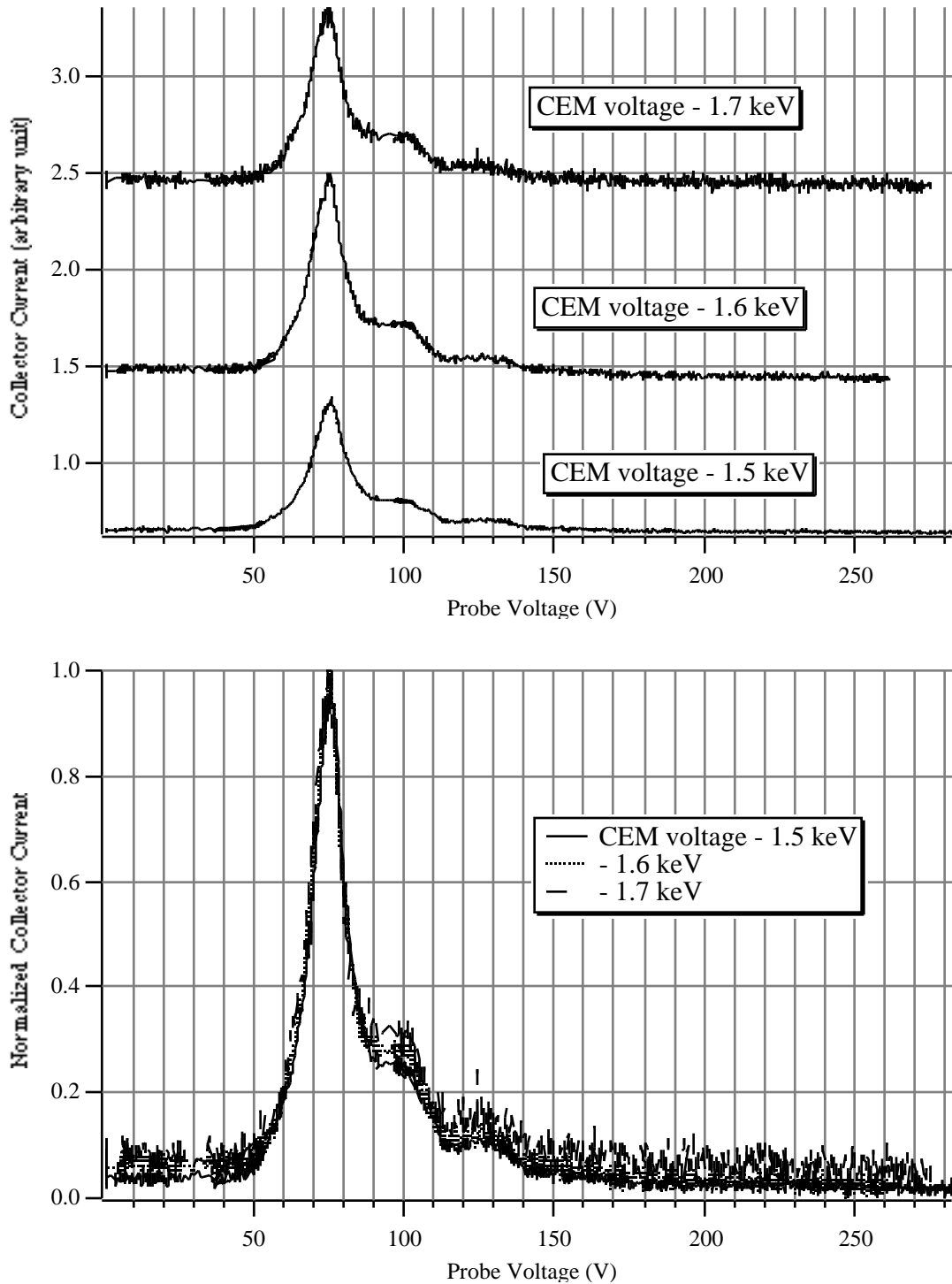


Figure 5-7 Comparison between ExB traces obtained with different CEM inlet voltages. The bottom graph shows the comparison of the traces in the top graph normalized with each trace's maximum value. It shows no influence of the CEM inlet voltage on the shape of the ExB probe traces,

though there is a tendency for noisier traces with increased CEM inlet voltage.

An important aspect of the CEM regarding the measurements of a multi-species ion beam must be noted: The number of electrons ejected from the multiplier channel surface by the initial ion impact is a function of the material properties of the surface and the energy and charge state of the impacting ion. Ions of the same energy and charge state will cause the ejection of electrons whose number is proportional to the number of the impacting ions. Therefore, the CEM serves as an ion counter rather than a charge counter as is the case with the electrostatic probes. However, the ions in the SPT-100 plume have different energies and charge states, and thus will complicate the interpretation of the probe trace. This will be discussed in detail later in this chapter.

The E-field bias plates and the permanent magnets were positioned so that the centerline of the **ExB** section was aligned with the center axis of the probe, along which the ions of the energy expressed by Eqn. 5-6 travel through the section without being deflected. The electric and magnetic fields at the edges of their field-generating surfaces will be distorted due to the potential of the surrounding surfaces. In order to minimize these fringing effects, the collimator and collector drift tubes were inserted into the **ExB** section 1.27 cm beyond the ends of the E-field bias plates (cf. Figure 5-2). Thus, the length of the **ExB** section along the probe axis was 25.4 cm.

As mentioned earlier in the discussion of the magnetic field, the **ExB** probe had to be calibrated because the magnetic flux density was not completely uniform throughout the **ExB** section. The ion energy values used for the calibration were quoted from the ion mass composition and energy investigation of the SPT-100 plume performed by King [4]. The ion energies of Xe^{1+} King measured at -40 degree, -10 degree, 10 degree, and 40 degree off thruster axis at 50 cm and 1 m distances from the thruster exit plane were compared with the **ExB** probe measurements at the same locations, and used to calibrate

the relation in Eqn. 5-6. The calibrated value of the magnetic flux density was 0.161 tesla, which was different from the measured average flux density of 0.162 tesla by only 0.6%.

The distance between the two E-field bias plates was 2.39 cm. Thus, using the mass of a xenon atom and the calibrated magnetic flux density of 0.161 tesla, V_p can be converted to E_i via the relation in Eqn. 5-6.

5.4 ExB Probe Output Current Considerations

As mentioned in the previous sections, the interpretation of the **ExB** probe trace was complicated by an inherent nature of the CEM: The multiplier is a particle detector based on secondary electron emission. The secondary electron emission refers to the phenomenon of the ejection of electrons from surfaces subjected to bombardment by energetic particles. The bombarding particles may be positive or negative ions, electrons (primary electrons), neutral atoms and molecules, and photons. The number of secondary electrons released per incident bombarding particle is the coefficient of secondary electron emission or secondary emission yield. Electron multipliers utilize the phenomenon of secondary electron emission in two ways: First, the incident particle current is converted into an equivalent electron current through secondary electron emission caused by the incident particle impacting the multiplier inlet surface. The second step is the amplification of the electron current obtained from the initial secondary electron emission. Therefore, the gain of the multipliers depends on the number of secondary electrons ejected by the bombardment of the impacting particles.

For ion detection, the multiplier operates by applying a large negative potential (1 to 2 keV) to the inlet of the multiplier tube while monitoring the current at the grounded exit of the tube (called the channel). The channel wall is a glass which is coated inside with a semiconducting silicon layer, and thus has a high secondary emission yield. The

high negative voltage applied to the multiplier inlet serves to efficiently collect incoming ions and draw them into the channel at high energies while repelling all electrons away. Neutral particles will still be collected by the multiplier though at much lower energies compared to the ions. The incoming ions impinge on the channel wall and eject a number of secondary electrons. The electrons are accelerated by the applied field towards the grounded channel exit, impacting the wall and ejecting more secondary electrons, thus greatly amplifying the current.

The numerical value of the secondary emission yield depends on the mass, energy, charge state, and chemical nature of the incident particles. Additional variables include the work function and physical condition of the bombarded surface (e.g. surface structure and temperature), and the angle of incidence [15, 16]. The energy and charge state of the incident ions are of concern for the CEM used in the study reported here since all other variables were considered to be constant. The multiplier gain increases with secondary emission yield, which, in turn, increases monotonically with incident ion energy and degree of ionization for “low energy” incident ions (~ 2 keV) [13, 15]. Note that the definition of “low energy” for secondary electron emission is much higher than that for electric propulsion. A rough estimate of the variation of the secondary emission yield due to incident ion energy and charge state is possible through the elementary theory of secondary electron emission and some experimental data. Please note that the definitions introduced in this subsection are only for the discussion of secondary emission yield and do not apply to the rest of this thesis.

The variation of secondary emission yield due to incident ion energy can be approximated by the elementary theory of secondary emission [15, 16]. Secondary emission yield can be written as follows:

$$= \int_0^d n(x, E_0) f(x) dx, \quad \text{Eqn. 5-11}$$

where $n(x, E_0) \cdot dx$ is the average number of secondary electrons produced per incident particle of energy E_0 at the depth x below the surface in the layer of thickness dx ; $f(x)$ is the probability for a secondary electron to migrate and escape from the surface; and d is the maximum penetration depth below the surface by the incident particle. It is generally assumed that $n(x, E_0)$ is proportional to the average energy loss of the incident particle per unit path length and related by:

$$n(x, E_0) = -\frac{1}{E} \frac{dE}{dx}, \quad \text{Eqn. 5-12}$$

where E is the energy required to excite one secondary electron inside the targeted solid.

The migration and escape probability $f(x)$ is expressed as:

$$f(x) = B e^{-x/x_s}, \quad \text{Eqn. 5-13}$$

where B is the escape probability and the exponential part represents the migration probability to the surface from a depth x . x_s may be considered as “the range of the secondaries” ready to escape upon impacts by incident particles. The basic assumption of the secondary emission theory is that the incident particles lose their energies according to a power law defined by [17]:

$$\frac{dE}{dx} = -\frac{A}{E^{n-1}}, \quad \text{Eqn. 5-14}$$

where A is a constant characteristic of the material and $n > 1$. From Eqn. 5-14, it follows that:

$$E^n(x) = E_0^n - A \cdot n \cdot x. \quad \text{Eqn. 5-15}$$

From Eqn. 5-15, the maximum penetration depth d is found from the value of x when $E(x) = 0$, and is expressed as $d = E_0^n / A \cdot n$. In the above definitions, ρ , B , x_s , and A are the constants that are characteristic to the material of the targeted solid. The value of the power-law exponent n had been taken as 2.00 using Whiddington's law [15]. An experimental determination by Young [18] found n to be 0.83 for light ions of 1 to 25 keV on aluminum target.

Since the channel surface of the CEM has a high secondary emission yield, x_s can be considered large. Also, the impact energy of ions in this study is low (1 to 8 keV) for the theory of secondary emission, and thus the penetration depth x can be considered small. Then, the migration and escape probability $f(x)$ may be taken equal to $f(0)$. Hence, in accordance with Eqn. 5-11, Eqn. 5-12, and Eqn. 5-14, the secondary emission yield is found to be:

$$Y = \frac{B}{A} E_0. \quad \text{Eqn. 5-16}$$

Thus, for the conditions in this study, the secondary emission yield should rise proportional to E_0 regardless of the value of the power-law exponent n .

Typical experimental data show that, for low impacting ion energy (1 to 5 keV), the secondary emission yields by doubly charged, triply charged, and quadruply charged ions are roughly 1.5, 3, and 5 times that by singly charged ions, respectively when the energies of all ion species are the same[13]. Then, since the gain of the CEM is proportional to the secondary emission yield by the initial ion impacts, the gains by doubly, triply, and quadruply charged ions will be roughly 3, 10, and 20 times the gain of singly charged ions for a typical voltage of 1250 V applied to the inlet of the CEM, assuming each ion species has experienced a similar acceleration voltage in the thruster

discharge chamber. Thus, the output current of the CEM is greatly affected by the variation of the gain due to the energies and charge states of different ion species.

However, this variation is small within each peak of the probe trace corresponding to each ion species because the variation of output current due to the charge state does not exist, and because the difference in E_0 is small among the ions of the same charge state. Assuming a spread of ± 60 V in the acceleration voltage, the output current of the CEM would vary less than 4% within each peak. Therefore, each peak on the probe trace may be considered a true representation of the ion energy distribution of the ion species. Consequently, the ion species fraction calculation is the only result of the **ExB** probe measurements which is affected by the variation of the output current of the CEM due to the differences in ion energy and charge state.

5.5 ExB Probe Measurement Error

In general, the sources of error in the **ExB** probe measurements can be categorized into four factors; 1) the uncertainty in the measurements of probe current and voltage, 2) the uncertainty in the ion energy measurements due to the calibration of the **ExB** probe, 3) the uncertainty in the ion energy measurements due to the resolution of the **ExB** probe, and 4) the uncertainty in the ion energy measurements due to particle build-up and collisions occurring inside the **ExB** probe. The following subsections will discuss each of these error sources.

5.5.1 Uncertainty in Probe Current and Voltage Measurements and Probe Calibration

The uncertainty in the probe current and voltage measurements is mostly from the least significant digits of the probe current and voltage. The average error associated with this uncertainty is estimated to be on the order of 2%.

The uncertainty in the ion energy measurements due to the calibration of the **ExB** probe depends on both the error in the measurements of the probe and the error in the energy values used for the calibration. The former is estimated above to be approximately 2%. The latter was estimated to be 2% [4]. Thus, the uncertainty due to the probe calibration is approximately 3%.

5.5.2 Uncertainty in Energy Measurements due to Probe Resolution

The resolution of the **ExB** probe can be found analytically. For the calculation of the probe resolution, let us assume that each species of the ions has a single energy. (This is not the case for the ions in the SPT-100 plume.) Then, a probe trace would look like the one in Figure 5-8, where V_c represents the probe voltage at which the ions of energy, $E_i = (M_i / 2 \cdot e) \cdot (V_c / (d \cdot B))^2$, are collected by the detector when the ions come into the **ExB** section in the direction of the probe axis (cf. Eqn. 5-6). The peaks on such a trace will have some width ($2w$) due to the probe resolution.

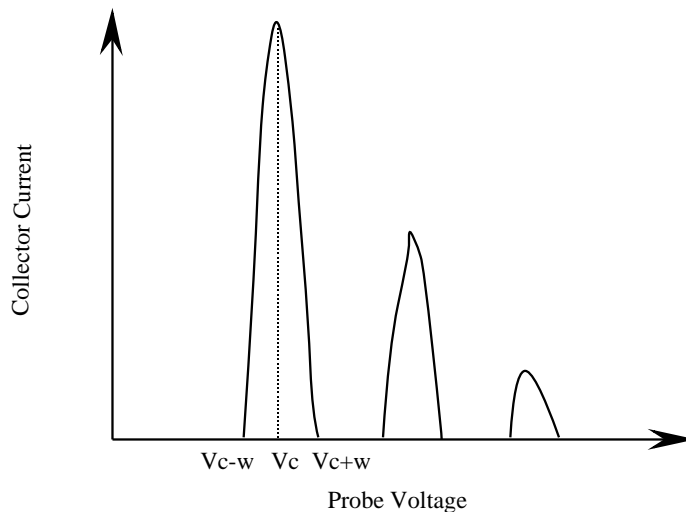


Figure 5-8 An example of an **ExB** probe trace for a multi-species ion plasma flow where each ion species has a single energy. The width of the peak, $2w$, is the probe resolution.

The maximum deviation, w , from the peak value V_c occurs when the ion enters the collimator at one end of the entrance aperture (a1), goes out the collimator at the opposite end of the exit aperture (a2), and then goes into the collector drift tube through the drift tube entrance (a3) at the same end where the ion first entered the collimator through a1. This is shown schematically in Figure 5-9. The expressions in Figure 5-9 will be used for the probe resolution calculation.

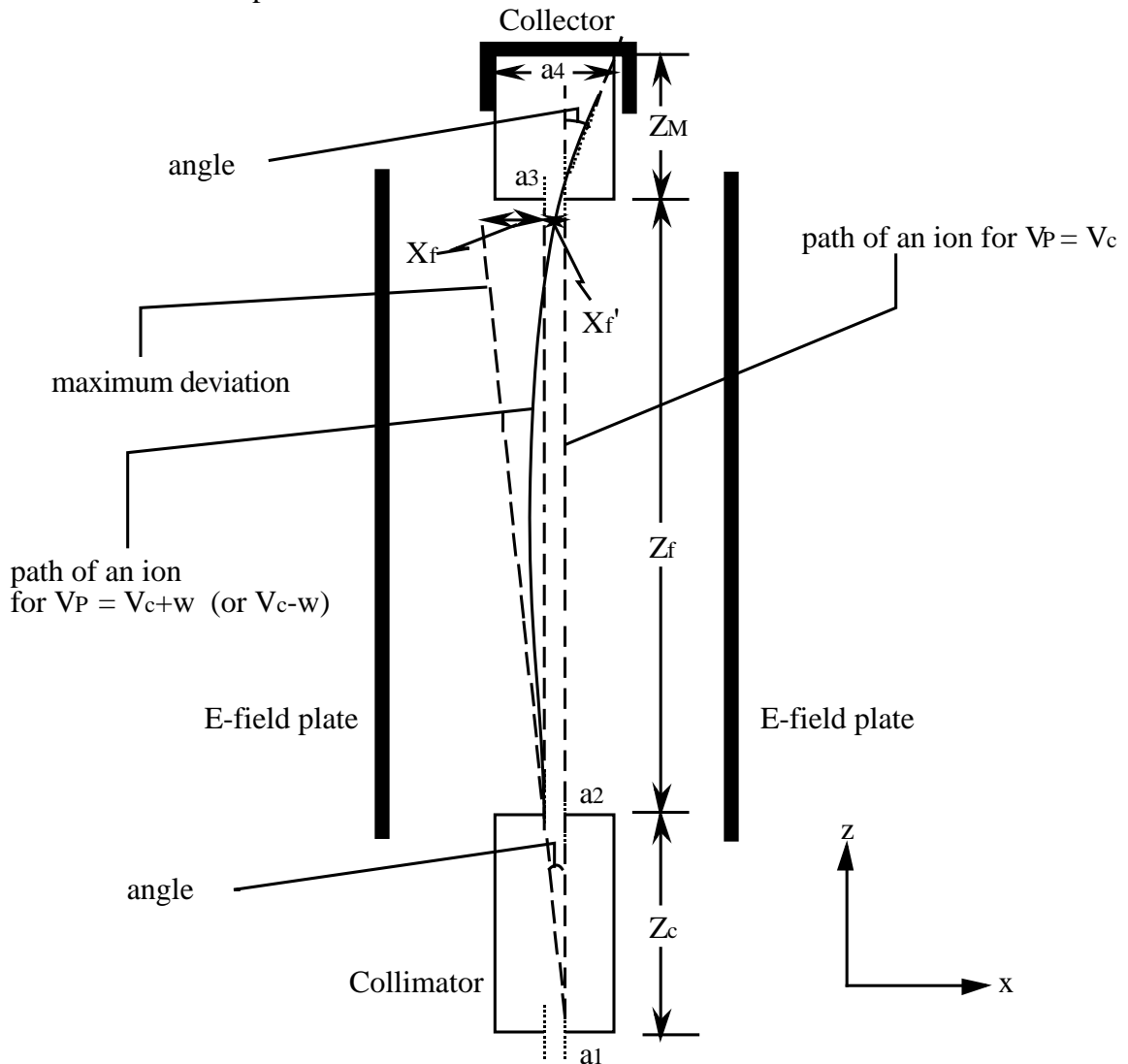


Figure 5-9 Schematic of the ExB probe resolution calculation. The curved line represents the path of an ion whose energy appears at $V_p = V_c + w$ (or $V_p - w$) on the ExB probe trace, but would have at $V_p = V_c$ if the ion came into the ExB section in the direction parallel to the probe axis (the normal entrance in the z-direction).

Let us consider the case where an ion of energy E_i , equivalent to the probe voltage of V_c (cf. Eqn. 5-6), enters the collimator at an angle θ and appears at the voltage of $V_c + w$ on the probe trace. (The case for $V_c - w$ is analogous to the case for $V_c + w$.)

The maximum deviation of ion path from the normal entrance through the collimator is $(a_1 + a_2) / 2$ in the x-direction at the exit of the collimator. This is represented by the angle θ where $\tan \theta = (a_1 + a_2) / (2 \cdot Z_c)$. In the same manner, x_f' can be written as :

$$x_f = \frac{a_2 + a_3}{2} \cdot \tan \theta \quad \text{Eqn. 5-17}$$

From simple geometry:

$$x_f = \frac{a_1 + a_2}{2} \cdot \frac{Z_f}{Z_c} \quad \text{Eqn. 5-18}$$

Now, let us assume that $\theta \ll 1$. Indeed, this assumption is valid for the **ExB** probe used in this study where $\theta = 0.48^\circ$. Then, the change in the ion velocity in the z-direction can be considered negligible, and the equation of motion with a constant acceleration a_x in the x-direction in the **ExB** section is:

$$M_i a_x = e q_i \frac{V_c + w}{d} - e q_i u_i B$$

but, we know that;

$$\frac{V_c}{d B} = u_i \quad \text{Eqn. 5-19}$$

and thus,

$$a_x = \frac{e q_i w}{M_i d}$$

Since the ion velocity change in the z-direction is negligible, the time it takes for the ion to travel the **ExB** section (the distance of Z_f) is expressed by:

$$t_f = \frac{Z_f}{u_i} = \frac{d}{V_c} \frac{B}{Z_f}. \quad \text{Eqn. 5-20}$$

There are two criteria for the ion to reach the CEM and be detected:

$$(A) \quad \frac{1}{2} a_x t_f^2 \leq x_f + x_f \quad \text{Eqn. 5-21}$$

and

$$(B) \quad \tan \theta \leq \frac{a_3 + a_4}{2 Z_M}. \quad \text{Eqn. 5-22}$$

The criterion (A) describes the condition that the ion must be able to enter the drift tube in order to be detected by the CEM. The criterion (B) describes the condition that, after the ion enters the drift tube, its velocity vector, represented by the angle θ , must be such that it reaches the inlet of the CEM before hitting the drift tube wall. Realizing that $\tan \theta$ is the ratio of the ion velocity in the x-direction to that in the z-direction, Eqn. 5-21 and Eqn. 5-22 becomes:

$$w = \frac{2 d V_i}{Z_f} \left(\frac{a1 + a2}{Z_c} + \frac{a2 + a3}{Z_f} \right), \quad \text{Eqn. 5-23}$$

$$w = \frac{d V_i}{Z_f} \left(\frac{a1 + a2}{Z_c} + \frac{a3 + a4}{Z_M} \right), \quad \text{Eqn. 5-24}$$

where V_p is replaced by V_i using Eqn. 5-6. Notice that w is dependent only upon the probe dimensions and the acceleration voltage V_i . Thus, the peaks for ions of different charge state that have experienced the same acceleration voltage will have the same w . Using the probe dimensions described in the previous section, the two criteria give $w = 1.6$ V and $w = 2.2$ V for $V_i = 245$ V (which was the most common acceleration voltage for Xe^{1+} ions in the SPT-100 plume). Therefore, the probe resolution is conservatively estimated to be 1% of a measured ion energy.

5.5.3 Uncertainty in Energy Measurements due to Particle Interactions inside the ExB Probe

The final category of the measurement error source is the uncertainty in the ion energy measurements due to the particle build-up and collisions occurring inside the probe. There was no practical method to measure the pressure inside the probe, and cross sections involving multiply charged xenon ions were scarce in the literature. Thus, a series of experiments were conducted to investigate the effects of particle build-up and collisions inside the probe on the measured ion energy distributions.

The probe had two 0.95 cm diameter holes on the back-end plate where the cables for the E-field bias plates went through. Therefore, the pressure inside the probe when the probe was facing sufficiently away from the ion beam was considered equal to the background pressure. In order to investigate the particle build-up inside the probe, the probe was first kept away from the ion beam for sufficient time to reduce the pressure inside the probe to the background pressure. Then, the probe was placed in the ion beam,

and the ion energy measurements were repeated five times while the probe stayed at one position in the plume over a period of time with the same probe parameters (for example, the CEM gain). These measurements were duplicated at various positions in the thruster plume. The results of these experiments are shown in Figure 5-10 and Figure 5-11. The position shown in each graph indicates the measurement position in the thruster plume; "1 m, -10°" represents the probe position of -10° off thruster axis 1 m downstream from the thruster center. The trace #'s in each graph represent the probe trace in the order of measurement time, i.e. Trace #4 is the probe trace taken fourth. The trace #'s are shown in each graph in the order of highest collector current to lowest from the top to bottom part of the graph.

The collector current was expected to either increase or decrease monotonically with measurement time, at least between the first and second measurements, if the number of particles inside the probe increases with time. However, as can be seen from the graphs in Figure 5-10 and Figure 5-11, the variation in the measured collector current with respect to measurement time exhibits no apparent pattern between different measurement positions. Furthermore, the effects of particle build-up was expected to be largest at the probe position in the plume where the ion density is highest, but the results in Figure 5-10 and Figure 5-11 show the contrary. The data at 25 cm, 5° where the ion density is highest shows the least variation in the collector current, and the data at 25 cm, -110° where the ion density is lowest shows the most variation in the collector current than any other data. Then, it seems that the effects of the particle build-up inside the probe on the ion energy measurements are small. Hence, the pressure inside the probe may be considered equal to the ambient background pressure.

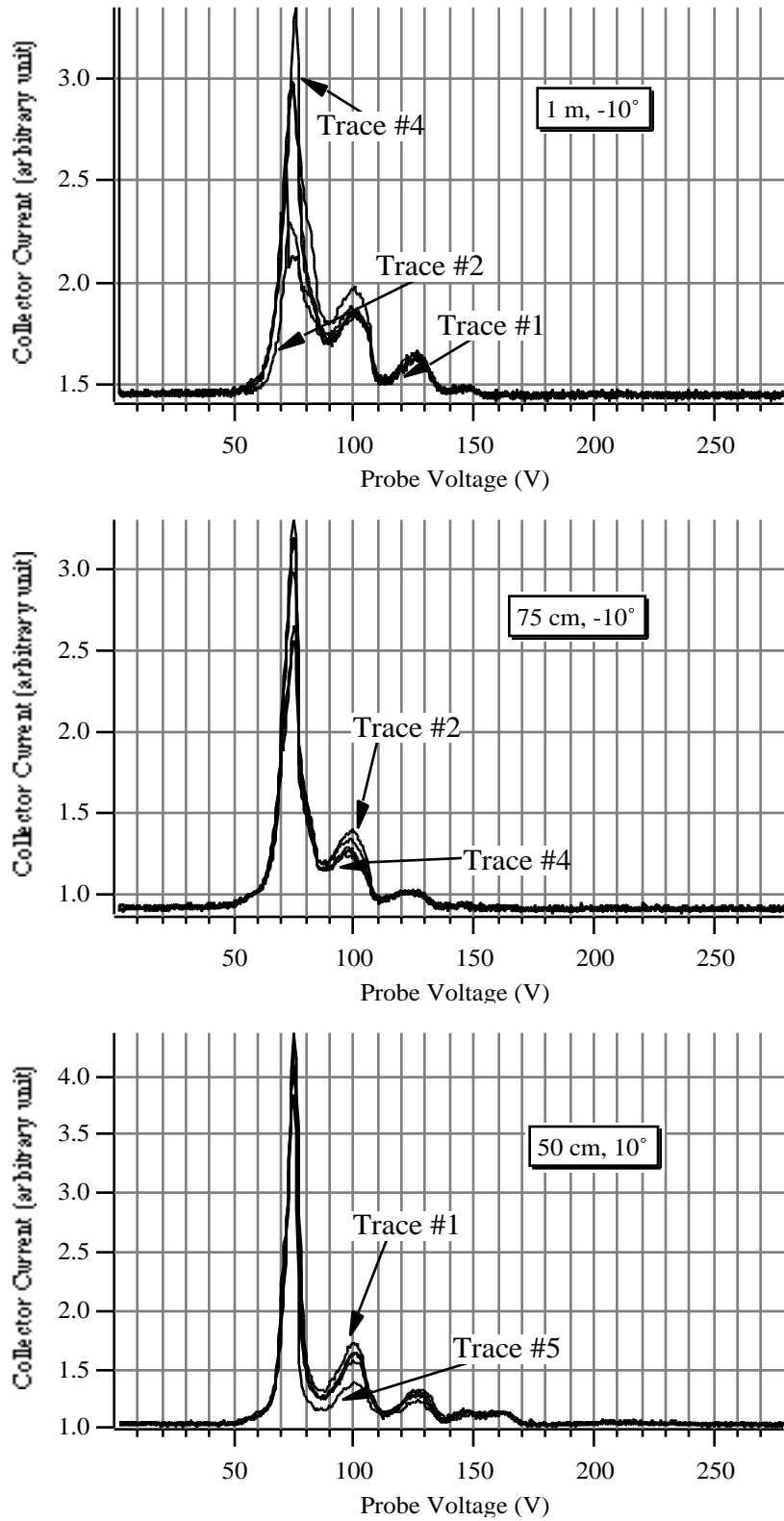


Figure 5-10 Comparisons of ExB traces obtained over a period of time at various positions in the thruster plume.

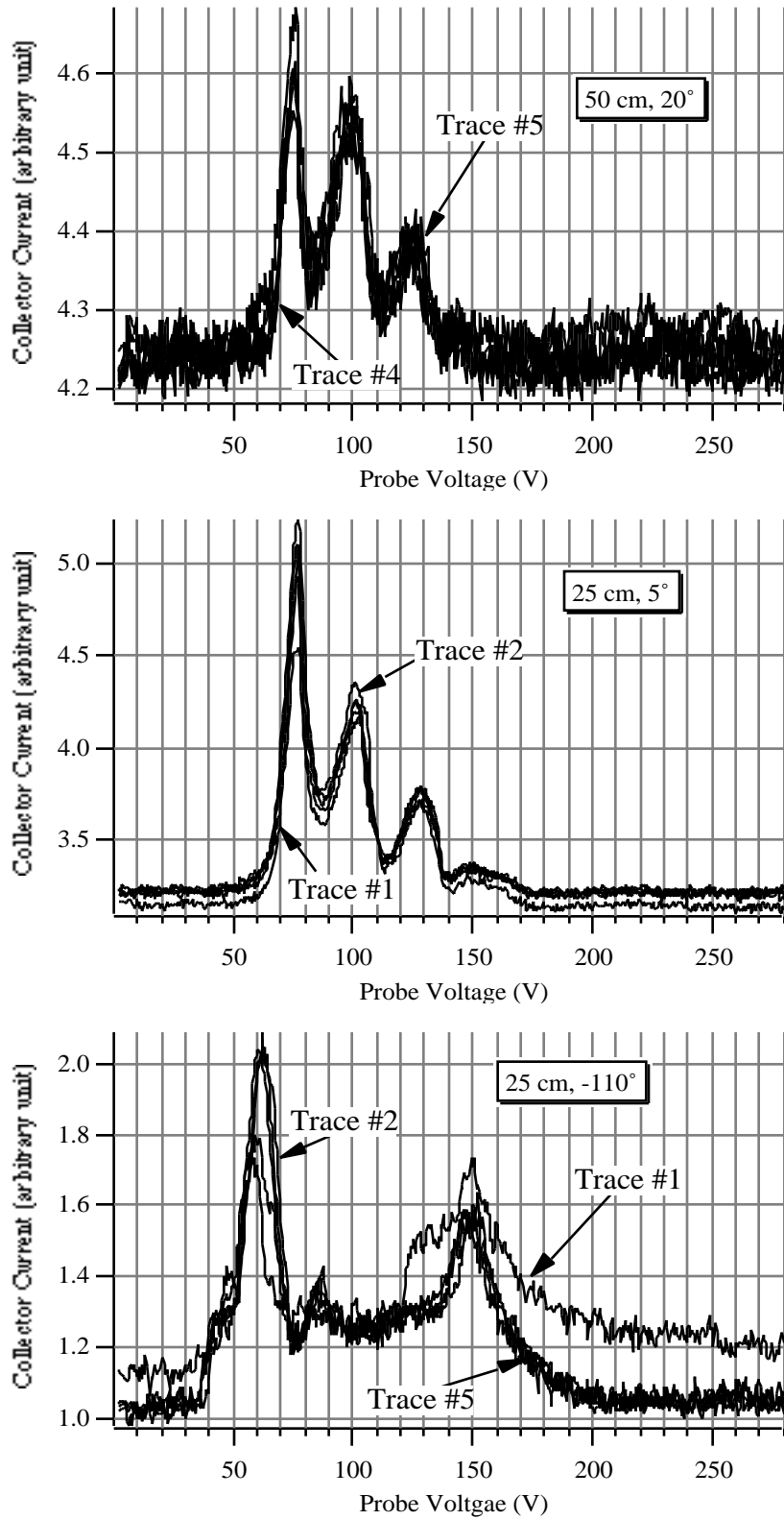


Figure 5-11 Comparisons of ExB traces obtained over a period of time at various positions in the thruster plume.

The effects of particle collisions inside the probe on the ion energy measurements was also investigated experimentally by examining the probe traces in Figure 5-10 and Figure 5-11 but with normalized collector current. These are shown in Figure 5-12 and Figure 5-13. The position and trace #'s shown in each graph are as explained earlier. Again, the trace #'s are shown in each graph in the order of highest collector current to lowest from the top to bottom part of the graph.

As in the discussion of the particle build-up in the probe, Figure 5-12 and Figure 5-13 show that the variation in the normalized collector current with respect to measurement time exhibits no apparent pattern between different measurement positions. The same experiments were performed several times, and the following was observed at all measurement positions. At a given measurement position, the variation in the normalized probe current with respect to measurement time was not repeatable between experiments, although the overall probe trace shape was repeatable. For example, the collector current of the fifth measurement was the largest in one experiment, but was not in another experiment at the same position in the plume. Also, the magnitude of the variation in the normalized collector current changed from one experiment to another. In summary, the series of experiments found that the variation in the normalized collector current followed no pattern with respect to measurement time or position. This suggests that the variation is not due to the collisions occurring inside the probe, but is a result of unstable plasma of the SPT-100 plume.

Instability in the Hall thruster plume plasma has been reported in many publications [19, 20, 21, 22, 23, 24]. Previous experiments showed that the discharge voltage of the SPT-100 varied as much as 20%, and the discharge current as much as 2 A peak-to-peak [25, 26, 27]. The most intense instability that is inherent to the Hall thruster plume plasma is "contour oscillations" [23]. Contour oscillations are developed by the instability of the location of the ionization zone, and have typical frequencies of 1 to 20 kHz. In the regimes of thruster operation where contour oscillations are developed, there

is almost a 100% modulation of the discharge parameters (I_d and V_d). Also, a high background pressure (5×10^{-5} Torr) has been found to cause very large discharge oscillations which have larger amplitude than the natural discharge oscillations of the SPT-100 such as contour oscillations [28]. The background pressure during the experiments reported here was 1.2×10^{-4} Torr (calibrated for xenon), and thus the background pressure induced discharge oscillations were expected in the thruster plume during the **ExB** probe measurements. Therefore, the uncertainty in the ion energy measurements due to the particle build-up and collisions occurring inside the probe may be considered small compared to the variation in ion energy due to the plasma instability.

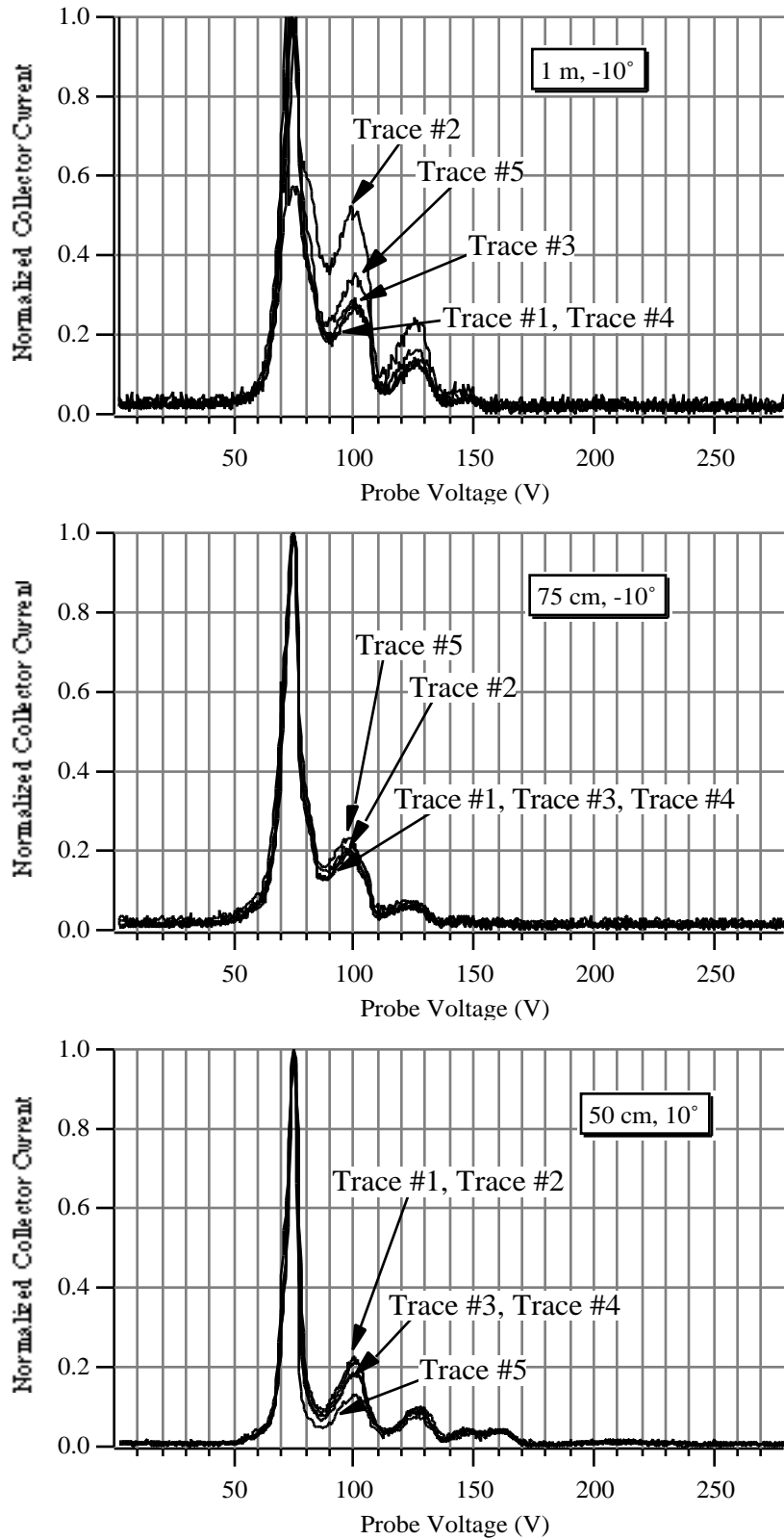


Figure 5-12 Comparisons of normalized ExB traces obtained over a period of time at various positions in the thruster plume.

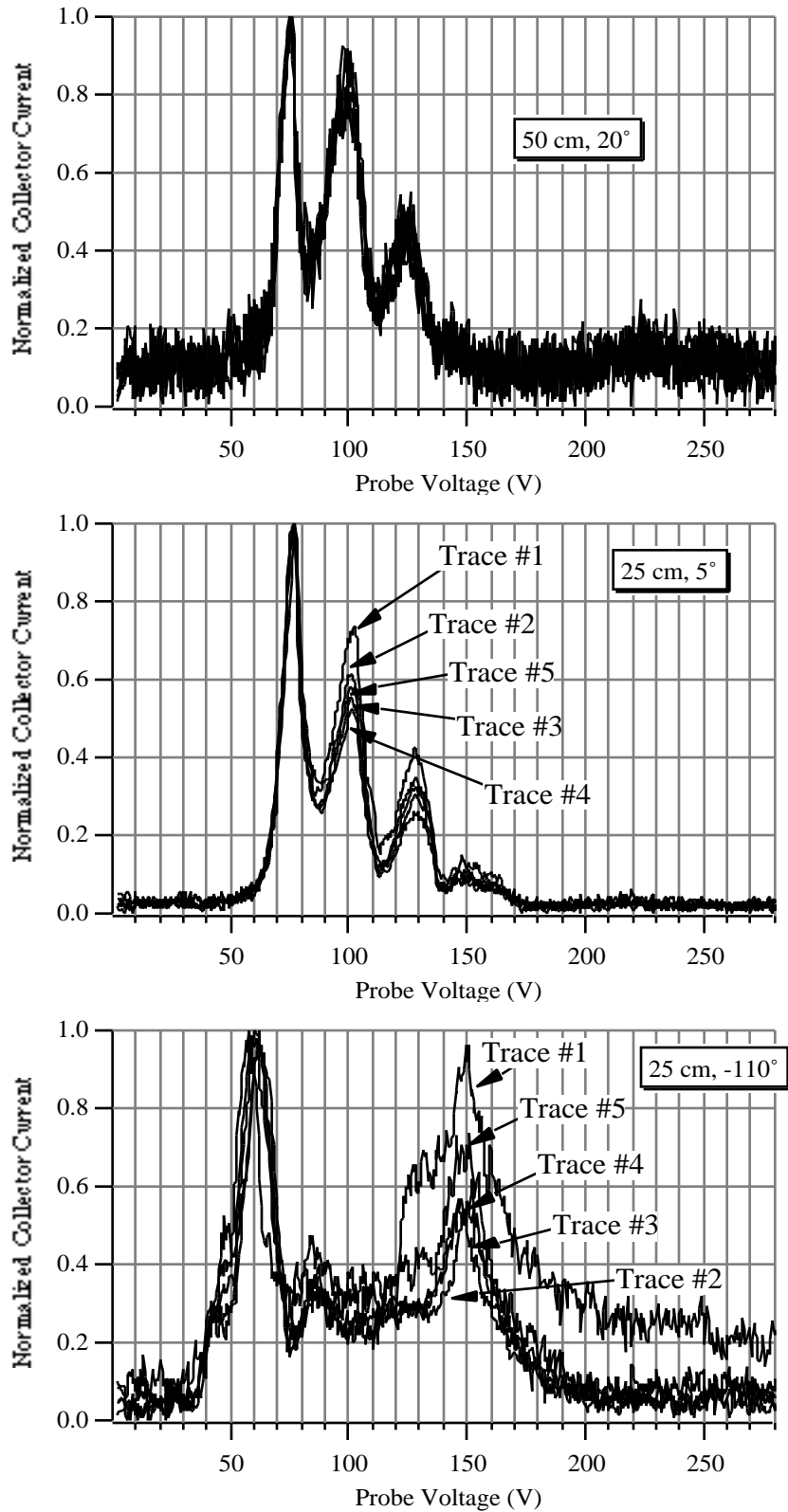


Figure 5-13 Comparisons of normalized ExB traces obtained over a period of time at various positions in the thruster plume.

5.5.4 Summary of ExB Probe Measurements Error

Combining all the uncertainties discussed above, the total error in the ion energy distribution measurements is estimated to be 2% for the ion current and 4% for the ion energy. It should be noted that the calculation of the probe resolution discussed earlier assumed that the apertures and opening of the collimator and collector drift tube were perfectly aligned. Although these apertures and opening were aligned using a laboratory laser, the non-zero alignment uncertainty was inevitable. However, the misalignment of the apertures would cause only a shift in the ion energy, and thus the necessary correction was already accomplished by the probe calibration. Therefore, it was not considered to affect the overall measurements error.

Recall that the output current of the CEM vary approximately 4% within each peak on the probe trace due to the variation in the multiplier gain as discussed in Section 4 of this chapter. If this is added to the above estimated error, the total error in the ion current measurements becomes 5%. It should be noted that this error value of 5% applies separately to each peak on the probe trace corresponding to each ion species. The larger increase or decrease in the magnitude of the ion current due to the variation in the multiplier gain over the entire probe trace will only affect the calculation of ion species fractions as discussed in Section 4, and thus is not included in measurements error. The error in the calculated ion species fractions due to the variation in the multiplier gain will be considered when the ion species fractions are discussed in Chapter 7.

5.6 Experimental Set-Up for ExB Probe Measurements

The stationary plasma thruster studies in this work is the Fakel SPT-100, which is described in Chapter 1. The operating point that was investigated with this thruster was 300 V and 4.5 A with a total xenon flow rate of 5.5 mg/s, with 0.28 mg/s of this going through the hollow cathode. The SPT-100 was stable over the measurement period.

Prior to taking measurements, the thruster was allowed to run approximately 30 minutes to reach thermal equilibrium.

Experiments were conducted in a 9-m-long by 6-m-diameter stainless-steel vacuum chamber (cf. Chapter 1, Section 5). The Polycold water cryopump was not used during the **ExB** measurements. During the thruster operation, the background pressure was 1.2×10^{-4} Torr (calibrated for xenon).

The ion energy distribution was measured at various angles off thruster axis at a constant axial distance from the thruster center. The thruster was mounted to a rotary table of the positioning system described in Chapter 1, Section 5. As in the near- and far-field study of the thruster plume, the thruster was mounted in such a way that the rotational axis of the rotary table coincided with the center of the thruster exit plane. The **ExB** probe was mounted on a stable, fixed platform in front of the positioning system, and aligned with the center of the thruster exit plane. With this arrangement, the thruster plume was sampled as a function of angular position at a fixed axial distance from the center of the thruster exit plane by rotating the thruster relative to the fixed probe. The schematic of this arrangement can be seen in Figure 4-1 with the **ExB** probe replacing the electrostatic probes. The schematic and photographs of the experimental set-up are shown in Figure 5-14, Figure 5-15, and Figure 5-16. Again, as in Chapter 4, the zero degree position indicates the probe position aligned with the thruster axis. The positive angles represent the probe data in the cathode side of the thruster plume while the negative angles represent the probe data in the non-cathode side of the thruster plume.

The angular measurements were taken at the axial distances of 25 cm, 50 cm, 75 cm, and 1m from the center of the thruster exit by moving the thruster and rotary table axially with the axial translation stage. Although the positioning system has the absolute accuracy of 0.15 mm in the axial and 0.1 degree in the rotational directions, initial alignment of the probe with a reference point was only accurate to within 5 mm in the

axial and 3 degrees in the rotational directions. Hence, the absolute positions for all data had an uncertainty of 5 mm and 3 degrees in the respective directions.

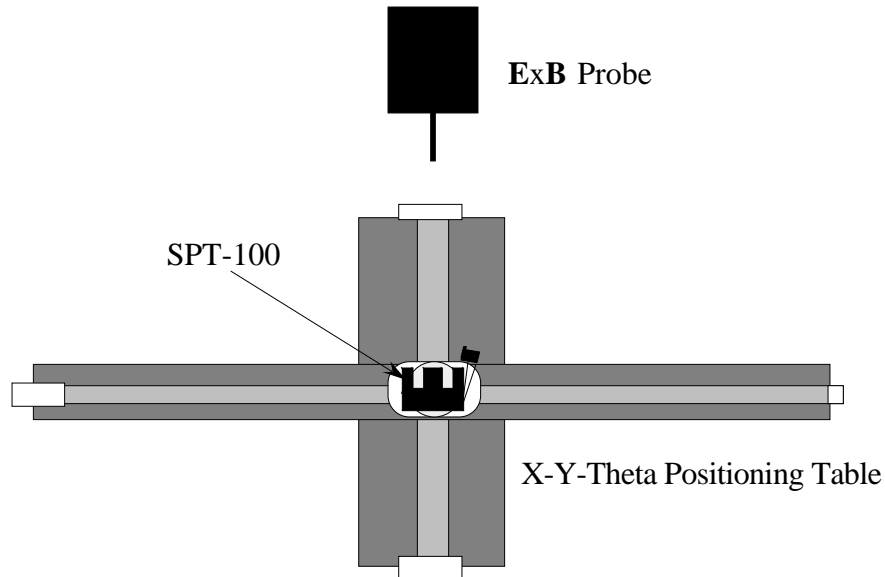


Figure 5-14 Schematic of the experimental set-up for the ExB probe measurements (not in real scale).

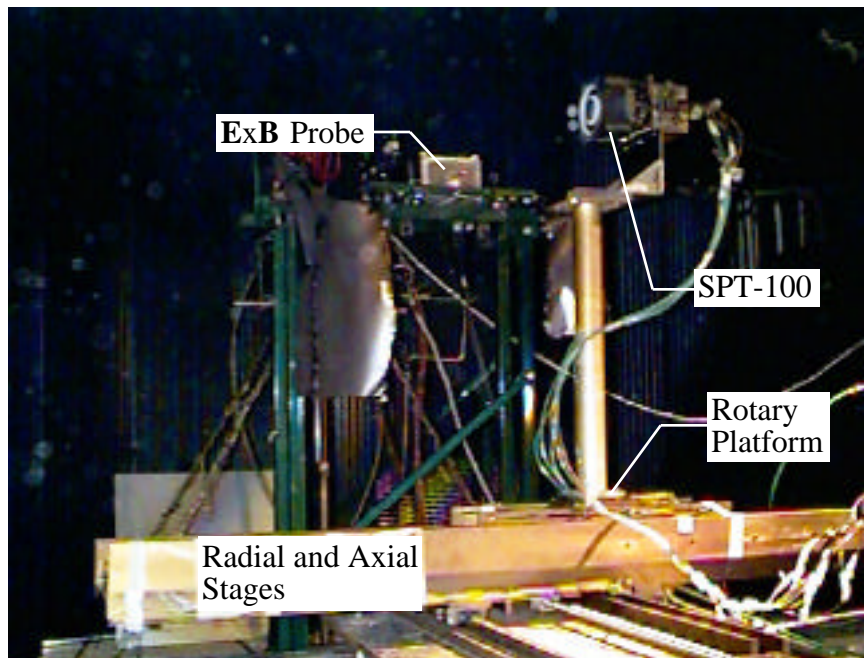


Figure 5-15 Photograph of the experimental set-up showing the relative position of the SPT-100 and the ExB probe. Also shown are the rotary platform and the positioning system.

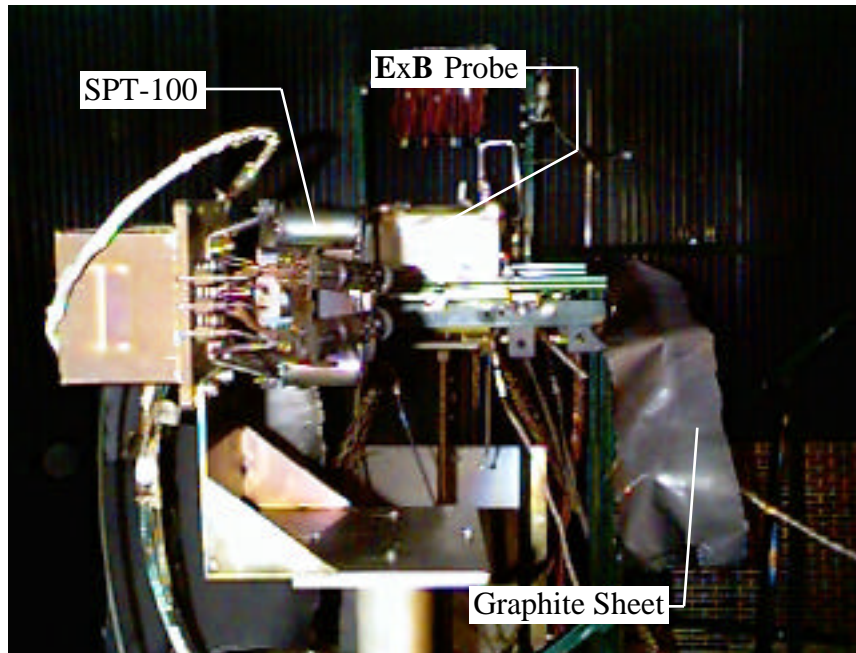


Figure 5-16 Photograph of the experimental set-up. The thruster-probe position shown here represents a measurement point at -90 degrees off thruster axis. During the measurements, the entire platform supporting the ExB probe was covered with low-sputter-yield flexible graphite sheets to prevent material damage and to minimize sputtering due to high energy ion impacts.

Data from the ExB probe were obtained using the probe circuit illustrated in Figure 5-17. The voltages to the two E-field bias plates were supplied using a Sorensen DCS 600-1.7 power supply. The voltage between the two plates was varied from 0 V to 300 V. One plate was ramped positive and the other was ramped to the same voltage magnitude negative with respect to ground, so that the potential on the probe center axis is at ground. The CEM inlet potential, which controlled the multiplier gain, was supplied by a high voltage power supply. The current signal from the CEM was measured using a Keithley 486 picoammeter, which converted the current signal to a voltage signal. This voltage signal and the two voltage signals from the E-field bias plate voltage power supply were sent to a Tektronics TDS 540 digital oscilloscope. The probe current-voltage trace stored in the oscilloscope was then exported for analysis to a computer using a National Instruments GPIB interface.

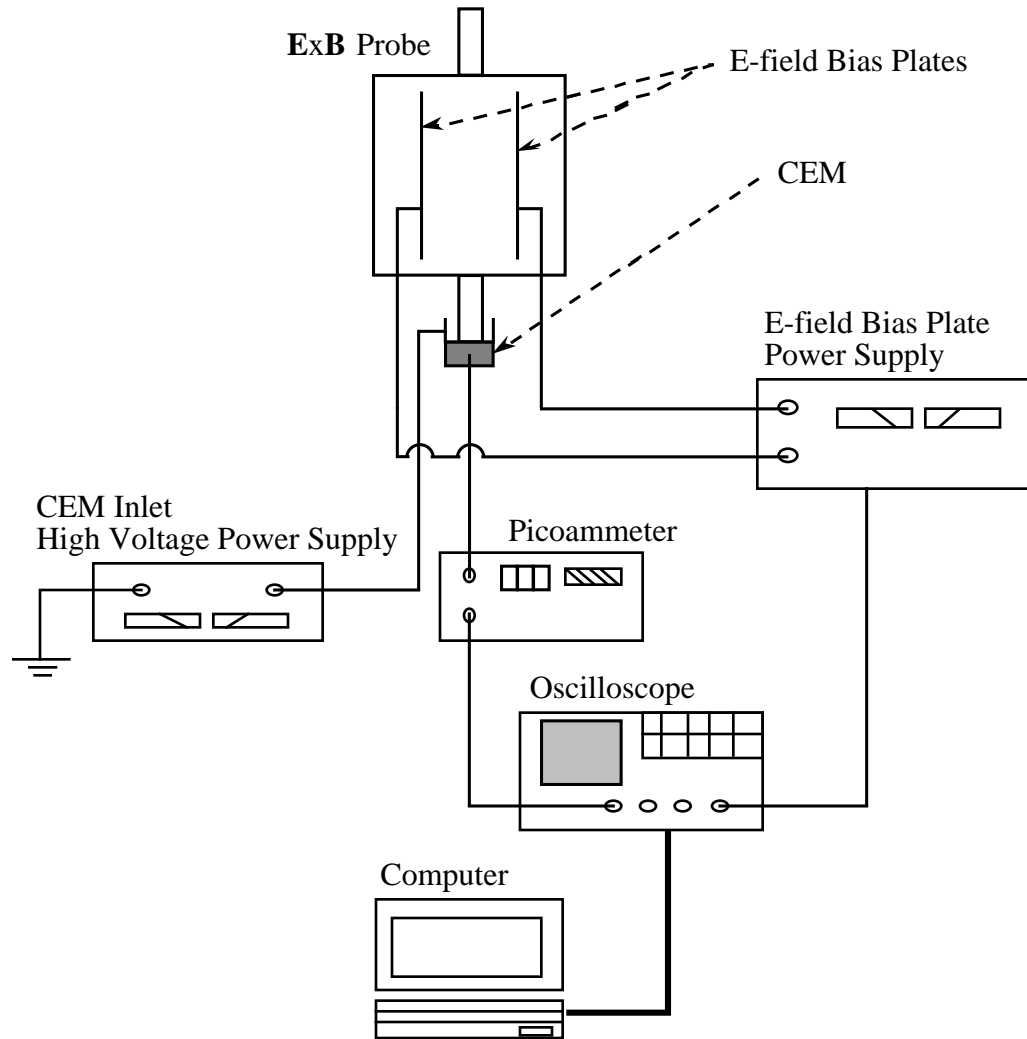


Figure 5-17 Schematic of the ExB probe circuit.

The probe body was kept at the floating potential in order to minimize the disturbance in the local plasma. The ions will still gain some energy as they approach the probe (since $V_f < V_p$). However, the necessary correction was included in the correction of the abscissa of the probe trace discussed in Section 2. The correction was for the energy imparted to the ions as they fell from the ambient plasma potential through the probe to ground potential on the center axis of the probe. The magnitude of the required correction is the plasma potential with respect to ground.

During the measurements, the entire platform supporting the ExB probe was covered with low-sputter-yield flexible graphite sheets to prevent material damage and to minimize sputtering due to high energy ion impacts.

A preliminary examinations of the probe measurements showed that the noise-to-signal ratio increased with increasing CEM inlet voltage, i.e. increasing gain (cf. Figure 5-7). Thus, for each measurement, the lowest gain of the CEM which provided a readily measurable output current was selected.

As discussed earlier, the probe trace varied with time due to the instability in the thruster plume plasma. Thus, the probe measurement was repeated five times at each measurement position, and those traces were averaged to give the final probe trace.

Reference to Chapter 5

- 1 Manzella, D.H., "Stationary Plasma Thruster Plume Emissions," IEPC-93-097, Sept. 1993.
- 2 Vahrenkamp, R.P., "Measurement of Double Charged Ions in The Beam of A 30 cm Mercury Bombardment Thruster," AIAA-73-1057, Oct. 1973.
- 3 Hutchinson, I., Principles of Plasma Diagnostics, Cambridge University Press, New York, 1987.
- 4 King, L.B., Ph.D. Thesis, University of Michigan, Department of Aerospace Engineering, 1998.
- 5 Sovey, J.S., "Improved Ion Containment Using A Ring-Cusp Ion Thruster," Journal of Spacecraft and Rockets, Vol. 21, No. 5, pp. 488-495, 1984.
- 6 Patterson, M.J., "Performance Characteristics of Ring-Cusp Thrusters with Xenon Propellant," AIAA-86-1392, June 1986.
- 7 Kuang, Y-Z, Guo-Qing, and Yang, S-T, "ExB Momentum Analyzer for Broad-Beam Ion sources," AIAA-87-1081, May 1987.
- 8 Takegahara, H., Kasai, Y, "Beam Characteristics Evaluation of ETS-VI Xenon Ion Thruster," IEPC-93-235, Sept. 1993.
- 9 Pollard, J.E., "Plume Angular, Energy, and Mass Spectral Measurements with the T5 Ion Engine," AIAA-95-2920, July 1995.
- 10 Anderson, J.R. and Fitzgerald, D., "Fullerene Propellant Research for Electric Propulsion," AIAA-96-3211, July 1996.
- 11 Nakayama, Y. and Takegahara, H., "C₆₀ Application to Ion Thruster - Inspection of Ionized and Extracted Particle -," IEPC-97-076, Aug. 1997.
- 12 Roboz, J., Introduction to Mass Spectrometry Instrumentation and Techniques, Interscience Publishers, New York, 1968
- 13 White, F.A, Mass Spectrometry in Science and Technology, John Wiley & Sons, Inc., New York, 1968.
- 14 Lochte-Holtgreven, W., Editor, Plasma Diagnostics, AIP Press, Woodbury, New York, 1995.

-
- 15 Bruining, H., Physics and Applications of Secondary Electron Emission, McGraw-Hill, New York, 1954.
- 16 Dekker, A.J., Solid State Physics, Prentice-Hall, Englewood Cliffs, New Jersey, 1965.
- 17 Dionne, G.F., "Effects of Secondary Electron Scattering on Secondary Emission Yield Curves," *Journal of Applied Physics*, Vol. 44, No. 12, pp. 5361-5364, Dec. 1973.
- 18 Young, J.R., "Penetration of Electrons and Ions in Aluminum," *Journal of Applied Physics*, Vol. 27, No. 1, pp. 1-4, Jan. 1956.
- 19 Simon, A., "Instability of a Partially Ionized Plasma in Crossed Electric and Magnetic Fields," *The Physics of Fluids*, Vol. 6, No. 3, pp. 382-388, March 1963.
- 20 Esipchuk, Y.V., Morozov, A.I., Tilinin, G.N., and Trofimov, A.V., "Plasma Oscillations in Closed-Drift Accelerators with an Extended Acceleration Zone," *Soviet Physics, Technical Physics*, Vol. 18, No. 7, pp. 928-932, Jan. 1974.
- 21 Shishkin, G.G. and Gerasimov, V.F., "Plasma Instabilities in Accelerators with Closed Electron Drift," *Soviet Physics, Technical Physics*, Vol. 20, No. 9, pp. 1171-1174, Sept. 1975.
- 22 Esipchuk, Y.V. And Tilinin, G.N., "Drift Instability in a Hall-Current Plasma Accelerator," *Soviet Physics, Technical Physics*, Vol. 21, No. 4, pp. 417-423, April 1976.
- 23 Zhurin, V., Kahn, J., Kaufman, H., Kozubsky, K., and Day, M., "Dynamic Characteristics of Closed Drift Thrusters," IEPC-93-095, Sept. 1993.
- 24 Darnon, F., Lyszyk, M., and Bouchoule, A., "Optical Investigation on Plasma Oscillations of SPT Thrusters," AIAA-97-3051, July 1997.
- 25 Kaufman, H.R., "Technology of Closed-Drift Thrusters," AIAA-83-1398, June 1983.
- 26 Garner, C.E., Polk, J.E., Pless, L.C., Goodfellow, K.D., and Brophy, J.R., "Performance Evaluation and Life Testing of the SPT-100," IEPC-93-091, Sept. 1993.
- 27 Sankovic, J.M., Hamley, J.A., and Haag, T.W., "Performance Evaluation of the Russian SPT-100 Thruster at NASA LeRC," IEPC-93-094, Sept. 1993.
- 28 Randolph, T., Kim, V., Kaufman, H., Kozubsky, K., Zhurin, V., and Day, M., "Facility Effects on Stationary Plasma Thruster Testing," IEPC-93-093, Sept. 1993.

CHAPTER 6

EXB PROBE MEASUREMENTS OF THE SPT-100 PLUME

6.1 Introduction

The ion current incident on the CEM was recorded as a function of the voltage applied between the two E-field bias plates of the **ExB** probe using the experimental set-up described in the previous chapter. Ion energy distributions in the SPT-100 plume would, then, be obtained by properly scaling the two axes of the probe trace (cf. Chapter 5, Section 2).

Before analyzing each peak of the probe traces quantitatively in the next chapter, this chapter shows the obtained **ExB** probe traces and provides some qualitative discussions of the ion energy distributions. The abscissa of each probe trace was corrected for the energy imparted to the ions as they fell from the local plasma potential through the probe to ground, and converted to ion energy via the relation in Eqn. 5-6 where the mass of a xenon atom was used for M_i , and the value of B was determined by the calibration described in Chapter 5, Section 3. It should be noted that the ion current was not divided by the square root of the ion energy, and thus the probe traces shown in this chapter are only approximate representations of the ion energy distribution functions (cf. Eqn. 5-10).

Note that, in this chapter, “ R ” will be used to denote the probe distance from the thruster center, and “ θ ” will be used to denote the probe angle with respect to the thruster axis (e.g. $R = 50$ cm, $\theta = -20^\circ$). Also, recall that the positive θ represents the probe data in the cathode side of the thruster plume while the negative θ represents the probe data in the non-cathode side of the thruster plume.

6.2 Identification of Peaks in ExB Probe Trace

Prior to the analysis of the ion energy distribution, each point in the **ExB** probe trace must be identified as to which ion species it represents. As can be seen from Eqn. 5-3, the probe collects ions of certain velocity regardless of their identities. Therefore, all ion species with the same velocity will appear at the same probe voltage in the probe trace. Consequently, the collector current at a certain probe voltage could be attributed to several different ion species, which complicates the identification of ion species in the probe trace. However, the following discussions will show that, for certain conditions in the SPT-100 plume, each point in the **ExB** probe trace may be considered to represent only xenon ions.

Collector current representing more than one ion species may occur through the collisions between plume particles and the entrainment of background gases by the thruster. Although there are a number of possible collisions that may occur in the thruster plume, previous studies have shown that the dominant collision process under the conditions of typical SPT-100 plume testing is charge exchange between plume and background gases, with elastic collisions between ion species accounting for approximately 10% of the total collisions [1, 2]. The following subsections will discuss each of the above processes.

6.2.1 Charge Exchange Collisions

A charge exchange collision is defined as an interaction between two particles where one or more electrons is transferred with no significant momentum change. Thus, the velocities of the interacted particles can be considered unchanged. Then, the ions will appear at the same voltage on the probe trace as they would have if they did not go through the charge exchange collision. The only effect to the probe trace is on the collected ion current which will increase or decrease due to the change in the charge state

of the ions. (Recall that the gain of the CEM depends on the charge state of the ions impacting the inlet surface.) Hence, charge exchange collisions do not affect the identification of ion species in the probe trace.

6.2.2 Elastic Collisions

Unlike charge exchange collisions, elastic collisions alter the velocities of the particles after the collisions, and thus change the voltage at which the ions appear on the **ExB** probe trace. Consider an elastic collision between two particles of energies E_1 and E_2 ($E_1 < E_2$) and of same mass, which simulates the most common elastic collisions in the SPT-100 plume between singly charged and doubly charged xenon ions. The energy lost by particle 2 due to an elastic collision with particle 1 is written as:

$$E_2 = (E_2 - E_1)\sin^2 \frac{\theta}{2},$$

where θ is the collision scattering angle. It follows from the above equation that the post-collision energy of particle 2 lies somewhere between E_1 and E_2 . Since the collision is elastic, from the conservation of momentum, the post-collision energy of particle 1 also lies between E_1 and E_2 . Therefore, the effect of an elastic collision on the ion energy distributions of particle 1 and particle 2 is the reduction of the original distributions and the increase in the population of ions whose energies lie between E_1 and E_2 . In the actual probe traces, the effect of elastic collisions will manifest itself as highly overlapped regions between the peaks representing the two ion species. However, the experimental results will show that the main peak of the pre-collision distribution (i.e. the original energy distribution) can still be identified.

6.2.3 Entrainment of Background Gases

The SPT-100 plume contains mostly xenon ions, but several minor species exist in the plume due to facility pumping limitations. These minor species consists mainly of atmospheric components (i.e. nitrogen and oxygen) and a large amount of hydrogen and water vapor (due to pumping difficulties associated with water). When the background pressure is sufficiently high, background gases can be ingested by the thruster and used as propellant [1]. This results in ionized minor species accelerated by the same electric field that has accelerated xenon ions. This process is called entrainment.

The mass spectra of ion species in the SPT-100 plume measured by King showed the following entrained minor species [2]; N_2^+ , N^+ , O_2^+ , O^+ , H_2^+ , H^+ , OH^+ , H_2O^+ , and C^+ . The presence of carbon ions stems from the sputtering of the flexible graphite sheet used to cover the surrounding vacuum chamber wall. The platform supporting the **ExB** probe was covered by the same graphite sheet in order to prevent material damage and to minimize sputtering due to high energy ion impacts, and thus carbon ions were also expected to exist during the experiments reported here. This was confirmed by the post-testing inspection which found a thin gray film deposited on metallic surfaces around the platform. Table 6-1 shows the probe voltages V_p and ion energies E_i at which these entrained minor species would appear in the probe trace if these ions are to be accelerated by the potential of 229 V ($V_i = 229$ V). This voltage was found to be the most probable acceleration voltage of the C^+ ions from the probe measurements. Thus, the calculated E_i would be the energy at which the most current will be collected for that species. Since the purpose of the discussion here is to determine if the presence of these entrained species affects the identification of xenon ion species in the probe traces, E_i in Table 6-1 is calculated using Eqn. 5-6 where the mass of a xenon atom is used for M_i instead of the mass of the entrained species.

Entrained Species	Atomic Weight	V_p (V)	E_i as Xe (eV)
N_2^+	28	153	1073
N^+	14	216	2139
O_2^+	32	143	938
O^+	16	202	1871
H_2^+	2	572	15001
H^+	1	809	30007
OH^+	17	196	1761
H_2O^+	18	191	1673
C^+	12	234	2500

Table 6-1 Probe voltages V_p and energies E_i of the entrained species in the SPT-100 plume when the entrained species are accelerated by the potential of 229 V. The energies are calculated as though these species were xenon ions. The bold numbers in the energy column indicates the energies less than 1200 eV, the maximum possible E_i for quadruply ionized xenon.

The maximum possible E_i of xenon ions were expected to be 1200 eV for quadruply charged xenon ions accelerated by 300 V which was the discharge voltage of the thruster. The bold numbers in the energy column of Table 6-1 indicates the energies less than 1200 eV. These energies of 938 eV and 1073 eV are within the range of energies expected for Xe^{4+} ions in the SPT-100 plume. Also, 938 eV is near the highest energy expected for Xe^{3+} ions (900 eV). Thus, the presence of N_2^+ and O_2^+ ions in the thruster plume may affect the identification of quadruply charged xenon ions and, to a lesser degree, triply charged xenon ions in the probe trace.

In an emission spectroscopic study of the SPT-100 plume, Manzella estimated the amount of background N_2^+ ions entrained by the thruster to be equivalent to approximately 2% of the supplied xenon mass flow [3]. This value is more than the fraction of Xe^{3+} and Xe^{4+} ions expected in the SPT-100 plume. However, the actual

amount of entrained N_2^+ ions must be considered less than what Manzella estimated due to the fact that, in his experiment, nitrogen was injected into the vacuum chamber for the purpose of increasing the background pressure. Furthermore, as King stated in the mass spectrometry study, N^+ and O^+ ions are much more likely to be produced in the thruster discharge chamber by electron impacts than N_2^+ and O_2^+ ions because the bond energy of each diatomic molecule is much less than the ionization potential of the molecule. In addition, recall that the gain of the CEM increases with the degree of ionization of the incoming particles. Therefore, a singly charged nitrogen molecular ion and a singly charged oxygen molecular ion would produce much less CEM output current than a triply or quadruply charged xenon ion (approximately 10 to 20 times less). Hence, the probe current due to N_2^+ and O_2^+ ions can be considered small compared to the probe current produced by Xe^{3+} and Xe^{4+} ions in the region of the thruster plume where appreciable amount of Xe^{3+} and Xe^{4+} ions exist.

The mass spectra obtained by King showed that the amount of N_2^+ and O_2^+ ions is less than that of the other entrained species in Table 6-1. Therefore, the region of the thruster plume where the collector current for N_2^+ and O_2^+ ions cannot be ignored may be safely assumed as the region where there is a significant amount of the collector current for the other entrained species. Note that the collector current at $E_i = 0$ eV should be zero since it represents the particles of zero velocity. In reality, the collector current is not zero at $E_i = 0$ eV due to the dark current (background noise) of the CEM and neutral particles diffusing (or streaming if from charge exchange collisions) into the probe. Then, the collector current at $E_i = 0$ eV can be considered the baseline of the probe measurements. Thus, evidence of significant entrainment can be found if the collector current at $E_i = 1600$ eV and above is larger than the base current at $E_i = 0$ eV. Figure 6-1 shows **ExB** probe traces at several angles off the thruster axis at the distance of 50 cm from the center of the thruster exit plane. The first three peaks from the left can clearly be attributed to Xe^{1+} , Xe^{2+} , and Xe^{3+} ions. The small peak around 1000 eV at $\theta = 0^\circ$ can

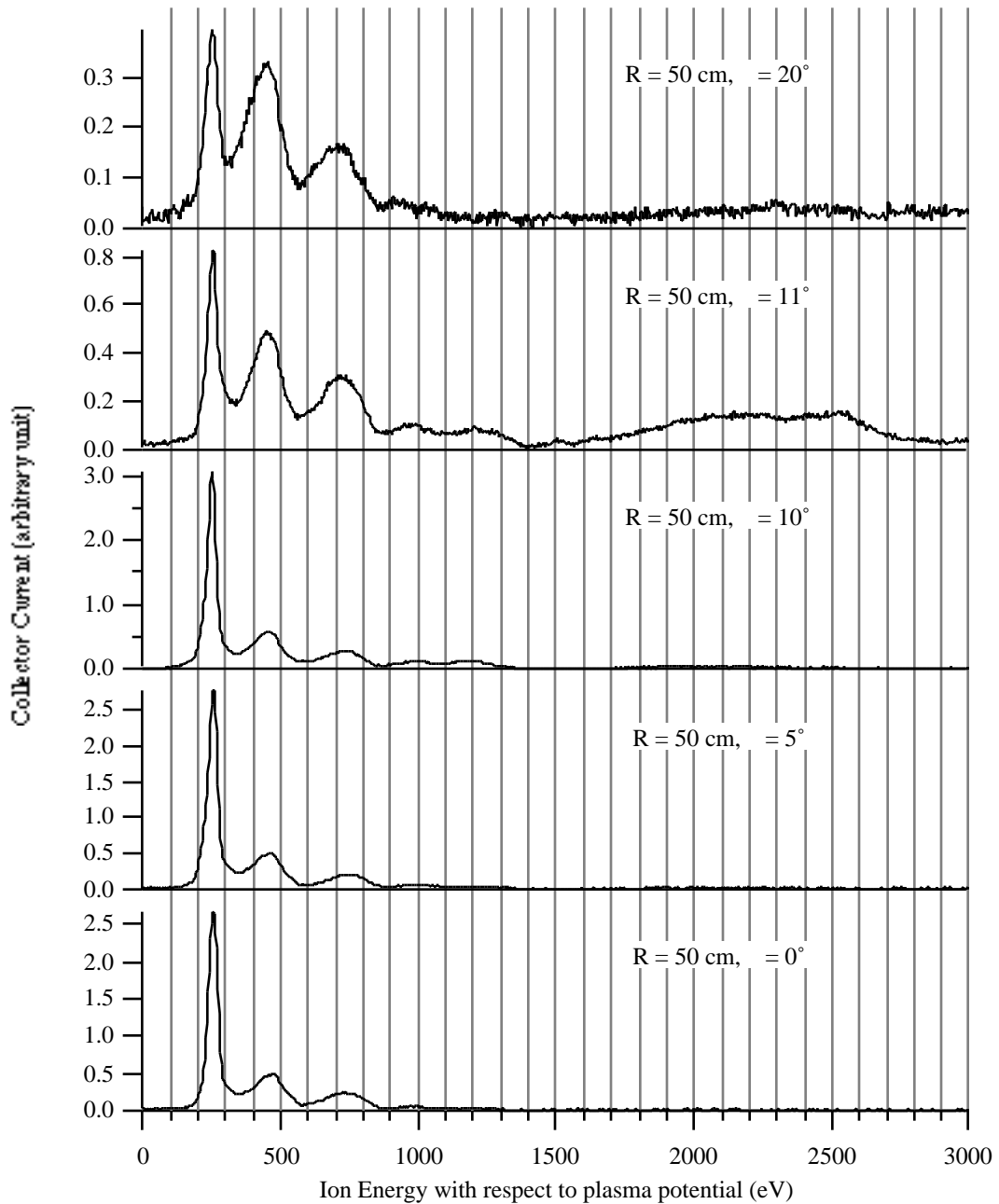


Figure 6-1 Ion current as a function of ion energy at 0°, 5°, 10°, 11°, and 20° off the thruster axis at 50 cm from the center of the SPT-100 exit plane.

be attributed to Xe^{4+} ions since the collector current at 1600 eV and above is zero indicating that there is no significant amount of collector current for the entrained background gases. The peak for Xe^{4+} ions is still identifiable even at $\theta = 5^\circ, 10^\circ,$ and 11°

where collector current for N_2^+ and O_2^+ ions is thought to exist at around 950 eV since there is an appreciable amount of collector current at 1600 eV and above representing the other entrained background gases of OH^+ , H_2O^+ , and C^+ . However, the amplitude of the collector current representing Xe^{4+} ions at these angles must be viewed with some skepticism due to the extra current added by the presence of N_2^+ and O_2^+ ions.

At first look, the amplitude of the collector current for Xe^{3+} ions with respect to that for Xe^{1+} ions seems to have increased due to the added collector current for N_2^+ and O_2^+ ions. However, the ratio of Xe^{3+} peak height to Xe^{1+} peak height at $\theta = 11^\circ$ (0.37) is less than that at $\theta = 20^\circ$ (0.43) while the collector current of the entrained gases is more at $\theta = 11^\circ$ than at $\theta = 20^\circ$. Furthermore, the ratio of Xe^{2+} peak height to Xe^{1+} peak height also increases as θ increases from 11° to 20° , which shows a trend that the number of multiply charged xenon ions with respect to the number of singly charged xenon ions increases as θ increases in this region of the plume. This trend was also observed at the other distances from the thruster. In addition, recall that the calculated E_i of O_2^+ ions 938 eV is beyond the range of energy for Xe^{3+} ions. Hence, it was concluded that the increase in the collector current for Xe^{3+} ions with respect to that for Xe^{1+} ions is inherent to the SPT-100, and is not due to the added current of N_2^+ and O_2^+ ions.

In summary, the entrained background gases do not affect the peaks for Xe^{1+} , Xe^{2+} , and Xe^{3+} ions in a **ExB** probe trace. The peak for Xe^{4+} can still be identified at some measurement points, but the amplitude of the peak is increased because the collector current for N_2^+ and O_2^+ ions is added. In each probe trace, a peak around $E_i = 245$ eV represents the energy distribution of Xe^{1+} ions while a peak around $E_i = 450$ eV portrays that of Xe^{2+} ions (equivalent to $V_i = 225$ V), and a peak around $E_i = 700$ eV portrays that of Xe^{3+} ions (equivalent to $V_i = 233$ V). A peak around $E_i = 900$ eV can be attributed to Xe^{4+} ions (equivalent to $V_i = 225$ V) when the collector current for the entrained background gases is negligible. The following sections show the obtained **ExB** probe traces and provides some qualitative discussions of ion energy distribution of each

xenon ion species at various measurement points in the SPT-100 plume. The probe traces are shown only for the range of ion energy E_i between 0 eV and 1500 eV, which is the range of energies for xenon ions. Again, note that the ion current was not divided by the square root of the ion energy, and thus the probe traces shown are only approximate representations of the ion energy distribution functions (cf. Eqn. 5-10).

6.3 Ion Energy Measurements at 25 cm from the Exit Plane

Figure 6-2 through Figure 6-6 show the **ExB** probe traces obtained at various angles off the thruster axis at the distance of 25 cm from the thruster exit center.

At $\theta = 0^\circ$, there is a small peak around $E_i = 950$ eV after the first three peaks representing Xe^{1+} , Xe^{2+} , and Xe^{3+} ions. This small peak is attributed to Xe^{4+} ions because the entrained background gases were not observed at $E_i = 1600$ eV and beyond. This confirms the existence of Xe^{4+} ions in the SPT-100 plume. The Xe^{4+} peak is still identifiable between $\theta = -15^\circ$ and 15° . The existence of Xe^{4+} ions at larger angles could not be stated for certain because of the probe measurement limitation.

The peaks for Xe^{1+} and Xe^{2+} ions are highly overlapped, and the peak widths are larger near the thruster axis ($\theta = 0^\circ$) compared to the peaks at larger θ . As discussed in Section 2.2 of this chapter, the highly overlapped peaks are the manifestation of elastic collisions between the two species. Thus, it can be concluded that elastic collisions between xenon ions occur mostly near the thruster axis in the SPT-100 plume.

In the cathode side of the thruster plume, the ratios of Xe^{2+} and Xe^{3+} ions to Xe^{1+} ions increase as θ increases from 0° position up to $\theta = 20^\circ$. Then, the peaks for Xe^{1+} and Xe^{3+} ions decrease as θ increases to larger angles, and the peak for Xe^{2+} ions becomes dominant between $\theta = 30^\circ$ and 60° . This shows that the ion ratios depend strongly on the angular position in the thruster plume. The probe trace could not be obtained beyond $\theta =$

60° because the cathode body was physically blocking the path of the ions to the probe near this region of the thruster plume.

In the non-cathode side of the thruster plume, the change in the ratios of multiply charged xenon ions to singly charged xenon ions is similar to that in the cathode side of the plume. However, the ratios seem larger at a given angle in the non-cathode side than at the opposite angle in the cathode side. The probe trace could not be obtained beyond $\theta = -100^\circ$ due to the probe measurement limitation.

The most curious aspect of the probe traces is that the current signals become so noisy that some or all peaks could not be identified between $\theta = -10^\circ$ and -50° . Although less prominent, the similar phenomenon can be observed in the cathode side of the thruster plume where the probe trace at $\theta = 15^\circ$ is noisier than those at $\theta = 10^\circ$ and 20° . The magnitude of the collector current in these regions of the plume was approximately 40 pA, which is well within the range of the measurable current of the picoammeter. Furthermore, the probe trace did not improve when the CEM gain was increased. Also, the noise did not decrease when the CEM inlet voltage was reduced. (Recall from Chapter 5 that there was a tendency for noisier traces with increased CEM voltage. See Figure 5-7). Therefore, the noisy current signals cannot be explained by the probe measurement limitations.

Recall from the discussion of ion current density in Chapter 4 that the ion current density at $R = 25$ cm had regions -20° -10° and 10° 20° where an unusually low ion current density was observed (cf. Figure 4-4 and Figure 4-5). This was ascribed to high occurrence of charge exchange collisions in the very-near-field of the plume, which resulted in fast moving directed neutrals and slow ions moving in arbitrary directions. As discussed in Section 2.1 of this chapter, charge exchange collisions do not affect the energy at which the ions appear on the probe trace, but do affect the magnitude of the collected ion current which will increase or decrease due to the change in the charge state of the ions. Thus, the observed noisy current signals may be attributed to a

significant amount of charge exchange ions. In addition, the fast moving neutrals will stream into the probe and add to the collector current noise, although this noise will be small since the charge exchange neutrals are not accelerated by the CEM inlet voltage. As will be discussed in the following sections, the same phenomenon is observed at the other distances from the thruster exit plane. However, the noisy current signals become less prominent at larger distances from the thruster. This observation agrees with the result in Chapter 4 where there is no apparent region of low ion current density at $R = 50$ cm, 75 cm, and 1 m.

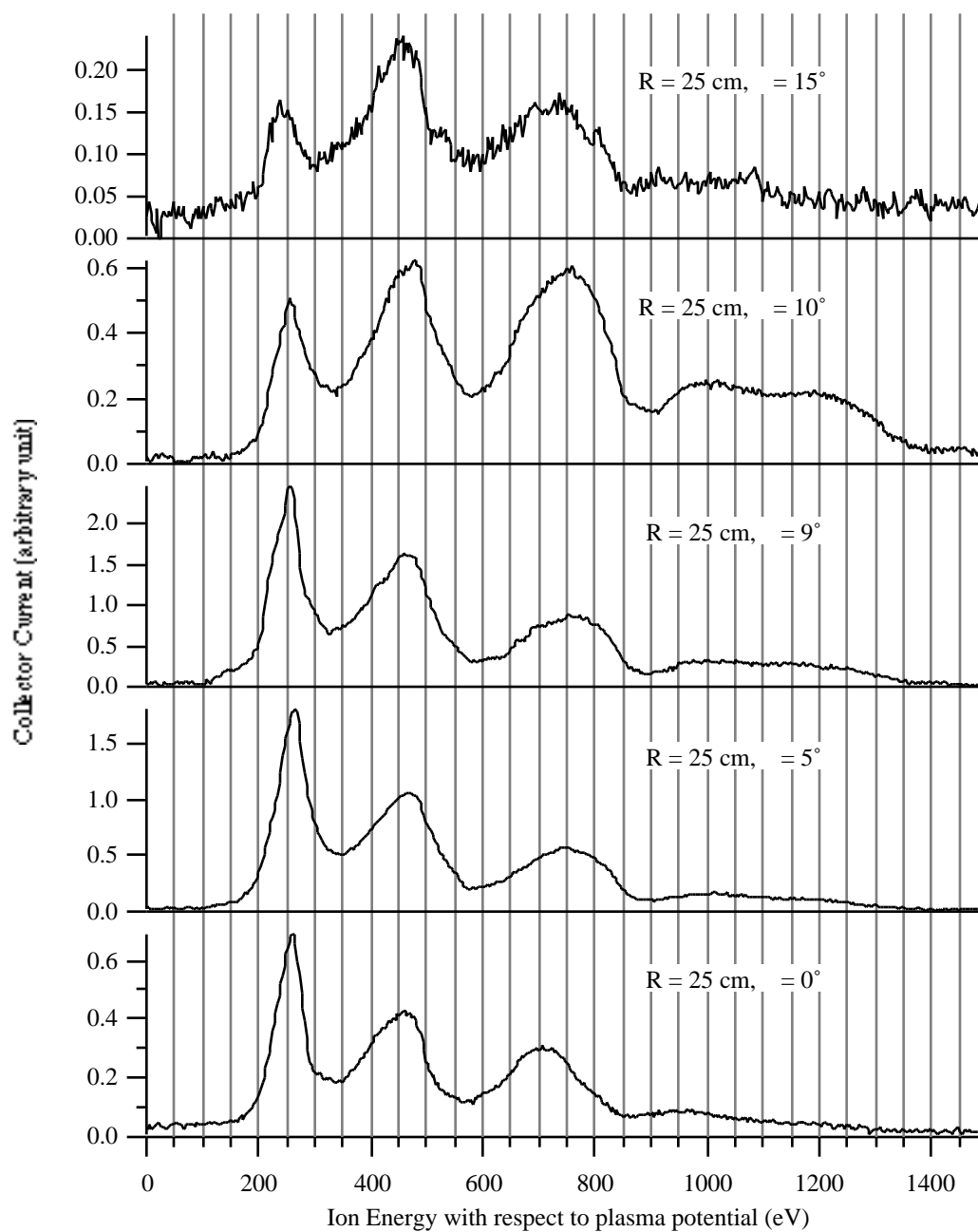


Figure 6-2 Ion current as a function of ion energy at 0° , 5° , 9° , 10° , and 15° off the thruster axis at 25 cm from the center of the SPT-100 exit plane.

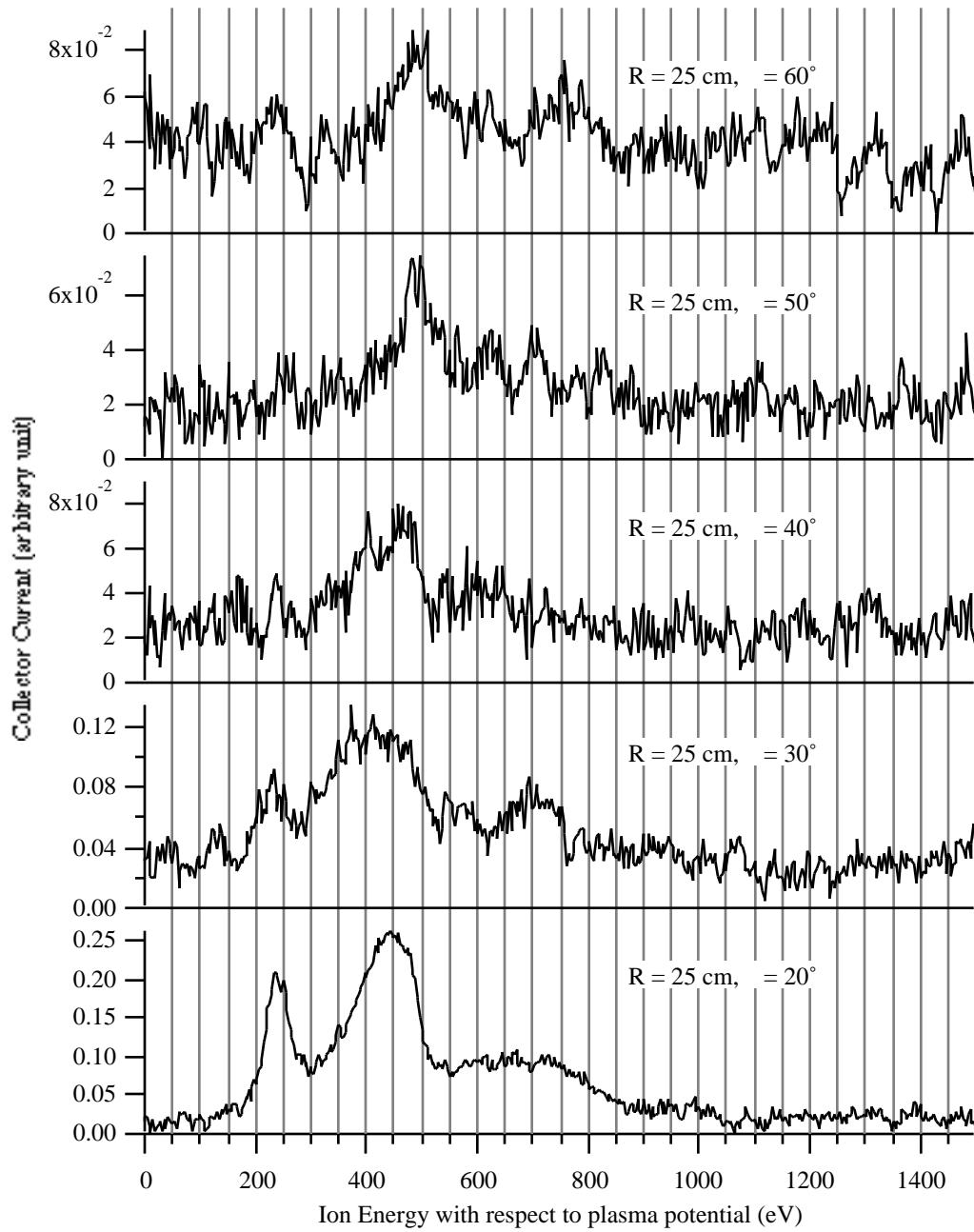


Figure 6-3 Ion current as a function of ion energy at 20°, 30°, 40°, 50°, and 60° off the thruster axis at 25 cm from the center of the SPT-100 exit plane.

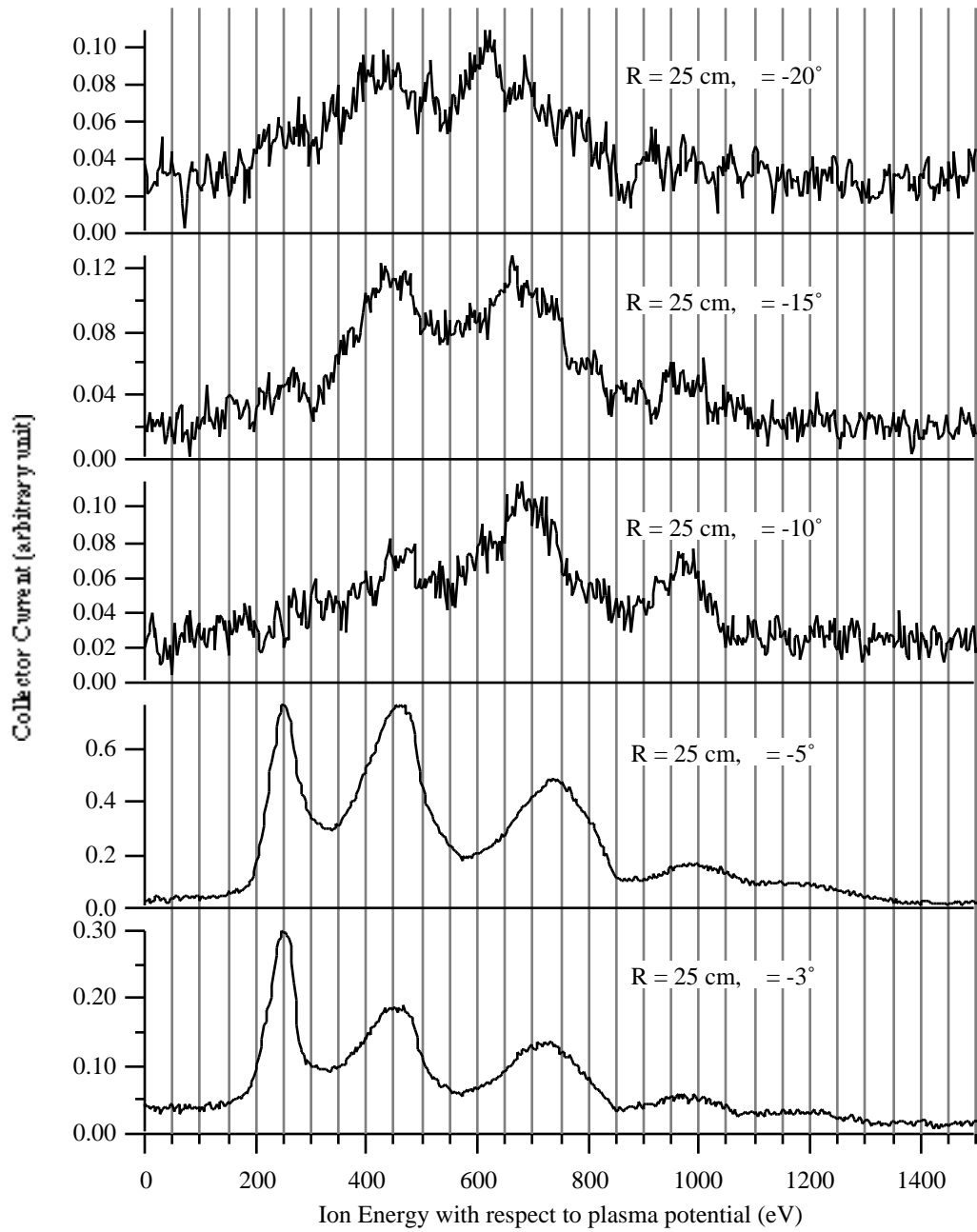


Figure 6-4 Ion current as a function of ion energy at -3° , -5° , -10° , -15° , and -20° off the thruster axis at 25 cm from the center of the SPT-100 exit plane.

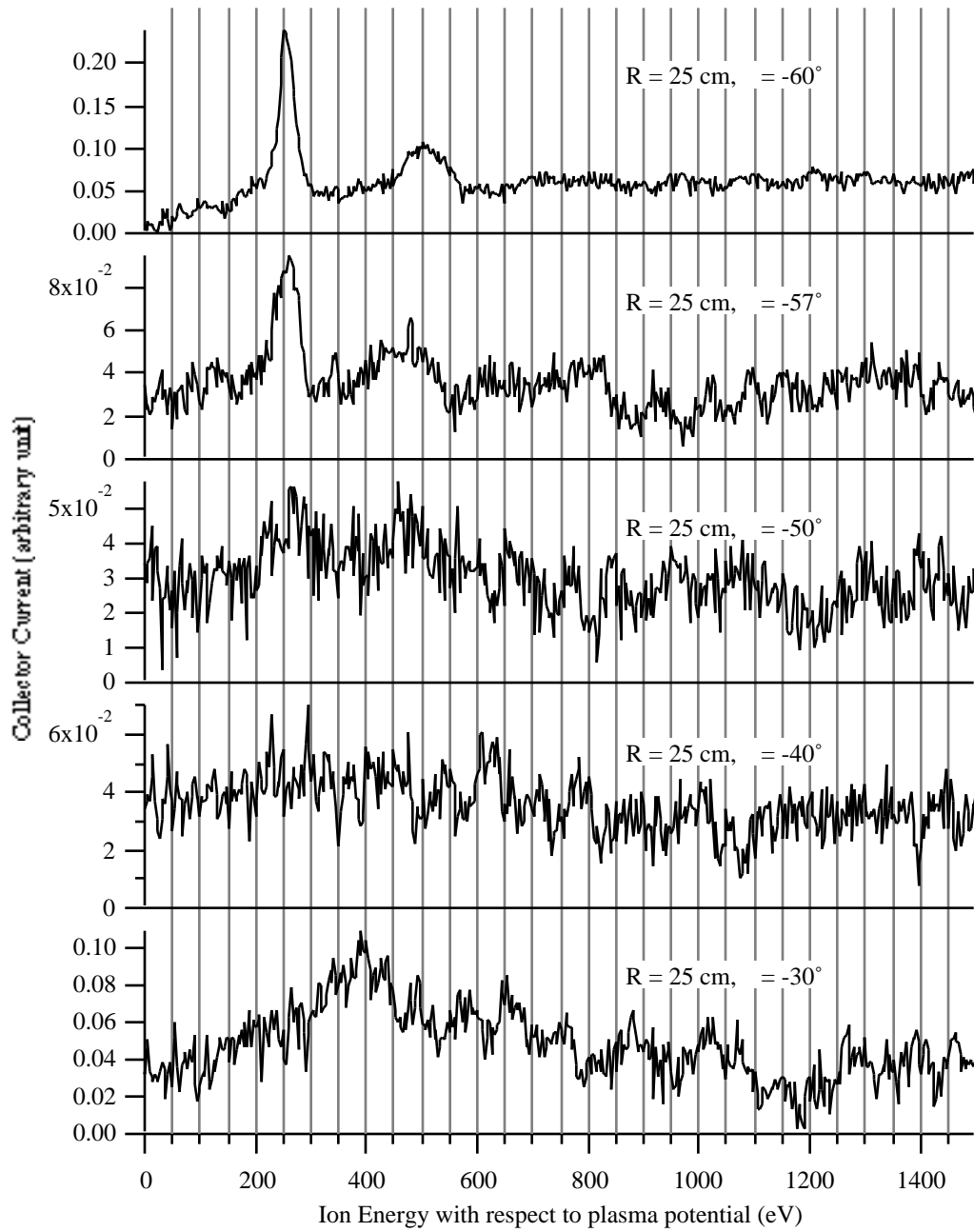


Figure 6-5 Ion current as a function of ion energy at -30° , -40° , -50° , -57° , and -60° off the thruster axis at 25 cm from the center of the SPT-100 exit plane.

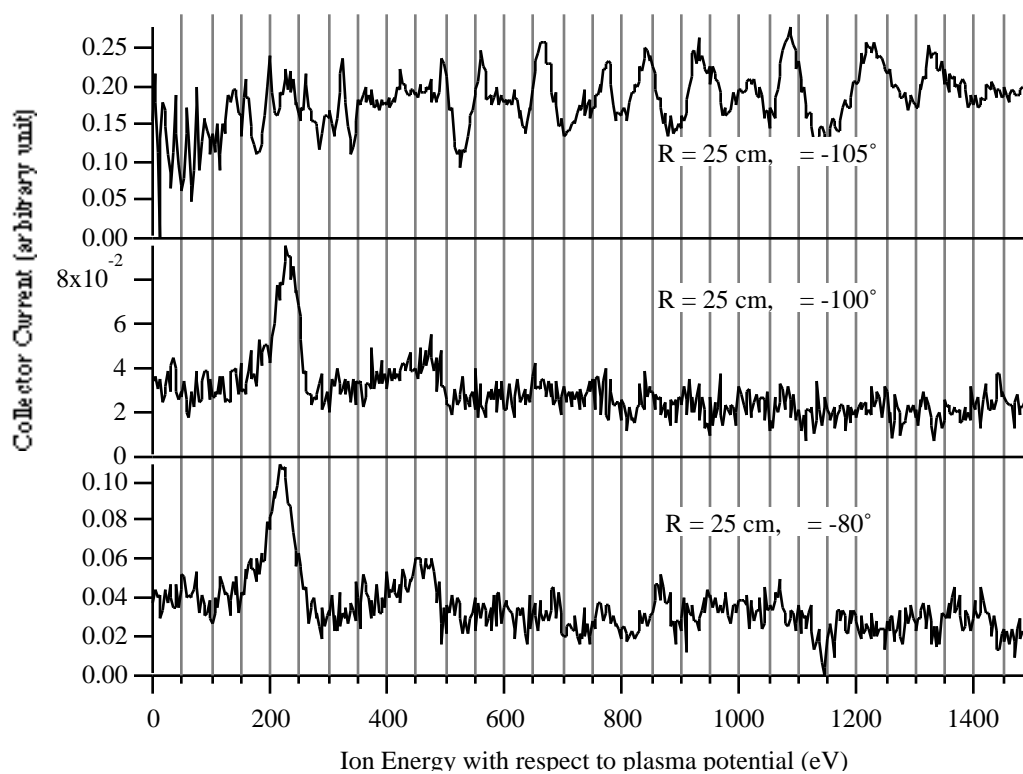


Figure 6-6 Ion current as a function of ion energy at -80° , -100° , and -105° off the thruster axis at 25 cm from the center of the SPT-100 exit plane.

6.4 Ion Energy Measurements at 50 cm from the Exit Plane

Figure 6-7 through Figure 6-11 show the **ExB** probe traces obtained at various angles off the thruster axis at the distance of 50 cm from the thruster exit center.

As in the data at $R = 25$ cm, the peak around $E_i = 950$ eV representing Xe^{4+} ions can be clearly identified at angles between $\theta = -11^\circ$ and 11° . Also, the probe traces show strong dependence of ion ratios on the angular measurement position. Comparing the probe traces at $\theta = 5^\circ, 10^\circ,$ and 11° with those at $\theta = -5^\circ, -10^\circ,$ and -11° , it can be seen that the ratios of Xe^{2+} and Xe^{3+} ions to Xe^{1+} ions are slightly larger in the non-cathode side of the thruster plume.

As in the data at $R = 25$ cm, the peaks for Xe^{1+} and Xe^{2+} ions are highly overlapped, and the peak widths are larger near the thruster axis ($\theta = 0^\circ$) compared to the peaks at larger θ , indicating that most of the elastic collisions between xenon ions occur near the thruster axis in the SPT-100 plume.

Unlike at $R = 25$ cm, the peak for Xe^{2+} ions is not the dominant peak at $\theta = 50^\circ$ and 60° . Instead, the peak for Xe^{1+} ions is comparable to the peak for Xe^{2+} ions. Also, the current signals at these angles are much less noisy than the data at $R = 25$ cm at the same angular positions. There are two possible explanations for these differences: 1) the fast moving xenon neutrals are diffused as they move away from the thruster, and thus, their density is lower at $R = 50$ cm. 2) the number of Xe^{2+} ions are decreased by charge exchange collisions with the fast moving xenon neutrals, resulting in recovery of Xe^{1+} ions. The second explanation is plausible due to the fact that there are many fast moving xenon neutrals at $R = 25$ cm which are moving away from the thruster and ready to exchange electrons with the beam ions since the probability for charge exchange collisions is greatest between ions and neutrals of similar velocities [4]. Also, single-charge transfer cross sections for xenon is proportional to $q_i^{1.3}$ [5]. Therefore, it is highly

probable that Xe^{2+} ions and the fast moving xenon neutrals in the plume undergo charge exchange collisions, resulting in Xe^{1+} ions.

Similarly to the data at $R = 25$ cm, the current signals become suddenly noisy in the region of the thruster plume -30° -11° and 12° 15° . Again, this may be attributed to the presence of a large number of charge exchange ions in this region of the thruster plume.

A meaningful probe trace could not be obtained beyond $\theta = 40^\circ$ because the cathode body was physically blocking the path of the ions to the probe near this region of the thruster plume. The probe trace could not be obtained beyond $\theta = -50^\circ$ due to the probe measurement limitation.

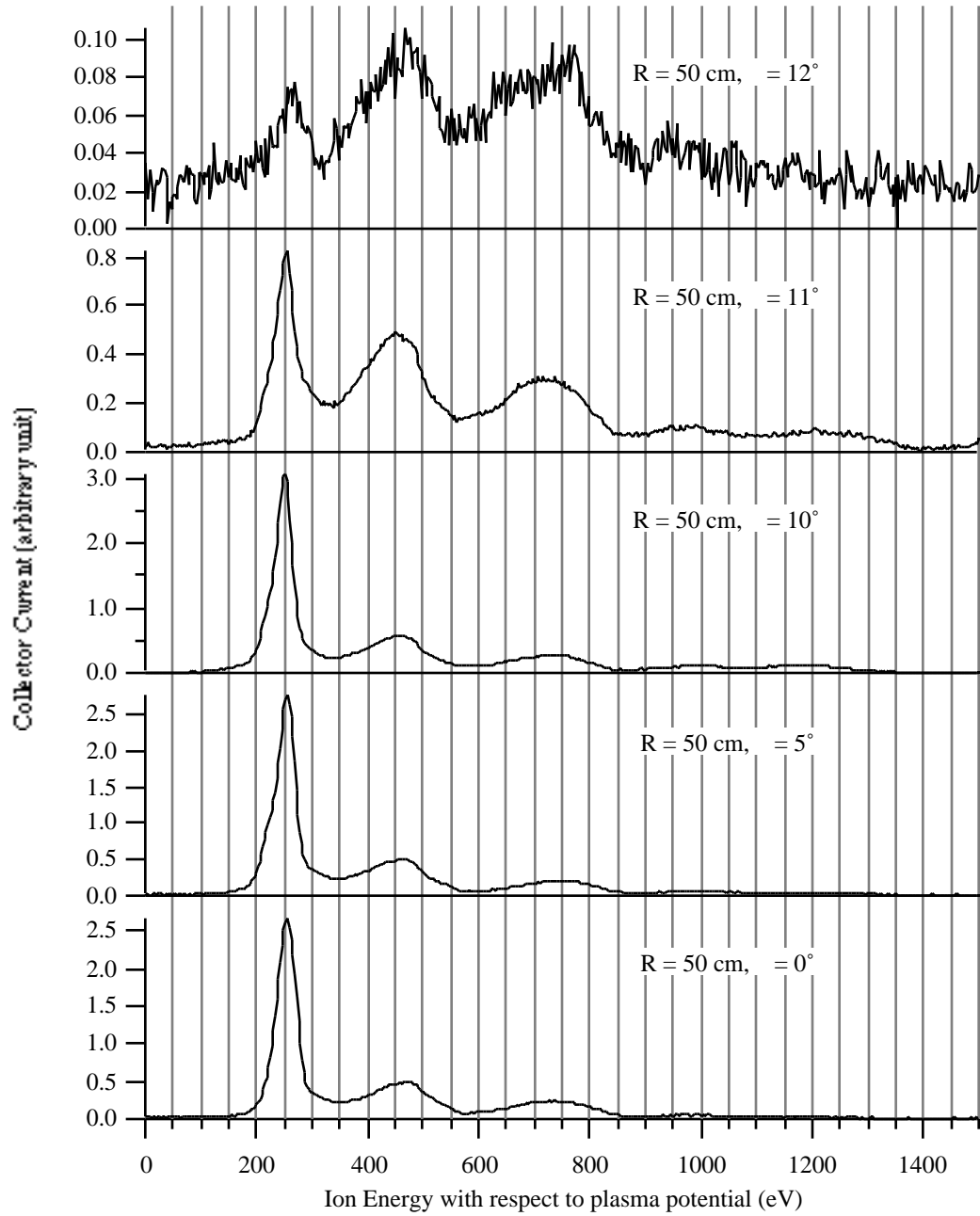


Figure 6-7 Ion current as a function of ion energy at 0°, 5°, 10°, 11°, and 12° off the thruster axis at 50 cm from the center of the SPT-100 exit plane.

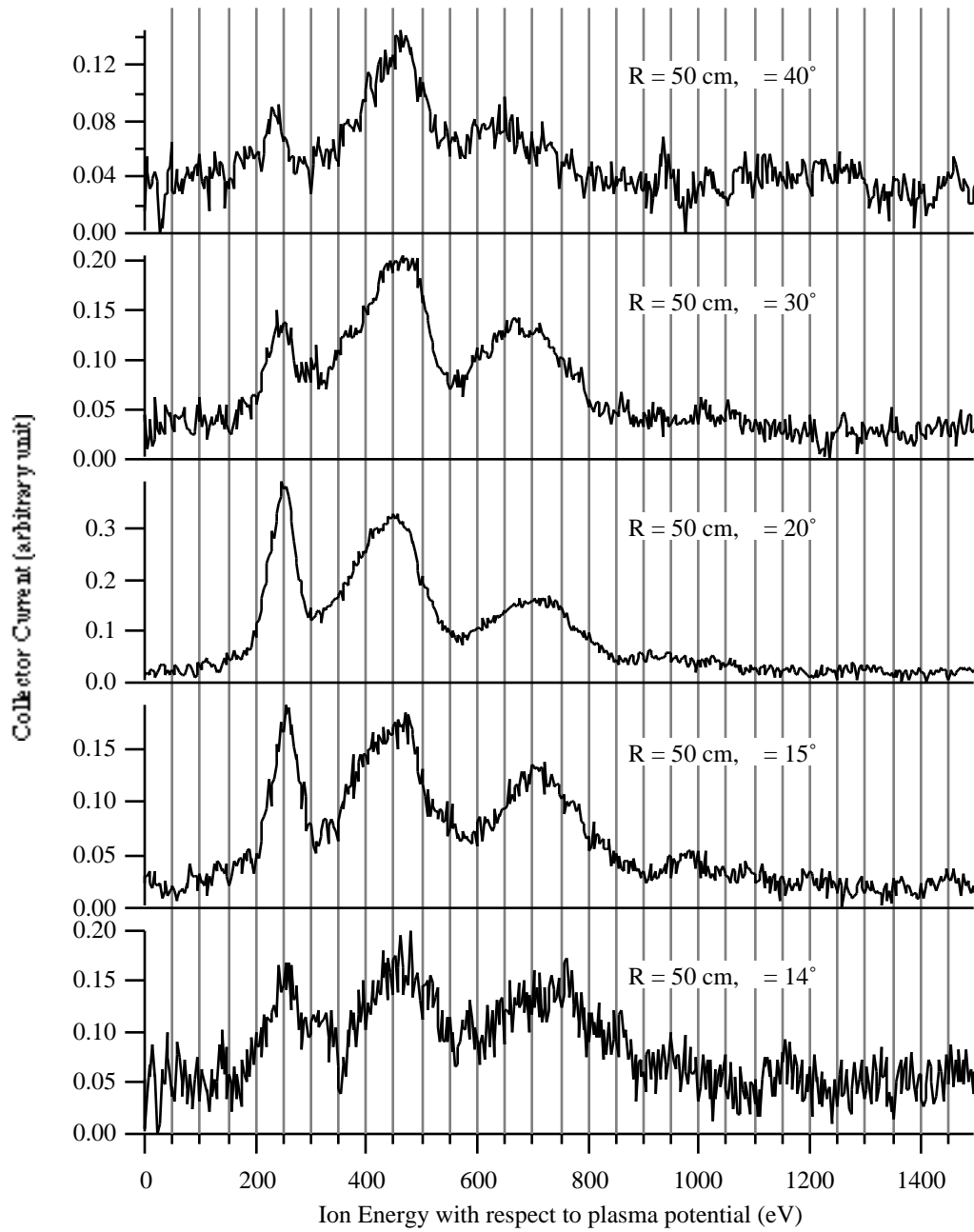


Figure 6-8 Ion current as a function of ion energy at 14°, 15°, 20°, 30°, and 40° off the thruster axis at 50 cm from the center of the SPT-100 exit plane.

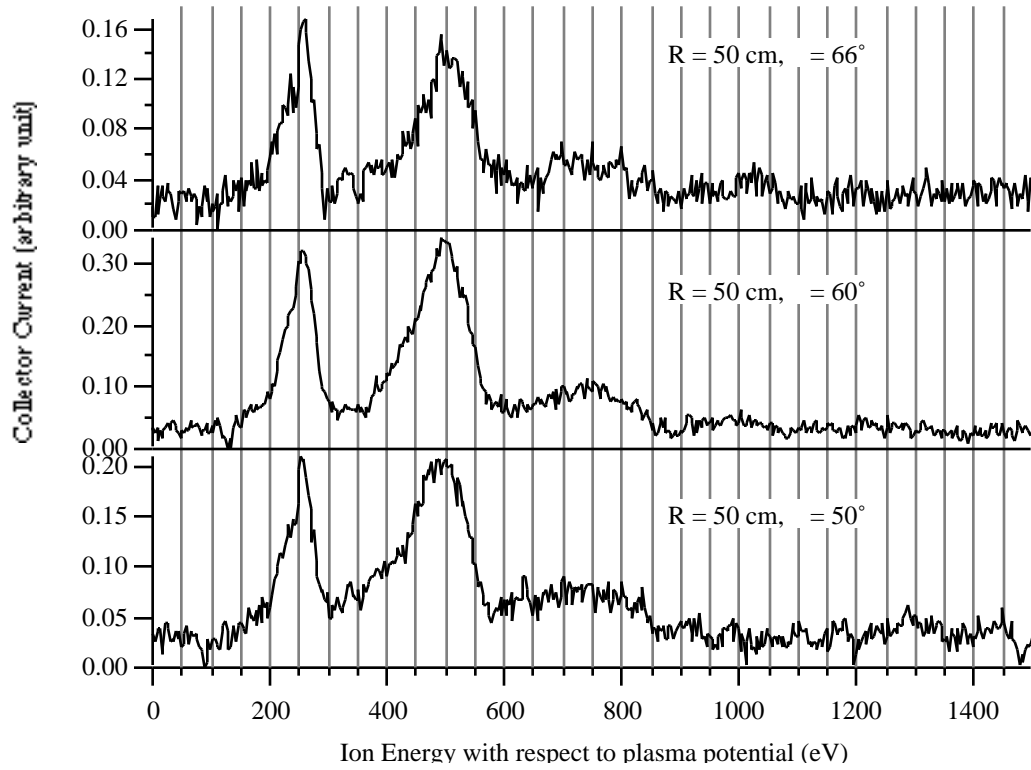


Figure 6-9 Ion current as a function of ion energy at 50°, 60°, and 66° off the thruster axis at 50 cm from the center of the SPT-100 exit plane.

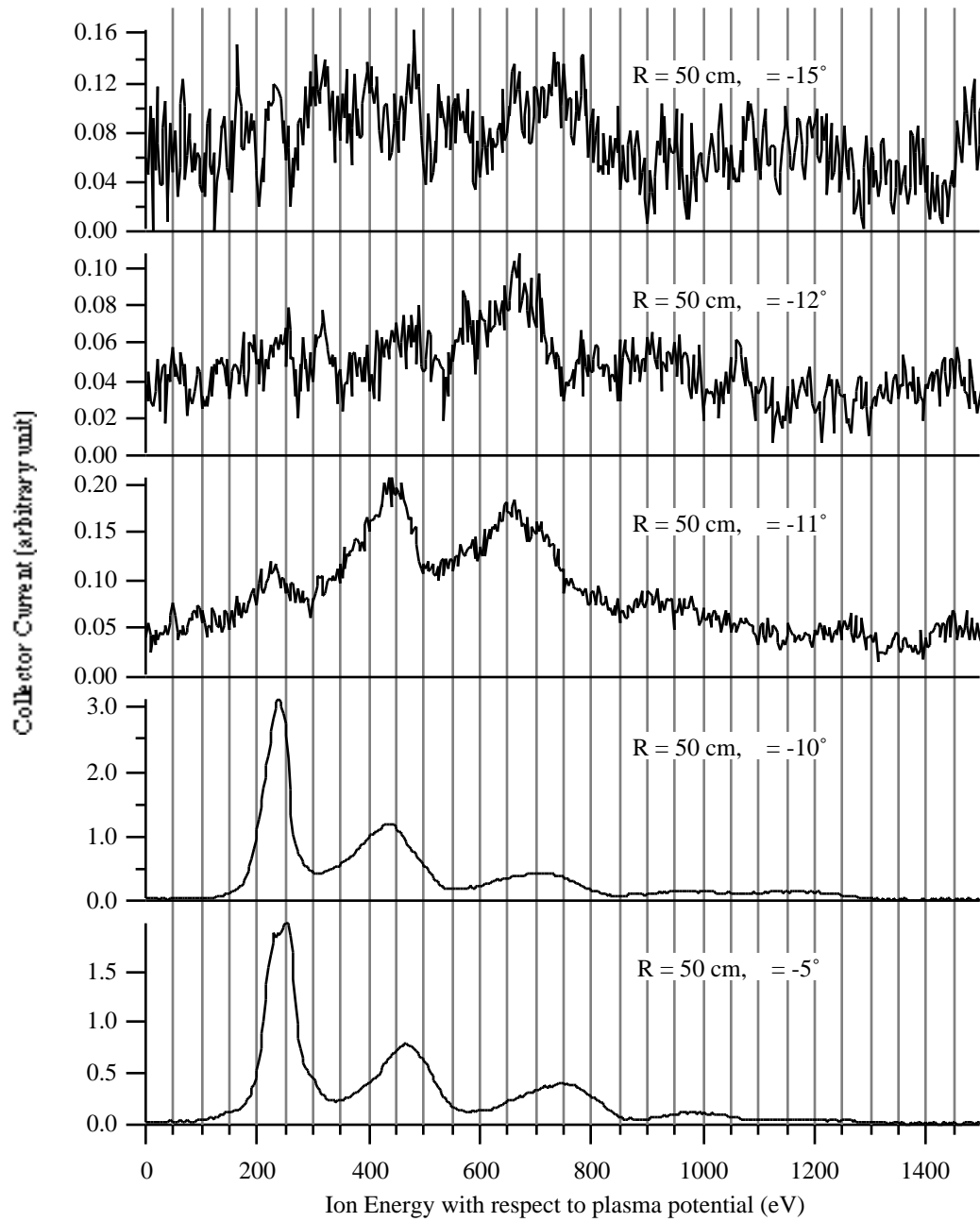


Figure 6-10 Ion current as a function of ion energy at -5° , -10° , -11° , -12° , and -15° off the thruster axis at 50 cm from the center of the SPT-100 exit plane.

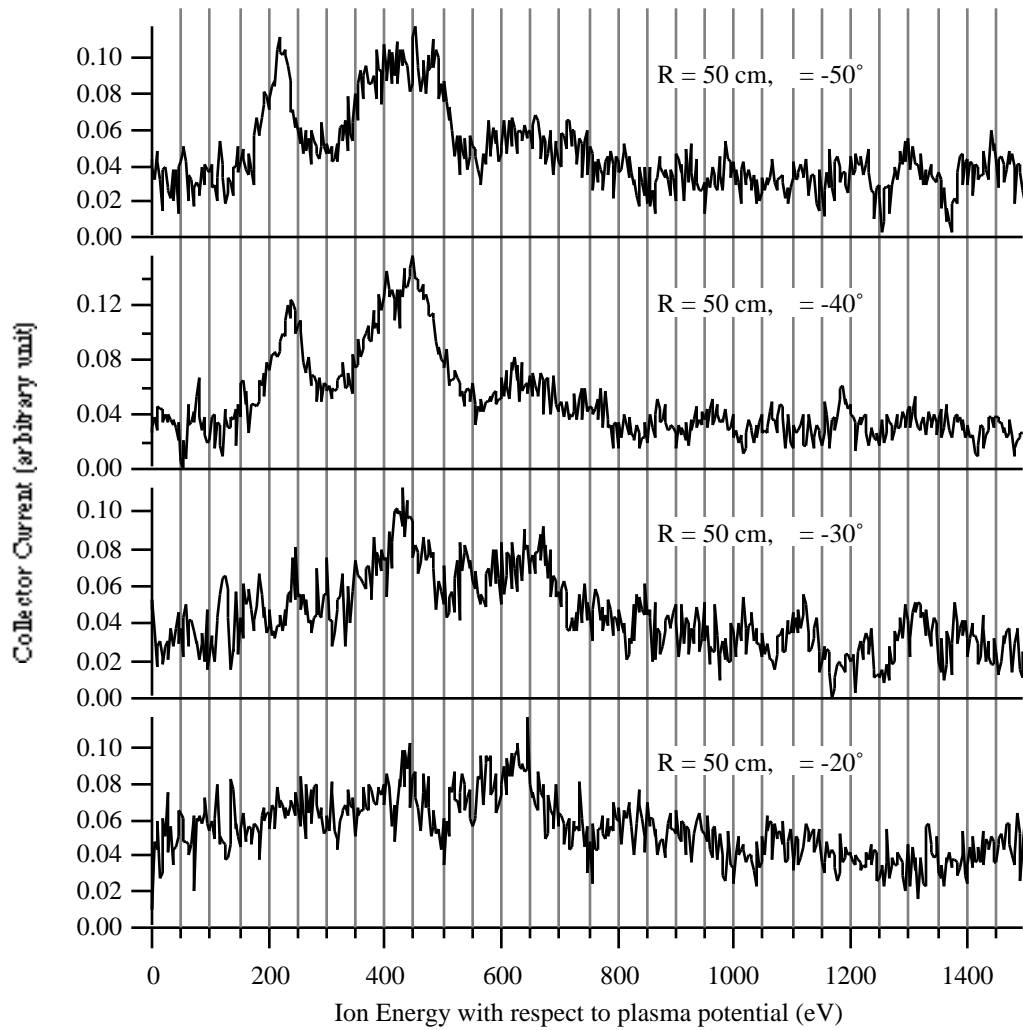


Figure 6-11 Ion current as a function of ion energy at -20° , -30° , -40° , and -50° off the thruster axis at 50 cm from the center of the SPT-100 exit plane.

6.5 Ion Energy Measurements at 75 cm from the Exit Plane

Figure 6-12 through Figure 6-15 show the **ExB** probe traces obtained at various angles off the thruster axis at the distance of 75 cm from the thruster exit center.

Since there was no current due to the entrained gases at $\theta = 0^\circ$, the peak around $E_i = 950$ eV is attributed to Xe^{4+} ions. This peak can be clearly identified at angles between $\theta = -13^\circ$ and 20° . As in the data at $R = 25$ cm and 50 cm, the probe traces show strong dependence of ion ratios on the angular measurement position. In the data at $R = 25$ cm and 50 cm, the ratios of Xe^{2+} and Xe^{3+} ions to Xe^{1+} ions are slightly larger in the non-cathode side of the thruster plume than in the cathode side. However, this asymmetry of the thruster plume seems to have disappeared at $R = 75$ cm.

The peaks for Xe^{1+} and Xe^{2+} ions are highly overlapped near the thruster axis ($\theta = 0^\circ$) compared to the peaks at larger θ , and are more so than the data at $R = 25$ cm and 50 cm. This implies that more elastic collisions occur near the thruster axis at $R = 75$ cm. At $\theta = 0^\circ$, the peak for Xe^{1+} is very sharp, and the beginning of the peak for Xe^{2+} ions is highly defined compared to those peaks at other θ . This suggests that, at $\theta = 0^\circ$, only ions of certain energies are involved in elastic collisions instead of ions of all energies. At $\theta = 0^\circ$ and 5° , a small peak can be seen near the tail end of the peak for Xe^{1+} ions. The origin of these peaks are not known at this time.

Similarly to the data at $R = 25$ cm and 50 cm, the current signals become suddenly noisy in the region of the thruster plume -30° to -15° . The observed phenomenon is less prominent at $R = 75$ cm than at $R = 25$ cm and 50 cm. Furthermore, the phenomenon is hardly observable in the cathode side of the thruster plume at $R = 75$ cm. Therefore, the influence of charge exchange collisions on the probe traces seems to decrease with increasing distance from the thruster.

A meaningful probe trace could not be obtained beyond $\theta = 70^\circ$ and $\theta = -50^\circ$ for the same reasons before.

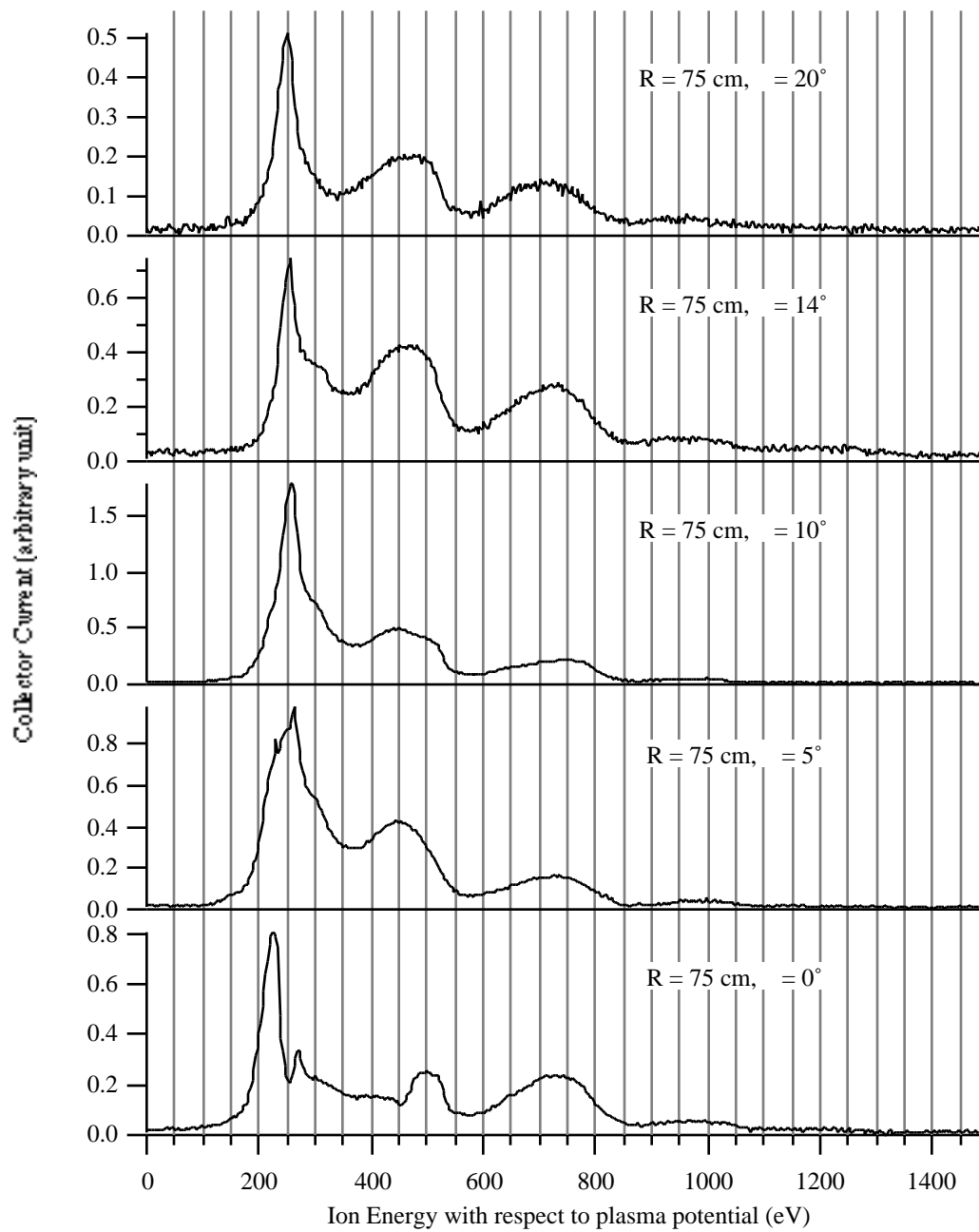


Figure 6-12 Ion current as a function of ion energy at 0° , 5° , 10° , 14° , and 20° off the thruster axis at 75 cm from the center of the SPT-100 exit plane.

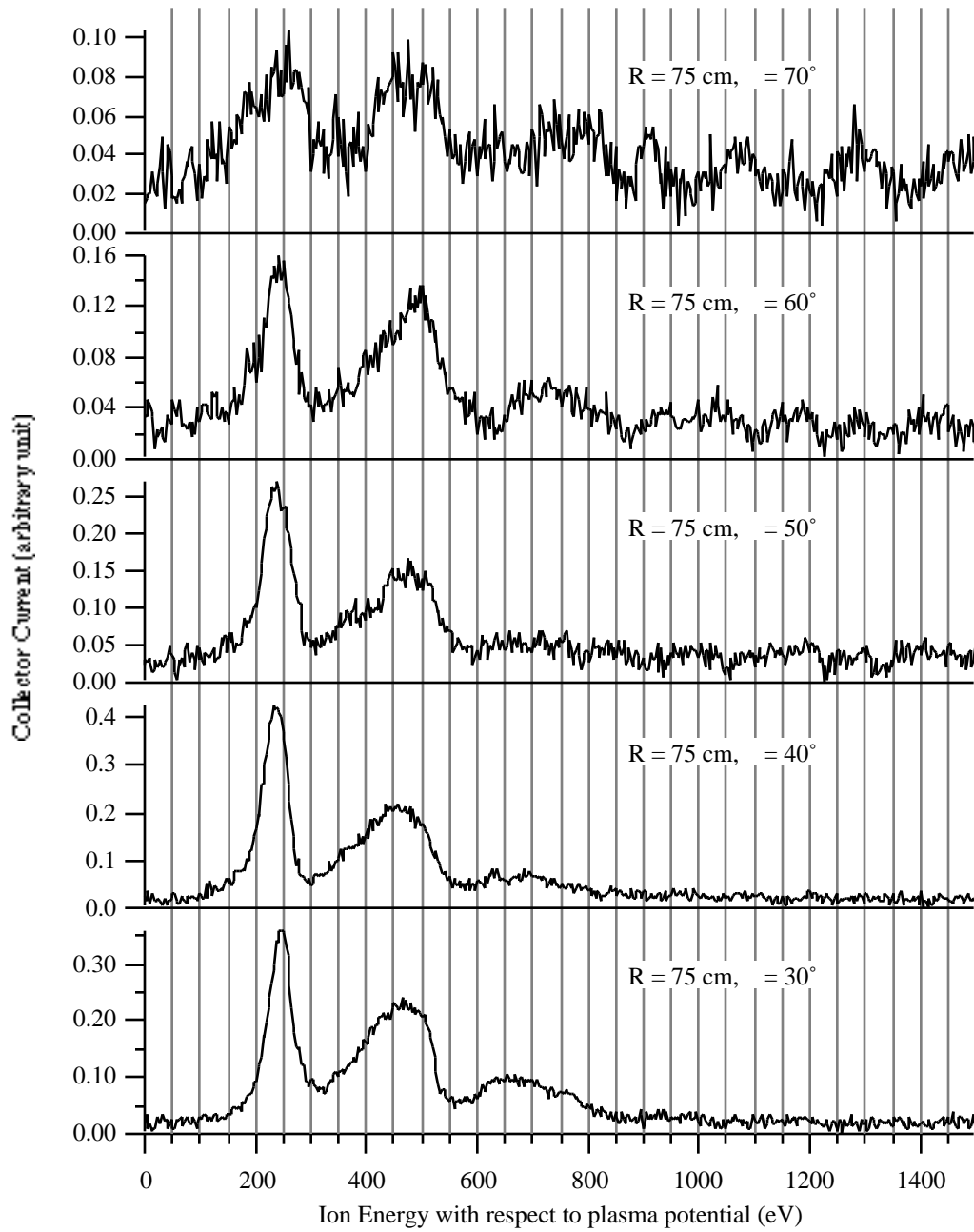


Figure 6-13 Ion current as a function of ion energy at 30°, 40°, 50°, 60°, and 70° off the thruster axis at 75 cm from the center of the SPT-100 exit plane.

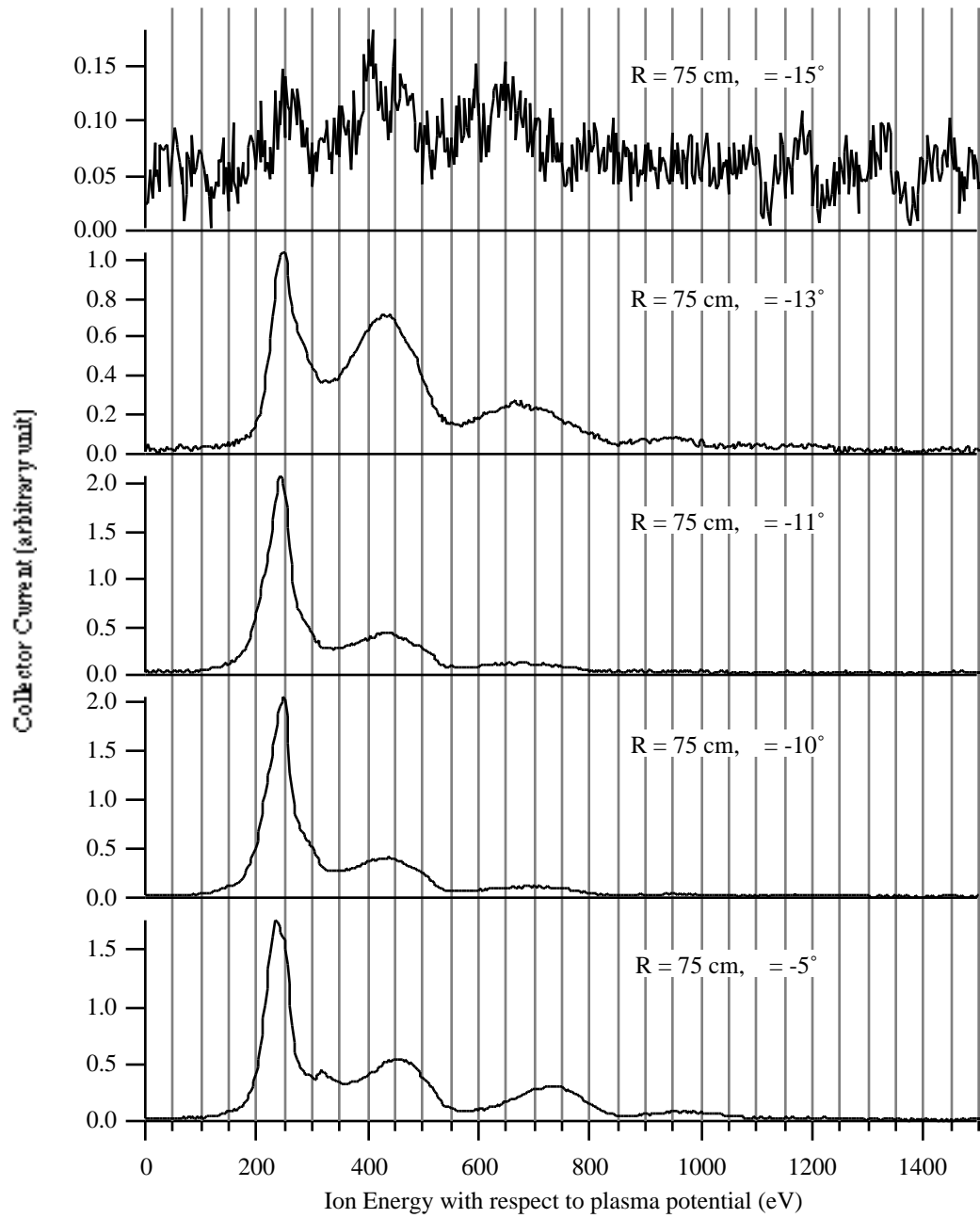


Figure 6-14 Ion current as a function of ion energy at -5° , -10° , -11° , -13° , and -15° off the thruster axis at 75 cm from the center of the SPT-100 exit plane.

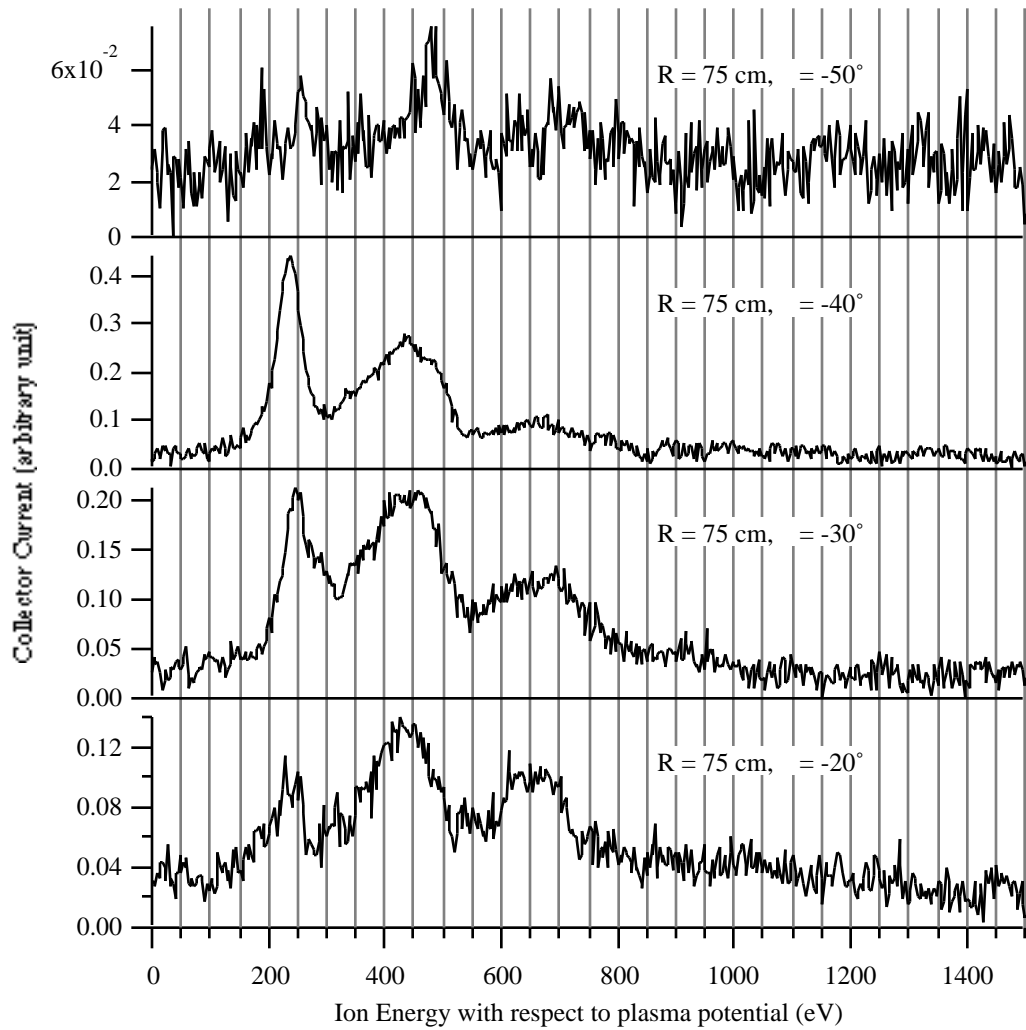


Figure 6-15 Ion current as a function of ion energy at -20°, -30°, -40°, and -50° off the thruster axis at 75 cm from the center of the SPT-100 exit plane.

6.6 Ion Energy Measurements at 1 m from the Exit Plane

Figure 6-16 through Figure 6-20 show the **ExB** probe traces obtained at various angles off the thruster axis at the distance of 1 m from the thruster exit center.

There was no current due to the entrained gases at $\theta = 0^\circ$, and therefore, the peak around $E_i = 950$ eV is attributed to Xe^{4+} ions. This peak can be clearly identified at angles between $\theta = -19^\circ$ and 20° . Strong dependence of ion ratios on the angular measurement position is also seen at $R = 1$ m as it was for the data at the other distances from the thruster exit. As in the data at $R = 75$ cm, the ratios of Xe^{2+} and Xe^{3+} ions to Xe^{1+} ions in the non-cathode side of the thruster plume is similar to those in the cathode side. Thus, the thruster plume seems to be symmetric at $R = 1$ m in terms of ion ratios.

The peaks for Xe^{1+} and Xe^{2+} ions are highly overlapped around the thruster axis ($\theta = 0^\circ$) compared to the peaks at larger θ . But, at $\theta = 0^\circ$, the tail end of the Xe^{1+} peak is well defined, which implies less elastic collisions at $\theta = 0^\circ$ than at the other θ around the thruster axis. This differs from the data at the other distances from the thruster exit where the two peaks for Xe^{1+} and Xe^{2+} ions were highly overlapped at $\theta = 0^\circ$.

Similarly to the data at the other distances from the thruster exit, the current signals become suddenly noisy in the region of the thruster plume -20° to -16° . However, the observed phenomenon is even less prominent at $R = 1$ m than at $R = 75$ cm. This further validates the conclusion in the previous section that the influence of charge exchange collisions on the probe traces decreases with increasing distance from the thruster.

The probe trace could not be obtained beyond $\theta = 70^\circ$ and $\theta = -40^\circ$ for the same reasons before.

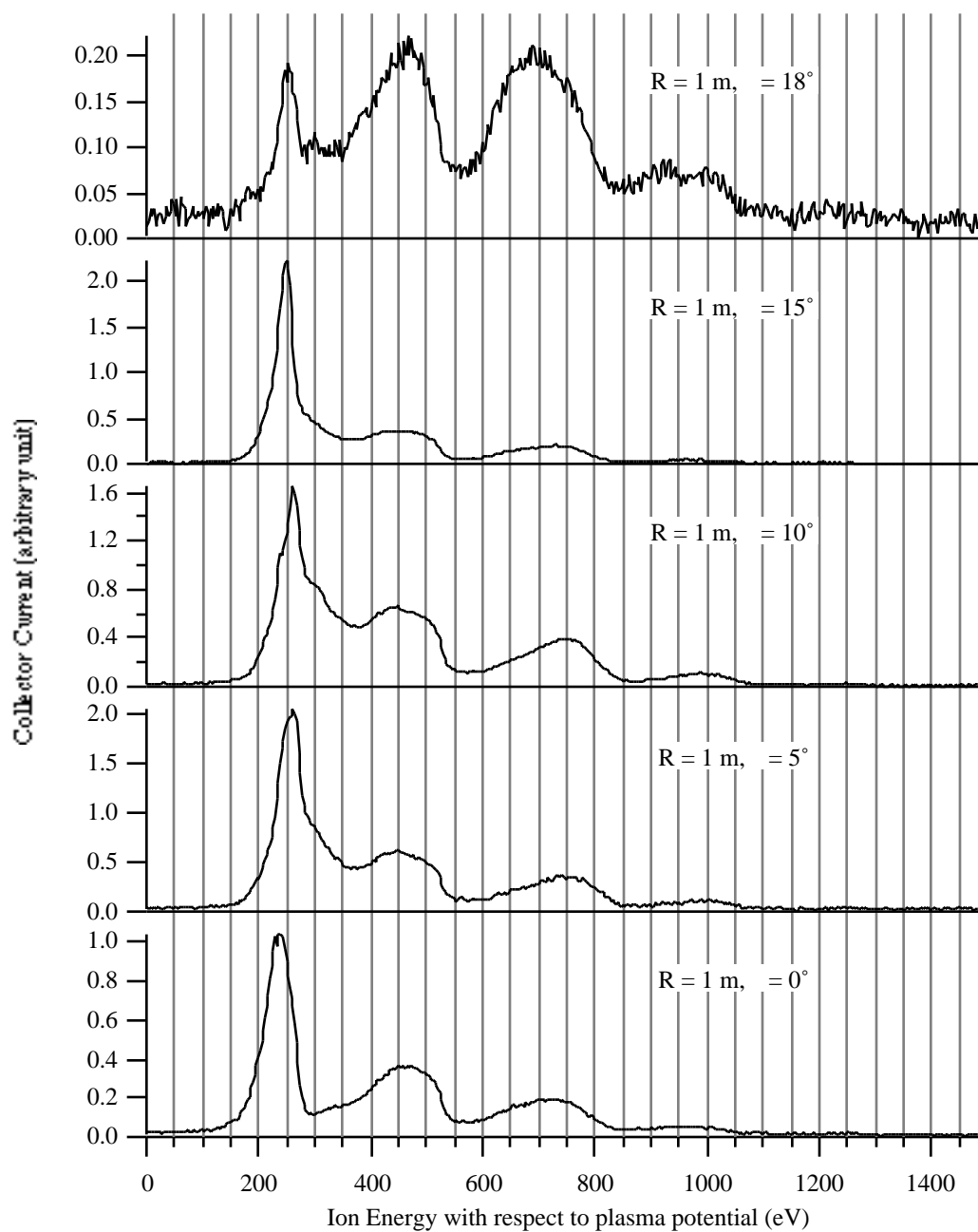


Figure 6-16 Ion current as a function of ion energy at 0°, 5°, 10°, 15°, and 18° off the thruster axis at 1 m from the center of the SPT-100 exit plane.

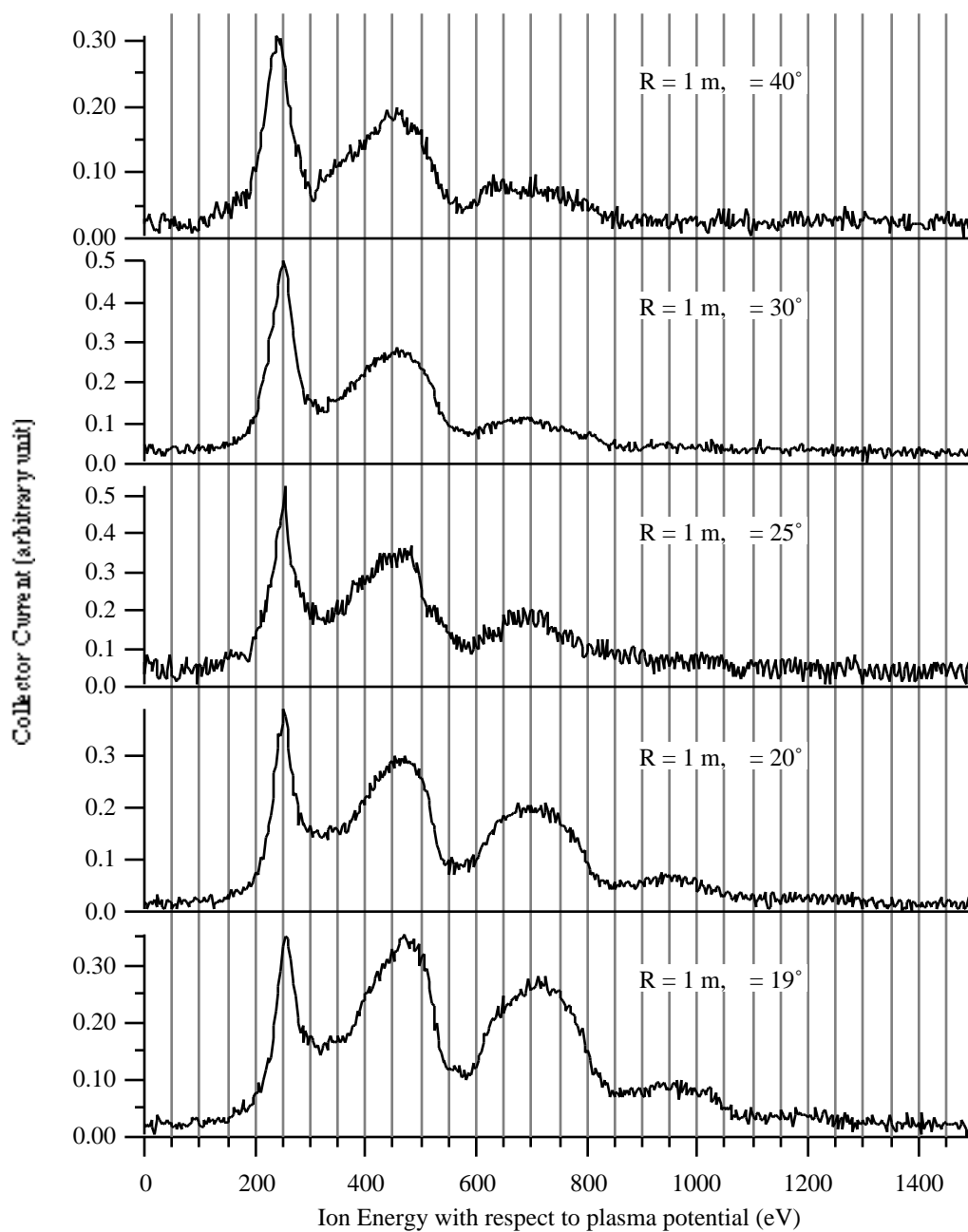


Figure 6-17 Ion current as a function of ion energy at 19°, 20°, 25°, 30°, and 40° off the thruster axis at 1 m from the center of the SPT-100 exit plane.

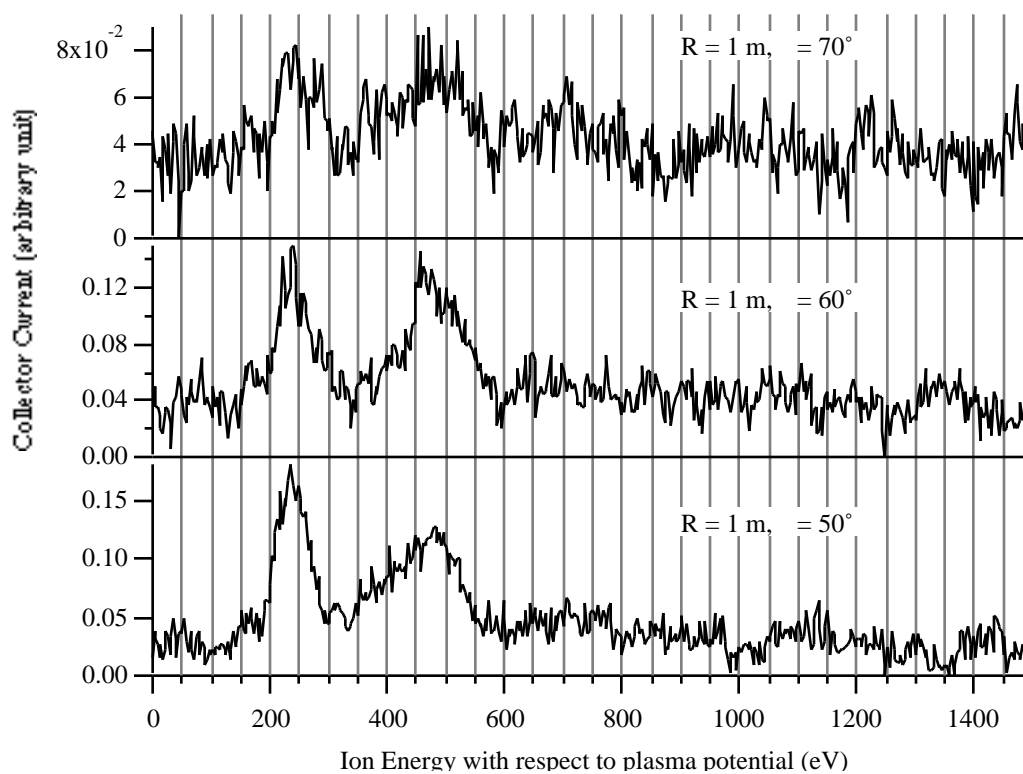


Figure 6-18 Ion current as a function of ion energy at 50°, 60°, and 70° off the thruster axis at 1 m from the center of the SPT-100 exit plane.

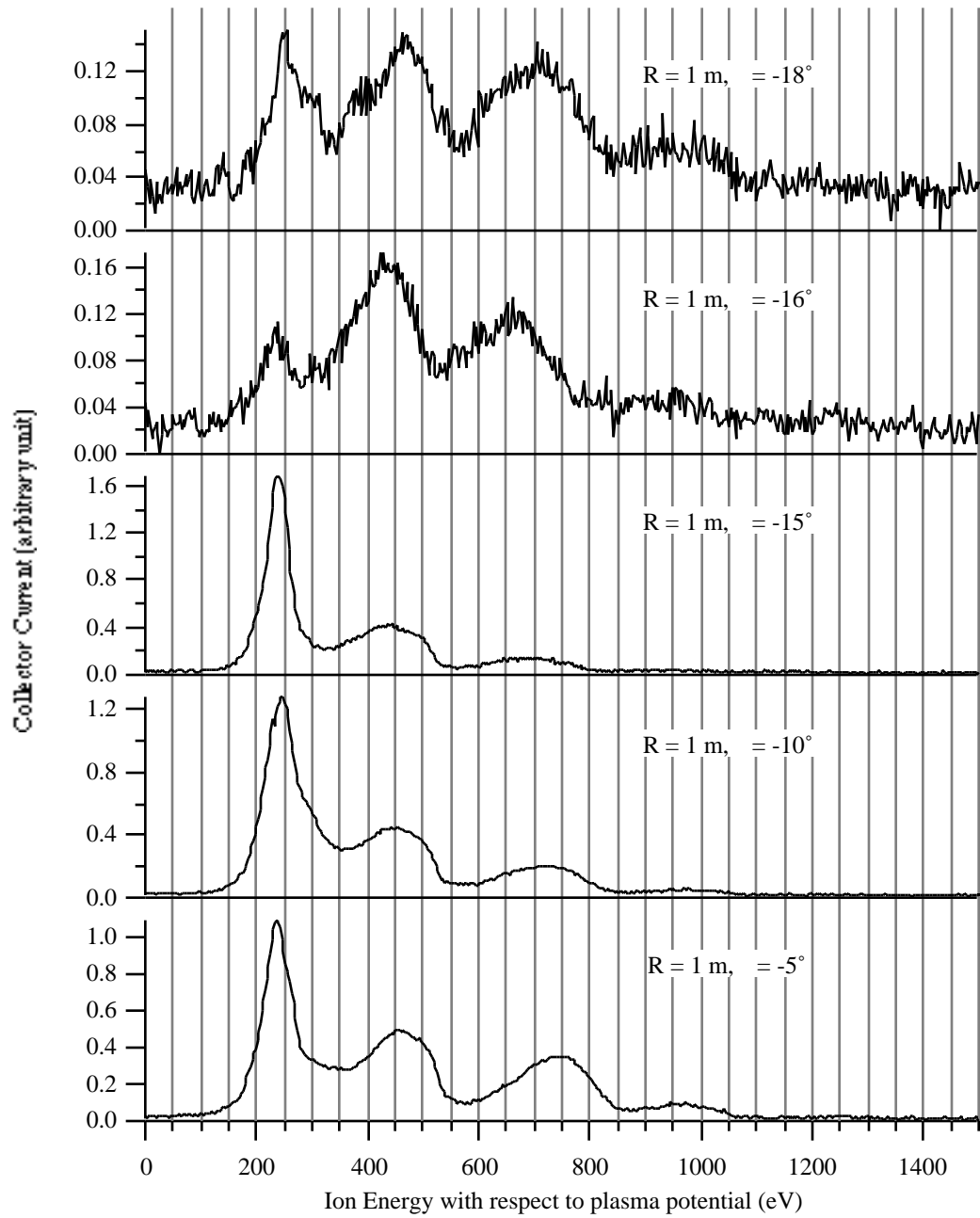


Figure 6-19 Ion current as a function of ion energy at -5° , -10° , -15° , -16° , and -18° off the thruster axis at 1 m from the center of the SPT-100 exit plane.

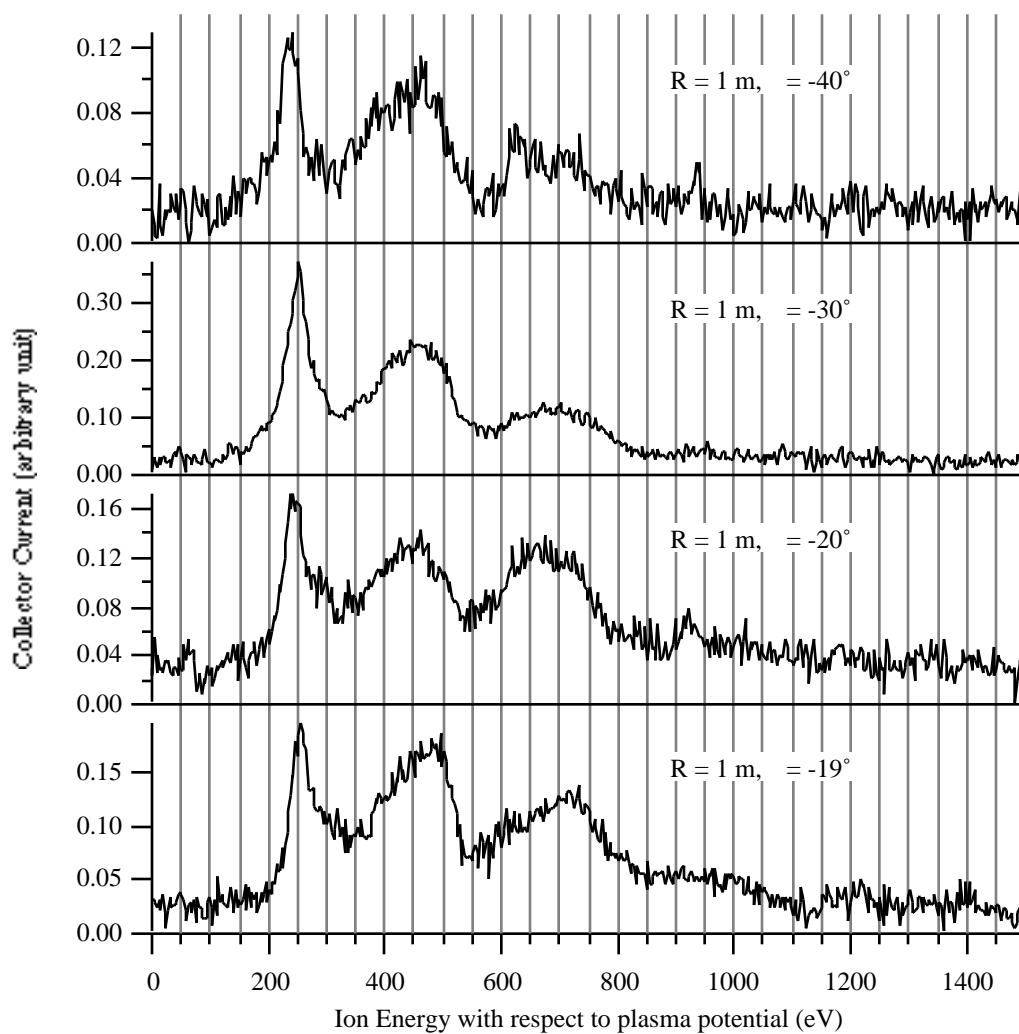


Figure 6-20 Ion current as a function of ion energy at -19° , -20° , -30° , and -40° off the thruster axis at 1 m from the center of the SPT-100 exit plane.

6.7 Conclusions

Upon a close examination of the **ExB** probe traces obtained at various measurement points in the SPT-100 plume, several observations were made that were common to the data at all distances from the thruster. There were also other aspects of the probe traces that were different at each distance from the thruster.

The peak representing Xe^{4+} ions were observed at all distances from the thruster at angles -10° to 10° . The existence of the entrained gases in the thruster plume and the probe measurement limitation precluded the confirmation of the existence of Xe^{4+} ions at larger angles. The **ExB** probe study is the first experiment that had directly measured the Xe^{4+} ions in the SPT-100 plume.

The two peaks for Xe^{1+} and Xe^{2+} ions were highly overlapped near the thruster axis ($\theta = 0^\circ$) at all distances from the thruster. This was a clear evidence of elastic collisions between Xe^{1+} and Xe^{2+} ions. The two peaks were more sharply defined at larger angles, which implies that elastic collisions occur mostly near the thruster axis in the SPT-100 plume where the local pressure is higher. However, on the thruster axis at $R = 75$ cm, the peak for Xe^{1+} ions was very sharp, and the beginning of the peak for Xe^{2+} ions was well defined. This suggests that only ions of certain energies were involved in elastic collisions on the thruster axis at $R = 75$ cm instead of ions of all energies. Also at $R = 1$ m, the tail end of the Xe^{1+} peak was well defined at $\theta = 0^\circ$, implying less elastic collisions at $\theta = 0^\circ$ than at the other angles around the thruster axis at $R = 1$ m.

The relative height of each peak in the probe trace depended on the angular position of the probe measurement point. The Xe^{1+} peak was the dominant peak at angles -10° to 10° at all distances from the thruster. Then, the peaks for Xe^{2+} and Xe^{3+} ions increased at larger angles. This could be related to the position in the discharge chamber at which each ion species is produced. A detailed analysis of the beam energy of each ion

species along with the angular profile of ion species fractions would provide a better picture. This will be discussed in the next chapter.

Finally, the probe trace became suddenly noisy in the regions of the thruster plume -30° -10° at $R = 25$ cm and 50 cm, -30° -15° at $R = 75$ cm, and -20° $< -15^\circ$ at $R = 1$ m. The magnitude of the collector currents in these regions were well above the lowest measurable current of the picoammeter. Also, increasing or decreasing the CEM inlet voltage did not improve the probe traces. A possible source of this phenomenon is a large number of charge exchange ions in these regions that was suggested from the analysis of ion current density discussed in Chapter 4. This phenomenon became less prominent as the probe measurement points moved away from the thruster (i.e. at larger R). This could be explained by decreasing density of charge exchange ions as they move away from the thruster. The same phenomenon was observed in the cathode side of the thruster plume, but the probe traces were less noisy in the cathode side than in the non-cathode side of the plume.

Reference to Chapter 6

1 Randolph, T., Kim, V., Kaufman, H., Kozubsky, K., Zhurin, V., and Day, M., "Facility Effects on Stationary Plasma Thruster Testing," IEPC-93-093, Sept. 1993.

2 King, L.B., Ph.D. Thesis, University of Michigan, Department of Aerospace Engineering, 1998.

3 Manzella, D.H., "Stationary Plasma Thruster Plume Emissions," IEPC-93-097, Sept. 1993.

4 Gombosi, T.I., Gaskinetic Theory, Cambridge University Press, New York, 1994.

5 Kusakabe, T., Horiuchi, T., Nagai, N., Hanaki, H., and Konomi, I., "Charge Transfer of Multiply Charged Slow Argon, Krypton, and Xenon ions on Atomic and Molecular Targets. Single-Charge Transfer Cross Sections," *Journal of Physics B: Atomic and Molecular Physics*, Vol. 19, pp. 2165-2175, 1986.

CHAPTER 7

KINETIC ANALYSIS OF EXB PROBE RESULTS

7.1 Introduction

The microscopic or kinetic properties of plasma are described by one basic function, the distribution function $f(\mathbf{v}, \mathbf{r}, t)$. Macroscopic parameters such as density, temperature, and transport properties can all be derived from $f(\mathbf{v}, \mathbf{r}, t)$ by forming its moments, i.e. integrals over velocity space. Then, it is obvious that, for a multi-species plasma like the SPT-100 plume, the distribution function of each ion species is needed to fully characterize the plasma properties. Therefore, it is of great interest to obtain $f(\mathbf{v}, \mathbf{r}, t)$ of each ion species in the plasma. For a steady-state plasma such as the SPT-100 plume, one tries to find $f(\mathbf{v})$ or $f(E_i)$ at a certain position in the plasma in order to derive the macroscopic parameters.

In spite of the importance of $f(E_i)$ to kinetic theories, there are only a few direct measurements of $f(E_i)$. The most commonly used device for measuring the ion energy distribution function is retarding potential analyzers (RPA) [1]. However, the raw RPA data must be differentiated numerically to obtain the energy distribution, and thus the noise of the raw data is magnified when the resulted distribution curves are calculated. Furthermore, the RPA technique cannot distinguish different ion species in the thruster plume. A new diagnostic technique developed by King [2] gave species-dependent ion energy distributions by compiling the ion mass spectra for different ion energies. However, this indirect method of obtaining the energy distribution of each ion species resulted in poor energy resolution.

As described in Chapters 5 and 6, an **ExB** probe was used to obtain the ion energy distribution functions of each ion species in the SPT-100 plume plasma. The velocity-filtering characteristic of the **ExB** probe allowed one to scan ion energies due to the fact that the energies of the ions in the SPT-100 plume was proportional to the square of their velocities. Also, a channel electron multiplier was used to collect ions, and thus the probe's collector current was proportional to the number density of the ions. The relation between the ion energy distribution function and the **ExB** probe trace (after the abscissa of the probe I-V characteristic was converted to ion energy) was derived in Chapter 5 and repeated here for convenience:

$$f(E_i) = \frac{I_i(E_i)}{E_i^{1/2}} \quad \text{Eqn. 7-1}$$

Hence, the **ExB** probe trace represents a true ion energy distribution function.

This chapter will describe the modeling scheme of energy distribution functions based on the kinetic theory of gases. The model will be used to fit the experimental data to provide the energy distribution functions of the ions in the SPT-100 plume. Finally, several macroscopic parameters will be obtained from the fitted curves and by forming their moments.

7.2 Modeling of Ion Energy Distribution Function

The ion energy distribution function, $f(E_i)$, in the SPT-100 plume plasma has been often assumed to be a Maxwellian in the past. Although the Maxwellian fits to the experimental data are in fair agreement, there were subtle disagreements between $f(E_i)$ and their Maxwellian fits. A Maxwellian distribution represents a gas in equilibrium where the equilibrium state is achieved by collisions between particles in the gas. The

width of the distribution is determined by the average kinetic energy of the particles in the gas. In general, a Maxwellian distribution can be written as the following:

$$f(E_i) = K E_i^{1/2} \exp(-E_i), \quad \text{Eqn. 7-2}$$

where τ characterizes the width of the distribution and K is a normalization constant.

However, the energies of the ions in the SPT-100 plume are closely related to the acceleration voltages, V_i , that the ions have experienced in the discharge chamber.

Therefore, the steady-state $f(E_i)$ of the plume ions could not be attributed entirely to the collisional processes in the thruster plume. Instead, $f(E_i)$ in the thruster plume is expected to depend strongly on V_i , the potential with respect to plasma at the location where the ions are produced. The width of $f(E_i)$ would, then, depend on the spread in V_i in the discharge chamber.

Another well-known distribution function is the Druyvesteyn distribution. An example of a Druyvesteyn distribution is a steady-state electron or ion distribution function in a uniform steady electric field and with elastic collisions between the particles and neutral gas atoms [3]. In general, a Druyvesteyn distribution can be written as the following:

$$f(E_i) = K E_i^{1/2} \exp(-E_i^2). \quad \text{Eqn. 7-3}$$

Distributions of this nature are associated with significant fractions of the particle populations having their energies close to the average energy. Since the ions in the SPT-100 plume would retain the energies that they have acquired through the uniform electric field in the discharge chamber, one could imagine that the ions in the thruster plume can be considered as if they were in the influence of a uniform steady electric field.

However, the other condition for the Druyvesteyn distribution to be valid, namely the

condition that the ions and neutral atoms must collide elastically, are not met for the ions in the SPT-100 plume.

From the discussions above, the ion distribution function in the SPT-100 plume is expected to be somewhat similar to both Maxwellian and Druyvesteyn distributions. Hence, an attempt was made to model the ion energy distribution function to a distribution having the form:

$$f(E_i) = K E_i^{1/2} \exp(-E_i^{n/2}). \quad \text{Eqn. 7-4}$$

A Maxwellian distribution corresponds to an n value of 2 while a Druyvesteyn distribution corresponds to an n value of 4. This approach was also encouraged by successful modeling of the electron energy distribution function with the similar equation as Eqn. 7-4 [4, 5].

For a beam plasma, as for the ion beam in the SPT-100 plume, an elementary Galilean transformation has to be carried out in Eqn. 7-4. More precisely, the ion velocity vector, \mathbf{u}_i , has to be replaced by the velocity, $\mathbf{u}_i - \mathbf{u}_b$, in the velocity distribution function where \mathbf{u}_b is the characteristic beam velocity of the ions. This is possible because both the thermal velocity and the beam velocity of the ions are non-relativistic. The ion speed distribution for Eqn. 7-4 can be written in terms of ion speed, u_i , as:

$$f(u_i) = K' u_i^2 \exp(-u_i^n), \quad \text{Eqn. 7-5}$$

where K' and n are the corresponding parameters. The exponential factor of 2 on the u_i in Eqn. 7-5 is not obvious at a glance. One might simply replace $E_i^{1/2}$ in Eqn. 7-4 with u_i to obtain the ion speed distribution since u_i is proportional to the square root of E_i . This holds true in one dimension. However, the distribution functions are treated as three-dimensional in this modeling, and the normalization processes of three-dimensional

distribution functions result in an extra factor of u_i . Now, u_i in the exponential function in Eqn. 7-5 has to be replaced by $\mathbf{u}_i - \mathbf{u}_b$. However, for the SPT-100, the ions are accelerated by the electric field in the discharge chamber, and the variation in the ion velocity is mostly due to the variation in the acceleration voltage. Thus, it is assumed that \mathbf{u}_i and \mathbf{u}_b are parallel to each other. Then, $\mathbf{u}_i - \mathbf{u}_b$ is just $(u_i - u_b)$. After the transformation, Eqn. 7-5 becomes:

$$f(u_i) = K u_i^2 \exp\left(- (u_i - u_b)^n\right). \quad \text{Eqn. 7-6}$$

Then, Eqn. 7-4 can be rewritten for a beam plasma as the following:

$$f(E_i) = K E_i^{1/2} \exp\left(- (\sqrt{E_i} - \sqrt{E_b})^n\right). \quad \text{Eqn. 7-7}$$

Again, the three-dimensional nature of the distribution functions results in a factor of 1/2 on the E_i that is not so obvious. This necessary transformation introduced a limitation for the modeling scheme. Notice that $(\sqrt{E_i} - \sqrt{E_b})$ can be both positive and negative, and thus the model can produce real number solutions only when n is an integer. Therefore, an assumption was made that the velocity distribution function, $f(\mathbf{u}_i)$, is symmetric around \mathbf{u}_b . Then, Eqn. 7-7 can be rewritten as:

$$f(E_i) = K E_i^{1/2} \exp - \left(\left| \sqrt{E_i} - \sqrt{E_b} \right| \right)^n. \quad \text{Eqn. 7-8}$$

Combining it with Eqn. 7-1, the \mathbf{ExB} probe traces were modeled as the following equation:

$$I_i(E_i) = K_0 + K_1 E_i \exp - \left(\left| \sqrt{E_i} - \sqrt{E_b} \right| \right)^n, \quad \text{Eqn. 7-9}$$

where K_0 , K_1 , σ , E_b , and n are fitting parameters.

Each peak of the measured **ExB** probe traces was curve-fitted using Eqn. 7-9. Fitting was accomplished by the computer application, Igor, which uses a Levenberg-Marquardt algorithm to search for the fitting parameters. A Levenberg-Marquardt algorithm is a form of non-linear least-squares fitting that minimizes chi-square. Chi-square is defined as:

$$\text{chi - square} = \sum_i \frac{(y - y_i)^2}{\sigma_i^2}, \quad \text{Eqn. 7-10}$$

where y is the fitted value, y_i is the value of the original data, and σ_i is the standard deviation for that point.

Figure 7-1 shows a typical fit of Eqn. 7-9 to the experimental data. It demonstrates that the model produced a fitted curve with an n value of 3.3 which agreed very well with the measured probe trace. Notice that this n value lies between 2 and 4, the values for a Maxwellian distribution and a Druyvesteyn distribution, respectively. Figure 7-1 also shows that the model deviates from the measured data at low and high energies. This can be seen more clearly in Figure 7-2, which shows the measured probe trace and the sum of the fitted curves of Xe^{1+} , Xe^{2+} , Xe^{3+} , and Xe^{4+} ions. The comparison in Figure 7-2 shows exceptional agreement in the upper part of the peaks. However, the curve-fits do not agree with the experimental data at low energy (~ 200 eV) and in the regions between the peaks. The disagreement at low energy ($E_i < 220$ eV) may be due to significant ion production downstream of the main ion production region which results in low energy ions. It may also be due to charge exchange collisions with neutral atoms, which also produce low energy ions. The disagreement in the regions between the peaks can be attributed to elastic collisions between the particles of the two ion species that the peaks represent. As discussed in Chapter 6, Section 2.2, the effect of elastic collisions

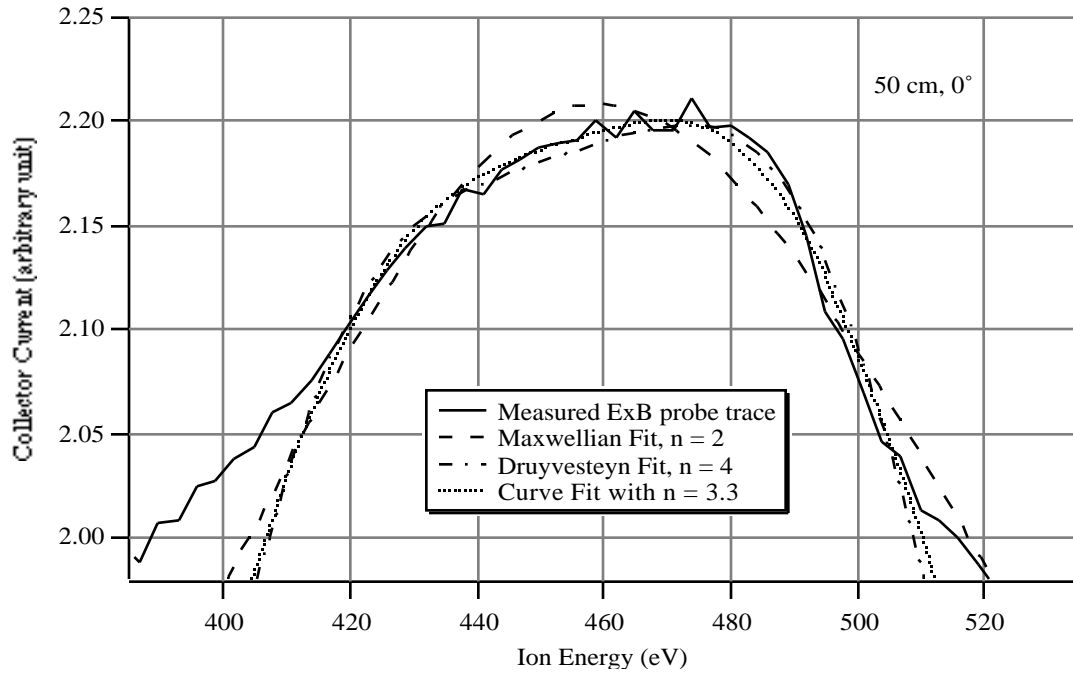


Figure 7-1 Comparisons between the Maxwellian fit, Druyvesteyn fit, and curve-fit of Eqn. 7-9 to the Xe^{2+} ion peak of the measured ExB probe trace on the thruster axis at 50 cm from the thruster exit.

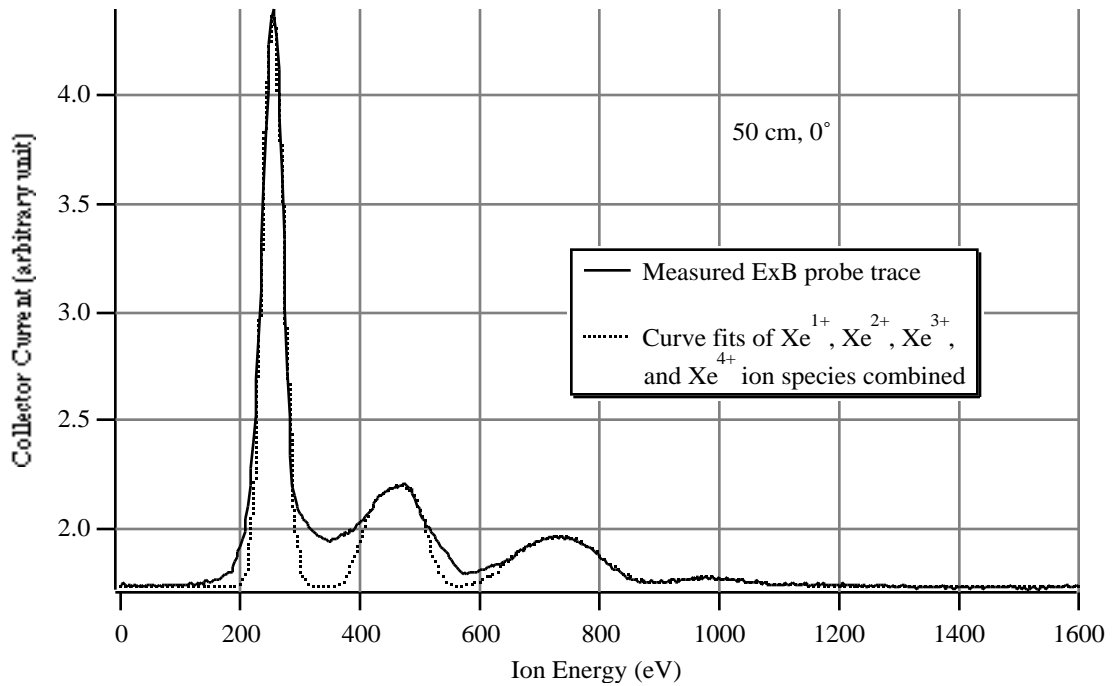


Figure 7-2 Sum of the curve fits of Eqn. 7-9 for Xe^{1+} , Xe^{2+} , Xe^{3+} , and Xe^{4+} ion peaks overlaid on the measured ExB probe trace on the thruster axis at 50 cm from the thruster exit.

manifest themselves in the probe trace as highly overlapped regions between the peaks representing the two ion species. For example, the overlapped region between the first peak (representing Xe^{1+} ions) and the second peak (representing Xe^{2+} ions) is the result of elastic collisions between Xe^{1+} ions and Xe^{2+} ions. Then, the fitted curves can be thought to represent the “pre-collision” distributions. As such, the peak height of the fitted curve must be lower than the true pre-collision distribution functions because the population of ions that have undergone elastic collisions shifts towards the region between the peaks.

In summary, the energy distribution function of the ions in the SPT-100 plume was modeled as the function in Eqn. 7-8, and the peaks in the measured ExB probe traces were curve-fitted using Eqn. 7-9. The model was limited to the distribution functions where $f(\mathbf{u}_i)$ was symmetric around \mathbf{u}_b . This was due to the necessary Galilean transformation for beam plasmas. Another limitation of the model was its inability to

predict the elastic collisions between the ion species. Also, the model underestimated the population of the low energy ions ($E_i < 220$ eV) which may be produced as a result of charge exchange collisions. The model would improve if it was incorporated with a scheme for predicting elastic collisions and charge exchange collisions. Such a scheme requires cross sections involving multiply charged xenon ions, all of which have not been found in the literature. However, it is evident, from the excellent agreement shown in the upper part of the peaks, that this simple model can produce pre-collision distribution functions very well.

7.3 Curve-Fit Results and Discussions

Each peak of the measured **ExB** probe traces shown in Chapter 6 was fitted using Eqn. 7-9, and the energy distribution functions were obtained as Eqn. 7-8. From the fitting parameters, E_b and n (the exponential factor) were found for each ion species at various locations in the SPT-100 plume. The spread in the acceleration voltage was calculated from the width of the distribution functions. Finally, a rough estimates of ion species fractions were calculated by integrating the distribution functions.

Recall from Chapter 6 that the peak for Xe^{4+} ions in the probe traces were clearly identifiable within ± 10 degrees off thruster axis, but were obscured by the probe current due to the entrained background gases of N^{2+} and O^{2+} ions at larger angle off thruster axis. Furthermore, a preliminary calculations of ion fractions showed that the fractions of Xe^{4+} ions were less than 0.005 (less than the uncertainty in the calculated ion fractions). Therefore, although the **ExB** probe measurements clearly showed the existence of Xe^{4+} ions in the SPT-100 plume, the plume ions were assumed to consist of Xe^{1+} , Xe^{2+} , and Xe^{3+} ions, and the results being discussed later in this chapter will only include these three ion species.

The errors in E_b and n were conservatively estimated from the errors in the fitting parameters in the curve-fits, which were calculated by computer as the standard deviation for the fitting parameters. The errors in the other reported data were calculated from the errors in the fitting parameters of the curve-fits. These curve-fit errors were, then, added to the **ExB** probe measurements error estimated in Chapter 5, Section 5. As mentioned in Chapter 5, the uncertainties in the measurement positions (i.e. the angles off the thruster axis and the axial distances from the center of the thruster exit) were 3 degrees in the rotational direction and 5 mm in the axial direction.

As in Chapter 6, “R” will be used to denote the probe distance from the thruster center, and “ θ ” will be used to denote the probe angle with respect to the thruster axis. Also, recall that the positive θ represents the probe data in the cathode side of the thruster plume while the negative θ represents the probe data in the non-cathode side of the thruster plume. The following subsections will discuss each of the ion parameters found from the curve-fits.

7.3.1 Exponential Factor n of the Ion Energy Distribution Functions

As can be seen from Eqn. 7-8, the value of n indicates how much the distribution is Maxwellian-like or Druyvesteyn-like, where $n = 2$ corresponds to a Maxwellian distribution and $n = 4$ corresponds to a Druyvesteyn distribution. Figure 7-3 through Figure 7-6 show the variations of n value with respect to angle off thruster axis at $R = 25$ cm, 50 cm, 75 cm, and 1 m.

The figures show that most of the ion species distribution functions were somewhere between a Maxwellian and a Druyvesteyn distribution. This result supports the modeling premise that the ion distribution function in the SPT-100 plume would be somewhat similar to both Maxwellian and Druyvesteyn distributions. Then, one determining factor of the nature of the ion distribution function in the SPT-100 plume is

the competing effect of the ion acceleration in the discharge chamber and the collisional processes beyond the ion production zone. The former (i.e. the influence of the uniform steady electric field) drives the ions towards a Druyvesteyn distribution, and the latter drives the ions towards a Maxwellian distribution.

The distribution functions for Xe^{1+} ions were closer to Maxwellian than those for other ion species at all R. Recall that a Maxwellian distribution represents a gas in equilibrium where the equilibrium state is achieved by collisions between particles in the gas. The collision probability in a given gas increases with increasing number density and decreases with increasing kinetic energy of the ions [6]. The measured $\mathbf{E} \times \mathbf{B}$ probe traces in Chapter 6 showed that there were more of Xe^{1+} ions than the other ion species in the SPT-100 plume. Also, the Xe^{1+} ions have the least kinetic energy compared with the other ion species. This is because the ions experience similar acceleration voltage in the discharge chamber, and thus the multiply charged ions gain more kinetic energy due to their higher charge state. Therefore, the Xe^{1+} ions are expected to undergo more collisions than the other ion species in the thruster plume. This explains why their distribution functions were closer to Maxwellian than the other ion species.

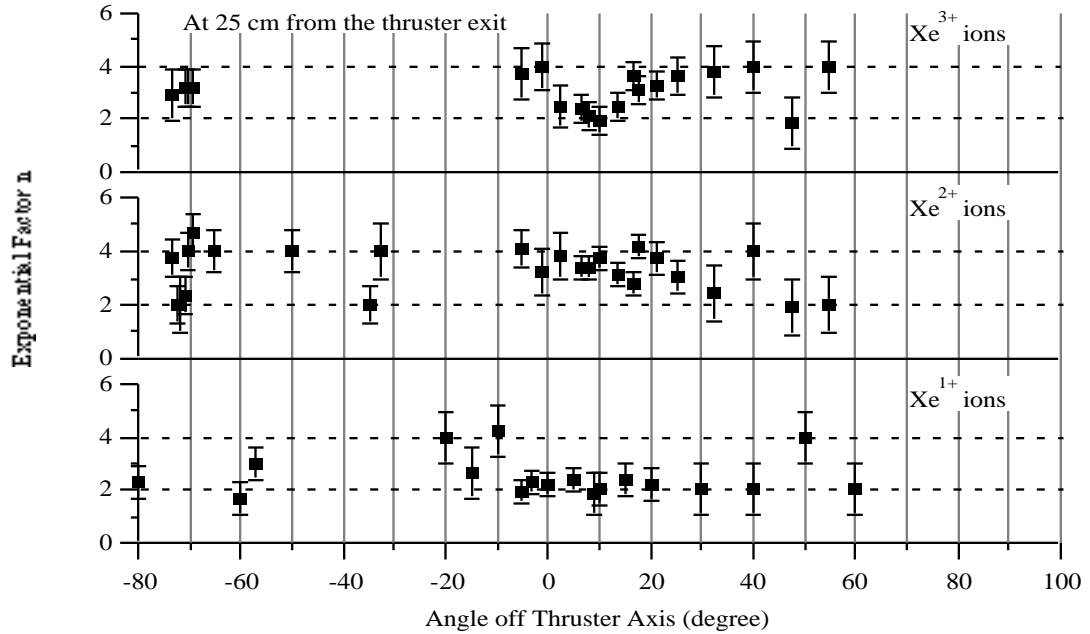


Figure 7-3 Exponential factor n for Xe^{1+} , Xe^{2+} , and Xe^{3+} ions energy distribution functions obtained from the curve-fits of the ExB probe data at 25 cm from the thruster exit.

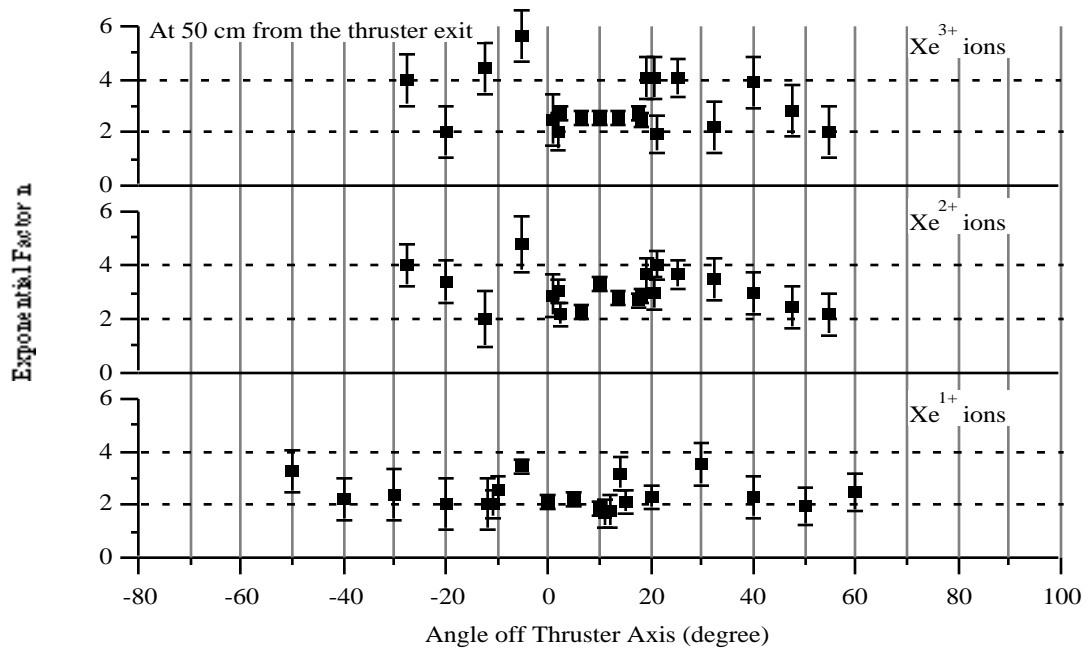


Figure 7-4 Exponential factor n for Xe^{1+} , Xe^{2+} , and Xe^{3+} ions energy distribution functions obtained from the curve-fits of the ExB probe data at 50 cm from the thruster exit.

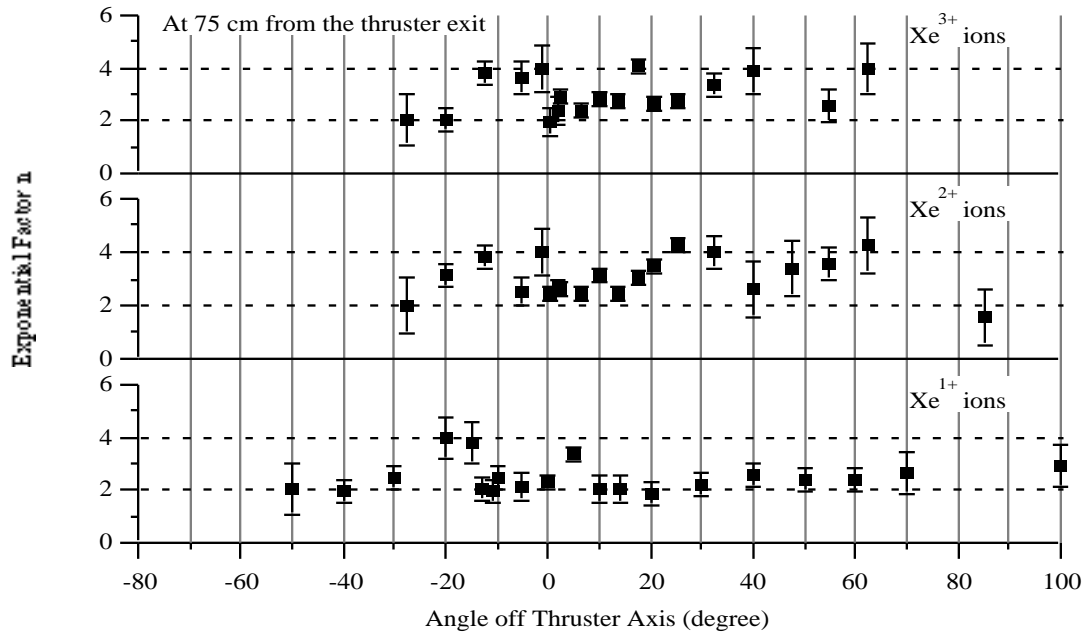


Figure 7-5 Exponential factor n for Xe^{1+} , Xe^{2+} , and Xe^{3+} ions energy distribution functions obtained from the curve-fits of the ExB probe data at 75 cm from the thruster exit.

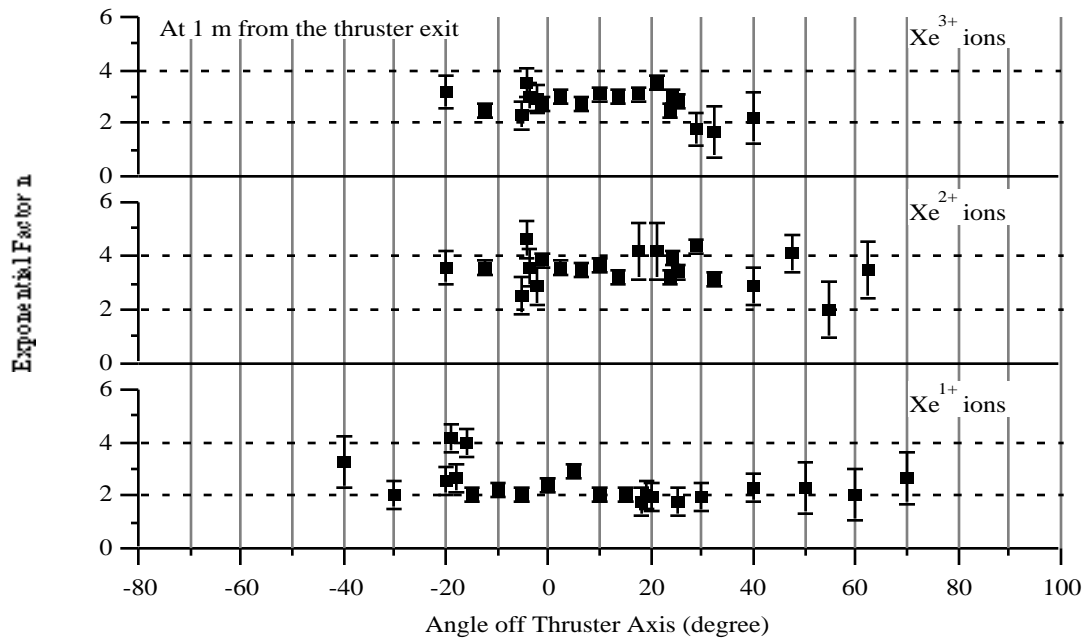


Figure 7-6 Exponential factor n for Xe^{1+} , Xe^{2+} , and Xe^{3+} ions energy distribution functions obtained from the curve-fits of the ExB probe data at 1 m from the thruster exit.

Note that the above discussion did not include the elastic collisions, evidence of which were seen in the measured \mathbf{ExB} probe traces (See Chapter 6). This is due to the inability of the model to predict collisional processes in the thruster plume. Strong evidence of elastic collisions were seen in the probe traces, especially between Xe^{1+} ions and Xe^{2+} ions near the thruster axis (-20° to 20°) at all R. Then, the actual distribution functions would be closer to Maxwellian than the results shown above since the collisional processes drive the ions towards Maxwellian.

7.3.2 Beam Energy E_b

The beam energies E_b were obtained from the curve-fits of the \mathbf{ExB} probe traces as one of the fitting parameters. Each E_b represents the most probable ion energy of that species at that measurement point in the thruster plume. As mentioned earlier, the ions in the SPT-100 plume would retain the energies that they have acquired through the uniform electric field in the discharge chamber (i.e. the acceleration voltage V_i). Since E_i is proportional to V_i via relation $E_i = q_i \cdot V_i$, E_b provides the most probable acceleration voltage for the ions. Then, if the electric field in the discharge chamber were mapped, the E_b data could reveal an approximate location of the primary ion production for each ion species.

The E_b data at $R = 25$ cm were expected to represent V_i most closely, compared to the data at other R, simply because they were measured closest to the thruster, so that the ions at $R = 25$ cm had suffered the least collisions in the thruster plume. Figure 7-7 shows the angular profiles of E_b / q_i of Xe^{1+} , Xe^{2+} , and Xe^{3+} ions at $R = 25$ cm. For the most part, E_b / q_i lied between 200 eV and 260 eV. The overall shapes of the profiles were similar for all three ion species, which have a peak structure around the thruster axis within -20° to 30° . But the top of the peak within -10° to 10° for Xe^{2+} ions was fairly flat, and the peak for Xe^{3+} ions was somewhat between that for Xe^{1+} ions and that

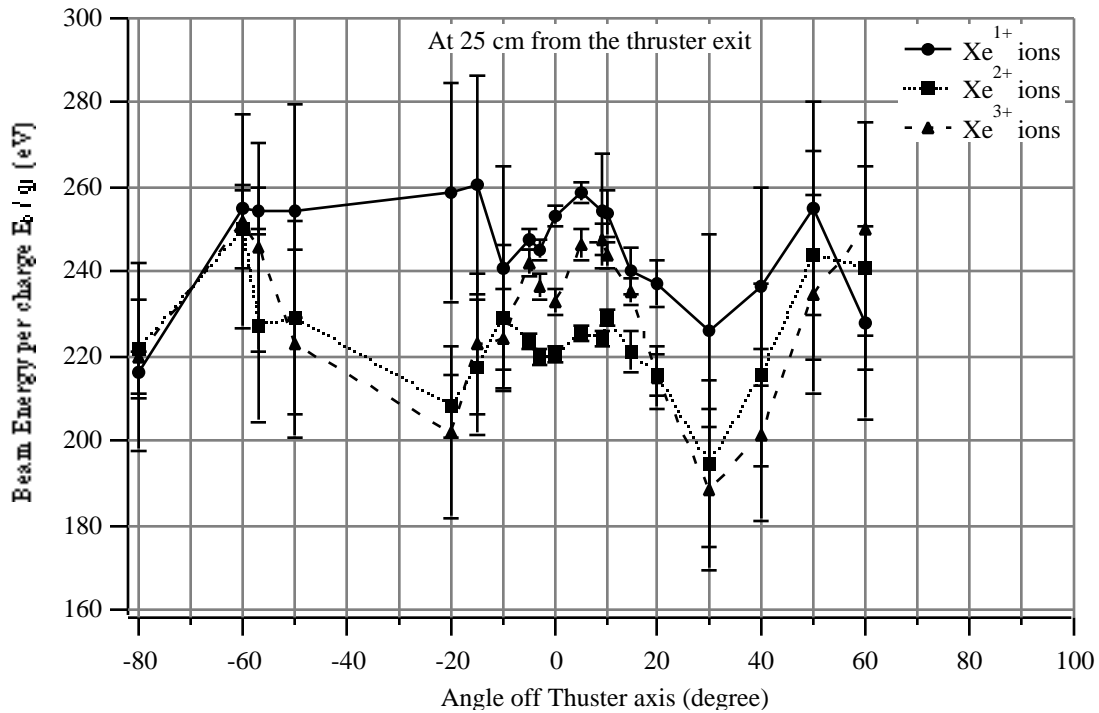


Figure 7-7 Angular profiles of beam energy per charge of Xe¹⁺, Xe²⁺, and Xe³⁺ ions in the SPT-100 plume at 25 cm from the thruster exit.

for Xe²⁺ ions. The peak E_b / q_i for Xe¹⁺ ions within this region was 258 eV at $\theta = 5^\circ$. This peak is 86% of the discharge voltage (300 V), which is what is expected for a well-developed Hall thruster [7]. The average E_b / q_i for Xe¹⁺ ions was approximately 245 eV which corresponds to an average ion speed of 19 km/s. This value is about 18% higher than the value a previous study has determined [8]. The peak E_b / q_i in this region was 229 eV at $\theta = 10^\circ$ for Xe²⁺ ions and 247 eV at $\theta = 5^\circ$ for Xe³⁺ ions. Thus, the peak E_b / q_i occurred a little bit off to the cathode side of the thruster plume. This peak structure around the thruster axis gives an insight into the acceleration mechanism in the discharge chamber. Barring the collisions with other particles, an ion can exit the thruster only if it does not hit the discharge chamber wall before it reaches the thruster exit. Since the ion Larmor radius is large in the discharge chamber of the SPT-100, the trajectory of the ions

can be considered straight lines. Therefore, in order for an ion to exit the thruster, the angle of the ion's velocity vector with respect to the thruster axis must decrease as the ion

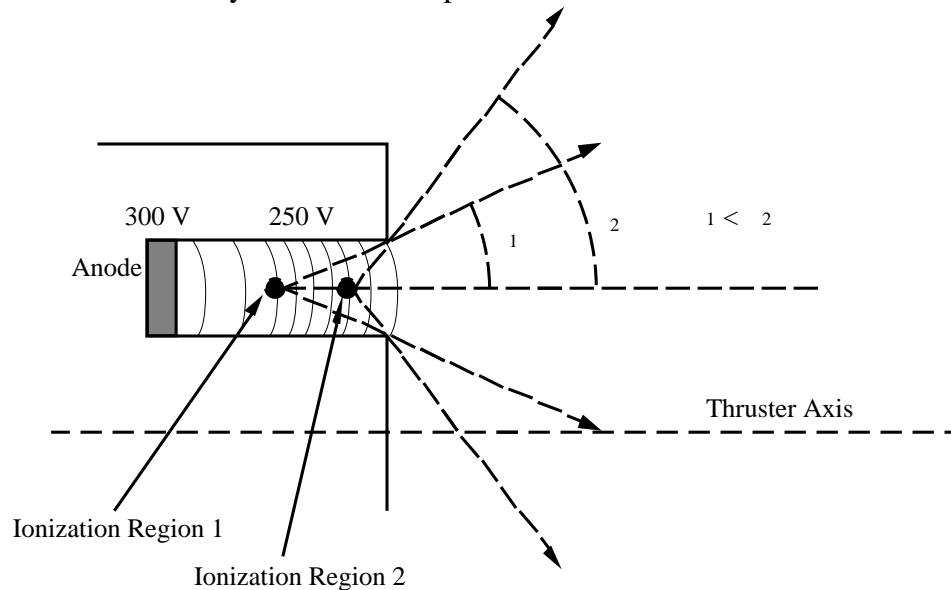


Figure 7-8 Schematic showing the relationship between the location of ionization and the possible angle of ion velocity vector with respect to the thruster axis. It shows that the possible exit angle of ion velocity vector increases as the location of ionization moves downstream in the thruster discharge chamber. Also shown is a schematic of the electric field line in the discharge chamber formed between the cathode and the anode.

production occurs farther upstream in the discharge chamber. In other words, as the ions are produced in the region closer to the thruster exit, they can exit the thruster at larger θ . This is shown schematically in Figure 7-8, which also shows an approximate lines of the electric field in the discharge chamber formed between the cathode and the anode (i.e. the discharge voltage). One can see from Figure 7-8 that the ions produced in Ionization Region 1 will be accelerated through a larger electric field and gain more energy than the ions produced in Ionization Region 2. Then, E_b / q_i for the ions produced in Region 1 will be higher than that for the ions produced in Region 2. Consequently, the ions which are produced upstream in the discharge chamber have larger E_b / q_i and are detected by the probe at small θ . The ions which are produced near the exit of the discharge chamber have smaller E_b / q_i and can be detected by the probe at small or large θ . Thus, E_b / q_i

should decrease or stay the same with increasing angle off thruster axis. E_b / q_i for Xe^{1+} ions in Figure 7-7 decreased from the peak value at $\theta = 5^\circ$ with increasing angle off thruster axis, and had no flat part at the top of the peak. This implies that the Xe^{1+} ions were created far upstream in the discharge chamber, and continued to be created in the downstream region of the discharge chamber. On the other hand, E_b / q_i for Xe^{2+} ions had a peak with flat top between $\theta = -10^\circ$ and 10° . This suggests that the Xe^{2+} ions were created more downstream in the discharge chamber. The peak for Xe^{3+} ions was in between the peaks for Xe^{1+} ions and Xe^{2+} ions, both qualitatively and quantitatively. This implies that the Xe^{3+} ions were created somewhere upstream of where the Xe^{2+} ions were first produced but downstream of early Xe^{1+} ion production region, and continued to be created in the downstream region.

E_b / q_i outside the region -20° to 30° seems to behave contrary to the acceleration mechanism discussed above where it increased with increasing angle off thruster axis. This discrepancy between the experimental data and the proposed acceleration mechanism is believed to be due to the noisy probe traces at these measurement points on which the curve-fits were performed to obtain E_b . Figure 6-2 through Figure 6-6 show that the probe traces outside the region -20° to 30° had high noise-to-signal ratios. Thus, the uncertainty in the obtained E_b was as large as the error bars in Figure 7-7 indicates.

As discussed above, the analysis of the peak structure of E_b / q_i , along with the proposed acceleration mechanism, suggested that the multiply charged ions were produced downstream of the region where the singly charged ions were produced earlier, and thus had less E_b / q_i than the singly charged ions. To view this more clearly, E_b / q_i for the singly charged ions was subtracted from E_b / q_i for the multiply charged ions at each measurement point, denoted as $\Delta(E_b / q_i)$, and is shown in Figure 7-9.

$\Delta(E_b / q_i) = 0$ eV indicates that the E_b / q_i of the ion species have the same E_b / q_i of the Xe^{1+} ions, and the negative value of $\Delta(E_b / q_i)$ indicates that the ion species have lower E_b / q_i than the Xe^{1+} ions. In fact, Figure 7-9 shows that E_b / q_i for Xe^{2+} and Xe^{3+} ions

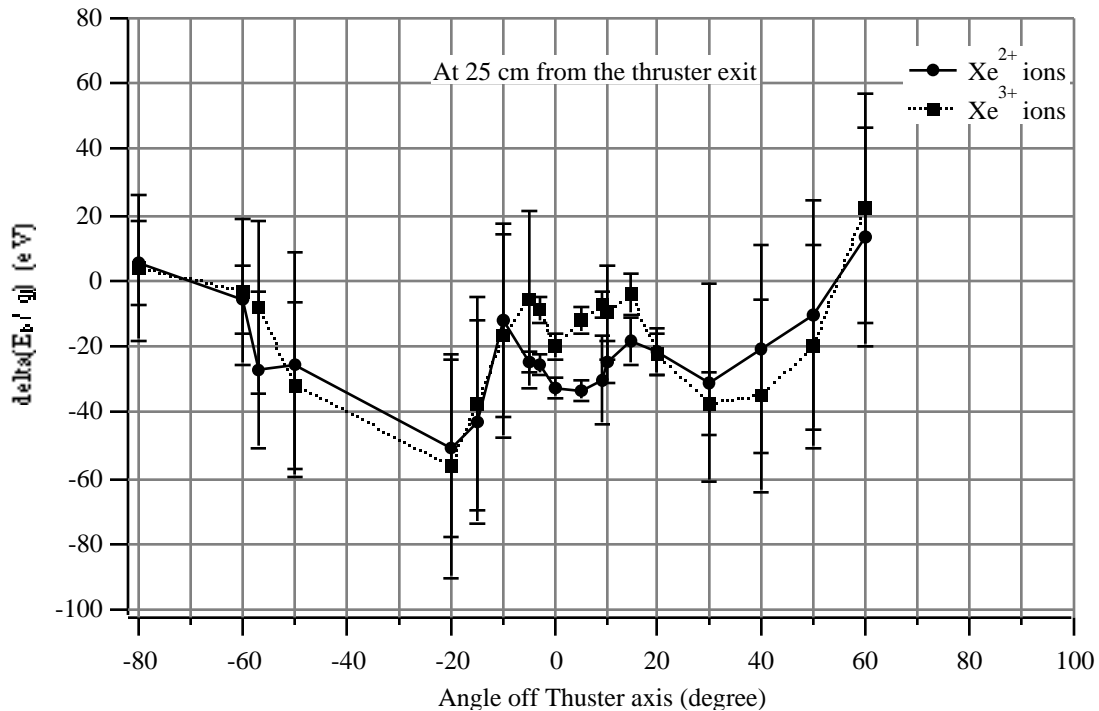


Figure 7-9 Angular profiles of the differences in beam energy per charge between Xe^{2+} and Xe^{1+} ions and between Xe^{3+} and Xe^{1+} ions in the SPT-100 plume at 25 cm from the thruster exit.

were almost always lower than E_b / q_i for Xe^{1+} ions. Figure 7-9 also shows downward peaks around the thruster axis for both Xe^{2+} and Xe^{3+} ions. The angular location of this downward peak coincided with the E_b / q_i peak around the thruster axis seen in Figure 7-7. These downward peaks are a result of the flat-top-peak of E_b / q_i for Xe^{2+} ions and Xe^{3+} ions. E_b / q_i for Xe^{1+} ions kept decreasing with increasing while the E_b / q_i for Xe^{2+} and Xe^{3+} ions remained fairly constant within -10° 10° .

An insight into the ionization mechanism is possible through the result of lower E_b / q_i for the multiply charged ions. A previous study revealed that the electron temperature in the discharge chamber of a Hall thruster attains a maximum in the region

of highest magnetic field strength, which occurs near the thruster exit [9]. It estimated the value of the maximum electron temperature to be approximately 25 eV for SPT-100 type thrusters. The ionization rate is also the highest in this region. A plasma model in the Hall thruster discharge chamber showed a similar results [10]. The very-near-field plume study in Chapter 3 showed the maximum electron temperature of 8.3 eV in front of the discharge chamber 10 mm downstream of the thruster exit (cf. Figure 3-6). The first, second, and third ionization potentials of a xenon atom are 12.13 eV, 21.21 eV, and 32.1 eV, respectively [11]. Then, the energy required for direct ionization by electron impact is 12.13 eV for Xe^{1+} ions, 33.3 eV for Xe^{2+} ions, and 65.4 eV for Xe^{3+} ions. Therefore, Xe^{1+} ions can be produced upstream of the region of the maximum electron temperature. On the other hand, it would be difficult for the direct ionization of Xe^{2+} or Xe^{3+} ions to occur even in the region of maximum electron temperature. A more plausible scenario is that the multiply charged ions are created from the singly charged ions by subsequent collisions with high energy electrons. Since the ions in the discharge chamber move towards the thruster exit, this implies that the multiply charged ions will be created downstream of the region where singly charged ions are created. As a result, these ions would experience less acceleration voltage and have smaller E_b / q_i than the singly charged ions. Hence, it reaches to the same conclusion of the analysis of E_b / q_i and the acceleration mechanism.

By the same argument, the triply charged ions would have smaller E_b / q_i than the doubly charged ions, but E_b / q_i for Xe^{2+} ions was almost always lower than that of Xe^{3+} ions. One possible explanation is that Xe^{2+} ions, after they are created for the first time, undergo various collisions and subsequent ionization. These ions will have smaller E_b / q_i because they are created downstream of the region of original ionization. This phenomenon will not affect Xe^{3+} ions as much as it affects Xe^{2+} ions since the collision probability increases with increasing particle density, and there are substantially more Xe^{2+} ions than Xe^{3+} ions. (A preliminary ion fraction calculation showed that the fraction

of Xe^{2+} ions is four times the fraction of Xe^{3+} ions.) In any case, the formation of multiply charged ions must involve complicated processes.

In summary, the basic ionization and acceleration mechanism based on the E_b / q_i data is as follows. Xe^{1+} ions are produced throughout the discharge chamber from near the anode to near the thruster exit. Since the energy required for direct ionization of Xe^{2+} or Xe^{3+} ions is high, the multi-step ionization is favored where the multiply charged ions are produced from the singly charged ions by subsequent collisions with high energy electrons. Consequently, Xe^{2+} and Xe^{3+} ions are created in the downstream region of the discharge chamber. The ions that are created in the upstream region in the discharge chamber have high ion beam energy, and can exit the thruster only at small angles off thruster axis. The ions that are created in the downstream region in the discharge chamber have low ion beam energy, and can exit the thruster at small or large angles off thruster axis. This ionization and acceleration mechanism was able to explain the experimental data very well for the thruster plume region of -20° to 30° , but the behavior of E_b / q_i outside of this region did not follow the proposed mechanism. This discrepancy is believed to stem from the inaccuracy of the experimental data in this region, where the observed signal-to-noise ratio of the probe traces was large. Another discrepancy is that the triply charged ions had higher E_b / q_i than the doubly charged ions, which contradicts the proposed ionization mechanism. One possible explanation is that Xe^{2+} ions undergo various collisions and subsequent ionization after they are created for the first time, and thus have lower E_b / q_i than they would have if they had not undergone collisions. Since the number of Xe^{2+} ions were approximately four times the number of Xe^{3+} ions from a preliminary ion fraction calculation, the collision probability for Xe^{2+} ions would be much higher than that for Xe^{3+} ions. Hence, this phenomenon would not affect Xe^{3+} ions as much as it affects Xe^{2+} ions. The formation of multiply charged ions must be complicated involving such processes as ions colliding with the chamber wall, elastic collisions with other ions, charge exchange collisions with neutral atoms and other

ions, and subsequent ionization, especially when a substantial number of the ions exists so that the collision probability is significant. It should be noted here that the trajectories of the ions in the discharge chamber are, in reality, parabola-like rather than straight lines. This will be explained later in the discussion of ion species fractions.

Figure 7-10 shows the angular profiles of E_b / q_i of Xe^{1+} , Xe^{2+} , and Xe^{3+} ions at $R = 50$ cm, and Figure 7-11 shows $\Delta(E_b / q_i)$ for Xe^{2+} and Xe^{3+} ions at $R = 50$ cm. The two figures show that E_b / q_i and $\Delta(E_b / q_i)$ at $R = 50$ cm have similar angular profiles and values to the data at $R = 25$ cm. E_b / q_i lied between 200 eV and 260 eV. There is a peak structure around the thruster axis between $\theta = -20^\circ$ and 20° even though the peak is less defined in the cathode side of the thruster plume than the peak seen in the data at $R = 25$ cm. The peak E_b / q_i within this peak structure was 253 eV at $\theta = 0^\circ$ for Xe^{1+} ions, 230 eV at $\theta = -5^\circ$ for Xe^{2+} ions, and 244 eV at $\theta = -5^\circ$ for Xe^{3+} ions. These peak values differ from the corresponding values at $R = 25$ cm by 1 to 5 eV which is within the experimental uncertainty. Therefore, the peak value of E_b / q_i have not changed as the ions moved from $R = 25$ cm to $R = 50$ cm. As with the data at $R = 25$ cm, E_b / q_i for Xe^{1+}

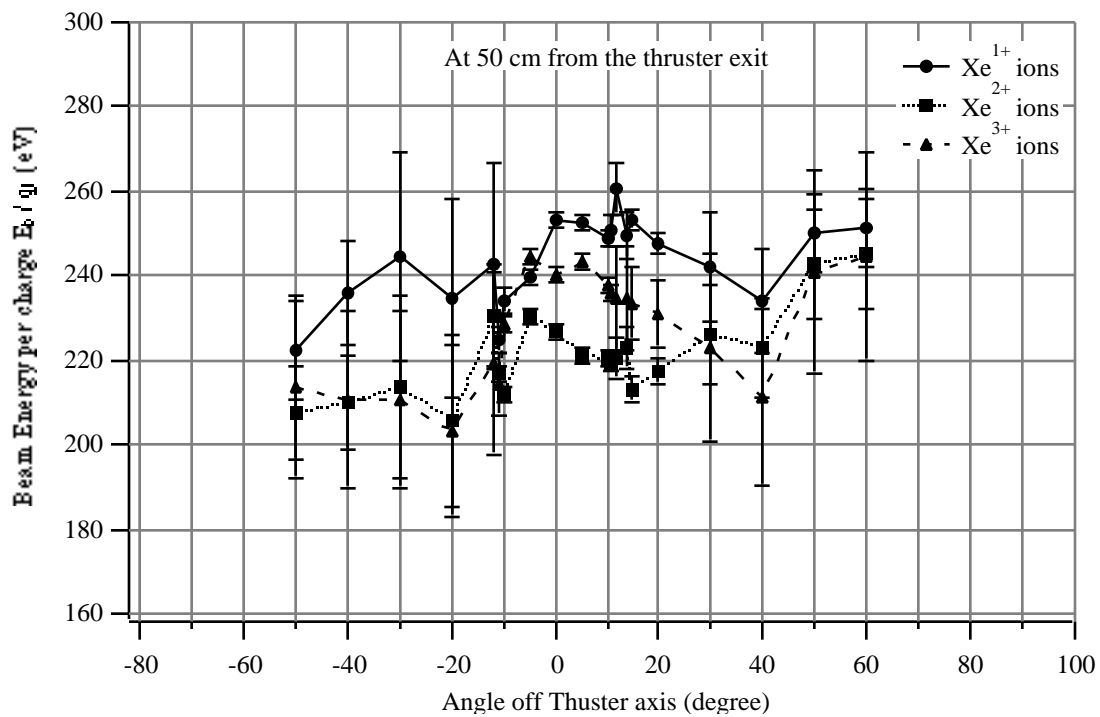


Figure 7-10 Angular profiles of beam energy per charge of Xe^{1+} , Xe^{2+} , and Xe^{3+} ions in the SPT-100 plume at 50 cm from the thruster exit.

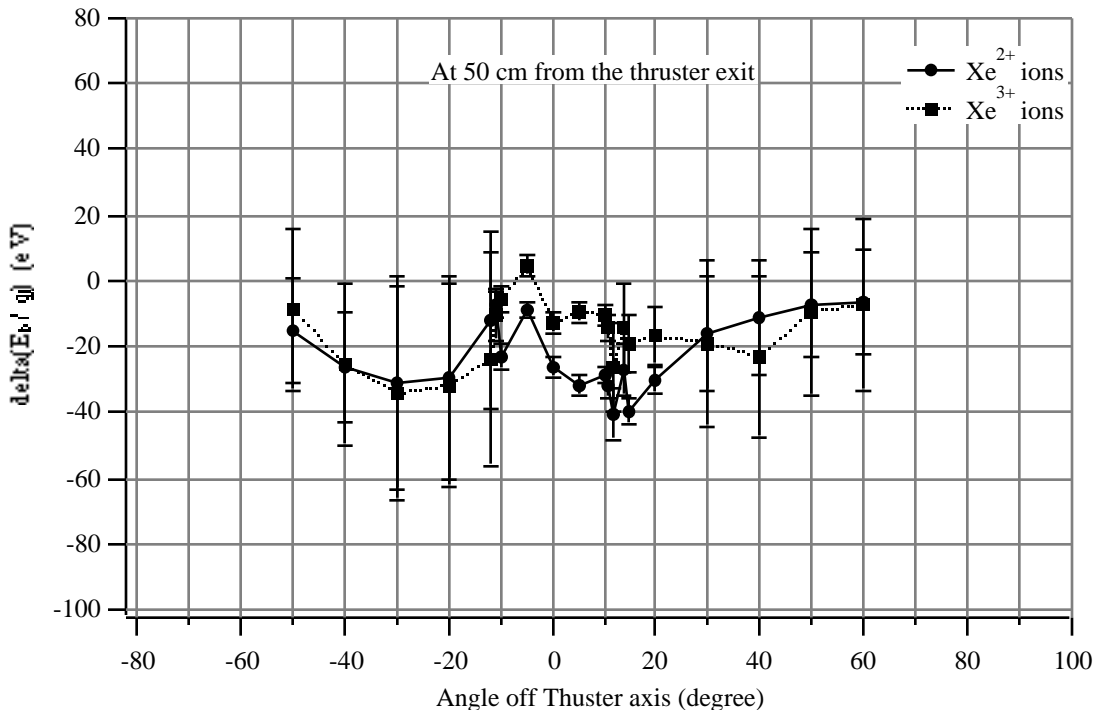


Figure 7-11 Angular profiles of the differences in beam energy per charge between Xe²⁺ and Xe¹⁺ ions and between Xe³⁺ and Xe¹⁺ ions in the SPT-100 plume at 50 cm from the thruster exit.

ions was the highest at almost all measurement points, and E_b / q_i for Xe²⁺ ions was almost always lower than that of Xe³⁺ ions.

Overall, the angular profiles of E_b / q_i at $R = 50$ cm were more level when compared to the data at $R = 25$ cm. This can be attributed to elastic and charge exchange collisions occurring in the thruster plume, which change ion energies and randomize the direction of ion velocities. As an example, the probability of charge exchange collisions between Xe¹⁺ ions and neutral xenon atoms will be roughly estimated. The charge exchange collision cross section for Xe¹⁺ -- Xe can be calculated according to:

$$\sigma_c = (-k_1 \ln v + k_2)^2 \times 10^{-16} \text{ cm}^2, \quad \text{Eqn. 7-11}$$

where $k_1 = 0.8821$, $k_2 = 15.1262$, and v is the average relative inter-particle speed in m/s [12]. The v is assumed to be 19 km/s ($E_i = 245$ eV) with negligible speed of the neutrals. Assuming that the neutral xenon atoms are at the ambient temperature of 300 K and at the ambient background pressure of 1.6×10^{-2} Pa (1.2×10^{-4} Torr.), and using the ideal gas law, the mean free path is approximately 60 cm. The fraction of ions which undergo a collision of the mean free path within a path length s is given by [13]:

$$P_{\text{coll}}(s) = 1 - \exp(-s / \lambda). \quad \text{Eqn. 7-12}$$

Eqn. 7-12 shows that about 34% of the ions exiting the thruster have undergone a charge exchange collision at $R = 25$ cm. This value increases to 56% at $R = 50$ cm, 71% at $R = 75$ cm, and 81% at $R = 1$ m. These numbers are only rough estimates, and in reality, the ions will suffer different kinds of collisions with other particles. However, the numbers above demonstrates that the effect of these collisions on the ions cannot be ignored.

Figure 7-12 shows the angular profiles of E_b / q_i of Xe^{1+} , Xe^{2+} , and Xe^{3+} ions at $R = 75$ cm, and Figure 7-13 shows $\Delta(E_b / q_i)$ for Xe^{2+} and Xe^{3+} ions at $R = 75$ cm.

Again, E_b / q_i lied between 200 eV and 260 eV. The angular profiles of E_b / q_i at $R = 75$ cm became more level than the data at $R = 25$ cm, which can, again, be attributed to elastic and charge exchange collisions occurring in the thruster plume. There was no longer a definable peak structure around the thruster axis as there were in the data at $R = 25$ cm and 50 cm. Similar to the data at $R = 25$ cm and 50 cm, E_b / q_i for Xe^{1+} ions was the highest at almost all measurement points, and E_b / q_i for Xe^{2+} ions was almost always lower than that of Xe^{3+} ions. $\Delta(E_b / q_i)$ was similar to the data at $R = 50$ cm, except near $\theta = 0^\circ$. This is mainly due to a curious local minimum of E_b / q_i for Xe^{1+} ions at $\theta = 0^\circ$. Xe^{2+} ions had a local maximum of E_b / q_i at the same point in the thruster plume. Recall from Chapter 6, Section 5 and Figure 6-12 that the peak for Xe^{1+} ions in the probe trace at $\theta = 0^\circ$ was very sharp, and that the beginning of the peak for Xe^{2+} ions was highly

defined compared to those peaks at other . Also, a small peak could be seen near the tail end of the peak for Xe^{1+} ions at 269 eV. The origin of this peak is not known, but it is certain that the curious local maximum and minimum of E_b / q_i mentioned above are consequences of the unusual characteristics of Xe^{1+} and Xe^{2+} ion peaks seen in the probe trace at $\theta = 0^\circ$, $R = 75$ cm.

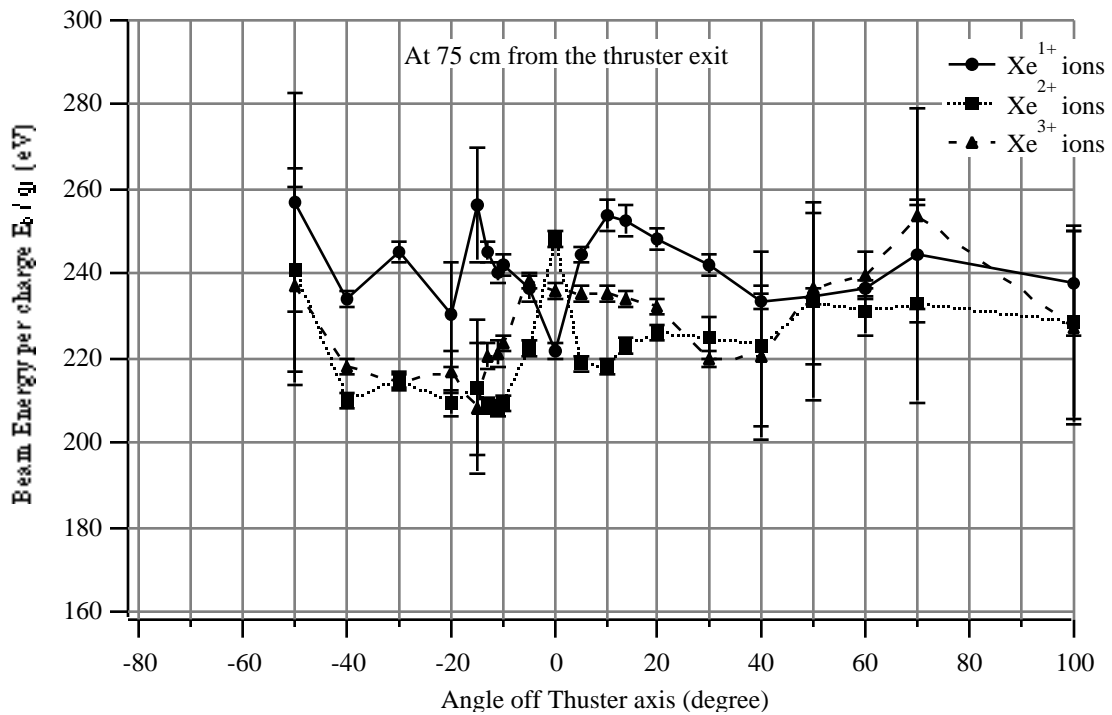


Figure 7-12 Angular profiles of beam energy per charge of Xe^{1+} , Xe^{2+} , and Xe^{3+} ions in the SPT-100 plume at 75 cm from the thruster exit.

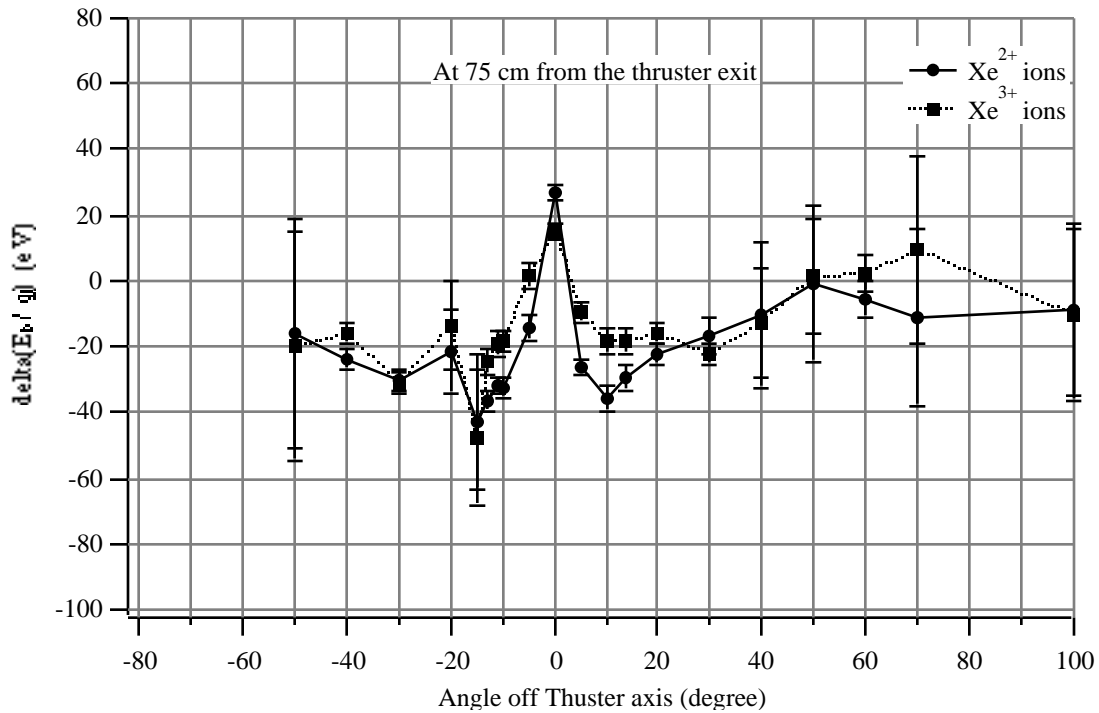


Figure 7-13 Angular profiles of the differences in beam energy per charge between Xe^{2+} and Xe^{1+} ions and between Xe^{3+} and Xe^{1+} ions in the SPT-100 plume at 75 cm from the thruster exit.

Figure 7-14 shows the angular profiles of E_b / q_i of Xe^{1+} , Xe^{2+} , and Xe^{3+} ions at $R = 1$ m, and Figure 7-15 shows $\Delta(E_b / q_i)$ for Xe^{2+} and Xe^{3+} ions at $R = 1$ m. Similarly to the data at other R , E_b / q_i lied between 200 eV and 260 eV. The angular profiles of E_b / q_i at $R = 1$ m was again more level than the data at $R = 25$ cm, which can, again, be attributed to collisional processes occurring in the thruster plume. But, the angular profile of E_b / q_i did not become more level from the data at $R = 50$ cm to the data at $R = 75$ cm and 1 m. This may be because the collision probability decreases with increasing distance from the thruster. Recall that the ions ejected from a Hall thruster follow diverging velocity vectors with respect to the thruster axis [8, 14]. Therefore, the number density of the ions decreases, thus decreasing the collision probability, as they move away from the thruster. There seems to be a peak structure of E_b / q_i for Xe^{2+} ions between $\theta = -16^\circ$ and 10° , but the data for Xe^{1+} ions and Xe^{3+} ions had no definable peak

structure. As in the data at other R, E_b / q_i for Xe^{1+} ions was the highest at almost all measurement points, and E_b / q_i for Xe^{2+} ions was almost always lower than that of Xe^{3+} ions. $\Delta(E_b / q_i)$ was similar to the data at $R = 50$ cm.

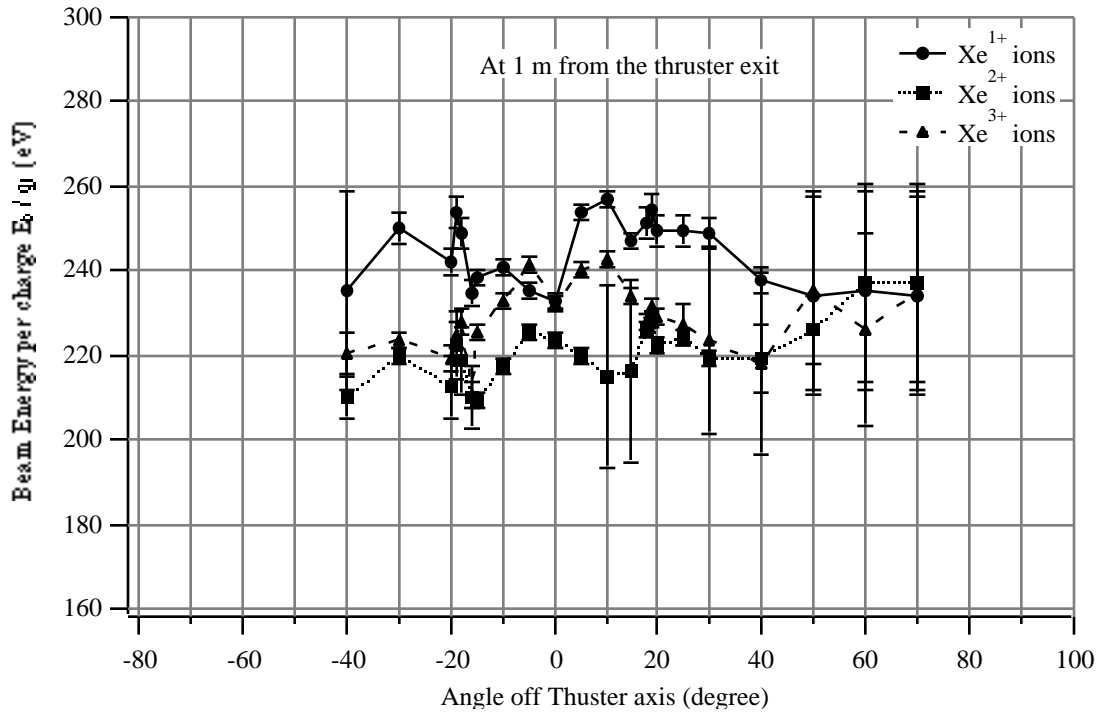


Figure 7-14 Angular profiles of beam energy per charge of Xe^{1+} , Xe^{2+} , and Xe^{3+} ions in the SPT-100 plume at 1 m from the thruster exit.

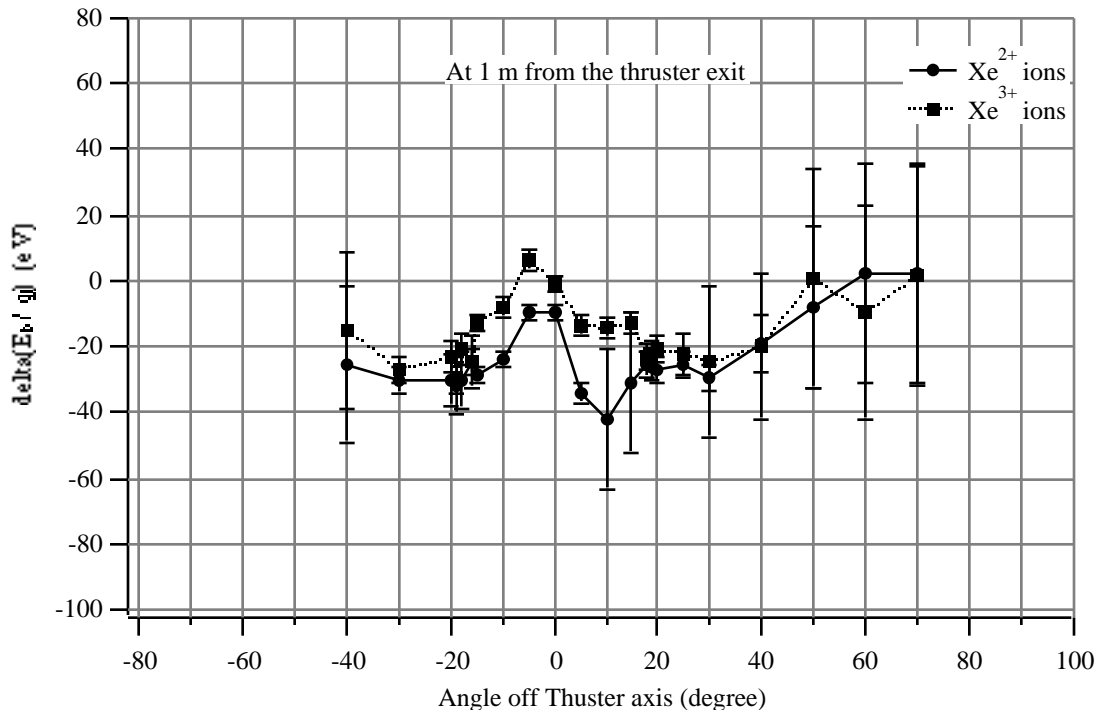


Figure 7-15 Angular profiles of the differences in beam energy per charge between Xe^{2+} and Xe^{1+} ions and between Xe^{3+} and Xe^{1+} ions in the SPT-100 plume at 1 m from the thruster exit.

Figure 7-16, Figure 7-17, and Figure 7-18 show comparisons of E_b/q_i at $R = 25$ cm, 50 cm, 75 cm, and 1 m for Xe^{1+} ions, Xe^{2+} ions, and Xe^{3+} ions, respectively. The data at different R were remarkably similar, especially near the thruster axis, both in shape and magnitude for all the ion species. This implies that the ions do not lose very much energy as they move farther downstream in the thruster plume, and that their trajectories remain fairly constant. This will be more true in space where the collisions between the plume ions and the background neutrals would be negligible.

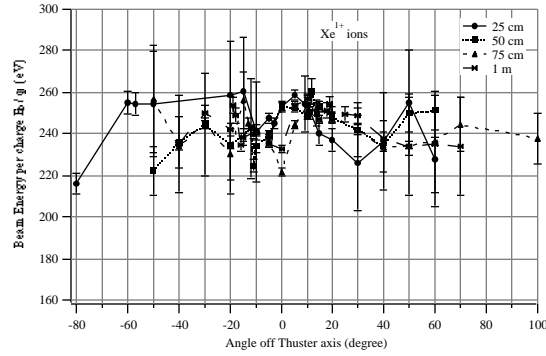


Figure 7-16 Comparison of beam energy per charge of Xe^{1+} ions in the SPT-100 plume between the data at 25 cm, 50 cm, 75 cm, and 1 m from the thruster exit.

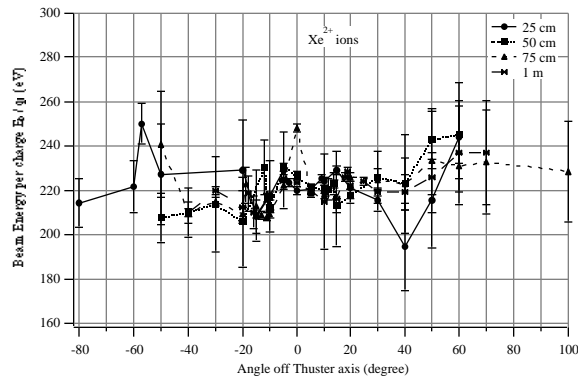


Figure 7-17 Comparison of beam energy per charge of Xe^{2+} ions in the SPT-100 plume between the data at 25 cm, 50 cm, 75 cm, and 1 m from the thruster exit.

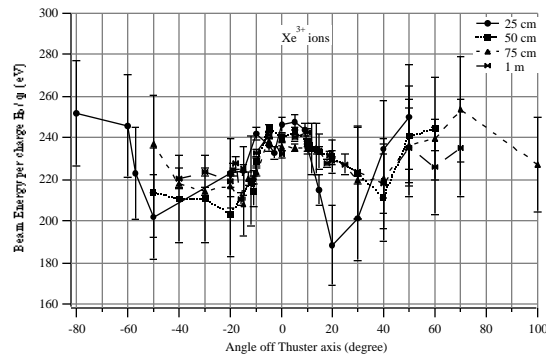


Figure 7-18 Comparison of beam energy per charge of Xe^{3+} ions in the SPT-100 plume between the data at 25 cm, 50 cm, 75 cm, and 1 m from the thruster exit.

7.3.3 Ion Energy Spread

The ion energy spread was calculated from the distribution function, obtained from the curve-fit of the **ExB** probe trace, as the half-width of $f(E_i)$ at the point where $f(E_i)$ has a value of e^{-1} times the peak value where $E_i = E_b$ at the peak. As mentioned in Section 2 of this chapter, $f(E_i)$ in the thruster plume is expected to depend strongly on V_i , the acceleration voltage. If the ions are created in a region of space with a potential difference (i.e. at different V_i), there will be a spread in ion energy corresponding to this potential difference. Then, the width of $f(E_i)$ would depend on the spread in V_i in the discharge chamber. Therefore, the ion energy spread would provide the location of the ionization layer if the electric field in the discharge chamber were mapped.

Two previous studies tried to determine the spread in ion energy in the SPT-100 plume, and reached very different values, which has become a source of confusion. In his laser induced fluorescence (LIF) study of the ion velocity in the SPT-100 plume [8], Manzella assumed that the ion distribution function was a Maxwellian and used the following equation to determine the width of the Doppler broadening in the measured fluorescence excitation spectrum which is the result of the spread in ion velocity:

$$\Delta \nu_D = \nu_0 \sqrt{\frac{8kT_i \ln 2}{M_i c^2}}, \quad \text{Eqn. 7-13}$$

where $\Delta \nu_D$ is the Doppler width (FWHM), ν_0 is the unshifted frequency of electronic transition, k is the Boltzmann's constant, T_i is the ion temperature, M_i is the ion mass, and c is the speed of light. $\Delta \nu_D$ is generally attributed to the random thermal motion of the ions. But, Manzella attributed the comparatively large temperature needed to model the axial ion velocity to a variation in acceleration voltage for the ions. From here, he determined the spread in ion energy to be approximately 3.4 eV. Then, the half-width of the ion energy distribution according to Manzella would be approximately 1.7 eV.

In his 45-degree energy analyzer study of the SPT-100 plume [2], King assumed the ion distribution to be a one-dimensional Maxwellian and modeled it with the following equation:

$$f(E_i) = K \exp -\sqrt{\frac{(E_i - E_b) / q_i e}{T_{ev}^2}}, \quad \text{Eqn. 7-14}$$

where K is a normalization constant, and T_{ev} is a representation of the spread in the ion distribution function. He defined the spread in ion energy similarly to the study reported here as the half-width of $f(E_i)$ at the point where $f(E_i)$ had a value of e^{-1} times the peak value where $E_i = E_b$. Mathematically;

$$\frac{(E_i - E_b) / q_i e}{T_{ev}} = 1, \quad \text{Eqn. 7-15}$$

at which $f(E_i) = 0.37 \cdot f(E_b)$. He obtained the half-width-half-maximum points directly from the measured ion energy distributions and determined the spread in ion energy to be approximately 20 to 40 eV, which is an order of magnitude larger than the value Manzella determined. A similarly defined spread in ion energy was determined to be approximately 60 eV in a RPA-measured data of the SPT-100 [15]. At first sight, the results of the two studies seem to disagree with each other. But, it will be shown that the **ExB** probe study can produce the results which agree with the both studies, and that the two studies are just looking at the data from two different points of view.

Recall, in Eqn. 7-8, ΔE_i characterizes the width of the distribution, and it is related to the ion temperature for a Maxwellian distribution. Thus, the “effective ion temperature T_{eff} ” was defined as $T_{\text{eff}} \propto \Delta E_i^{-2/n}$. Then, Eqn. 7-8 becomes the following:

$$f(E_i) = K E_i^{1/2} \exp - \frac{|\sqrt{E_i} - \sqrt{E_b}|}{\sqrt{T_{\text{eff}}}} \quad \text{Eqn. 7-16}$$

T_{eff} was obtained from each of the curve-fits of the **ExB** probe traces as one of the fitting parameters. Also, as mentioned earlier, the ion energy spread was calculated from each distribution function as the half-width of $f(E_i)$ at the point where $f(E_i) = e^{-1} \cdot f(E_b)$. As an example, Figure 7-19 shows the comparison between T_{eff} and the ion energy spread to the right of the distribution peak for Xe^{2+} ions at $R = 50$ cm. (Note that there are two ion energy spreads corresponding to the $e^{-1} \cdot f(E_b)$ point on either side of the peak.) T_{eff} was approximately 2 to 5 eV which agrees with Manzella’s value, and the ion energy spread was approximately 30 to 50 eV which agrees with King’s data. Therefore, as promised, the **ExB** probe data produced the results that are consistent with both Manzella’s and King’s data.

Much confusion between the two data stems from the assumption that the measured ion distribution is a one-dimensional distribution. According to Eqn. 7-14 and Eqn. 7-15 which are equations for a one-dimensional Maxwellian, the actual peak spread in the distribution function, i.e. $\Delta E_i = E_i - E_b$ at the point where $f(E_i) = e^{-1} \cdot f(E_b)$, must be equal to T_{ev} . However, the distribution functions obtained from the **ExB** probe measurements were three-dimensional distributions and were modeled as such with Eqn. 7-16. The important difference between Eqn. 7-14 and Eqn. 7-16 (and thus between one-dimensional and three-dimensional equations) is that the latter has the factor $E_i^{1/2}$.

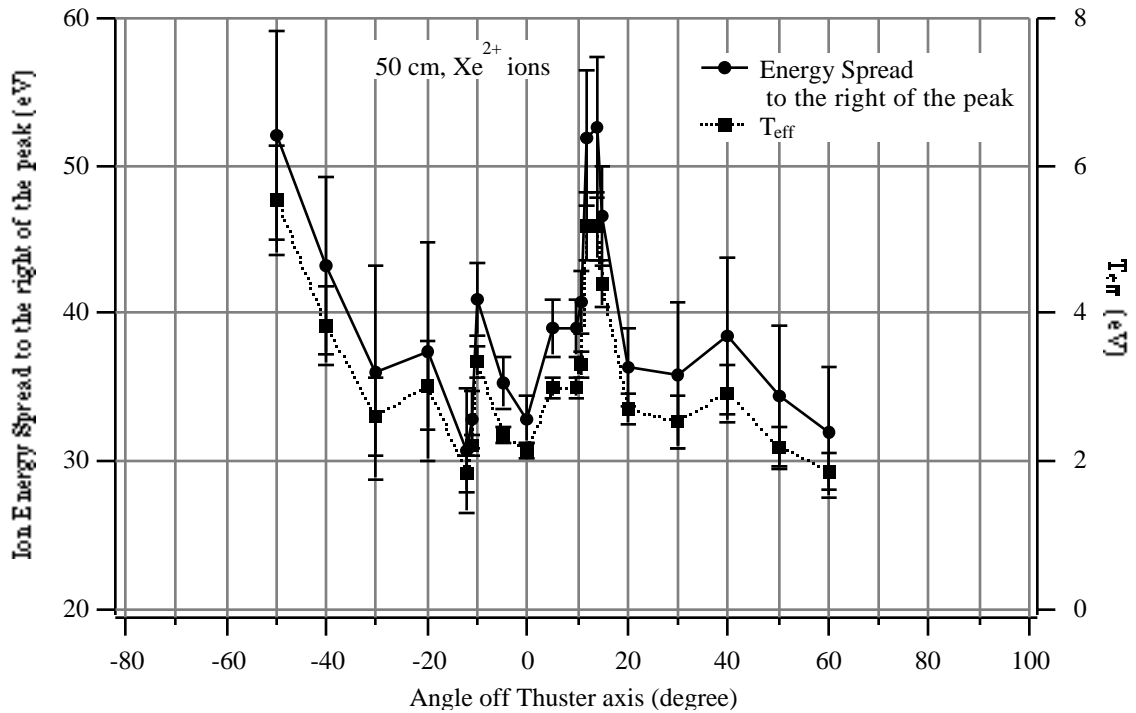


Figure 7-19 Comparison between the ion energy spread obtained from the distribution function and T_{eff} for Xe^{2+} ions at 50 cm from the thruster exit.

Thus, E_i does not have to be equal to T_{eff} for a three-dimensional distribution such as in Eqn. 7-16. Therefore, it was possible for the ExB probe data to produce both Manzella's data ($= T_{\text{eff}}$) and King's data ($= E_i$). As can be seen from Eqn. 7-16, T_{eff} and Manzella's results provided the theoretical "ion temperature" according to Maxwellian-like distribution while the ion energy spread and King's results provided the actual width of the distribution function. Thus, the two sets of data are consistent with each other.

However, the ion energy spread is more meaningful for the discussion of ionization and acceleration mechanism in the SPT-100. It should be noted that, even though Figure 7-19 shows that the angular profiles of the ion energy spread and T_{eff} were the same, this result was not expected since the ion energy spread is related to the directed ion kinetic energy, and T_{eff} is related to the random motion of the ions.

The reason why the **ExB** probe data had to be treated as three-dimensional is found in the journal by Stenzel, et al. who developed a RPA with a microchannel plate for measuring electron distribution functions in various plasmas [16]. The plate consisted of a large array of long, narrow, parallel holes through which particles had to pass in order to reach the RPA. Therefore, the plate acted as a geometric filter, i.e. a collimator in front of a particle energy analyzer. This is exactly the same scheme in which the **ExB** probe is used (See Chapter 5). Stenzel, et al.'s derivation of the probe current shows that the experimental data obtained using an energy analyzer with a collimator in front of it is in three-dimensional.

As mentioned earlier, two ion energy spreads can be found in the distribution function corresponding to the $e^{-1} \cdot f(E_b)$ point on either side of the peak. Figure 7-20 shows the comparison between the energy spread to the left of the peak and the energy spread to

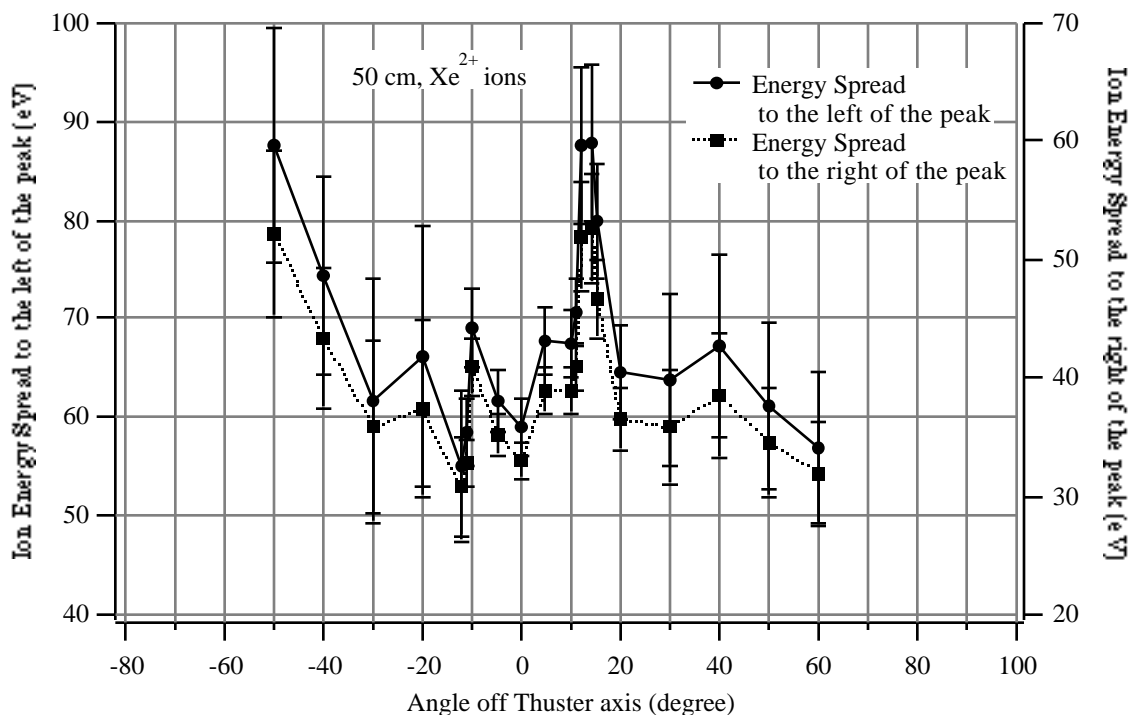


Figure 7-20 Comparison between the ion energy spread to the left of the peak and that to the right of the peak for Xe^{2+} ions at 50 cm from the thruster exit.

the right of the peak for Xe^{2+} ions at $R = 50$ cm. The angular profiles of the two energy spreads were the same, but the energy spread to the left was approximately 30 eV larger than the energy spread to the right.

Similar results were observed for Xe^{2+} and Xe^{3+} ions at other R . Recall that the results of the measured beam energy E_b and the proposed ionization and acceleration mechanism in the previous subsection suggested that the multiply charged ions were involved in such processes as colliding with the chamber wall, elastic collisions with other ions, charge exchange collisions with neutral atoms and other ions, and subsequent ionization as they move downstream in the discharge chamber. Therefore, the energy spread to the left ($E_i < E_b$) was expected to be larger than the energy spread to the right ($E_i > E_b$). The experimental results shown in Figure 7-20 support this conclusion. For Xe^{1+} ions, the two ion energy spreads were similar both in shape and magnitude. This is believed to be due to the fact that the Xe^{1+} ions in the SPT-100 plume were close to Maxwellian as the data of the exponential factor n of the ion energy distribution functions showed in Section 3.1 of this chapter. In the discussion below, only the ion energy spread to the right of the peak ($E_i > E_b$) will be shown for the following reasons: it does not involve the various collisions and subsequent ionization, and the curve-fits had better agreement with the experimental probe traces on the right side of the peak. Again, note that the angular profiles of the left- and right-energy spreads were the same for all data, that the spread to the left was approximately 30 eV larger than the spread to the right for multiply charged ions, and that the two energy spreads had the same magnitude for Xe^{1+} ions.

Figure 7-21 through Figure 7-24 show the results of the ion energy spread (to the right of the peak) calculations at $R = 25$ cm, 50 cm, 75 cm, and 1 m. The energy spread varied between 20 eV to 60 eV depending on the angle off thruster axis and the ion species. However, the energy spread was approximately 38 eV within 20 degrees off thruster axis at all R . At $R = 25$ cm, the energy spread was very similar among the different ion species within -20° to 20° . But, the difference in the energy spread

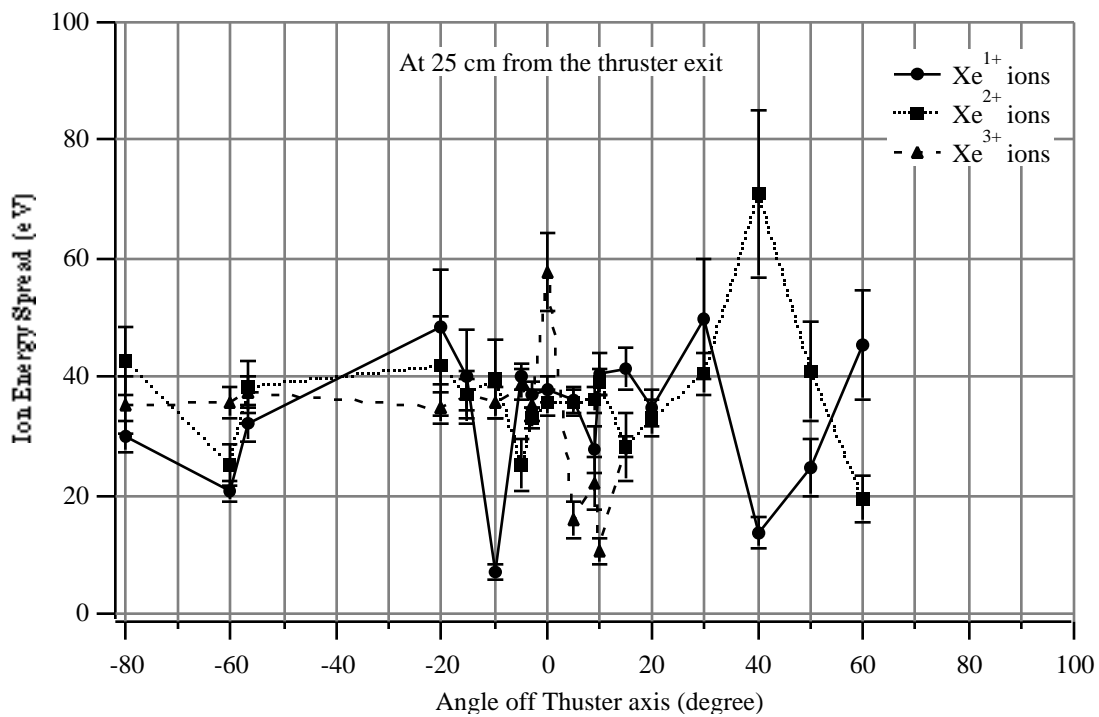


Figure 7-21 Ion energy spread for Xe¹⁺, Xe²⁺, and Xe³⁺ ions in the SPT-100 plume at 25 cm from the thruster exit.

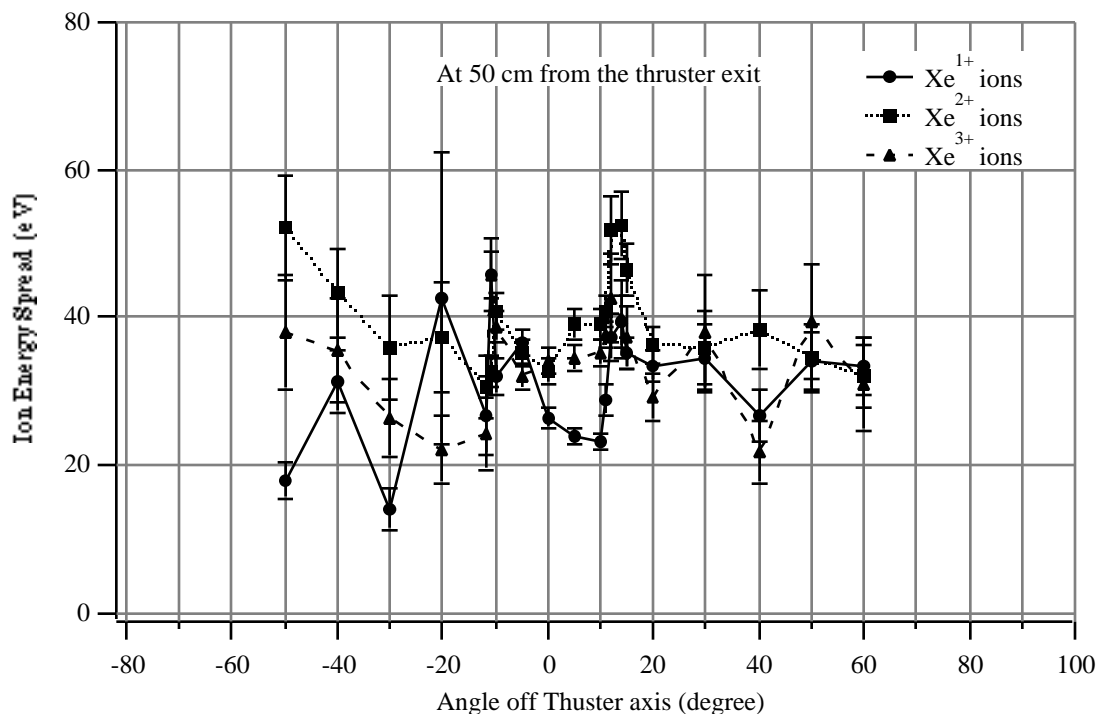


Figure 7-22 Ion energy spread for Xe¹⁺, Xe²⁺, and Xe³⁺ ions in the SPT-100 plume at 50 cm from the thruster exit.

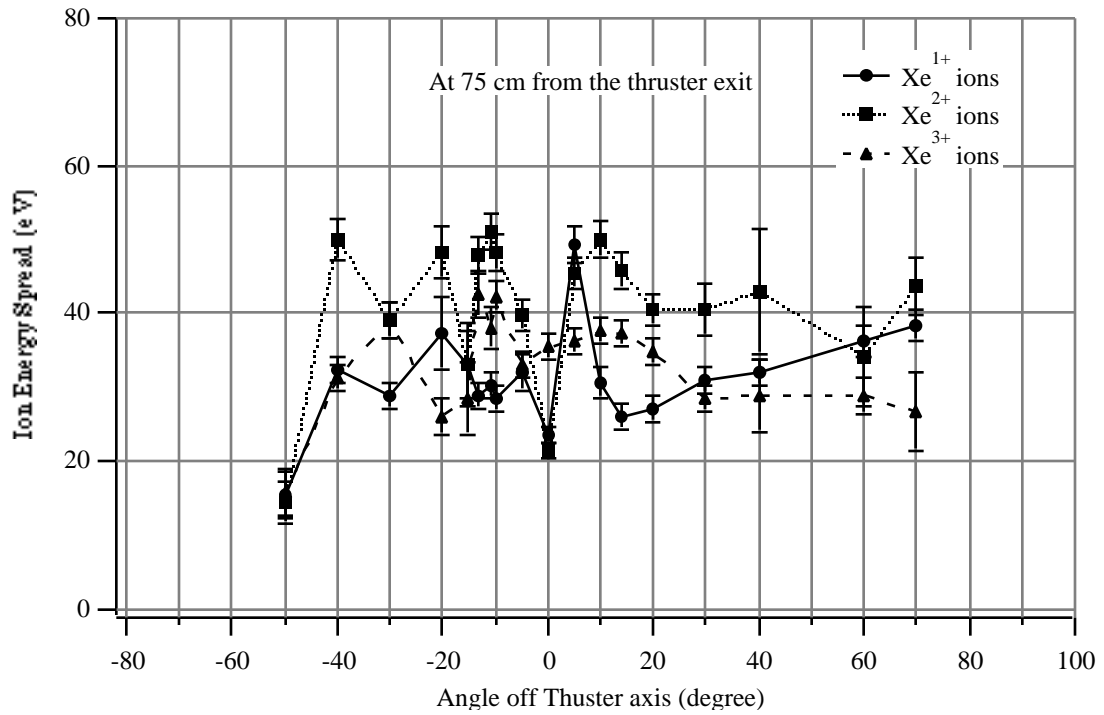


Figure 7-23 Ion energy spread for Xe¹⁺, Xe²⁺, and Xe³⁺ ions in the SPT-100 plume at 75 cm from the thruster exit.

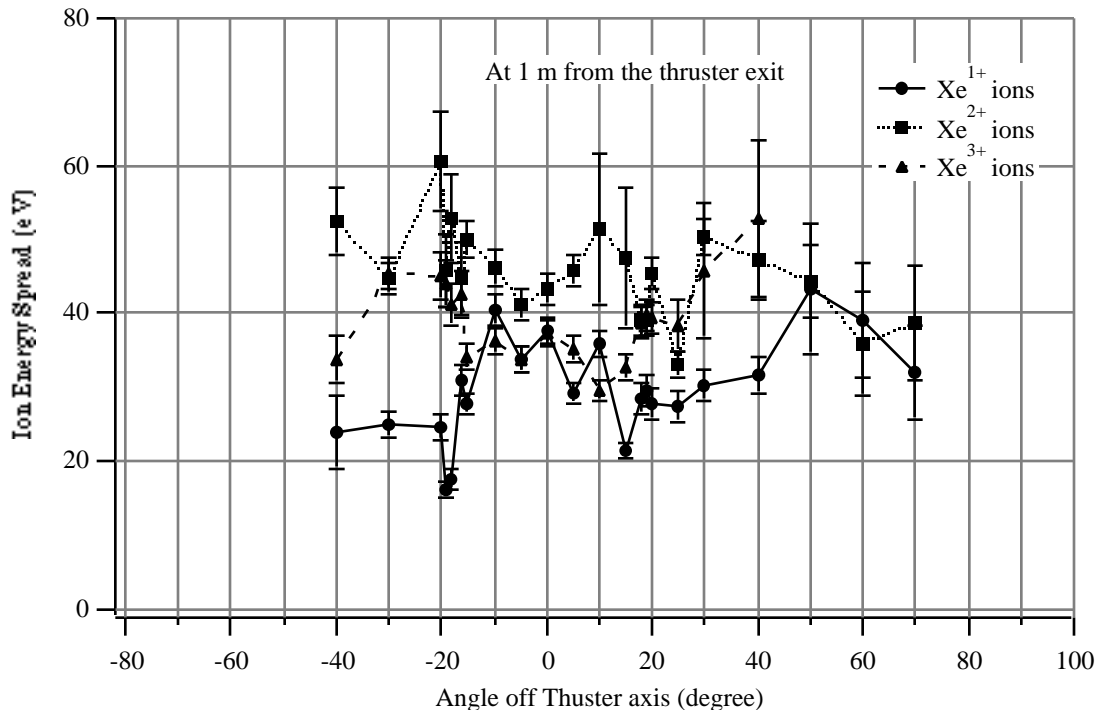


Figure 7-24 Ion energy spread for Xe¹⁺, Xe²⁺, and Xe³⁺ ions in the SPT-100 plume at 1 m from the thruster exit.

between different ion species seems to increase with increasing R , i.e. as the ions move away from the thruster. Also, Xe²⁺ ions had the broadest energy spread at $R = 50$ cm, 75 cm, and 1 m.

Similarly to the E_b data, the energy spread data at $R = 25$ cm were expected to represent the spread in V_i in the discharge chamber most closely, compared to the data at other R , simply because they were measured closest to the thruster. According to the ionization and acceleration mechanism in the discussion of beam energy E_b , Xe¹⁺ ions had the broadest range of ionization location upstream of the primary ionization region in the discharge chamber. Meanwhile, Figure 7-21 shows that all the ion species had the similar energy spread to the right of the peak. Recall that the ion energy spread was defined as $E_i = E_1 - E_b$ at the point where $f(E_i) = e^{-1} \cdot f(E_b)$. Then, the ion energy spread represents the spread in V_i within the primary ionization layer. Therefore, the results in

Figure 7-21 suggests that the spread in V_i within the primary ionization layer was similar for Xe^{1+} , Xe^{2+} , and Xe^{3+} ions even though the range of ionization locations in the discharge chamber was different for different ion species.

7.3.4 Ion Species Fractions

The ion species fractions were calculated at each data point by determining the first moment of the distribution functions for each ion species (i.e. number density, n_i) and calculating the fractions of n_i 's at the data point. Note that the CEM gain was changed for each probe measurement point, and thus one can only compare n_i 's of different ion species in one probe trace. If one wishes to compare all n_i 's regardless of measurement points, he/she needs to convert the probe output current to the total ion flux according to the CEM gain curve. This was not done for the study reported here for lack of an accurate gain curve.

The ion species fractions at $\theta = 5^\circ$ at $R = 50$ cm were compared with the similar data obtained by King [2] and Manzella [17]. This comparison is shown in Table 7-1.

Ion Species	Ion Species Fractions from ExB probe	Ion Species Fractions from King's data	Ion Species Fractions from Manzella's data
Xe^{1+} ions	0.79	0.888	0.89
Xe^{2+} ions	0.16	0.110	0.119
Xe^{3+} ions	0.05	0.002	(not measured)

Table 7-1 Comparison between ExB probe-measured ion species fractions with values obtained by King [2] and Manzella [17].

The disagreement between the **ExB** probe data and the other two data is attributed to the underestimation of Xe^{1+} ion fraction due to the curve-fit limitations discussed before and exhibited in Figure 7-2. The discrepancy could also be attributed to the overestimation of Xe^{2+} and Xe^{3+} ion fractions. Recall from Chapter 5, Section 4 that a

number of multiply charged ions will result in higher output current than the same number of singly charged ions because the output current of the CEM, the ion collector in the **ExB** probe, depended on the secondary emission yield of the inlet surface. A rough estimate of the variation of the secondary emission yield was made using the elementary theory of secondary electron emission (See Chapter 5, Section 4), and it was found that the output current of Xe^{2+} ions and Xe^{3+} ions would be 3 and 10 times larger, respectively, than that of the same number of Xe^{1+} ions. Then, the ion species fractions, corrected for the CEM output current variation, would be 0.93 for Xe^{1+} ions, 0.06 for Xe^{2+} ions, and 0.006 for Xe^{3+} ions. Thus, the variation of the secondary emission yield over-corrected the **ExB** data. Also, the particle detector King had used in his mass spectroscopy device was a CEM. Hence, the discrepancy is believed to stem mostly from the underestimation of Xe^{1+} ion fraction due to the curve-fit limitations.

Figure 7-25 through Figure 7-28 show the ion species fractions at $R = 25$ cm, 50 cm, 75 cm, and 1 m. The angular profiles of ion species fractions exhibit a sudden change near -20° -10° , 10° 20° .

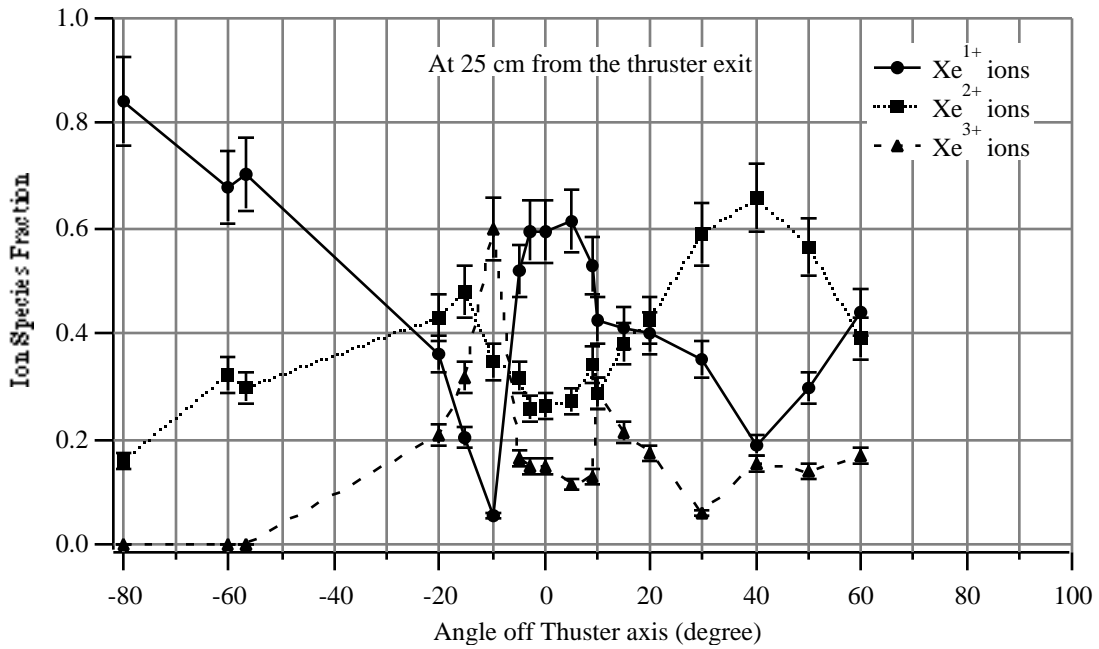


Figure 7-25 Ion species fractions of Xe¹⁺, Xe²⁺, and Xe³⁺ ions in the SPT-100 plume at 25 cm from the thruster exit.

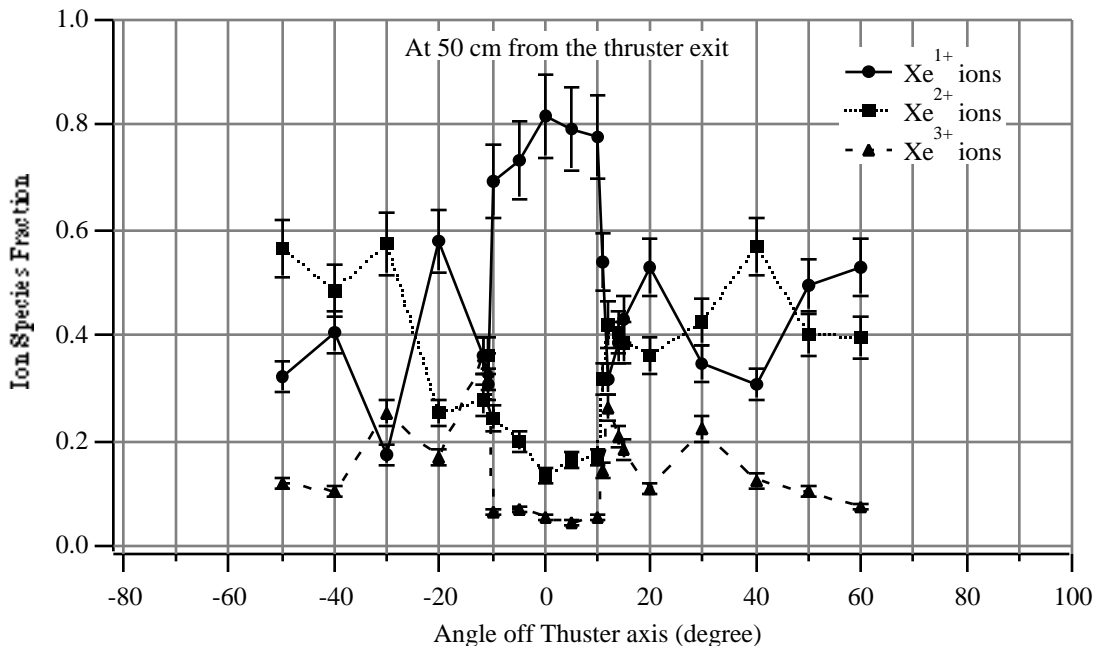


Figure 7-26 Ion species fractions of Xe¹⁺, Xe²⁺, and Xe³⁺ ions in the SPT-100 plume at 50 cm from the thruster exit.

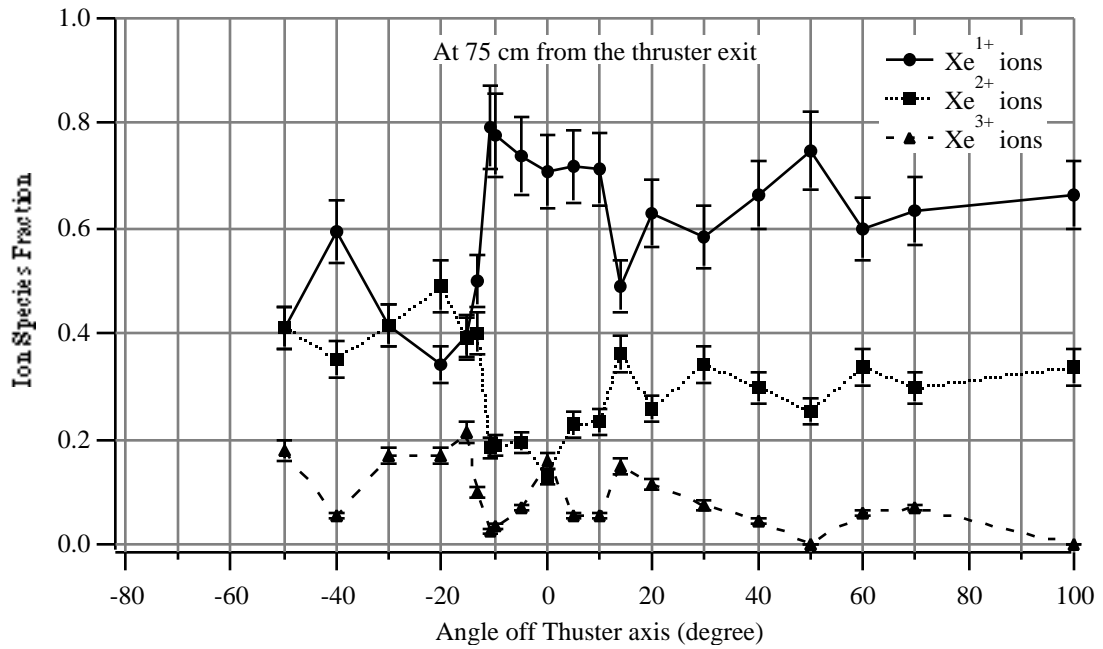


Figure 7-27 Ion species fractions of Xe¹⁺, Xe²⁺, and Xe³⁺ ions in the SPT-100 plume at 75 cm from the thruster exit.

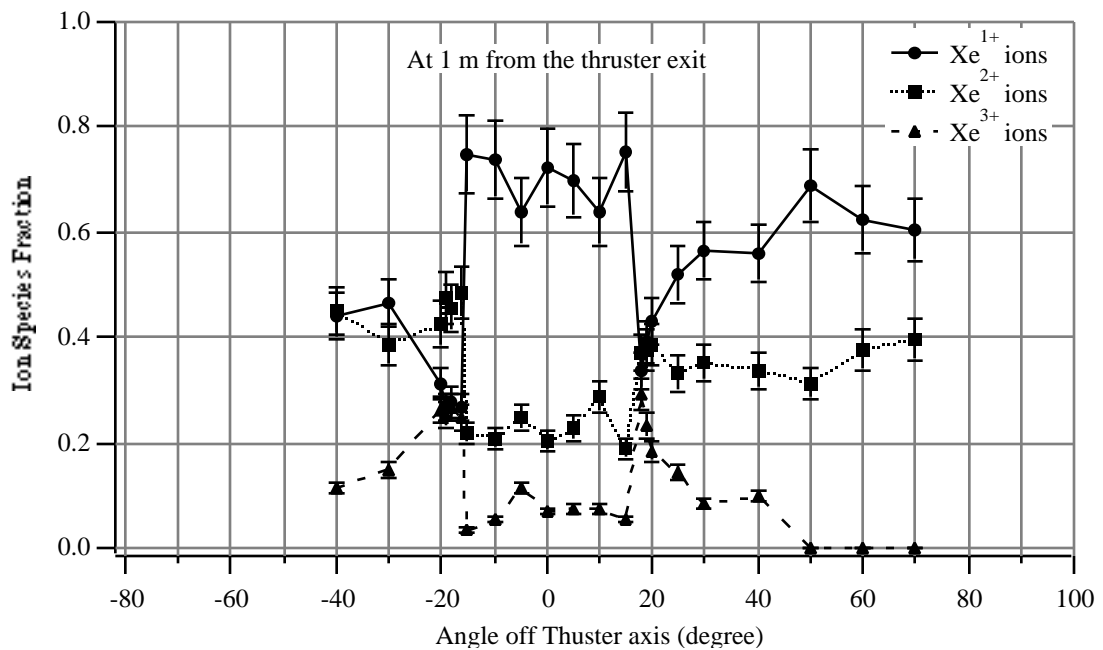


Figure 7-28 Ion species fractions of Xe¹⁺, Xe²⁺, and Xe³⁺ ions in the SPT-100 plume at 1 m from the thruster exit.

The majority of ions in the thruster plume were Xe^{1+} ions within 10 degrees off thruster axis, while the fractions of Xe^{2+} ions increased significantly outside of this region. Recall, from the earlier discussion of the ionization and acceleration mechanism, that an ion can exit the thruster only if it does not hit the discharge chamber wall before it reaches the thruster exit. Therefore, in order for an ion to exit the thruster, the angle of the ion's velocity vector with respect to the thruster axis must decrease as the ion production occurs farther upstream in the discharge chamber. Then, the angular profiles of the ion species fractions in Figure 7-25 through Figure 7-28 imply that the Xe^{2+} ions and Xe^{3+} ions were produced near the thruster exit, and that the Xe^{1+} ions were produced farther upstream in the discharge chamber. This result collaborates with the result of beam energy E_b in supporting the proposed ionization and acceleration mechanism.

The sudden change in the fractions occurred near $\theta = \pm 10^\circ$ at $R = 25$ cm, near $\theta = \pm 12^\circ$ at $R = 50$ cm, near $\theta = \pm 15^\circ$ at $R = 75$ cm, and near $\theta = \pm 20^\circ$ at $R = 1$ m. Thus, the region of high Xe^{1+} ion fractions grew slightly as the ions moved away from the thruster. This sharp change in the ion species fractions near -20° , -10° , 10° , 20° has a significant implication: the region of the primary production for Xe^{1+} ions is clearly separated from the region of the primary production for Xe^{2+} and Xe^{3+} ions by a narrow boundary in the discharge chamber. According to the proposed ionization and acceleration mechanism, this boundary would be located where the line of sight from this region to the exit of the outer discharge chamber wall forms approximately 10 to 20 degrees with respect to the thruster axis. If this is true, and if the primary ion production occurs near the inner wall of the discharge chamber as a previous study suggested [9], the primary production of multiply charged ions will occur too far upstream in the discharge chamber (almost at the anode). The previous study did not specify which ion species were produced in that region, and thus it is possible that the multiply charged ions might have been produced near the outer wall of the discharge chamber. However, the study showed that the electrons, which collide with the propellant atoms and ionize them,

obtained the maximum temperature near the inner wall of the discharge chamber. Thus, it is more likely for multiply charged ions to be produced near the inner wall than near the outer wall of the discharge chamber. Then, the factor limiting the angle of ion velocities may be more than just the discharge chamber geometry for the case of straight-line ion trajectories as the proposed ionization and acceleration mechanism assumed. Another angle-limiting factor can be the influence of the electric field in the discharge chamber on the ions, which makes the trajectories of the ions in the discharge chamber more parabola-like rather than straight lines. This is because the radial component of the initial ion velocity remains constant while the axial component is increased continuously by the electric field in the discharge chamber. This is similar to the classic physics problem of a thrown body under the influence of the earth's gravity (but not the same because the accelerating force of the electric field is not constant as the ions move downstream in the discharge chamber). Therefore, the actual angle off thruster axis with which the ions can emerge from the discharge chamber will be smaller than the angle with which the ions could emerge if their trajectories were straight lines. Thus, both the discharge chamber geometry and the accelerating force of the electric field in the discharge chamber limit the angle of ion velocities exiting the thruster.

7.4 Conclusions

The ion energy distribution, $f(E_i)$, of each ion species in the SPT-100 plume was obtained at various locations in the thruster plume by curve-fitting each peak in the measured \mathbf{ExB} probe traces with a model based on the kinetic theory of gases. From the exponential factor n of the distribution function, the distributions of Xe^{1+} ions were found to be close to Maxwellian. The comparison of the angular profiles of beam energy E_b for each ion species at different distances from the thruster exit revealed that the ions lost little energy and that their trajectories remained fairly constant as they move downstream

in the thruster plume. The angular profiles of beam energy E_b and ion species fractions gave rise to a simple ionization and acceleration mechanism in the SPT-100 discharge chamber. Although the proposed mechanism did not describe the plasma in the discharge chamber completely, it matched very well with the behavior of the plume data within -20° to 20° . The sharp change in the ion species fractions near -20° to -10° , 10° to 20° implied a significant fact: the region of the primary production for Xe^{1+} ions was clearly separated from the region of the primary production for Xe^{2+} and Xe^{3+} ions by a narrow boundary in the discharge chamber. From the ion species fractions data and a simple geometric calculation, it was found that both the discharge chamber geometry and the accelerating force of the electric field in the discharge chamber limited the angle of ion velocities exiting the thruster. This accelerating force makes the ion trajectories parabola-like rather than straight lines. The ion energy spread data showed that the results of two previous studies, which seemed to disagree by an order of magnitude, were actually describing the same parameter from different points of view. This was accomplished due to the three-dimensional nature of the ion distribution function.

Reference to Chapter 7

- 1 Hutchinson, I., Principles of Plasma Diagnostics, Cambridge University Press, New York, 1987.
- 2 King, L.B., Ph.D. Thesis, University of Michigan, Department of Aerospace Engineering, 1998.
- 3 Lieberman, M.A. and Lichtenberg, A.J., Principles of Plasma Discharges and Materials Processing, John Wiley & Sons, Inc., New York, 1994.
- 4 Rundle, H.W., Clark, D.R., and Deckers, J.M., "Electron Energy Distribution Functions in an O₂ Glow Discharge," *Canadian Journal of Physics*, Vol. 51, pp. 144-148, 1973.
- 5 Foster, J.E., Ph.D. thesis, University of Michigan, Department of Applied Physics, 1996.
- 6 Brown, S.C., Basic Data of Plasma Physics, AIP Press, New York, 1994.
- 7 Zhurin, V.V., Kaufman, H.R., and Robinson, R.S., "Physics of Closed Drift Thrusters," IEPC-97-191, August 1997.
- 8 Manzella, D.H., "Stationary Plasma Thruster Ion Velocity Distribution," AIAA-94-3141, June 1994.
- 9 Bishaev, A.M. and Kim, V., "Local Plasma Properties in a Hall-Current Accelerator with an Extended Acceleration Zone," *Soviet Physics, Technical Physics*, Vol. 23, No. 9, pp. 1055-1057, 1978.
- 10 Baranov, V.I., Nazarenko, Y.S., Petrosov, V.A., Vasin, A.I., and Yashnov, Y.M., "Energy Model and Mechanisms of Acceleration Layer Formation for Hall Thrusters," AIAA-97-3047, July 1997.
- 11 Weast, R.C., CRC Handbook of Chemistry and Physics, 69th Edition, CRC Press, Inc., Boca Raton, FL, 1988.
- 12 Rapp, D. And Francis, W., "Charge Exchange Between Gaseous Ions and Atoms," *Journal of Chemical Physics*, Vol. 37, No. 11, pp. 2631-2645, 1962.
- 13 Gombosi, T.I., Gaskinetic Theory, Cambridge University Press, New York, 1994.
- 14 Gavryushin, V.M. and Kim, V., "Effect of the Characteristics of a Magnetic Field on the Parameters of an Ion Current at the Output of an Accelerator with Closed Electron Drift," *Soviet Physics, Technical Physics*, Vol. 26, No. 4, pp. 505-507, April 1981.

15 Oh, D. And Hastings, D., "Experimental Verification of a PIC-DSMC Model for Hall Thruster Plumes," AIAA-96-3196, June 1996.

16 Stenzel, R.L., Gekelman, W., Wild, N., Urrutia, J.M., and Whelan, D, "Directional Velocity Analyzer for Measuring Electron Distribution Functions in Plasmas," Review of Scientific Instruments, Vol. 54, No. 10, pp. 1302-1310, Oct. 1983.

17 Manzella, D.H., "Stationary Plasma Thruster Plume Emissions," IEPC-93-097, Sept. 1993.

CHAPTER 8

CONCLUSIONS AND SUGGESTED FUTURE WORK

8.1 Conclusions

In this work, the plasma parameters and ion energy distribution in the plasma exhaust plume of the SPT-100 Hall thruster were studied using electrostatic probes and an **ExB** probe. The significance of this work stems from the need to understand and characterize the behavior of multiply charged propellant ions in the thruster plume. The interest in the behavior of multiply charged propellant ions is largely due to the adverse effects of these ions upon the efficiency and lifetime of the thruster and, ultimately, the operation and lifetime of the spacecraft on which the thruster will be used. Therefore, understanding and characterizing the behavior of multiply charged propellant ions is an important aspect of engine development. A great deal of insight into the behavior of these ions can be obtained from the plasma properties in the thruster plume.

To characterize the plasma properties in the SPT-100 plume, plasma parameters were measured using electrostatic probes over an extensive volume of the thruster plume from the very-near-field to near- and far-field. To characterize the species-dependent ion parameters in the SPT-100 plume, an **ExB** probe was utilized to measure ion energy distributions of each ion species over a large volume of the thruster plume in the near- and far-field. Then, the measured probe traces were curve-fitted with a distribution function model to obtain ion energy distribution functions. Although there have been many studies of the SPT-100 plume characteristics, the combined data of the very-near-field and the near- and far-field plume studies provided the most comprehensive collection of plasma parameters in the SPT-100 plume. Also, the **ExB** probe technique

was the first high-resolution, species-dependent, direct measurements of ion energy distribution in the Hall thruster plume.

In the very-near-field plume study (10 mm to 200 mm downstream of the thruster exit), the radial ion current density profile exhibited distinct peak structures. The variation of the ion current density with axial distance from the thruster indicated that the ion beam began as an annulus diverging from the exit of the discharge chamber both inward and outward radially, and then, merged into a single body beam at or near 100 mm from the thruster exit plane and defocused at larger axial positions. The total ion current calculation revealed that the SPT-100 plume included multiply charged xenon ions. The radial electron number density profiles, compared with the radial ion current density profiles, revealed that the electron population in the SPT-100 plume was controlled by the competing effects of two phenomena; the electric and magnetic field influences on the electrons, which was dominant in the plume region close to the thruster exit, and the quasineutrality in the plasma which was dominant in the plume farther downstream of the thruster exit. The boundary of the two regions was somewhere between 50 mm and 100 mm from the thruster exit.

In the near- and far-field plume study (25 cm to 1 m downstream of the thruster exit plane), the angular profile of ion current density exhibited a peak on the thruster axis. The apparently low ion current density observed around -15° and 15° off thruster axis at 25 cm from the thruster exit was attributed to charge exchange collisions occurring near the inner boundary of the annular ion beam in the very-near-field of the thruster plume. The variation of the ion current density with increasing distance from the thruster suggested that the plume ions moved in trajectories close to linear, and that those trajectories varied little as the ions moved away from the thruster. The similarity in shape and size of the plasma potentials at different distances from the thruster also supported this conclusion. The measured total ion current was larger than the total ion current that would be measured if each propellant atom was singly charged, implying that there were

multiply charged propellant ions in the thruster plume. The angular profiles of electron number density had similar shape with that of the beam ion current density. The variation of those profiles with increasing distance from the thruster was also similar. These results suggested that the ions and electrons followed the same path in the thruster plume.

The ion energy distributions measured by the **ExB** probe revealed that there existed Xe^{4+} ions in the plume. This was the first experiment that had directly measured the Xe^{4+} ions in the SPT-100 plume. The two peaks for Xe^{1+} and Xe^{2+} ions were highly overlapped near the thruster axis at all distances from the thruster. This was a clear evidence of elastic collisions between Xe^{1+} and Xe^{2+} ions. The two peaks were more sharply defined at larger angle off thruster axis, which suggests that elastic collisions occur mostly near the thruster axis. The relative height of each peak in the probe trace depended on the angular position of the measurement, revealing that the ion species fractions change in the thruster plume.

The ion energy distribution functions, $f(E_i)$, of each ion species were obtained by curve-fitting each peak in the measured **ExB** probe traces with a distribution function model based on the kinetic theory of gases. Because of its inability to predict the elastic collisions between the ion species, the model could not produce the highly overlapped region between the peaks of the ion species involved in the collisions. However, the excellent agreement between the measured probe trace and the model in the upper part of the trace peaks suggested that this simple model could produce “pre-collision” distribution functions very well. $f(E_i)$ provided several ion parameters at various locations in the SPT-100 plume; namely, the exponential factor n of the distribution function which was a measure of how much the distribution was Maxwellian-like or Druyvesteyn-like, the beam energy of the ions, the spread in the ion energy, and ion species fractions. From the exponential factor n of the distribution function, it was found that the distributions of Xe^{1+} ions were close to Maxwellian at most measurement points

in the thruster plume. The comparison of the angular profiles of beam energy at different distances from the thruster exit showed that the energies and trajectories of the plume ions changed very little as the ions moved downstream in the thruster plume. The angular profiles of beam energy and ion species fractions gave rise to a simple ionization and acceleration mechanism in the SPT-100 discharge chamber. Although the proposed mechanism did not paint a complete picture of ionization and acceleration processes in the discharge chamber, it matched very well with the behavior of the plume data within -20° to 20° . The sharp change in the ion species fractions near -20° to -10° , 10° to 20° implied a significant fact that the region of the primary production for Xe^{1+} ions was clearly separated from the region of the primary production for Xe^{2+} and Xe^{3+} ions by a narrow boundary in the discharge chamber. From the ion species fractions data and a simple geometric calculation, it was found that both the discharge chamber geometry and the accelerating force of the electric field in the discharge chamber were the factors limiting the angle of ion velocities exiting the thruster. This electric field makes the ion trajectories parabola-like rather than straight lines in the discharge chamber. The ion energy spread data showed that the results of two previous studies, which seemed to disagree by an order of magnitude, were actually describing the same parameter from different points of view. The confusion was cleared by the three-dimensional nature of the ion distribution function.

8.2 Future Work

The work reported here provides an extensive data base of plasma characteristics in the exhaust plume of the SPT-100, including species-dependent ion parameters. Although the collected data can be used as an input to the plasma-surface interaction models, the integration issues were not incorporated into this thesis. Then, the foremost future work should be to study the integration issues utilizing the data collected in this

work. The species-dependent ion parameters at many locations in the thruster plume, which had not been available before, will be most helpful in obtaining a more accurate assessment of erosion and deposition rates. These data should also be very useful in determining the correction factors for thrust, thruster efficiency, and mass utilization. Direct calculations of thruster performance parameters can be possible if an accurate gain curve of the CEM is available. One can convert the output current of the CEM to the ion flux using the CEM gain curve. Then, the number density and current density of each ion species can be calculated. These numbers can, in turn, be used to determine thrust, specific impulse, efficiency, and the correction factors for these parameters.

The first attempt of using the **ExB** probe technique in measuring ion energy distributions was proven to be successful in this work. However, there is plenty of room for improvement. One of the possible improvements is to supply a voltage to the two E-field bias plates using a high-voltage, high-frequency power supply. The E-field bias voltage was ramped by hand, and five traces were obtained at each measurement point to be averaged later, which was very time consuming. If a high frequency power supply is synchronized with the digital oscilloscope, many traces can be acquired in seconds, and the fast electronics of the oscilloscope can average the traces as they are acquired. This will not only save time, but also result in cleaner traces filtering out the unwanted noises. Another way of improving the **ExB** probe might be to use an amplifier circuit to boost the output current of the CEM. This will allow the collimator to have a smaller aperture diameter, improving the energy resolution of the probe. This might also reduce the probe size, thus reducing the perturbation of the local plasma at the measurement point.

Among the limitations of the distribution function model used in this work, the most significant one was its inability to predict the highly overlapped region between the peaks of two ion species that were involved in elastic collisions with each other. The model would improve if it can account for elastic collisions and other collisional processes occurring in the thruster plume. However, such a scheme requires cross

sections involving multiply charged xenon ions, and those cross sections are not all available at this time.

Finally, many studies have shown that the effects of background pressure on the thruster testing can be significant if the background pressure is high enough. As the background pressure of the vacuum chamber increases, background gas can be entrained by the thruster and used as propellant, thus affecting the thruster performance measurements. High background pressure has also been found to cause large discharge oscillations. Additionally, high background pressure leads to an increase in charge exchange collision frequency between the plume and background gas species. A previous study of facility effects on the thruster testing concluded that a background pressure of less than 5×10^{-5} Torr will ensure the accuracy of the testing [1]. The background pressure during the testing in this work was 1.2×10^{-4} Torr (calibrated for xenon). Thus, the obtained data must be viewed with care. Recall from Chapter 4 that there were points of low ion current density around -15° and 15° off thruster axis at 25 cm from the thruster exit. This was attributed to charge exchange collisions occurring near the inner boundary of the ion beam in the very-near-field of the thruster plume. Also recall from Chapter 6 that the unexpectedly high noise-to-signal ratio around -25° off thruster axis was observed at every axial distance from the thruster exit. This might have been caused by the high density of charge exchange ions in these regions of the plume. These effects would be negligible if the experiments were conducted at or below 5×10^{-5} Torr. The vacuum chamber used for this study recently underwent an upgrade that resulted in a transition to using cryopumps instead of oil diffusion pumps. This upgrade reduces the background pressure during the nominal SPT-100 operation by more than an order of magnitude (to 5×10^{-6} Torr). Therefore, it would be beneficial to make **ExB** probe measurements now that charge exchange collisions are far less probable.

Reference to Chapter 8

1 Randolph, T., Kim, V., Kaufman, H., Kozubsky, K., Zhurin, V., and Day, M., "Facility Effects on Stationary Plasma Thruster Testing," IEPC-93-093, Sept. 1993.

BIBLIOGRAPHY

- Absalamov, S.K., Andreev, V.B., Colbert, T., Day, M., Egorov, V.V., Gnizdor, R.U., Kaufman, H., Kim, V., Korakin, A.I., Kozubsky, K.N., Kudravzev, S.S., Lebedev, U.V., Popov, G.A., and Zhurin, V.V., "Measurement of Plasma Parameters in The Stationary Plasma Thruster (SPT-100) Plume and Its Effect on Spacecraft Components," AIAA-92-3156, July 1992.
- Anderson, J.R. and Fitzgerald, D., "Fullerene Propellant Research for Electric Propulsion," AIAA-96-3211, July 1996.
- Baranov, V.I., Nazarenko, Y.S., Petrosov, V.A., Vasin, A.I., and Yashnov, Y.M., "Energy Model and Mechanisms of Acceleration Layer Formation for Hall Thrusters," AIAA-97-3047, July 1997.
- Bishaev, A.M. and Kim, V., "Local Plasma Properties in a Hall-Current Accelerator with an Extended Acceleration Zone," Soviet Physics, Technical Physics, Vol. 23, No. 9, pp. 1055-1057, 1978.
- Bobei, A., Kim, V., Loroteev, A., et al, "State of Work on Electrical Thrusters in the USSR," IEPC-91-003, 1991.
- Brophy, J.R., Barnett, J.W., Sankovic, J.M., and Barnhart, D.A., "Performance of the Stationary Plasma Thruster: SPT-100," AIAA-92-3155, July 1992.
- Brown, S.C., Basic Data of Plasma Physics, AIP Press, New York, 1994.
- Bruining, H., Physics and Applications of Secondary Electron Emission, McGraw-Hill, New York, 1954.
- Bugrova, A., Kim, V., Maslennikov, N., and Morozov, A.I., "Physical Processes and Characteristics of Stationary Plasma Thrusters with Closed Electrons Drift," IEPC-91-079, Oct. 1991.
- Chung, P.M., Talbot, L., and Touryan, K.J., "Electric Probes in Stationary and Flowing Plasmas: Part 1. Collisionless and Transitional Probes," AIAA Journal, Vol. 12, No. 2, pp. 133-154, Feb. 1974.
- Darnon, F., Lyszyk, M., and Bouchoule, A., "Optical Investigation on Plasma Oscillations of SPT Thrusters," AIAA-97-3051, July 1997.

- Day, M., Gnizdor, R.U., Kaufman, H., Kim, V., et al, "Measurement of Plasma Parameters in the Stationary Plasma Thruster (STP-100) plume and its Effect on Spacecraft Components," AIAA-92-3156, July 1992.
- Dekker, A.J., Solid State Physics, Prentice-Hall, Englewood Cliffs, New Jersey, 1965.
- Dionne, G.F., "Effects of Secondary Electron Scattering on Secondary Emission Yield Curves," *Journal of Applied Physics*, Vol. 44, No. 12, pp. 5361-5364, Dec. 1973.
- Dudzinski, L. and Myers, R., "Advanced Propulsion Benefits to New Millennium Class Missions," Presented at 9th AIAA/Utah State University Conference on Small Satellites, Sept. 1995.
- Esipchuk, Y.V. And Tilinin, G.N., "Drift Instability in a Hall-Current Plasma Accelerator," *Soviet Physics, Technical Physics*, Vol. 21, No. 4, pp. 417-423, April 1976.
- Esipchuk, Y.V., Morozov, A.I., Tilinin, G.N., and Trofimov, A.V., "Plasma Oscillations in Closed-Drift Accelerators with an Extended Acceleration Zone," *Soviet Physics, Technical Physics*, Vol. 18, No. 7, pp. 928-932, Jan. 1974.
- Foster, J.E., Ph.D. thesis, University of Michigan, Department of Applied Physics, 1996.
- Gallimore, A.D., Gilchrist, B.E., King, L.B., Ohler, S.G., and Ruffin, A.B., "Plume Characterization of the SPT-100," AIAA-96-3298, July 1996.
- Gallimore, A.D., Kim, S-W, Foster, J.E., King, L.B., and Gulczinski III, F.S., "Near- and Far-field plume studies of a 1 kW arcjet," *Journal of Propulsion and Power*, Vol. 12, No. 1, Jan-Feb 1996.
- Garner, C.E., Brophy, J.R., Polk, J.E., and Pless, L.C., "A 5,730-Hr Cyclic Endurance Test of The SPT-100," AIAA-95-2667, July 1995.
- Garner, C.E., Polk, J.E., Pless, L.C., Goodfellow, K.D., and Brophy, J.R., "Performance Evaluation and Life Testing of the SPT-100," IEPC-93-091, Sept. 1993.
- Gavryushin, V.M. and Kim, V., "Effect of the Characteristics of a Magnetic Field on the Parameters of an Ion Current at the Output of an Accelerator with Closed Electron Drift," *Soviet Physics, Technical Physics*, Vol. 26, No. 4, pp. 505-507, 1981.
- Gavryushin, V.M., Kim, V., Kozlov, V.I., Kozubsky, K.N., Popov, G.A., Sorokin, A.V., Day, M.L., and Randolph, T., "Study of the Effect of Magnetic Field Variation,

Channel Geometry Change and Its Walls Contamination upon The SPT Performance,” AIAA-94-2858, June 1994.

- Godard, R. and Laframboise, J.G., “Total Current to Cylindrical Collectors in Collisionless Plasma Flow,” *Planet. Space Sci.*, Vol. 31, No. 3, pp. 275-283, 1983.
- Gombosi, T.I., Gaskinetic Theory, Cambridge University Press, New York, 1994.
- Griem, H.R., Plasma Spectroscopy, McGraw-Hill, New York, 1964.
- Gulczinski, F.S. and Spores, R.A., “Analysis of Hall-Effect Thrusters and Ion Engines for Orbit Transfer Missions,” AIAA-96-2973, July 1996.
- Hill, P. and Peterson, C., Mechanics and Thermodynamics of Propulsion, Second Edition, Addison-Wesley Publishing Company, Reading, MA, 1992.
- Huddlestone, R.H. and Leonard, S.L., Editors, Chen, F.F., Contributing author, Plasma Diagnostic Techniques, Chapter 4, Academic Press, New York, 1965
- Hutchinson, I., Principles of Plasma Diagnostics, Cambridge University Press, New York, 1987.
- Jahn, R.G., The Physics of Electric Propulsion, McGraw-Hill Book Company, New York, 1968.
- Kaufman, H.R., “Technology of Closed-Drift Thrusters,” AIAA-83-1398, June 1983.
- Kaufman, H.R., “Theory of Ion Acceleration with Closed Electron Drift,” *Journal of Spacecraft*, Vol. 21, No. 6, pp. 558-562, Nov.-Dec. 1984.
- Kaufman, H.R., Robinson, R.S., Day, M.L., and Haag, T.W., “End-Hall Thrusters,” AIAA-90-2595, July 1990.
- King, L.B. and Gallimore, A.D., “Ionic and Neutral Particle Transport Property Measurements in the Plume of an SPT-100,” AIAA-96-2712, July 1996.
- King, L.B., Ph.D. Thesis, University of Michigan, Department of Aerospace Engineering, 1998.
- Komurasaki, K., Hirakawa, M., and Arakawa, Y., “Plasma Acceleration Process in a Hall-Current Thruster,” IEPC-91-078, Oct. 1991.
- Kuang, Y-Z, Guo-Qing, and Yang, S-T, “ExB Momentum Analyzer for Broad-Beam Ion sources,” AIAA-87-1081, May 1987.
- Kusakabe, T., Horiuchi, T., Nagai, N., Hanaki, H., and Konomi, I., “Charge Transfer of Multiply Charged Slow Argon, Krypton, and Xenon ions on Atomic and Molecular

- Targets. Single-Charge Transfer Cross Sections,” *Journal of Physics B: Atomic and Molecular Physics*, Vol. 19, pp. 2165-2175, 1986.
- Laframboise, J.G., “Theory of Spherical and Cylindrical Langmuir Probes in a Collisionless, Maxwellian Plasma at Rest,” UTIAS Report No. 100, Toronto, Ontario, June 1966.
 - Lecture Notes for the Course, “Production and Diagnosis of Process Plasmas,” Princeton Scientific Consultants, Inc., Princeton, New Jersey, Nov. 1984.
 - Lieberman, M.A. and Lichtenberg, A.J., Principles of Plasma Discharges and Materials Processing, John Wiley & Sons, Inc., New York, 1994.
 - Lochte-Holtgreven, W., Editor, Plasma Diagnostics, AIP Press, Woodbury, New York, 1995.
 - Manzella, D.H. and Sankovic, J.M., “Hall Thruster Ion Beam Characterization,” AIAA-95-2927, July 1995.
 - Manzella, D.H., “Stationary Plasma Thruster Ion Velocity Distribution,” AIAA-94-3141, June 1994.
 - Manzella, D.H., “Stationary Plasma Thruster Plume Emissions,” IEPC-93-097, Sept. 1993.
 - Morozov, A.I., “Stationary Plasma Thruster (SPT) Development Steps and Future Perspectives,” IEPC-93-101, Sept. 1993.
 - Morozov, A.I., Esipchuk, Y.V., Kapulkin, A.M., Nevrovskii, V.A., and Smirnov, V.A., “Effect of The Magnetic Field on a Closed-Electron-Drift Accelerator,” *Soviet Physics, Technical Physics*, Vol. 17, No. 3, pp. 482-487, Sept. 1972.
 - Morozov, A.I., Esipchuk, Y.V., Tilinin, G.N., Trofimov, A.V., Sharov, Y.A., and Shchepkin, G.Y., “Plasma Accelerator with Closed Electron Drift and Extended Acceleration Zone,” *Soviet Physics, Technical Physics*, Vol. 17, No. 1, pp. 38-45, July 1972.
 - Myers, R.M. and Manzella, D.H., “Stationary Plasma Thruster Plume Characteristics,” IEPC-93-096, Sept. 1993.
 - Nakayama, Y. and Takegahara, H., “C₆₀ Application to Ion Thruster - Inspection of Ionized and Extracted Particle -,” IEPC-97-076, Aug. 1997.
 - Oh, D. and Hastings, D., “Axisymmetric PIC-DSMC Simulations of SPT plumes,” IEPC-95-160, Sept. 1995.

- Oh, D. And Hastings, D., “Experimental Verification of a PIC-DSMC Model for Hall Thruster Plumes,” AIAA-96-3196, June 1996.
- Ohler, S., Gilchrist, B., and Gallimore, A.D., “Microwave Plume Measurements of an SPT-100 using Xenon and a Laboratory Model SPT using Krypton,” AIAA-95-2931, July 1995.
- Oleson, S, Myers, R., Kluever, C., Riehl, J., and Curran, F., “Advanced Propulsion for Geostationary Orbit Insertion and North-South Station Keeping,” AIAA-95-2513, July 1995.
- Palmer, D.W., Thompson, M.W., and Townsend, P.D., Editors, Atomic Collision Phenomena in Solids, (North-Holland Publishing Company, Amsterdam, 1970.), Parilis, E.S., “A Mechanism for Sputtering of Non-Metals by slow Multiply-Charged Ions,” pp. 324-327.
- Patterson, M.J., “Performance Characteristics of Ring-Cusp Thrusters with Xenon Propellant,” AIAA-86-1392, June 1986.
- Pencil, E., Randolph, T., and Manzella, D., “End-of-Life Stationary Plasma Thruster Far-Field Plume Characterization,” AIAA-96-2709, July 1996.
- Pollard, J.E., “Plume Angular, Energy, and Mass Spectral Measurements with the T5 Ion Engine,” AIAA-95-2920, July 1995.
- Randolph, T., Kim, V., Kaufman, H., Kozubsky, K., Zhurin, V., and Day, M., “Facility Effects on Stationary Plasma Thruster Testing,” IEPC-93-093, Sept. 1993.
- Randolph, T., Pencil, E., and Manzella, D., “Far-Field Plume Contamination and Sputtering of the Stationary Plasma Thruster,” AIAA-94-2855, June 1994.
- Rapp, D. And Francis, W., “Charge Exchange Between Gaseous Ions and Atoms,” Journal of Chemical Physics, Vol. 37, No. 11, pp. 2631-2645, 1962.
- Rhee, M.S. and Lewis, M.J., “Numerical Simulation of Stationary Plasma Thruster Exhaust Plume,” AIAA-95-2928, July 1995.
- Roboz, J., Introduction to Mass Spectrometry Instrumentation and Techniques, Interscience Publishers, New York, 1968
- Rundle, H.W., Clark, D.R., and Deckers, J.M., “Electron Energy Distribution Functions in an O₂ Glow Discharge,” Canadian Journal of Physics, Vol. 51, pp. 144-148, 1973.
- Sankovic, J.M., Hamley, J.A., and Haag, T.W., “Performance Evaluation of the Russian SPT-100 Thruster at NASA LeRC,” IEPC-93-094, Sept. 1993.

- Shishkin, G.G. and Gerasimov, V.F., "Plasma Instabilities in Accelerators with Closed Electron Drift," *Soviet Physics, Technical Physics*, Vol. 20, No. 9, pp. 1171-1174, Sept. 1975.
- Simon, A., "Instability of a Partially Ionized Plasma in Crossed Electric and Magnetic Fields," *The Physics of Fluids*, Vol. 6, No. 3, pp. 382-388, March 1963.
- Sonin, A.A., "Free Molecular Langmuir Probe and its Use in Flowfield Studies," *AIAA Journal*, Vol. 4, No. 9, pp. 1588-1596, 1966.
- Sovey, J.S., "Improved Ion Containment Using A Ring-Cusp Ion Thruster," *Journal of Spacecraft and Rockets*, Vol. 21, No. 5, pp. 488-495, 1984.
- Stenzel, R.L., Gekelman, W., Wild, N., Urrutia, J.M., and Whelan, D., "Directional Velocity Analyzer for Measuring Electron Distribution Functions in Plasmas," *Review of Scientific Instruments*, Vol. 54, No. 10, pp. 1302-1310, Oct. 1983.
- Takegahara, H., Kasai, Y., "Beam Characteristics Evaluation of ETS-VI Xenon Ion Thruster," *IEPC-93-235*, Sept. 1993.
- Vahrenkamp, R.P., "Measurement of Double Charged Ions in The Beam of A 30 cm Mercury Bombardment Thruster," *AIAA-73-1057*, Oct. 1973.
- Volkov, V., Morozov, A., Sveshnikov, A., Jakunin, S., "Numerical Modeling of Ion Dynamics in Systems with Closed Drift," *Fizika Plazmi*, Vol. 7, No. 2, pp. 245-253.
- Weast, R.C., CRC Handbook of Chemistry and Physics, 69th Edition, CRC Press, Inc., Boca Raton, FL, 1988.
- White, F.A., Mass Spectrometry in Science and Technology, John Wiley & Sons, Inc., New York, 1968.
- Young, J.R., "Penetration of Electrons and Ions in Aluminum," *Journal of Applied Physics*, Vol. 27, No. 1, pp. 1-4, Jan. 1956.
- Zharinov, A.V. and Popov, Y.S., "Acceleration of Plasma by a Closed Hall Current," *Soviet Physics, Technical Physics*, Vol. 12, No. 2, pp. 208-211, Aug. 1967.
- Zhurin, V., Kahn, J., Kaufman, H., Kozubsky, K., and Day, M., "Dynamic Characteristics of Closed Drift Thrusters," *IEPC-93-095*, Sept. 1993.
- Zhurin, V.V., Kaufman, H.R., and Robinson, R.S., "Physics of Closed Drift Thrusters," *IEPC-97-191*, August 1997.
- Zubkov, I.P., Kislov, A.Y., and Morozov, A.I., "Experimental Study of a Two-Lens Accelerator," *Soviet Physics, Technical Physics*, Vol. 15, No. 11, pp. 1796-1800, May 1971.

